AD-A236 213

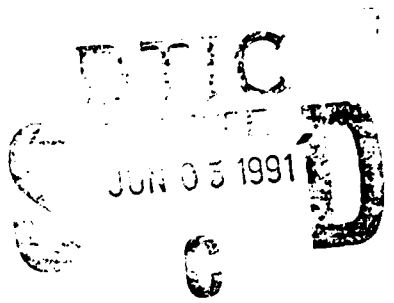

OFFICE OF NAVAL RESEARCH
Contract N00014-87-K-0514

Technical Report
May, 1991

PARTICLE EMISSION AND CHARGING EFFECTS INDUCED BY FRACTURE

J. Thomas Dickinson

DISTRIBUTION STATEMENT A
Approved for public release;
Distribution Unlimited

Washington
State University

DEPARTMENT OF PHYSICS

91 6 4 001

91-01116

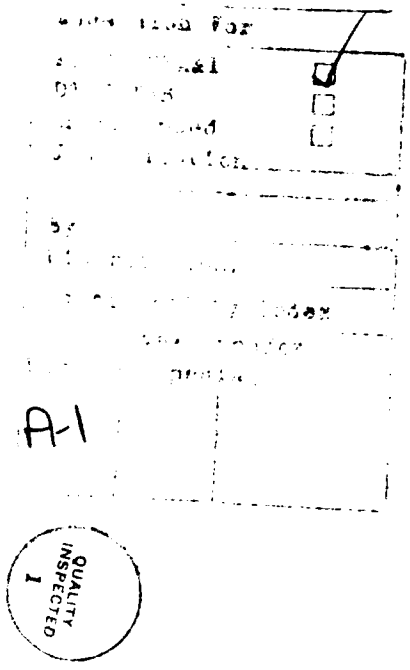

OFFICE OF NAVAL RESEARCH
Contract N00014-87-K-0514

Technical Report
May, 1991

PARTICLE EMISSION AND CHARGING EFFECTS INDUCED BY FRACTURE

J. Thomas Dickinson

Department of Physics
Washinton State University
Pullman, WA 99164-2814

Reproduction in whole or part is permitted for any purpose of the United States Government.

Approved for public release; distribution unlimited.

SECURITY CLASSIFICATION OF THIS PAGE

REPORT DOCUMENTATION PAGE

Form Approved
OMB No. 0704-0188

1a. REPORT SECURITY CLASSIFICATION UNCLASSIFIED	1b. RESTRICTIVE MARKINGS
2a. SECURITY CLASSIFICATION AUTHORITY	3. DISTRIBUTION / AVAILABILITY OF REPORT APPROVED FOR PUBLIC RELEASE DISTRIBUTION UNLIMITED
2b. DECLASSIFICATION / DOWNGRADING SCHEDULE	
4. PERFORMING ORGANIZATION REPORT NUMBER(S) FRACTO 91	5. MONITORING ORGANIZATION REPORT NUMBER(S)
6a. NAME OF PERFORMING ORGANIZATION / 6b. OFFICE SYMBOL (If applicable)	7a. NAME OF MONITORING ORGANIZATION OFFICE OF NAVAL RESEARCH PROPULSION AND ENERGETICS PROGRAM
6c. ADDRESS (City, State, and ZIP Code) WASHINGTON STATE UNIVERSITY PULLMAN, WA 99164-2814	7b. ADDRESS (City, State, and ZIP Code) 800 NORTH QUINCY STREET ARLINGTON, VA 22217
8a. NAME OF FUNDING / SPONSORING ORGANIZATION / 8b. OFFICE SYMBOL (If applicable)	9. PROCUREMENT INSTRUMENT IDENTIFICATION NUMBER
8c. ADDRESS (City, State, and ZIP Code)	10. SOURCE OF FUNDING NUMBERS PROGRAM ELEMENT NO. / PROJECT NO. / TASK NO. / WORK UNIT ACCESSION NO.

11. TITLE (Include Security Classification)

PARTICLE EMISSION AND CHARGING EFFECTS INDUCED BY FRACTURE

12. PERSONAL AUTHOR(S)

J. THOMAS DICKINSON

13a. TYPE OF REPORT	13b. TIME COVERED	14. DATE OF REPORT (Year, Month, Day)	15. PAGE COUNT
TECHNICAL	FROM 6/1/89 TO 5/30/91	May 20,1991	232

16. SUPPLEMENTARY NOTATION

17. COSATI CODES			18. SUBJECT TERMS (Continue on reverse if necessary and identify by block number)
FIELD	GROUP	SUB-GROUP	CRACK PROPAGATION, FRACTURE, PARTICLE EMISSION, FRACTO-EMISSION ENERGETIC MATERIALS, RDX, RADIATION DAMAGE, INTERFACIAL FAILURE, ELECTRICAL BREAKDOWN, MICROCRACKING, LASER ABLATION, SURFACE CHARGE, FRACTOGRAPHY, CRYSTAL DEFECTS, SCANNING TUNNELING MICROSCOPY

19. ABSTRACT (Continue on reverse if necessary and identify by block number)

We report on three research areas that have been based on our capabilities to a) detect and characterize particle release from surfaces on fast time scales, and b) to obtain high resolution topographical information utilizing scanning tunneling and atomic force microscopy. The three areas of study have been fracto-emission, Scanning tunneling microscopy studies of fracture surfaces of crystals and polymers, and UV laser interactions with surfaces. These studies have focused on the examination of the energetic processes accompanying fracture, particularly those involving heat generating mechanisms such as dislocation motion and plastic deformation, phenomena at interfaces (often involving charge transfer processes), and high energy UV lasers interacting with inorganic and organic materials. A novel study of the interaction of 248 nm excimer laser radiation with single crystal RDX is included.

20. DISTRIBUTION / AVAILABILITY OF ABSTRACT ☒ UNCLASSIFIED/UNLIMITED ☐ SAME AS RPT ☐ DTIC USERS	21. ABSTRACT SECURITY CLASSIFICATION UNCLASSIFIED
22a. NAME OF RESPONSIBLE INDIVIDUAL R. S. MILLER	22b. TELEPHONE (Include Area Code) 202 964-4404 / 22c. OFFICE SYMBOL

DD Form 1473, JUN 86 Previous editions are obsolete.

SECURITY CLASSIFICATION OF THIS PAGE

UNCLASSIFIED

TABLE OF CONTENTS

I.	Technical Summary	1
II.	Introduction	1
III.	Atomic and Molecular Emission Following Fracture of Alkali Halides: A Dislocation Process	9
IV.	Atomic and Molecular Emission Accompanying Fracture of Single-Crystal Ge: A Dislocation Driven Process	23
V.	Alkali Emission Accompanying Fracture of Sodium Silicate Glasses	27
VI.	Fractal Character of Crack Propagation in Epoxy and Epoxy Composites as Revealed by Photon Emission During Fracture	56
VII.	Fracto-Emission from Deuterated Titanium: Supporting Evidence for a Fracto-Fusion Mechanism	70
VIII.	Fracto-Emission from Embedded Interfaces	84
IX.	Electrical Transients During Interfacial Debonding and Pullout of a Metal Rod from an Epoxy Matrix	121
X.	Fracto-Emission During the Interfacial Failure of a Metal-Oxide-Semiconductor System: Au-SiO_2-Si	146
XI.	Scanning Tunneling Microscope Observations of MgO Fracture Surfaces	152
XII.	Scanning Tunneling Microscope Observations of Polymer Fracture Surfaces	161
XIII.	Consequences of Simultaneous Exposure of Inorganic Solids to Excimer Laser Light and an Electron Beam	202
XVI.	Precursors to the Photo-Ablation of Sodium Trisilicate Glass Due to UV Excimer Irradiation	208
XV.	Negative Charge Emission Due to Excimer Laser Bombardment of Sodium Trisilicate Glass	216
XVI.	Mass Spectroscopy Study of Products from Exposureof Cyclotrimethylene-trinitramine Single Crystals toKrF Excimer Laser Radiation	222

I. Technical Summary

Three areas have been pursued intensively utilizing our capabilities to a) detect and characterize particle release from surfaces on fast time scales, and b) to obtain high resolution topographical information utilizing scanning tunneling and atomic force microscopy. The three areas of study have been:

a) fracto-emission,
b) STM and AFM studies of fracture surfaces, and
c) UV laser interactions with surfaces

Our goals have been to examine the energetic processes accompanying fracture, particularly those involving heat generating mechanisms such as dislocation motion and plastic deformation, phenomena at interfaces (often involving charge transfer processes), and high energy UV lasers interacting with inorganic and organic materials.

What follows are short descriptions of our recent work.

II. Introduction

Dislocation-related Emissions: Some fracto-emission components from alkali halides appear to be related not to bond-breaking during the fracture event, but to the recovery of fracture-induced plastic deformation. We have shown that neutral emission from single-crystal NaCl and LiF is due to the emergence at the fracture surface of dislocations driven into the bulk material during crack growth. This emission is delayed by a few ms from the time of fracture. We discuss the neutral atom and molecular emissions from the alkali halides in **Section III**. This work recently appeared in J. Mater. Res. **6**, 112 (1991). Evidence for the relaxation of plastic deformation by dislocation motion toward fracture surfaces has been provided by careful X-ray topography on indented single crystals ["X-ray topography evidence for energy dissipation at indentation cracks in MgO crystals," K. C. Yoo et al., J. Mater. Sci. Lett. 3(6), 560-562 (1984)]. However, these studies provide little information on the time scales of these relaxations. As this process deposits considerable energy in a very small volume of material, this dislocation motion has important implications in the fracture of sensitive energetic materials, including explosives and rocket propellants, i.e. fracture could in principle result in unexpected ignition. Our results indicate that dislocation emergence deposits this energy on times scales of 1 ms or less, suggesting that the *rate* of energy deposition is also high. Preliminary results on a model energetic material, ammonium perchlorate, show delayed spikes of certain neutral molecules, suggesting that a similar process does indeed occur in important energetic materials.

A related study on a fundamental material, single crystal Ge, is presented in **Section IV** and has recently appeared in Phys. Rev. Letters **66**, 2120 (1991), where we see the delayed emission of Ge and Ge_2, again attributed to dislocation activity accompanying dynamic fracture. We were able to obtain a rough measurement of the velocity of the Ge atoms which is ~ 700 m/s and supports a *non-thermal* emission mechanism.

An exciting and related study on alkali containing silicates shows that even in very brittle glasses, stored deformation related energy can be released in a concerted fashion to emit alkali atoms, thus relates nicely to the crystalline materials. This work is discussed in **Section V** and will appear in the June issue of J. Mat. Res.

Fractal Character of Crack Propagation. We have examined the phE and EE during crack propagation in a common epoxy, Shell Epon 828/Z Hardner, filled at 0, 20 and 40 % (by weight) with ~7 μm Al_2O_3 particles. The particular measurement of interest involves examination of the fluctuations in the photons accompanying fracture of this epoxy (acquired at 5 ns intervals); measurements on this resin system support our earlier results showing that the phE exhibited *chaotic* as opposed to stochastic, random behavior. We examine in more detail these signals and discuss possible relations to fracture toughness and length scales involved. This work is presented in **Section VI** and was published in J. Mat. Res **6** 183 (1991).

Possible Fracto-Fusion Mechanism for Observed Neutrons in Deuterated Metals. In the heat of excitement associated with the possibility that the observed bursts of neutrons seen by Jones, Scaramuzzi, and Menlove (separate groups) are due to microcrack-induced charge separation which accelerates deuterons-- we collaborated with workers at Los Alamos in examining the fracto-emission accompanying the fracture of deuterated Titanium. This was to explore the possibility that the so-called fracto-fusion model was the origin of such

neutron emission. We showed that charged particles are in fact produced by fracture, both negative and positive and are pursuing measurements of energy as well as species of these emissions. No claim of observations of fusion products was made nor expected. It is our understanding to date that most of the neutron signals **have not been reproducible;** Thus, our study is of more interest in terms of a materials science interest. The work is described in **Section VII.**

Photon Emission from Interfacial Failure at Embedded Interfaces: By use of semi-transparent materials, we have been able to detect interfacial failure at interfaces *inside* a polymer matrix. We have also used simultaneous electron emission measurements to determine the exact instant when cracks reach the surface of the sample relative to the internal failure. We have completed measurements include the pullout process of metal cylinder from an epoxy matrix. We also investigated the frictional failure of single rod pullout (following debonding) to determine if fracto-emission signals can be detected from this process where stick-slip behavior is observed. This work is described in **Section VIII** and has been submitted for publication to J. Appl. Phys.

Measurements of Electrical Transients during Internal Debonding: We have used fast electrical measuring techniques to examine the transient currents generated in a steel rod-epoxy matrix system, similar to that used above. Interfacial failure in the steel rod-epoxy matrix system was seen to be accompanied by distinctive voltage and current signals which are correlated with interfacial failure events inferred from small changes in rod strain. We have developed a model for the current generated during debonding as well as during the initial pullout event immediately following fracture. This work is discussed in **Section IX** and has been submitted to J. Appl. Phys.

Fracto-Emission From a Model Interface: Au-SiO_2-Si: We have measured electron and photon emission during the detachment of gold films vapor deposited on oxidized Si, a system where energy levels and electronic structure has been well studied. We show that the resulting emissions are consistent with the effects of charge separation predicted from the initial formation of the Au-SiO_2 interface, yet greatly modified by charge transfer through the oxide layer to and from the Si substrate. This study is discussed in **Section X** and has been published in J. Vac. Sci. Technol. A 8 2401 (1990).

Scanning Tunneling Microscopy of Fracture Surfaces: In the fracture of semi-brittle materials, we expect that the fractography of the surface to be intimately related to energy dissipation and failure mechanisms. These can occur on a number of size scales, including the nanometer scale. We have finished two studies using scanning tunneling microscopy (STM) to examine topography of fracture surfaces on very small length scales. We present here: (1) observations of fracture surfaces of single crystal MgO (**Section XI** -- published in J. Vac. Sci. Technol. A 8 3470 (1990) and (2) studies of fracture surfaces of polymers (poly(methyl methacrylate), polystyrene, and polycarbonate (**Section XII** -- submitted for publication to J. Mat. Res.).

Excimer Laser Interactions with Solid Surfaces. We have examined in the influence of UV Excimer radiation on Na_2O $3SiO_2$ glass. We have characterized the damage to the surfaces of this material as well as determinations of the type of particles and their velocities due to the pulsed laser bombardment. This includes measurements of the charged particle emission (photoelectrons, ±ions, and neutral emission (both ground state and excited) as a function of photon flux. We examined in detail the onset of significant removal of matter from the glass (ablation), where we see evidence for laser *induced* absorption at 248 nm (thus a threshold in exposure for damage to occur), an electrostatic acceleration of positively charged particles interacting with laser heated electrons (inverse bremstrahlung) resulting in ~30 eV Na atoms in high lying Rydberg states.

Most recently, we made a new discovery concerning the process of inducing etching of wide bandgap materials, namely the strong influence of the simultaneous application of beams of electrons *and* laser light. We showed direct evidence of a synergism between these radiation sources. This work is presented in **Section XIII** and has been published in J. Appl. Phys. **68**, 1831 (1990). Related work on a mechanistic model describing the effects of intense UV radiation pulses on materials is outlined in **Section XIV** which as been published in Mat. Res. Soc. Symp. Proc. **158**, 463 (1990). Measurements of the negative charge emission accompanying laser bombardment of a silica glass are presented in **Section XV** (published in J. Appl. Phys. **68**, 4253 (1990).

Decomposition of RDX by Excimer Laser Radiation. We completed a study of consequences of excimer radiation on single crystal RDX, an explosive molecular crystal, where we showed that decomposition of the crystalline material occurs and that photochemical processes dominate. Furthermore, the resulting etching of the molecular crystal is related to the induced chemical reactions, as seen in the product distributions coming from the crystal as a function of laser fluence. Finally, we showed that there was a sustained reaction following the laser pulse which we could quantify with the luminescence coming from the reaction products. This work is described in Section XVI and is published in J. Appl. Phys. 67 3641 (1990).

II. Participants, Collaborators, Recent Presentations, Publications

Faculty:	J. T. Dickinson, PI John Hirth, Professor Dick Hoagland, Professor Ed Donaldson, Professor Emeritus
Postdoctoral Researchers:	Alberto Annunziata, Visiting Postdoc Materials Research Institute (ISRIM), Terni, Italy.
	Leo Nick, Visiting Postdoc, Chemistry Department University of Clausthal, Germany.
	Steve Langford, WSU
Research Staff:	Les Jensen, Research Physicist
Visiting Scientists:	Jack Mecholsky, Material Sciences Department University of Florida
	Dr. Yoshihisa Watanabe, Dept. of Mathematics and Physics National Defense Academy of Japan Hashirimizu, Yokosuka Kabagawa 239 JAPAN
	Dan Bloom, Chair Physics Department Winona State University.
Graduate Research Assistants	Digala Kulawanza Ma ZhenYi Sunkyo Lee
Undergraduate Lab Assistants	Kurt Zimmermann Larry Hiller Ron Washburn

Invited Talks

"Fracto-Emission from Interfaces and Composites," DOW Chemical Co., January, 1989.

"Fracto-Emission from Polymers and Interfaces", Boeing Co, January, 1989

"Fracto-Emission from Cohesive and Adhesive Failure of Materials", Materials Science Dept. U. of Michigan, March, 1989.

"Fracto-Emission from Interfacial Failure", Symposium on Adhesion, Materials Research Society, San Diego, April, 1989.

"Fracto-Emission from Elastomers", Frontiers in Elastomer Science Symposium, ACS, Mexico City, May, 1989.

"Fracto-Emission Accompanying Adhesive Failure", Symposium on Adhesion, ACS, Seattle, June, 1989.

"Fracto-Emission from Insulators and Interfaces", International Conference on Fracture, Irsee, Germany, June, 1989.

"Fracto-Emission: Recent studies in Particle Emission Accompanying Fracture," Sandia National Laboratories, July, 1989.

"Electrical Phenomena Accompanying Fracture," Sandia National Laboratories, July, 1989.

"Localized Energetic Processes During Fracture," ONR-NIST Workshop on Fundamental Concepts in Theory of Fracture, Gaithersburg, 1989.

"Fracto-Emission Accompanying Adhesive Failure", Case Western Reserve University, November, 1989.

"Particle Emission Studies of Fracture," Ohio Section of American Vacuum Society, Cleveland, November, 1989.

"Fracto-Emission: Recent studies in Particle Emission Accompanying Fracture," Dept. of Physics, University of Texas-El Paso, November, 1989.

"Excimer Laser Ablation of Materials," Dept. of Physics, University of Texas-El Paso, November, 1989.

"Fracto-Emission: Recent studies in Particle Emission Accompanying Fracture," Dept. of Physics, Montana State University, April, 1990.

"Excimer Laser Interactions at Surfaces," Dept. of Physics, Montana State University, April, 1990.

"Atomic and Molecular Processes Accompanying Fracture", BioSym Technology Symposium, Dallas, April, 1990.

"Fracto-Emission from Polymer Surfaces and Interfaces," ACS Macromolecular Sectariat, Boston, April, 1990.

"Fracto-Emission from Polymers and Interfacial Failure," Dow-Corning Co., Midland, MI, June, 1990.

"Fracto-Emission from Ceramics and Glasses," Dow Chemical Co., Midland, MI, June, 1990.

"Fracto-Emission From Glass Surfaces and Interfaces," Gordon Conference on Glass, June, 1990.

"Fracto-Emission from Polymers and Composites," Prague International Conference on Polymers, Prague, Czechoslovakia, July, 1990.

Fracto-Emission from Thermoplastics," Dow Chemical Co., September, 1990.

"Characterization of Fracture Surfaces," Pacific Coast Meeting of American Ceramics Society Meeting, Oct., 1990.

"Fracto-Emission: Recent studies in Particle Emission Accompanying Fracture," Xerox Corporation, Rochester, NY, October, 1990.

"Excimer Laser Interactions at Surfaces," Dept. of Materials Science, University of Washington, October, 1990.

"Fracto-Emission: Recent studies in Particle Emission Accompanying Interfacial Fracture," 3M Co., St. Paul, MN, February, 1991.

"Give Me a Break: A Molecular View of Fracture, Washington State University Distinguished Faculty Address, February, 1991.

To be presented:

"Fracto-Emission: Recent studies in Particle Emission Accompanying Fracture," International Symposium on Fracture Mechanics of Ceramics, Nagoya, Japan, July, 1991.

"Excimer Laser Surface Interactions," SPIE, San Jose, CA, September, 1991.

16 Lectures on Energetic Processes Accompanying Fracture, National Defense Academy of Japan, October, 1991.

Contributed Talks

"Observations of Single Crystal MgO Fracture Surfaces by Scanning Tunneling Microscopy, American Vacuum Society, Boston, October, 1989.

"Precursors to Photo-Ablation of Sodium Trisilicate Glass Due to UV Excimer Irradiation," American Vacuum Society, Boston, October, 1989.

"Fracto-emission during the interfacial failure of a metal-oxide-semiconductor system," American Vacuum Society, Boston, October, 1989.

"Fluctuations in Photon Emission During Epoxy Fracture: Evidence for Chaos," Materials Research Society, Boston, November, 1989.

"Precursors to Photo-Ablation of Sodium Trisilicate Glass Due to UV Excimer Irradiation," Materials Research Society, Boston, November, 1989.

"Fracto-Emission Studies of Interfacial Failure in Composites," Materials Research Society, Boston, November, 1989.

"The Time Dependence of Photon Emission During Fracture of Filled and Unfilled Epoxy: Evidence for Chaos," American Physical Society March Meeting, Anaheim, March, 1990.

"Scanning Tunneling Microscope Observations of MgO Fracture Surfaces," American Physical Society March Meeting, Anaheim, March, 1990.

"Precursors to Photo-Ablation of Sodium Trisilicate Glass Due to UV Excimer Irradiation," American Ceramics Society, Dallas, April, 1990.

"Fracto-emission during the interfacial failure of Au-oxide-Si," American Ceramics Society, Dallas, April, 1990.

"Characterization of Single Crystal MgO Fracture Surfaces by Scanning Tunneling Microscopy, American Ceramics Society, Dallas, April, 1990.

"Scanning Tunneling Microscopy studies of Fracture Surfaces: MgO and LiF," American Ceramics Society--Pacific Coast Conference, Seattle, October, 1990.

"Evidence for Chaos in Fracture of Composites," American Ceramics Society--Pacific Coast Conference, Seattle, October, 1990.

"Fracto-Emission Accompanying Adhesive Failure of Embedded Interfaces," American Vacuum Society, Toronto, October, 1990.

"Delayed Atomic and Molecular Emission from Alkali Halides Following Cleavage Fracture," American Vacuum Society, Toronto, October, 1990.

"Fracto-Emission During Debonding and Pullout of a Metal Rod from Epoxy", APS March Meeting, Cincinnati, OH March, 1991.

"STM observations of Crack Initiation Zones in Glass and Glassy Polymers," APS March Meeting, Cincinnati, OH March, 1991.

"Atomic and Molecular Emission following Fracture of Alkali Halides: a Dislocation Driven Process," APS March Meeting, Cincinnati, OH March, 1991.

"STM observations of Crack Initiation Zones in Glass and Glassy Polymers," American Ceramics Society Meeting, Cincinnati, OH April, 1991.

"Atomic and Molecular Emission following Fracture of Alkali Halides: a Dislocation Driven Process," American Ceramics Society Meeting, Cincinnati, OH April, 1991.

"Alkali Emission Accompanying Fracture of Soda Silicate and Soda Lime Glasses," American Ceramics Society Meeting, Cincinnati, OH April, 1991.

Photo-Etching of Inorganic Materials Due to UV Excimer Irradiation and Electron Bombardment," Workshop on Laser Ablation Mechanisms and Applications, Oak Ridge, TN, April, 1991.

To be presented:

"Photo-Etching of Inorganic Materials Due to UV Excimer Irradiation and Electron Bombardment," 35th Int. Symposium on Electron, Ion, and Photon Beams, Seattle, WA, May, 1991.

Publications

J. T. Dickinson and L. C. Jensen, "Radiation Induced Crack Initiation and Crack Growth in Polymers, " to appear in *Proceedings of the 9th International Symposium on Exoelectron Emission and Applications*," Wroclaw, Poland, 1988.

W. G. Durrer, H. Poppa, and J. T. Dickinson, "The Decomposition of Unsaturated Hyrocarbons on Small Pd Particles," J. Catalysis 115, 310 (1989).

S. C. Langford, Ma Zhenyi, and J. T. Dickinson, "Photon emission as a probe of chaotic processes accompanying fracture", J. Mat. Research 4, 1272 (1989).

J. T. Dickinson, "Fracto-Emission from Interfacial Failure", (invited review paper) Materials Research Society Symposium Proceedings 153, *Interfaces Between Polymers, Metals, and Ceramics*, B. M. DeKoven, A. J. Gellman, and R. Rosenberg ed., pp. 331-344, (1989).

S. C. Langford and J. T. Dickinson, "The Emission of Particles and Photons from the Fracture of Minerals and Inorganic Materials," (invited review) in *Spectroscopic Characterization of Minerals and Their Surfaces*, L. M. Coyne, S. W. McKeever, and D. F. Blake eds, ACS Symposium Series Publication 415, pp. 224-244, (1990).

J. T. Dickinson, "Fracto-Emission from Adhesive Failure", Invited Review, *Adhesive Bonding*, L. H. Lee, Ed., Plenum Press, New York (1990).

J. T. Dickinson, L. C. Jensen, H. Schreuder-Stacer, Electron and Photon Emission from Fracture of Metal-Elastomer Interfaces," to appear in Journal of Rubber Chemistry and Technology.

J. T. Dickinson, L. C. Jensen, S. C. Langford, R. R. Ryan, and E. Garcia, "Fracto-Emission from Deuterated Ti: Supporting Evidence for a Fracto-Fusion Mechanism," J. Mat. Res. 5, 109 (1990).

D. L. Doering, S. C. Langford, J. T. Dickinson, and P. Xiong-Skiba, "Fracto-emission during the interfacial failure of a metal-oxide-semiconductor system: Au-SiO_2-Si," J. Vac. Sci. Technol. A. 8, 2401 (1990).

E. E. Donaldson, J. T. Dickinson, and Naiqiang Wu, "Fracto-Emission Induced Electrical Breakdown in Vacuum," Transactions IEEE Elec. Insul. 25, 549 (1990).

S. C. Langford, L. C. Jensen, Ma Zhenyi, and J. T. Dickinson, "Scanning Tunneling Microscopy Analysis of MgO Fracture Surfaces, J. Vac. Sci. Technol. A 8, 3470 (1990).

J. T. Dickinson, L. C. Jensen, D. L. Doering, and R. Yee, "Mass spectroscopy study of products from exposure of RDX single crystals to KrF Excimer laser radiation," J. Appl. Phys. 67, 3641 (1990).

J. T. Dickinson, "Fracto-Emission", (invited review), Chap. 10 in *Non-Destructive Testing of Fibre-Reinforced Plastic Composites - II,* J. Summerscales, ed. Elsevier Applied Science, London (1990), pp. 429-482.

J. T. Dickinson, S. C. Langford, L. C. Jensen, P. A. Eschbach, L. R. Pederson and D. R. Baer, "Consequences of simultaneous exposure of inorganic solids to excimer laser light and an electron beam," J. Appl. Phys. 68, 1831 (1990).

P. A. Eschbach, J. T. Dickinson, S. C. Langford, L. C. Jensen, L. R. Pederson and D. R. Baer, "Precursors to the Photo-Ablation of sodium Trisilicate Glass due to UV Excimer Irradiation", Mat. Res. Soc. Symp. Proc. 158, (1990), pp. 463-469.

J. T. Dickinson and Ma Zhenyi, "Fracto-Emission Accompanying Adhesive Failure in A Model Fiber Pull-out System," submitted to Die Macromoleculare Chemie, Macromoleuclar Symposia.

Ma Zhenyi, S. C. Langford, and J. T. Dickinson, M. H. Engelhard and D. R. Baer, "Fractal Character of Crack Propagation in Epoxy and Epoxy Composites as Revealed by Photon Emission during Fracture," to appear in J. Mat. Research.

S. C. Langford, L. C. Jensen, J. T. Dickinson, and L. R. Pederson, "Negative charge emission due to excimer laser bombardment of sodium trisilicate glass," J. Appl. Phys. 68, 4253 (1990).

J. T. Dickinson, L. C. Jensen, S. C. Langford, and J. P. Hirth, "Atomic and Molecular Emission Following Fracture of Alkali Halides: A Dislocation Driven Process," to appear in J. Mat. Research.

_. C. Langford, L. C. Jensen, J. T. Dickinson, and L. R. Pederson, "Alkali emission accompanying fracture of sodium silicate glasses," J. Mat. Research 6, 112 (1991).

J. T. Dickinson, S. C. Langford, L. C. Jensen, " Atomic and molecular emission accompanying fracture of single crystal Ge: A Dislocation Driven Process," Phys. Rev. Lett. 66, 2120 (1991).

J. T. Dickinson, L. C. Jensen, H. Schreuder-Stacer, Electron and Photon Emission from Fracture of Metal-Elastomer Interfaces," to appear in Journal of Rubber Chemistry and Technology.

Ma Zhen-Yi and J. T. Dickinson, "Fracto-emission from embedded interfaces," submitted to J. Appl. Phys.

K. A. Zimmermann, S. C. Langford, and L. C. Jensen, "Electrical transients during interfacial debonding and pullout of a metal rod from an epoxy matrix," submitted to J. Appl. Phys.

D. M. Kulawansa, S. C. Langford, J. T. Dickinson, and R. P. Dion, "Scanning Tunneling Microscope Observations of Polymer Fracture Surfaces," submitted to J. Mat. Research.

III. Atomic and molecular emission following fracture of alkali halides: A dislocation driven process

J.T. Dickinson, L.C. Jensen, S.C. Langford, and J.P. Hirth
Physics Department, Washington State University, Pullman, Washington 99164-2814

(Received 15 June 1990; accepted 28 September 1990)

During and following fracture of a number of materials, the emission of photons, electrons, ± ions, and neutral species are observed; these emissions are collectively known as *fracto-emission*. In this work, we present measurements of the neutral particle emission following fracture of two single crystal fcc alkali halides: NaCl and LiF. We observe no measurable emission attributable to release during the fracture event itself. However, after relatively long time intervals of −0.5–250 ms, we observe rapid bursts of alkali atoms, as well as molecular species which include NaCl and $(LiF)_n$ where $n = 1, 2, 3$. Bursts of alkali containing species also occur during loading prior to fracture and for unloaded specimens during heat treatment. We argue that these bursts are due to energetic emergence ("popout") of dislocations at free surfaces.

I. INTRODUCTION

The fracture of many materials in vacuum is accompanied by fracto-emission (Refs. 1–8 and references therein), i.e., the emission of photons, charged particles, and neutral species. The photon, electron, and ion emission intensities are readily sampled on ns time scales and, with appropriately instrumented samples, these emissions can be correlated in time with the fracture event. In the vast majority of our previous work, most emissions exhibited their highest emission intensities *during* the fracture event. Such measurements can provide a great deal of information concerning rapid (km/s) crack growth. In previous work,[3–8] we also showed that a number of neutral species are released with fracture. In the case of silicate glasses,[8] to within a time resolution of 10^{-5} s, major atomic and molecular emission occurs *during* the fracture event. A number of these materials have emissions with properties that are consistent with bond breaking induced decomposition. However, in the case of NaCl and LiF single crystals, we observe no detectable neutral emission during fracture; instead, strong bursts of neutrals are consistently detected *after* fracture, typically delayed 0.5–250 ms from the time of fracture. We shall argue that these delayed bursts are due to energetic processes accompanying the arrival of dislocations from the near surface region at the fracture surface. These signals could provide a relatively simple way of investigating dislocations generated by fracture, indentation, and tribological loading, as well as the kinetics of dislocation motion following rapid mechanical stimulation.

II. EXPERIMENTAL

Single crystals of NaCl and LiF were obtained from Optovac, Incorporated (North Brookfield, Massachusetts). Rectangular samples, 2.5 × 6 × 13 mm^3, were cut and mechanically polished to 0.25 μm diamond grit. The samples were mounted in one of two multiple sample holders, the first a carousel apparatus which allowed the samples to be rotated into place between a loading manipulator and the detectors. The second holder utilized a sample injection mechanism which moved successive samples into position for loading. Both sample holders allowed the rectangular specimens to be loaded in three point bend at a rate of 70 μm/s.

Alkali emission was measured by two techniques. Surface ionization of alkali atoms provided high sensitivity measurements of the total alkali emission, while quadrupole mass spectrometry provided the identities and relative intensities of the major emission components. Figure 1(a) shows schematically a surface ionization detector[9] used with the carousel. Adsorbed alkali metal atoms and compounds on high work function metal surfaces undergo strong charge transfer. At elevated temperatures, this can result in the evaporation of positive alkali metal ions with a probability given by the Saha–Langmuir equation.[10] In our experiments, the ionizing surface was a Pt ribbon, 50 μm × 8 mm × 20 mm, heated to 1200–1300 °C by passing ~32 A dc current through the ribbon. Pt temperatures were determined by optical pyrometry through a Pyrex window viewing the back surface of the ribbon. At these temperatures, Pt has an 80% efficiency for ionization of Na metal atoms and 20% for Li.[9] Efficiencies are somewhat reduced for the alkali halide molecules. The ion collector was connected to the input of a Keithley 602 Electrometer floated at 20 V below ground; at zero current, this potential appears on the collector and thus attracts positive ions. The resulting signals represent the collective alkali atom content of the emission; i.e., no discrimination of alkali atoms from alkali + halide

 © 1991 Materials Research Society

Apparatus for Detection of Emission from Fracture

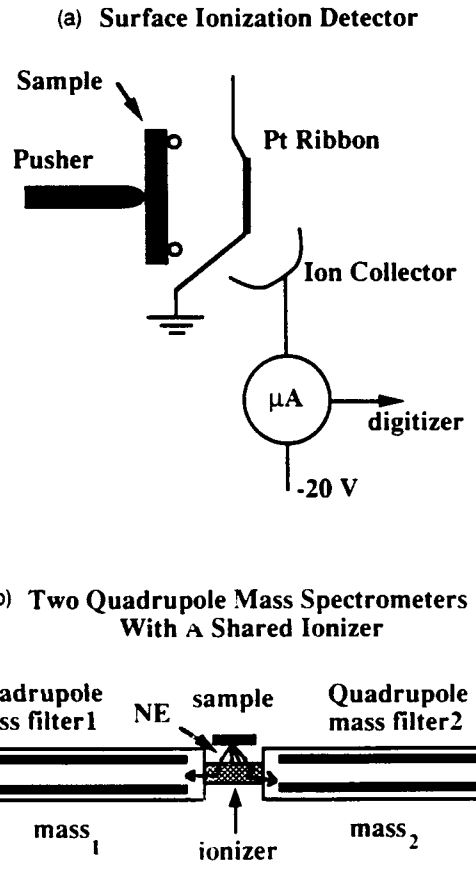

FIG. 1. Schematic diagrams of neutral emission detectors: (a) hot Pt ribbon surface ionization detector sensitive to all alkali metal containing species; (b) two-quadrupole mass spectrometer for time-resolved, simultaneous detection of two mass peaks.

compounds is possible using surface ionization detection. At the Pt surface temperatures used here, the time constant associated with release of the ions from the surface is $\sim 10^{-6}$ s.

A unique two-quadrupole mass spectrometer system, shown schematically in Fig. 1(b), was used to identify the more intense components of alkali emission. The electron impact ionizer was symmetrically situated between two identical quadrupole mass filters. The injector sample holder allowed the sample to be positioned 1 cm from the ionizer, thus providing a reasonable solid angle for detecting emitted neutrals. The electron energy in the ionizer was 70 eV and the emission current during the experiment was kept constant at 1.7 mA. The E fields within the ionizer are such that ions created toward mass filter 1 would most likely enter mass filter 1, and conversely for ions created near mass filter 2. The two focus plate voltages and average positive potential inside the ionizer ("ion energy") were adjusted to maximize sensitivity and mass resolution (~1 amu). The detected ion currents following electron multiplication were measured with identical electrometers. In both detector arrangements, the electrometer outputs were digitized at 20 μs intervals with a Lecroy Digitizer Model 6810. The 25–50 μs rise times and 25–100 μs decay times of these electrometers were the major limitations for describing the temporal behavior of the detected atom and molecular bursts.

Measurements of the applied load were recorded simultaneously with the neutral emission measurements. The drop in load provided a time-of-fracture reference accurate to within 40 μs for comparison with the time-of-occurrence of the bursts. Although the duration of the fracture event was typically not more than a few μs, the emission signals were significantly slower so that this time resolution was sufficient. Emission and load measurements were recorded continuously during loading and stopped after a predetermined interval following fracture. Frequently, the load drop at fracture provided a convenient stop pulse for the digitizers.

To examine the role of dislocations in the emission of neutrals, experiments were undertaken with annealed samples. As noted below, annealing significantly affects dislocation motion in the alkali halides. NaCl samples were polished, annealed at 300 °C for 90 min, and cooled to room temperature in approximately 90 min. The samples were mounted in a sample carousel along with unannealed samples for comparison of the surface ionization emissions accompanying fracture.

Additional experiments were undertaken to determine if neutral emission spikes could be observed when LiF and NaCl samples were heated, in the absence of fracture. Dislocation mobility is known to increase with temperature, so that at sufficiently high temperatures, near-surface dislocations are expected to move to the surface and emerge. Near-surface dislocations are introduced in the polishing process. We also heated indented samples, expecting that the deformation accompanying indentation would result in very high local dislocation densities. Typically 10–20 indents were formed in a Rockwell hardness tester with a spherical metal indenter. Samples were mounted on a Ta strip positioned about 1 cm from and perpendicular to a Pt ribbon for surface ionization detection of alkali-containing emission. Both sample and ribbon dimensions were similar to those used in the fracture work. A chromel-alumel thermocouple was attached to the Ta strip to measure its temperature. The hot Pt filament was sufficiently close to the sample to produce adequate heating rates without auxiliary heaters. Ionization current and thermocouple output measurements were recorded for the first fifty pulses to exceed the digitizer trigger level following the onset of heating. From these records, the

time of occurrence, pulse height, and temperature were easily derived.

III. RESULTS

A. Surface ionization experiments

Figure 2 shows (a) the drop in load and (b) the corresponding ion current versus time produced by the surface ionization detector from the fracture of NaCl. The ion current represents a collective signal for all Na metal containing species (e.g., Na, NaCl, etc.). To be noted first is the delay from fracture of the two bursts, the first at 3 ms after fracture and the second at 6 ms after fracture. Similar signals from a number of samples were consistently delayed by times ranging from 0.5–250 ms, and in some cases as long as 1000 ms. From the integrated area under these two bursts we estimate a lower limit to the number of alkali atoms detected, namely 10^7 and 10^8, respectively. This is somewhat less than the actual number atoms/molecules emitted due to a nonunity detector efficiency plus a solid angle limitation. Considering that one expects only 10^{14} alkali atoms on a 10 mm^2 fracture surface, 10^8 atoms is a large number. An average of four delayed bursts per fracture event was observed in NaCl.

Very small peaks are often seen in higher numbers during deformation (i.e., before fracture) and following fracture. In Fig. 3 we see data taken on a more sensitive electrometer scale, showing a number of these smaller bursts occurring both *before* and *after* fracture. Most of the bursts occurred after fracture. Immediately after fracture a series of large bursts drove the electrometer off-scale. If one examines the raw data carefully, an even larger number of smaller bursts not seen on this graph can be identified both before and after fracture. These smaller bursts range in size from 10^5 to 10^7 detected alkali atoms.

When single crystals of LiF were fractured near the surface ionization detector very similar results were observed. Figure 4 shows data acquired at two different electrometer gain settings, where (b) was taken with an electrometer gain 10 times higher than (a). In Fig. 4(a), similar to the NaCl, we see multiple bursts of alkali-containing emission, the first small peak appearing −2 ms after fracture. A variety of delay times and burst amplitudes are evident. In Fig. 4(b), again a number of smaller bursts are seen, with several off-scale bursts of alkali emission about 30 ms after fracture; the more intense peaks usually showed signs of multiple bursts. The first small burst in this (b) set was 5 ms after fracture. In contrast to the NaCl measurements, in LiF there were rarely any measurable bursts prior to fracture nor bursts after a time delay of 100 ms. The intensity of the LiF emission, after correcting for the relative surface

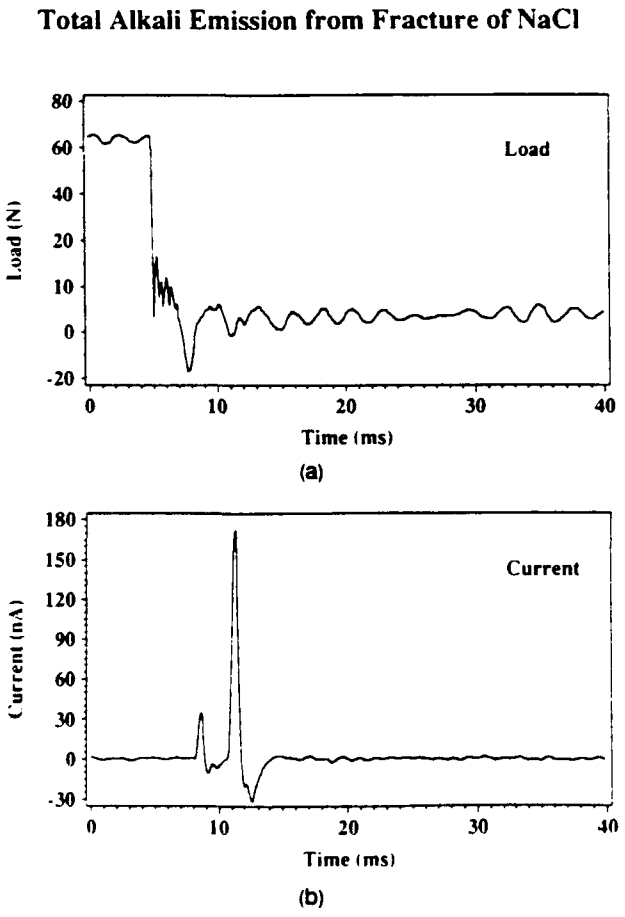

FIG. 2. Simultaneous measurements of (a) load and (b) surface ionization current accompanying the fracture of a NaCl sample. Two strong peaks are seen, delayed by several ms from the fracture event.

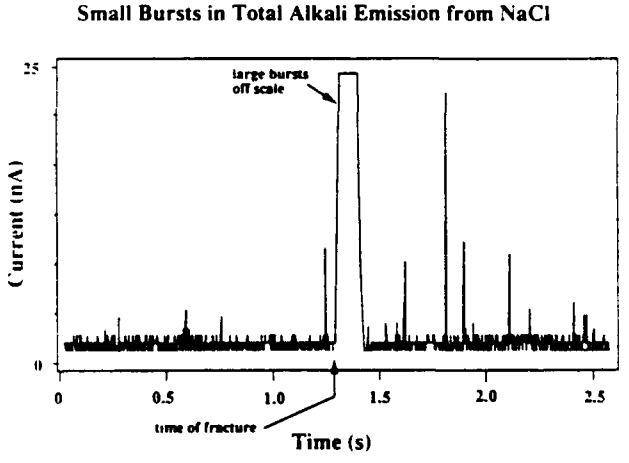

FIG. 3. Alkali containing emission accompanying fracture of NaCl on a more sensitive (×10) electrometer scale. The central region viewed on a narrower time scale is seen to be made up of a series of off-scale bursts. The time delay between the load drop and the onset of the first large burst is about 1 ms.

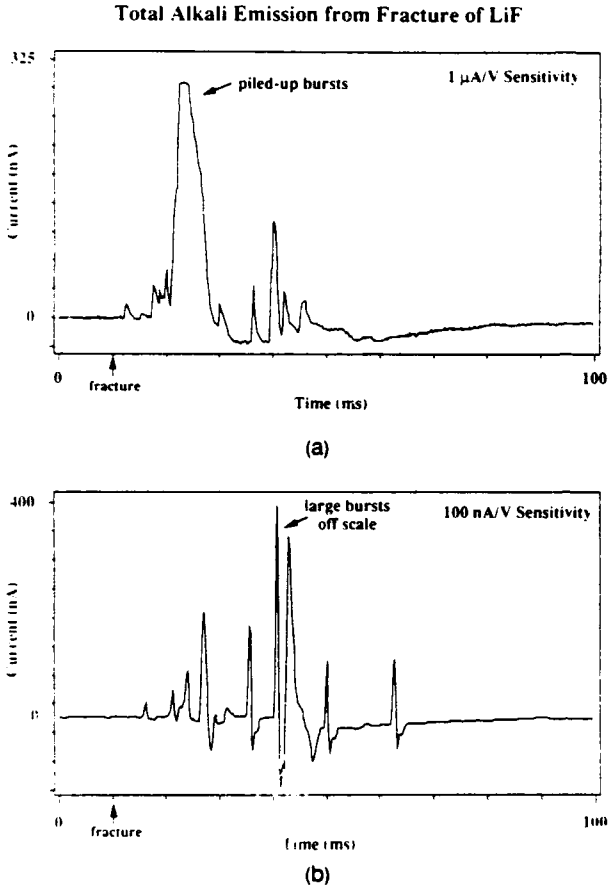

FIG. 4. Alkali containing emissions accompanying fracture of two different LiF samples. The data of (b) were acquired at a more sensitive (×10) electrometer scale than the data of (a). The higher sensitivity of (b) allows the detection of much smaller peaks; however, the largest bursts of (a) and (b) peak at roughly the same current (order of magnitude).

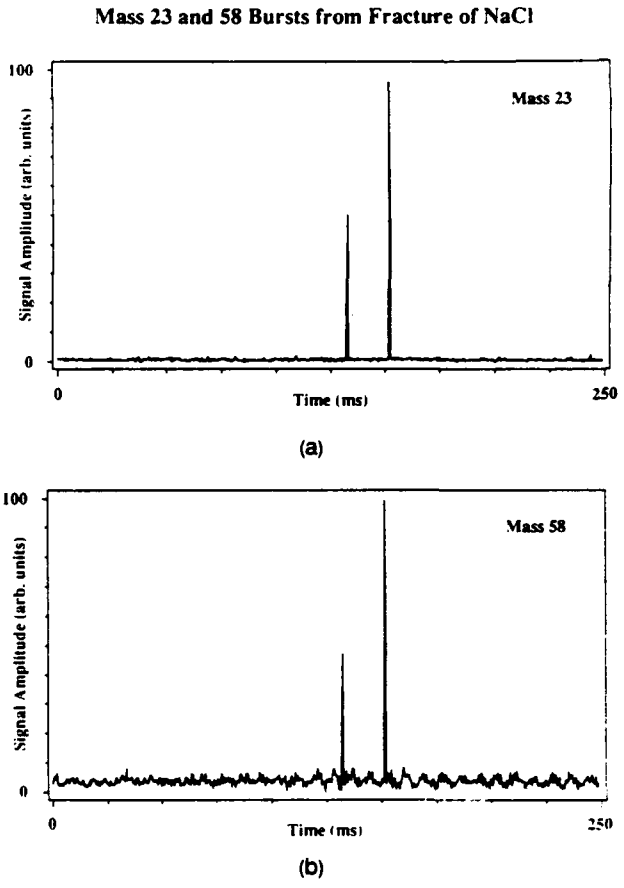

FIG. 5. Simultaneous, two-quadrupole emission measurements at (a) mass 23 (Na^+) and (b) mass 58 ($NaCl^+$) accompanying the fracture of NaCl.

ionization probabilities,[9] is typically a factor of ~2 larger than the NaCl emission. Even with potentially stronger emission, the smaller peaks from LiF may have been difficult to observe due to the lower surface ionization probability for Li.

B. Mass spectrometer experiments

Despite the relatively low sensitivity of the two-quadrupole mass spectrometer, the larger bursts following fracture are readily observed at several mass settings. Figures 5 and 6 show simultaneous measurements of mass pairs from NaCl over time intervals of 250 ms for the major mass peaks observed. In each case, mass measurements were made at mass 23. After correcting for the relative detection efficiencies of the two quadrupoles, the mass 23 signal was used to infer the relative intensities of the other mass peaks. The relative intensities averaged over 10 samples for these peaks are shown in Fig. 7. Using typical cracking fractions for molecular NaCl (parent peak of 58 amu),[11] we can show that the mass 23 and mass 35 peaks are not cracking fractions of NaCl, but are both predominantly due to atomic Na and atomic Cl emission. No Na_2, Cl_2, or $(NaCl)_n$, where $n > 1$, was observed. Thus, in order of intensity, the large neutral emission bursts following fracture of NaCl are composed of Na°, Cl°, and NaCl° in approximate ratio of 25:4:1, without correcting for relative ionization efficiencies. The relative ionization efficiencies of these species increase in the order NaCl° > Na° ≫ Cl°, so that the actual flux of Na° and Cl° from the sample relative to that of NaCl° should be greater than that suggested by the uncorrected peak heights.

In Fig. 8 we compare simultaneous Na and Cl peaks on an expanded time scale. The time behavior of the Cl signal is similar to that of Na, except for a distortion induced by 60 Hz noise. Note that relative to the bursts acquired with the surface ionization detector these peaks are narrow: on the order of 2 ms wide. Accounting for the contribution of instrumental response to the peak width, the actual burst duration may be ≤1 ms. We also note that these peaks appear to be simultane-

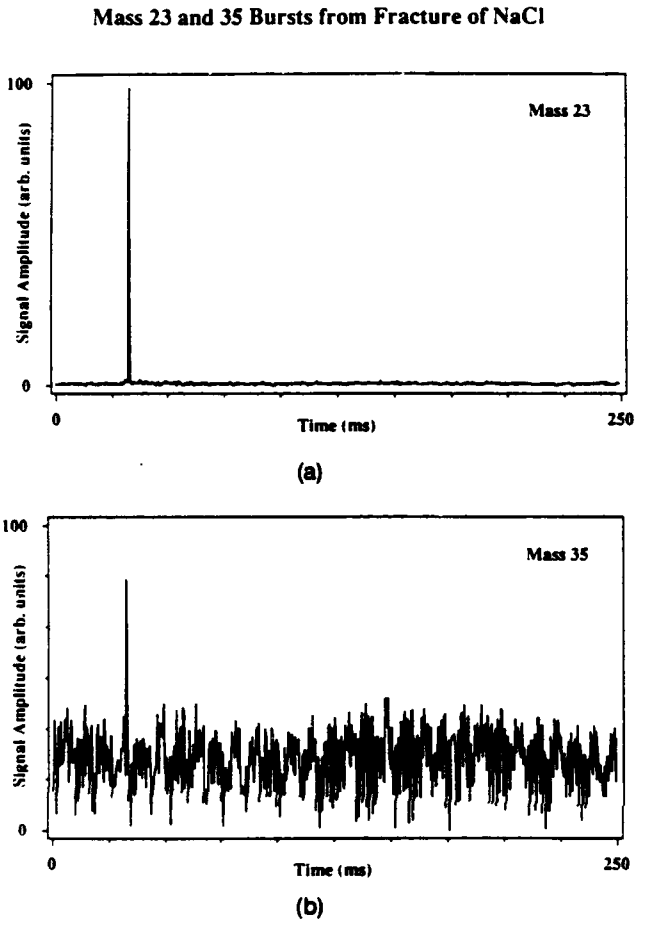

FIG. 6. Simultaneous, two-quadrupole emission measurements at (a) mass 23 (Na^+) and (b) mass 35 (Cl^+) accompanying the fracture of NaCl.

ous. Since these two species have nearly equal masses (and thus nearly equal velocities at a given energy), we conclude that the neutral Na and Cl are being emitted from the sample surface at the same time to within ± 20 μs. Similarly, mass 58 ($NaCl^\circ$) is detected in coincidence with mass 23, consistent with the only slightly slower velocities expected of this species; this implies that the emission of $NaCl^\circ$ molecules from the surface is simultaneous with that of Na° and Cl° atoms.

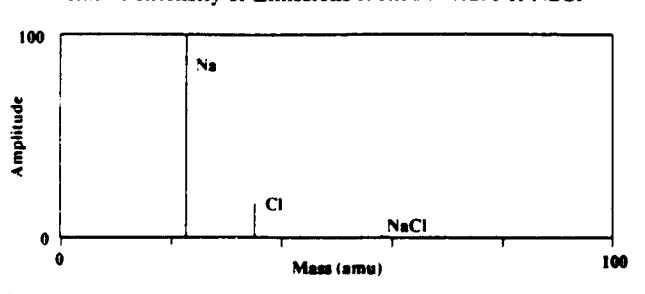

FIG. 7. Relative intensities of mass peaks due to fracture of NaCl.

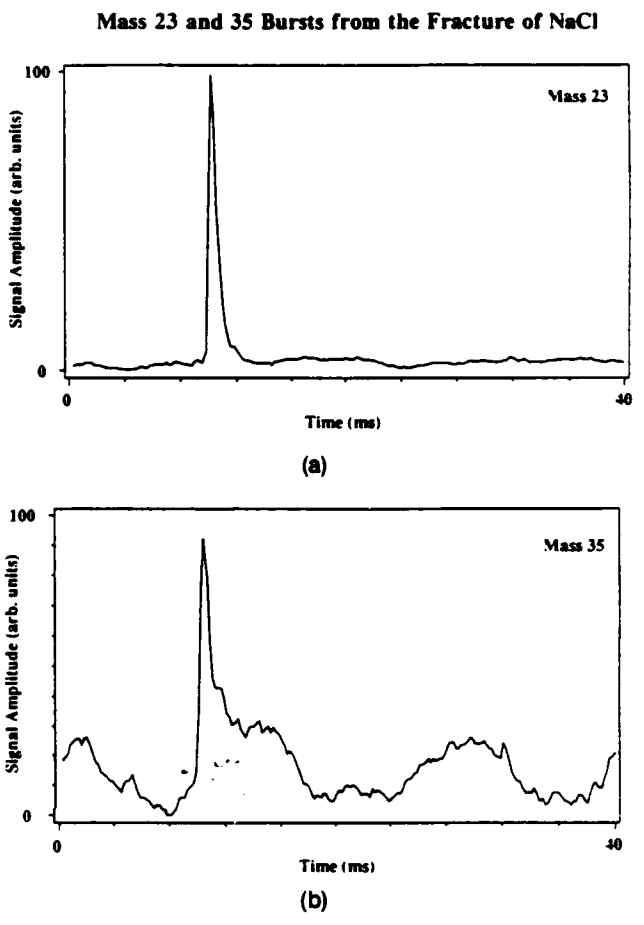

FIG. 8. Simultaneous, two-quadrupole emission measurements at (a) mass 23 (Na^+) and (b) mass 35 (Cl^+) made on faster time scales. (Compare Fig. 6.) The data of (b) at mass 35 were taken at an increased sensitivity ($\times 10$) relative to that of (a).

A histogram of the burst frequency versus time after fracture, taken from the two-quadrupole data, appears in Fig. 9. A broad peak in arrival times extends from about 5 ms to about 55 ms after fracture, with a long tail following. The relative insensitivity of the quadrupole detectors limits the peaks plotted in this summary to the large bursts. The surface ionization data indicate that actual range of emission times is somewhat broader; nevertheless, the most probable time delays are still within 10–15 ms after fracture.

Two-quadrupole measurements of the major emission components from LiF fractured in three point bend are shown in Figs. 10–13. The relative intensities of the emission at various masses were referenced to the intensity of the mass 26 (LiF^+) signal. Note the expanded time scale used to display the signal at mass 85 [$Li(LiF)_3^+$] in Fig. 13; on slower time scales, the noise all but buries the mass 85 burst. On this faster time scale, the delay of the heavier species relative to the lighter mass 26 is clearly observed.

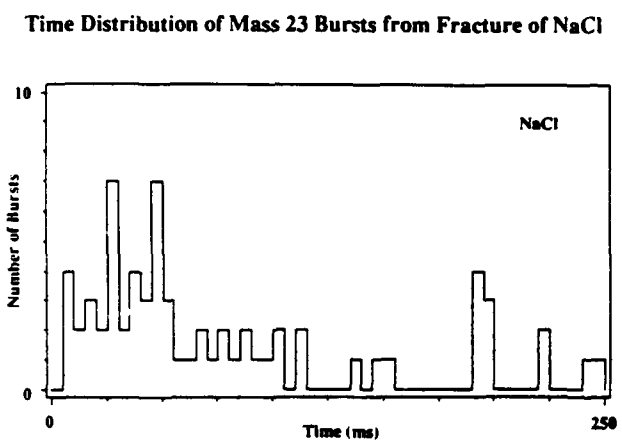

FIG. 9. A histogram of the number of emission peaks detected per 5 ms interval versus time after fracture, summed over a series of 19 fracture events. The peaks were taken from two-quadrupole data only.

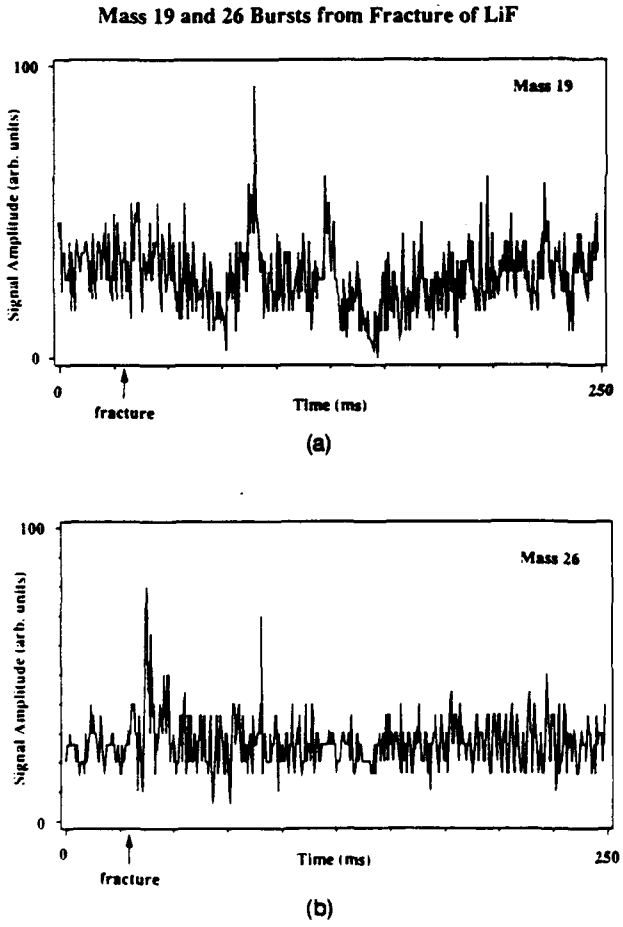

FIG. 10. Simultaneous, two-quadrupole emission measurements at (a) mass 19 (F^+) and (b) mass 26 (LiF^+) accompanying the fracture of LiF. The spike immediately after fracture in (b) is a ringing signal which appears to be a transient noise event. The time from fracture to the emission peak is 62 ms.

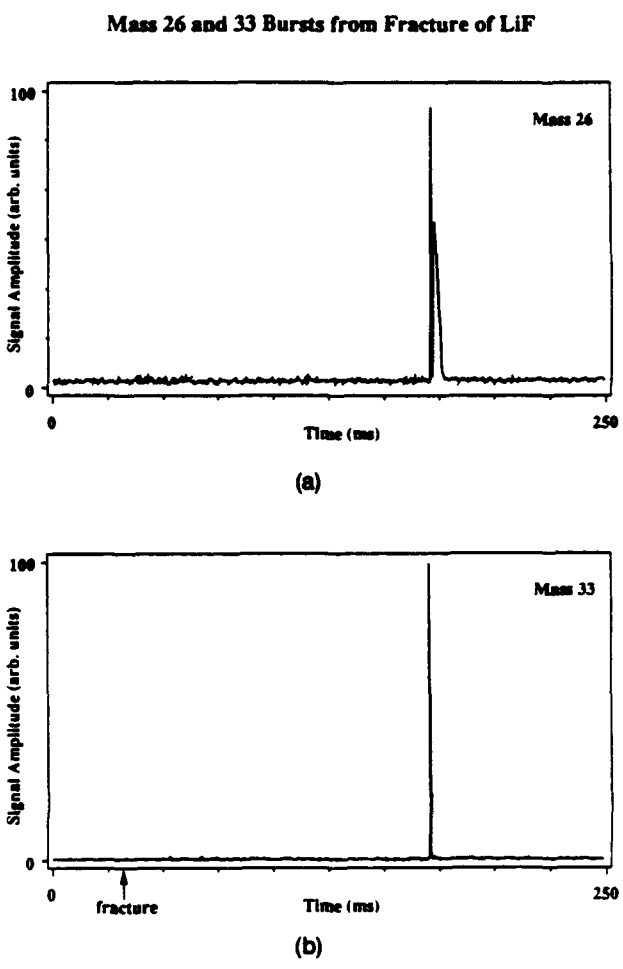

FIG. 11. Simultaneous, two-quadrupole emission measurements at (a) mass 26 (LiF) and (b) mass 33 Li(LiF) accompanying the fracture of LiF. The time from fracture to the emission peak is 141 ms.

The average relative intensities of the various masses computed from 10 fracture events are shown in Fig. 14. By far the most intense emission was observed at mass 33, which corresponds to the $Li(LiF)^+$ ion. Small, but detectable signals are also observed at masses 59 [$Li(LiF)_2^+$] and 85 [$Li(LiF)_3^+$]. Although neutral analogs of these cluster ions may in principle be emitted, mass spectroscopy studies[11,12] of alkali halide vapors containing monomers, dimers, trimers, etc. show that the alkali-rich ions are fragments produced by electron bombardment ionization. This is due to an inherent instability of ions of the form $(LiF)_n^+$.[12] These ions quickly decompose into the Li-rich cluster ions + a neutral halogen atom. Therefore, masses 33, 59, and 85 most likely represent emissions of neutral $(LiF)_2$, $(LiF)_3$, and $(LiF)_4$. Mass 26 (LiF^+) is not a cracking fraction of these polymeric molecular species, so that the mass 26 signal can be attributed entirely to LiF. In LiF vapors, mass 7 (Li^+) arises only as a cracking fraction of LiF. We note by comparison that the intensity of

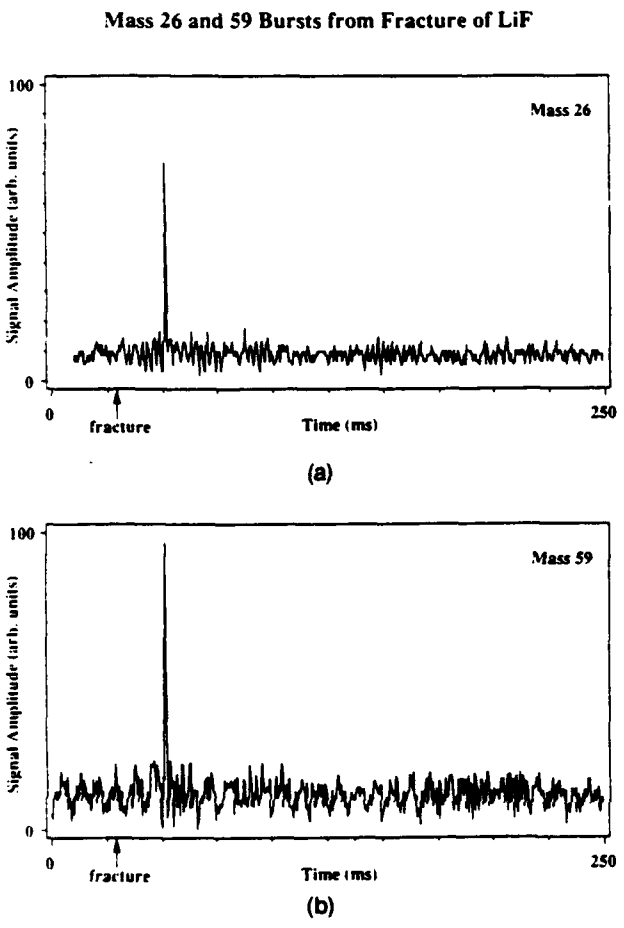

FIG. 12. Simultaneous, two-quadrupole emission measurements at (a) mass 26 (LiF^+) and (b) mass 59 $Li(LiF)_2^+$ accompanying the fracture of LiF. The time from fracture to the emission peak is 22 ms.

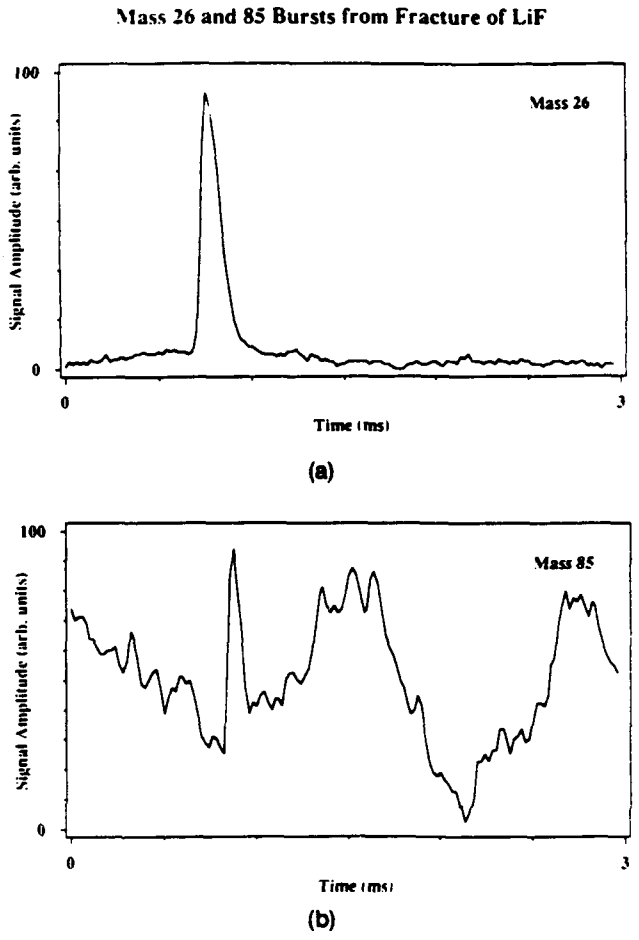

FIG. 13. Simultaneous, two-quadrupole emission measurements at (a) mass 26 (LiF^+) and (b) mass 85 $Li(LiF)_3^+$ accompanying the fracture of LiF. Note the expanded time scale relative to Figs. 10–12, and the increased sensitivity employed in (b) relative to (a). The time from fracture to the emission peak is 34 ms.

the fracture-related mass 7 signal is somewhat larger than that expected if it were solely a cracking fraction of mass 26, (LiF). Fluorine is a neutral fragment from electron bombardment of all the $(LiF)_n$ species which requires a second electron collision for detection. The mass 19 signal is therefore expected to be weak, as is observed. In contrast to NaCl, we find no convincing evidence of atomic emission (Li and F) in the neutral bursts from LiF.

To rule out the possibility that the observed emissions were due to the ejection of macroscopic alkali halide particles during fracture (ejecta),[13] both surface ionization and dual quadrupole measurements were undertaken with a fine grid between the sample and detector. The openings in the grid were ~5 μm square and its transmission was 25%. Care was taken to block any arcing trajectories which would be necessary to explain the delayed emission. In each case, for both NaCl and LiF, the presence of the grid appeared to reduce the intensities of the observed bursts but did not appear to affect the number of bursts observed per fracture event. This is consistent with a decreased transmission of atomic and molecular emissions, and inconsistent with the blocking of larger ejecta (assuming one particle produces one burst). On rare occasions when relatively large ejecta fragments were visually observed to pass through the quadrupole ionizer, a *decrease* rather than

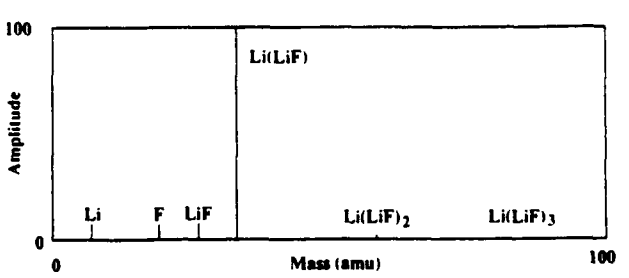

FIG. 14. Relative intensities of mass peaks due to fracture of LiF.

an increase in ion current was observed. These results along with (a) observation of small bursts prior to fracture, (b) thermally induced bursts from damaged crystals (see below), (c) the wide time span of fracture induced bursts, and (d) the relatively uniform shape of the bursts are all inconsistent with ejecta as the source of the observed bursts. The observed emission is conclusively atomic and molecular in nature.

C. Thermal treatment experiments

The magnitude of the observed neutral emission from the alkali halides would seem to require the collective activity of at least 10^6 to 10^8 atoms at some variable time(s) following fracture. Dislocation motion is a prime candidate for such collective activity. To test the dependence of the surface ionization peaks on aspects of sample preparation/treatment which are known to affect dislocation density and mobility, we compared the emissions from annealed NaCl samples with samples which were polished only. The surface ionization current and load drop (time of fracture) accompanying fracture of an annealed NaCl sample are shown in Fig. 15. Relative to the unannealed samples, emission from the fracture of annealed samples typically shows fewer, smaller bursts. *No* bursts were observed prior to fracture of the annealed samples. The bursts are typically an order of magnitude smaller than those observed from unannealed samples. The first of the smaller bursts from the annealed samples were found to occur sooner after fracture than the smaller bursts from the unannealed samples, usually within 1 ms after fracture. However, the first large bursts from both annealed and unannealed samples were delayed from fracture by quite similar times, i.e., 20–40 ms.

The different emissions from the annealed and unannealed samples are again consistent with different dislocation dynamics in the two materials. We expect the size distribution of defects in the annealed samples to be weighted heavily toward smaller defect aggregates relative to the unannealed samples. These smaller aggregates provide less resistance to dislocation motion than the larger aggregates, although their relatively high number density reduces the average dislocation length between pinning points (aggregates). Assuming that the size of an alkali burst is simply related to average dislocation length between pinning points, we expect smaller bursts from the annealed samples. The increased dislocation mobility in the annealed samples should allow the dislocations nearest the surface to reach the surface before those in an otherwise equivalent unannealed sample. The observation of fewer bursts in the annealed samples may merely be an effect of the increased sensitivity required for their observation. Thus the behavior of alkali bursts from the annealed samples supports a dislocation-related emission mechanism.

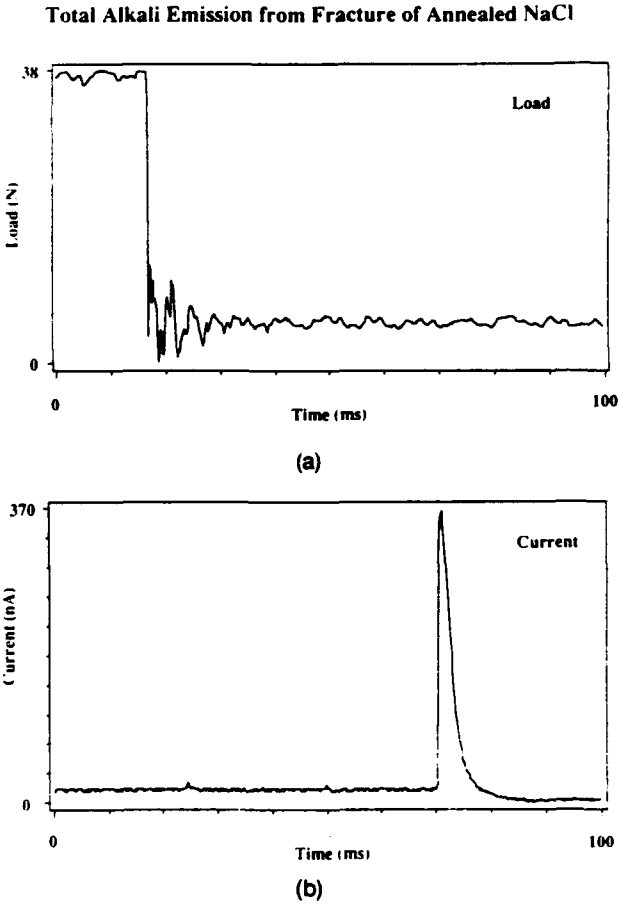

FIG. 15. Simultaneous measurements of (a) load and (b) surface ionization current accompanying the fracture of an annealed NaCl sample.

Neutral emission spikes could also be produced by heating samples identical to those used in the fracture experiments. Figures 16 and 17 show emission versus time plots for polished only and polished + indented NaCl samples; each emission peak is represented by a bar of the appropriate height. Corresponding plots of thermocouple readings versus time are also shown to give an indication of the accompanying rise in temperature. For both polished only and polished + indented samples, emission started at about the same temperature, namely 50–100 °C. However, the indented sample shows much higher count rates at significantly lower temperatures. Under roughly equivalent conditions, the first fifty bursts from the indented sample were detected before the sample tray reached 200 °C. The polished-only sample required sample tray temperatures on the order of 300 °C before fifty bursts were recorded. (Note that some of the difference between Figs. 16 and 17 can be attributed to different heating rates.) The higher burst rate from the indented sample is consistent with the high density of shallow dislocation loops near the

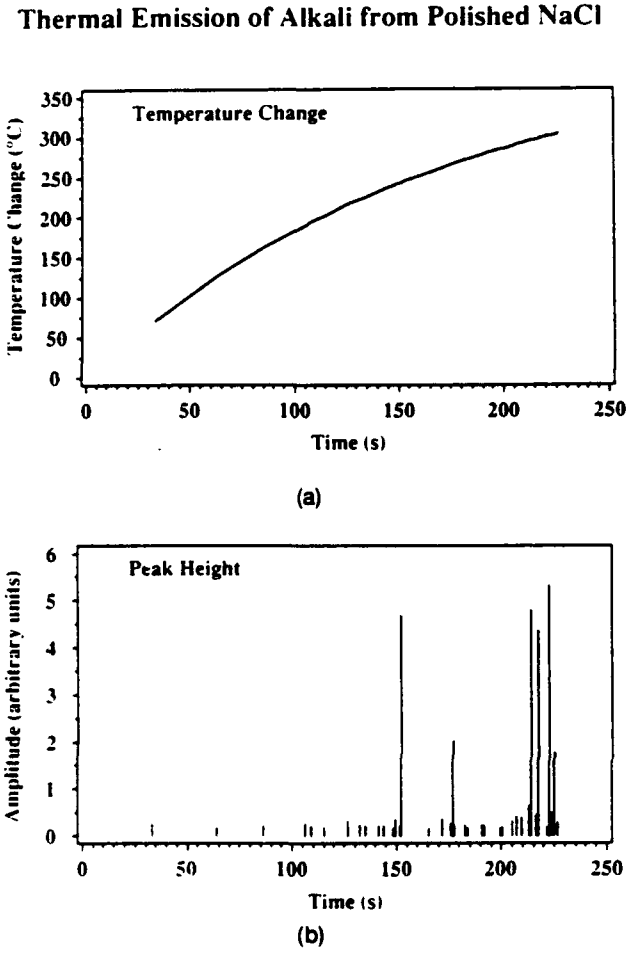

FIG. 16. The (a) temperature change of the sample holder and (b) emission peak heights as a function of time during the heating of a polished (not indented) NaCl sample. Data collection ceased after the first fifty bursts.

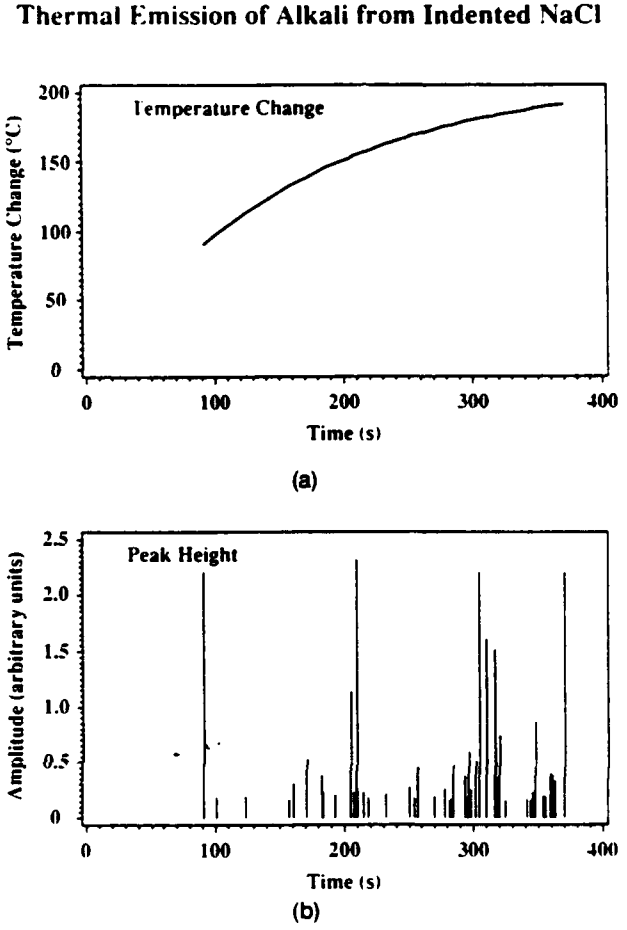

FIG. 17. The (a) temperature change of the sample holder and (b) emission peak heights as a function of time during the heating of a polished and indented NaCl sample. Data collection ceased after the first fifty bursts.

indented region. In both samples, taking the sample through a cooling and heating cycle raised the temperature for the onset of emission. This behavior is consistent with a gradual annealing of dislocations in the near surface region.

These annealing/thermal treatment studies thus lend strong support to the hypothesis that both the small bursts observed during mechanical loading and the small and large bursts seen following fracture of NaCl and LiF are indeed due to dislocations interacting with free surfaces.

IV. DISCUSSION

Several authors have reported particle and photon emission accompanying the deformation and fracture of alkali halides, and in some cases have attributed these effects to dislocation processes. Long lived electron and positive ion emission from the fracture of *cleaved* LiF has been attributed to the motion of charged dislocations to the fracture surface after fracture.[14] It appears that this prolonged emission is associated with the severely damaged region where the cleavage blade contacts the sample.[15] Surface charge measurements of LiF crystals cleaved in vacuum also show the presence of localized surface charge which is closely associated with localized sources of optically stimulated electron emission.[16] Poletaev and Shmurak report bursts of photons and electrons during the compression of LiF (without fracture), which they attribute to charge carried to the surface by moving dislocations.[17,18] These observations indicate that dislocations are created during fracture and that energetic processes occur upon arrival at the surface.

However, electron and photon emission measurements in this lab suggest that the dislocation-related neutral emission intensities far exceed those of dislocation-related electron and photon emissions. LiF fractured in three point bend yields rapidly decaying photon and electron emissions (10–20 ms decays) with-

out the delayed spikes observed in neutral emission.[15] In contrast, neutral emission is not observed at fracture, but shows delayed bursts. Although charge carried to the surface by moving dislocations can yield intense electron and photon emission, the dislocation activity and charge densities accompanying fracture of material with low defect densities (e.g., of F-centers) in three point bend appear to be far too low to account for the observed photon and electron emissions.

To investigate the ability of dislocation emergence to provide the energy required for emission bursts many ms after fracture, we constructed a numerical model of the process. The model dislocation was a half-loop lying in a plane normal to the surface of an isotropic material. The dislocation was allowed to contract under the influence of the image force from an initial radius R until it vanished, i.e., until "popout." Assuming the loop maintains its semicircular geometry as it contracts to the surface, the equation of motion for acceleration under the image force, normalized to unit dislocation length, is given by[19]

$$\frac{\alpha \ln[(4R/\rho) - 2] \cdot \ddot{R}}{c_t^2} = -\frac{\alpha \ln[(4R/\rho) - 1]}{R}, \qquad (1)$$

where R is the loop radius, c_t is the shear wave velocity in the glide plane, and ρ is a core cutoff parameter. Here we take $\rho = \mathbf{b}/2$, where $\mathbf{b}$ is the Burgers vector. α is given by

$$\alpha = \frac{\mu b^2(2 - \nu)}{8\pi(1 - \nu)}, \qquad (2)$$

where μ is the shear modulus, b is the magnitude of the Burgers vector, and ν is Poisson's ratio. Using values appropriate to slip in LiF on the $\{110\}\langle 110\rangle$ system, we obtain $\alpha = 3.79 \times 10^{-10}$ N. "Relativistic effects," which limit the dislocation velocity to speeds on the order of c_t, were neglected, except as noted below.

In the absence of damping forces, such a loop disappears very rapidly. Damping forces were included on the basis of velocity versus stress measurements made by Johnston and Gilman.[20] Their data were modeled by a term linear in velocity ($V = \dot{R}$), which describes phonon damping effects, and a term in $(V/V_0)^m$, which empirically describes the effects of jog dragging and impurities. The force per unit length on the dislocation was estimated by

$$F/l = -b\sigma_0\left(\frac{|\dot{R}|}{V_0}\right)^m - \beta|\dot{R}|, \qquad (3)$$

where the parameters $\sigma_0 = 6.5$ MPa, $V_0 = 5$ nm/s, $\beta = 1.42 \times 10^{-4}$ Pa·s, and $m = (1/23)$ were chosen to fit the data of Fig. 5 in Ref. 20. The parameter σ_0 depends strongly upon the thermal history (and thus defect distribution) of the sample, while V_0 is a function of dislocation character, differing a factor of 50 between screw and edge dislocations. No attempt was made to distinguish between screw and edge components of the dislocation half loop in this model; the value of ν_0 appropriate for screw dislocations was used exclusively.

The full equation of motion then becomes

$$\frac{\alpha \ln[(4R/\rho) - 2] \cdot \ddot{R}}{c_t^2} + b\sigma_0\left(\frac{|\dot{R}|}{V_0}\right)^m + \beta|\dot{R}| + \frac{\alpha \ln[(4R/\rho) - 1]}{R} = 0. \qquad (4)$$

This equation of motion is unstable near the surface, where the image force diverges, and at diameters greater than about 1 μm, where the damping forces are dominated by the term in V^m. Near the surface, dislocation velocities are high and thus the precise character of the solution has little effect on the estimated popout times. To study the character of the solution at loop diameters greater than about 1 μm, we take advantage of the fact that the accelerations at these diameters are small enough that we can reasonably neglect the acceleration term, yielding the more stable equation of motion

$$b\sigma_0\left(\frac{|\dot{R}|}{V_0}\right)^m + \beta|\dot{R}| + \frac{\alpha \ln[(4R/\rho) - 1]}{R} = 0. \qquad (5)$$

For loops initially greater than about 1 μm, composite solutions were constructed from the solutions of Eq. (5) at large radii and Eq. (4) at small radii, using the final conditions of the solution of Eq. (5) as initial conditions for Eq. (4). Some error is introduced in the formation of the composite solution, largely due to the use of Eq. (5) in regions where the neglect of the acceleration term of Eq. (4) is not negligible. However, the dislocation loop at this point is shrinking quickly, so that the effect of this error on popout times is small.

A typical composite solution is plotted in Fig. 18. The loop spends most of its existence at large radii. Eventually a catastrophic contraction begins and the loop rapidly accelerates to the surface. The rise in velocity just prior to popout is markedly super-exponential. This is true not only of the composite solutions, but of solutions of the full equation for small loops. The initial velocity of loop contraction is quite sensitive to the initial loop radius. Since the loop spends by far the bulk of its travel time at low velocities, the popout time also displays this sensitivity. The popout time in this example was almost 6 ms, not untypical of our measurements. The high contraction velocity also suggests that the process may be sufficiently energetic to result in neutral emission.

A graph of the predicted popout times versus initial loop radii (or depth) is shown in Fig. 19. The time is displayed on a logarithmic scale because of the extreme range spanned by the results. The plot shows two regions of rapid decrease in popout time, corresponding

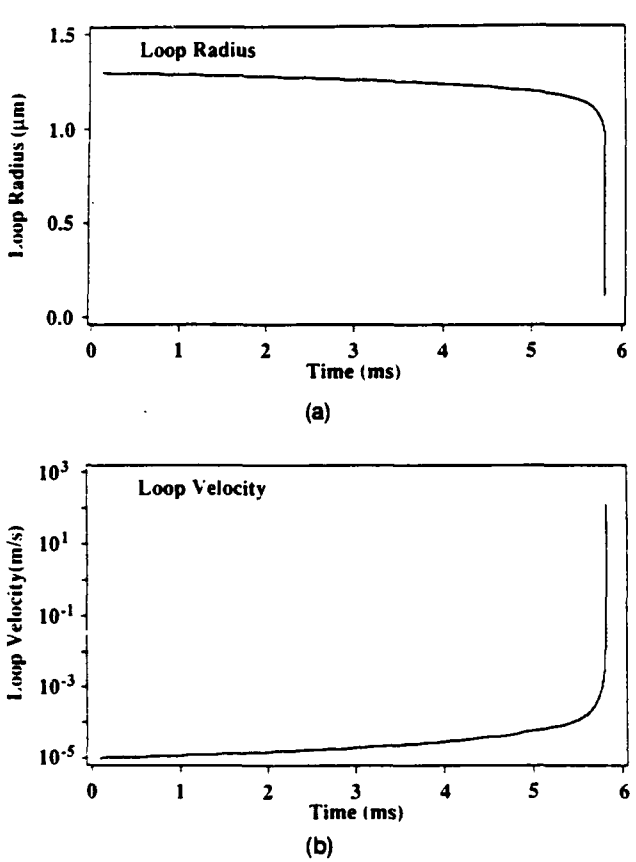

FIG. 18. Typical (a) loop radius and (b) contraction velocity computed from Eqs. (4) and (5) from a dislocation half-loop of 1.3 μm initial radius.

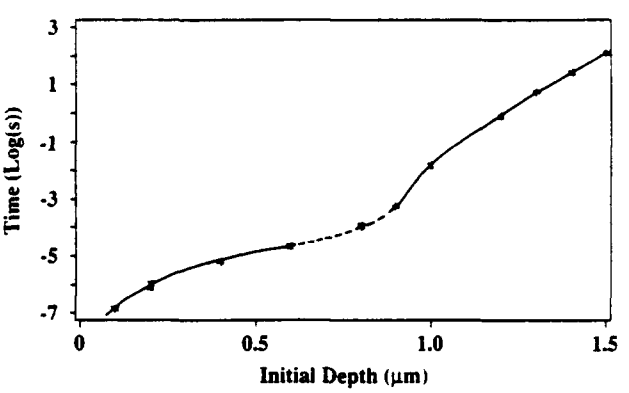

FIG. 19. Predicted dislocation popout times versus initial loop radii from solutions of Eqs. (4) and (5). The line is meant only to guide the eye. Popout times dominated by V^m and linear damping are marked with solid lines joined by a dotted line.

roughly to the regions in which the image force overpowers first the V^m damping term, then the linear damping term. Popout times corresponding to initial dislocation depths of 0.5 to 1.5 μm span the experimentally observed delays for the most intense bursts. Despite the crudeness of the model, the extreme sensitivity of popout time to initial loop diameter appears to be fundamental, and would explain the delayed emissions even if the details of the model were substantially altered.

The long popout times associated with the larger loops explain the lack of large alkali emission peaks immediately after fracture. This delay in emission is evident in the histogram of Fig. 9 and was initially a most puzzling feature of our observations. Presumably the larger peaks are associated with the bigger, slower loops. Smaller peaks would be due to smaller loops, which could be faster due to their proximity to the surface. We attribute the smaller peaks immediately prior to fracture to the popout of shallow or tightly pinned loops introduced on the tensile side of the sample during polishing. Dislocations of the proper orientation can be driven toward the surface by the high stresses at the tensile surface immediately prior to fracture. Similarly, the heated samples can yield neutral emission when pinned loops escape via thermal activation.

A substantial amount of energy can be delivered to the near surface region by a contracting dislocation loop. The potential energy of a half-loop of 1 μm radius is on the order of 70 keV. Only a small fraction of this energy is likely to reach the surface due to dissipation by phonon interactions. However, there is reason to expect that the phonon drag is markedly reduced (on the order of a factor of 10^{-3}) at velocities above about 6 km/s, when the thermal relaxation time (~470 fs) exceeds the time for a dislocation to move the length of a Burgers vector.[21] At this velocity, phonons lack time to equilibrate with the dislocation core as it jumps from plane to plane. In our model, this velocity is reached at loop radii of about 250 Å, even with relativistic corrections. The remaining potential energy of the loop (~1 keV) should then be converted efficiently to kinetic energy and thus be available for emission processes.

This energy is still too low to account for neutral emission bursts composed of millions of atoms (~10^7 for a typical large burst). The amount of energy required can be estimated from the results of sublimation experiments. These measurements indicate that the emission of an LiF monomer[22] requires about 2.9 eV (versus about 2.2 eV for a NaCl monomer[23]). The energy required for fracture-related emission should be somewhat lower than that for sublimation because the fracture surface will lack the equilibrium surface charge density which develops during sublimation. For instance, the dipole force on a NaCl molecule departing from a surface with the equilibrium charge is expected to contribute about 0.25 eV to the energy of sublima-

tion.[23] Sublimation of dimers and trimers appears to be even more energetic (per monomer unit).[11] Thus the large emission bursts that we observe require total energies on the order of MeV.

Therefore, it appears that a dislocation loop with an initial radius of 1 μm could result in the ejection of a few hundred alkali atoms. This is still a substantial number. A loop which reaches the critical velocity for negligible phonon interactions at a radius of 250 Å will have enough energy to kick out a row or two of LiF molecules along the entire 500 Å diameter of the loop. Despite the crudeness of the model, the intense emission peaks appear to require collective dislocation effects. The most likely effect is the avalanche of piled-up dislocations.[24] An avalanche on one crystalline plane could easily stimulate depinning events on nearby slip planes. The total energy delivered to the near surface region by such an array would include a large contribution from dislocation interaction energies.

Other considerations may also substantially increase our estimates of the energy available at the surface. Accounting for the actual geometry of a collapsing loop could easily increase the energy estimates an order of magnitude. The high velocities of dislocation edge components relative to screw components in the low velocity (V^m dominated) regime[20] should flatten the loop in the dimension normal to the surface. (Loops with the envisioned geometry have Burgers vectors with a component normal to the surface. These loops have predominantly screw character at the surface and edge character deep in the bulk.) Thus the total length of a loop when it reaches relativistic velocities would be far greater than its depth below the surface. If the potential energy per unit length of the elliptical loop is comparable to that of the model loop, the energy delivered to the surface would be far greater. A more sophisticated model of dislocation popout would also include the effects of the anisotropy of the alkali halides and the orientation of the slip planes with respect to the surface.

The nonequilibrium nature of the popout event may significantly enhance the efficiency of the emission process. Atoms at the step created during loop collapse should possess a great deal of *directed* energy, as opposed to thermally random energy. An LiF "molecule" arriving at the surface with the shear wave velocity (c_t) would have a kinetic energy of ~1.7 eV. Although c_t is an upper limit on the dislocation velocity, relaxation of the dislocation core displacements at the surface will substantially increase the effective energy. In the case of relativistic dislocations, relaxation of stresses associated with the dislocation core is minimized prior to popout by relativistic effects. The stress distribution about the core experiences a "relativistic" contraction along the direction of motion. Collective effects, such as the emission of clusters or linear chains of molecules (an unzipping along the dislocation line), might also significantly lower the energy required for emission.

The dislocations participating in this process are both those produced during fracture and, in the case of emission prior to fracture, those introduced in the polishing process. "Grown in" dislocations are usually tightly pinned by defects which accumulate along their length during the cooling process after crystal growth. Dislocation loops are also nucleated by crack growth, especially at relatively low crack velocities (<60 m/s) where crack growth is unstable.[25,26] Burns and Webb observed that the largest fracture-related loops extend 3–5 μm below the surface.[26] They observed the remnants of very long dislocation structures parallel to the direction of crack motion. These structures are believed to break up into smaller loops as the shallower portions move to the surface under the influence of the image force. If several rather long, parallel fragments were to pop out in unison, enough energy would be available for the emission of several millions of alkali atoms.

However, fracture in three point bend generally involves higher crack speeds than those considered by Burns and Webb, and other dislocation structures appear. Cleavage steps are produced in rapid crack growth, and these are often sites of significant deformation.[27] X-ray topography has revealed other, less well defined plastic deformation resulting from high speed crack growth.[28] Locally one may expect dislocation pileups to form in some of these structures. Scanning tunneling microscope observations of LiF fracture surfaces in our laboratory indicate that they can be quite rough on nm scales. An example of a large area STM scan on a LiF fracture surface is shown in Fig. 20, taken with techniques described in Ref. 29. The observed roughness is consistent with considerable localized crack branching or plastic deformation. Thus we expect that dislocation loops of appropriate sizes are present in the near surface region of LiF fractured in three point bending.

Neutral emissions may be significant indicators of the local energy release due to dislocation popout. X-ray topographic measurements of strain around indentation cracks in MgO indicate significant energy release has occurred due to the popout of dislocation pileups after the formation of the indentation cracks.[30] These results are used to infer the generation of local "hot spots" on the fracture surface due to the collapse of these dislocation pileups. The existence of intense neutral emission bursts accompanying popout suggests that these hot spots are quite small and thus involve very high energy densities. These energy densities (eV/atom) appear to be sufficient to drive chemical reactions in reactive materials, given adequate coupling to the appropriate atomic and molecular excitations. This is perhaps of most significance in energetic materials, where

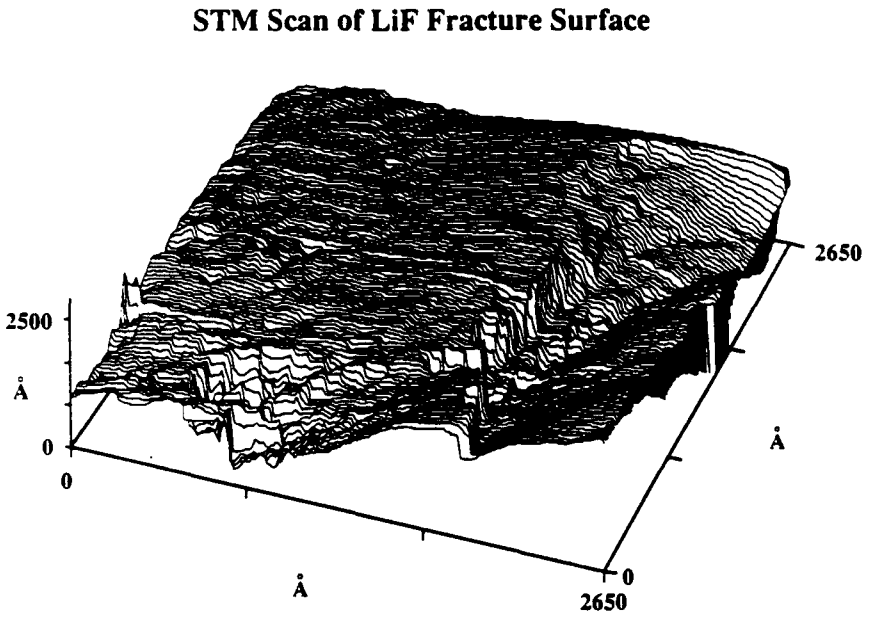

FIG. 20. A scanning tunneling microscope scan of a LiF fracture surface created from three point bend loading. Surface conductivity was provided by a thin gold coating (see Ref. 29).

local hot spots due to cracking might result in or contribute to explosive ignition.

A dislocation mechanism may also explain a related behavior in the Mg neutral emission accompanying the fracture of MgO.[6] These emissions also do not peak at fracture but grow more slowly to a peak some hundreds of ms following fracture. The atomic Mg emission also displays spikes delayed from fracture. We are currently investigating the possible role of dislocation motion subsequent to fracture of MgO.

V. CONCLUSION

We have shown that the fracture of LiF and NaCl is accompanied by the emission of neutral alkali and halide atoms, as well as several molecular species. These emissions display sharp spikes which in general are not simultaneous with fracture, but delayed. In some cases the delay is a major fraction of a second. Smaller peaks are often delayed less and can actually precede the fracture event. We attribute these emissions to the arrival of dislocations at the surface. The smaller peaks prior to fracture result from the popout of dislocations introduced during sample preparation, while the emission subsequent to fracture is largely due to dislocations produced during crack growth. A simple numerical model of the popout process indicates that dislocation dynamics can explain the delayed emission of alkali satisfactorily. However, the details of how the dislocation energy is transferred to the emitted species are not entirely clear. In some circumstances, dislocation/surface interactions may contribute to surface heating accompanying fracture.[24]

Similar emissions were observed to accompany the heating of polished and indented NaCl samples. The temperature required for the onset of significant emission increased dramatically with subsequent heating cycles, consistent with the gradual annealing of dislocations in the near surface region. This supports a dislocation source for these emissions and suggests that they are a rather general feature of dislocation popout in the alkali halides. Such intense emission requires this popout to be a relatively high energy process.

The emission of atoms and molecules accompanying dislocation popout may provide a useful tool for monitoring this process on fast time scales. Substantial information on the energetics of the process appears to be available. Although the time resolution of this work was limited to the ms time scale, even ms time scale resolution is substantially faster than can be obtained by electron and other microscopies. Furthermore, in other work on neutral and ion emission in our laboratory, substantial improvements in time resolution have been made, down to sub-microsecond time scales. Other particle detection techniques, such as laser induced fluorescence, would allow the extension of these techniques to materials for which surface ionization is impractical, as well as allow the investigation of the directionality of these emissions. If particle momentum at the instant of popout is "conserved" in the emission process, one might expect highly peaked angular distributions in these emissions.

ACKNOWLEDGMENTS

We wish to thank Robb Thomson, NIST, and Ron Armstrong, University of Maryland, for very helpful discussions. We also thank Digala Kulawansa for performing the STM scans of LiF fracture surfaces. This work was supported by the Office of Naval Research

under Contract No. N00014-87-K-0514, the Ceramics and Electronics Materials Division of the National Science Foundation under Grant DMR 8912179, and the Washington Technology Center.

REFERENCES

[1]J.T. Dickinson, L.C. Jensen, and S. Bhattacharya, Die Makromolekulare Chemie: Macromolecular Symposia **7**, 129 (1987).
[2]S. C. Langford, Ma Zhenyi, and J.T. Dickinson, J. Mater. Res. **4**, 1272 (1989).
[3]S. C. Langford and J.T. Dickinson, in *Spectroscopic Characterization of Minerals and Their Surfaces*, edited by L. M. Coyne, S.W. McKeever, and D. F. Blake, ACS Symposium Series Publication 415, pp. 224–244 (1990).
[4]J.T. Dickinson, "Fracto-Emission from Adhesive Failure," to appear in *Adhesive Bonding*, edited by L-H. Lee (Plenum Press, New York, 1990).
[5]J.T. Dickinson, "Fracto-emission," to appear in *Non-Destructive Testing-Composites*, edited by J. Summerscales (Elsevier, Amsterdam).
[6]J.T. Dickinson, L.C. Jensen, M.R. McKay, and F. Freund, J. Vac. Sci. Technol. A **4**, 1648 (1986).
[7]J.T. Dickinson, L.C. Jensen, and M.R. McKay, J. Vac. Sci. Technol. A**5**, 1162 (1987).
[8]J.T. Dickinson, S.C. Langford, L.C. Jensen, J. Kelso, C. Pantano, and G. McVay, J. Vac. Sci. Technol. A **6**, 1084 (1988).
[9]S. Datz and E.H. Taylor, J. Chem. Phys. **25**, 389 (1956).
[10]E.Ya. Zandberg and N.I. Ionov, *Poverkhnostnaya ionizatsiya* (Nauka, Moscow, 1960) [*Surface Ionization*, translated by E. Harnik (Israel Program for Scientific Translations, Jerusalem, 1971)].
[11]J. Berkowitz and W.A. Chupka, J. Chem. Phys. **29**, 653 (1958).
[12]J. Berkowitz, C.H. Batson, and G.L. Goodman, J. Chem. Phys. (Paris) **77**, 631 (1980).
[13]E.E. Donaldson, J.T. Dickinson, and S.K. Bhattacharya, J. Adhesion **25**, 281 (1988).
[14]A.G. Lipson, V.A. Kuznetsov, V.A. Klyuev, Yu.P. Toporov, and B.V. Deryagin, Dokl. Akad. Nauk SSR **294**, 1161 (1987) [Dokl. Phys. Chem. **294**, 575 (1987)].
[15]J.P. Mathison, S.C. Langford, and J.T. Dickinson, J. Appl. Phys. **65**, 1923 (1989).
[16]J. Wollbrandt, U. Brückner, and E. Linke, Phys. Status Solidi (a) **77**, 545 (1983).
[17]A.V. Poletaev and S.Z. Shmurak, Fiz. Tverd. Tela (Leningrad) **26**, 3567–3575 (1984) [Sov. Phys. Solid State **26**, 2147 (1984)].
[18]M.I. Molotskii, Fiz. Tverd. Tela (Leningrad) **25**, 121 (1983) [Sov. Phys. Solid State **25**, 67 (1983)].
[19]J.P. Hirth and Jens Lothe, *Theory of Dislocations*, 2nd ed. (John Wiley & Sons, New York, 1982), pp. 168–169.
[20]W.G. Johnston and J.J. Gilman, J. Appl. Phys. **30**, 129 (1959).
[21]W.P. Mason, in *Dislocation Dynamics*, edited by A.R. Rosenfield, G.T. Hahn, A.L. Bement, Jr., and R.I. Jaffee (McGraw-Hill, New York, 1968), pp. 487–505.
[22]D.L. Hildenbrand, W.F. Hall, F. Ju, and N.D. Potter, J. Chem. Phys. **40**, 2882 (1964).
[23]D.W. Short, R.A. Rapp, and J.P. Hirth, J. Chem. Phys. **57**, 1381 (1972).
[24]R.W. Armstrong, C.S. Coffey, and W.L. Elban, Acta Metall. **30**, 2111 (1982).
[25]J.J. Gilman, C. Knudsen, and W.P. Walsh, J. Appl. Phys. **29**, 601 (1958).
[26]S.J. Burns and W.W. Webb, Trans. Metall. Soc. AIME **236**, 1165 (1966).
[27]M.V. Swain, B.R. Lawn, and S.J. Burns, J. Mater. Sci. **9**, 175 (1974).
[28]C.T. Forwood and B.R. Lawn, Philos. Mag. **13**, 595 (1966).
[29]S.C. Langford, Ma Zhenyi, L.C. Jensen, and J.T. Dickinson, J. Vac. Sci. Technol. A **8**, 3470 (1990).
[30]K.C. Yoo, R.G. Rosemeier, W.L. Elban, and R.W. Armstrong, J. Mater. Sci. Lett. **3**, 560 (1984).

IV. Atomic and Molecular Emission Accompanying Fracture of Single-Crystal Ge: A Dislocation-Driven Process

J. T. Dickinson, L. C. Jensen, and S. C. Langford

Physics Department, Washington State University, Pullman, Washington 99164-2814

(Received 18 December 1990)

We present evidence for the emission of atomic Ge and Ge_2 molecules accompanying dynamic fracture at room temperature of single-crystal Ge under flexure loading. The emission follows the completion of crack propagation by several milliseconds and occurs in bursts, typically 1–2 ms in duration. A dislocation-driven mechanism for this emission is presented suggesting that considerable dislocation activity is accompanying failure of these samples.

PACS numbers: 62.20.Mk, 61.70.Le, 81.40.Np

The fracture of many materials in vacuum is accompanied by the emission of photons, charged particles, neutral atoms, and molecules,[1-3] collectively known as fracto-emission. In general, most fracto-emission intensities reach their peak *during* the fracture event and thereafter decay. Recent measurements of alkali and alkali-halide neutral emission accompanying the fracture of single-crystal NaCl and LiF show rapid, intense bursts of atomic and molecular emissions that arise *after* fracture, typically delayed 0.5–250 ms from the time of fracture,[1] with little detected neutral-particle emission during fracture. We presented evidence that these emissions are due to the ejection of atoms and molecular clusters accompanying the arrival of rapidly moving dislocations at the fracture surface. These neutral-emission bursts therefore probe the relaxation of metastable plastic deformation associated with fracture in the relatively ductile alkali halides. The presence of plastic deformation during crack growth in *brittle* materials is an open question. If this deformation were metastable rather than strictly irreversible, the apparent absence of fracture-related dislocations on fracture surfaces of more brittle materials would be explained. Single-crystal Ge, which is a covalent, monatomic solid with a diamond lattice, is quite brittle at room temperature. The goals of this particular study are to determine (a) if neutral emission occurs at all from fracture of such a material, and (b) if dislocation activity during and following fracture might explain the observed emission.

Samples of Ge were prepared from portions of a single boule. The samples were cut with a diamond saw to nominal dimensions of $10\times4\times2$ mm^3 and polished in successive stages; the final stage used 1-μm diamond paste. The samples were cleaned in ethanol, mounted in vacuum systems maintained at pressures below 1×10^{-6} Pa, and loaded to fracture in three-point bend. Samples of various orientation were prepared; however, fractographic characterization showed that fracture generally followed (111) cleavage planes. Generally, no significant differences were observed among samples of different orientations. Neutral-emission measurements were made with a UTI Model 100C quadrupole mass spectrometer (QMS). The masses of the Ge isotopes are well removed from typical vacuum-system contaminants, thus facilitating emission measurements with high sensitivity. The QMS ionizer was positioned 6 cm from the tensile surface of the sample.

Figures 1(a) and 1(b) show typical emissions at 74 amu (the most abundant atomic Ge isotope) for two different samples. The emission bursts were typically delayed 10–100 ms from the time of fracture (as determined by the drop in applied load). The time of fracture is indicated by the arrows on the time axis. (The duration of fracture is typically 1–2 μs.) Some shorter and longer delays were occasionally observed. The peak width was typically 1–2 ms FWHM, which is close to the limit of the response of the electronics at the sensitivity employed. Taking into account ionizer efficiencies, these peaks corresponded to $\sim10^6$–10^8 atoms passing through the QMS ionizer. An estimate of the total neu-

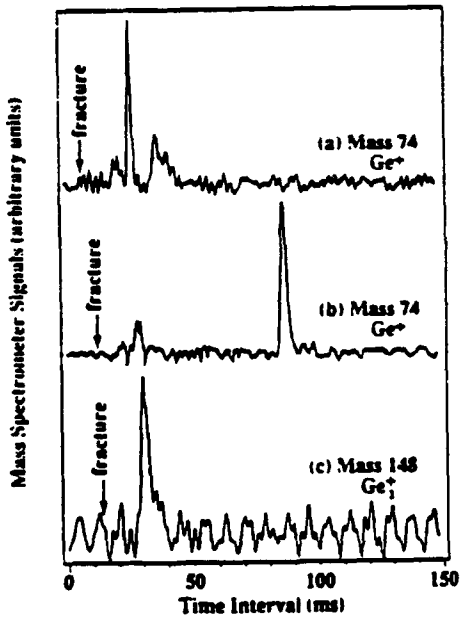

FIG. 1. Quadrupole-mass-spectrometer signals accompanying the fracture of single-crystal Ge. The signals of (a) and (b) are both for mass 74 and were acquired during two representative fracture experiments. They are primarily from the emission of atomic Ge. (c) A similar signal for mass 148 (Ge_2) from the fracture of a third (larger cross section) sample. The peaks have been normalized to a common height for presentation purposes. The peak electrometer currents were (a) 0.5 nA, (b) 0.6 nA, and (c) 4 nA.

© 1991 The American Physical Society

tral emission would require knowledge of the angular distribution of the emissions and the escape probabilities associated with the crack geometry at the time of emission. Estimation of these factors is problematic at this point and will not be attempted here. However, it is clear that the emissions can be substantial. Given the sample geometry, the emission represents a minimum of 10^{-9}–10^{-7} of the Ge atoms in the first monolayer of the fracture surface (ignoring surface roughness).

Some measurements were also made at 148 amu, the mass of the most abundant Ge_2 dimer. Relatively intense emission bursts of the dimer were also observed; a typical result is shown in Fig. 1(c). Based on a limited sample set (eight bursts), the intensities of the bursts at 148 amu are very similar in intensity to those at 74 amu after correcting for the relative transmission and detection efficiencies at these two masses. The delays in the dimer bursts are also comparable to those of the monomer bursts. The relative intensities of the dimer and monomer bursts suggest that most of the emission at 74 amu is due to emission of Ge atoms from the fracture surface, and not due to dissociation of the dimer in the QMS ionizer. The existence and relative intensity of the dimer peak is also inconsistent with a thermal-emission mechanism. First, we found no discussion in the literature of thermal emission (vaporization) of Ge_2 directly from a liquid Ge surface. Furthermore, Knudsen-cell–QMS studies of *equilibrium* Ge vapors at temperatures of 1400–2200 K yield typical Ge_2/Ge ratios <0.01,[4] far below the observed ratio from fracture (on the order of unity).

The chief potential source of artifacts in the emission measurements is the vaporization of small Ge fragments (ejecta) striking the quadrupole ionizer. Depending on the stress at fracture, the ejected particles can be numerous, and their velocities are often sufficiently low to account for a significant delay from fracture. Fairly large pieces of ejecta were only occasionally observed to strike the ionizer filament (W at −2200 K). This resulted in long, intense signals at 74 amu which decayed over some minutes. These signals are readily distinguished from the sharp bursts shown in Fig. 1. Furthermore, the detection of the dimer is inconsistent with such an artifact. If ejecta were captured by the ionizer filament, it is highly unlikely that dimers would be directly emitted from the hot W surface.

To further test for such artifacts, several fracture experiments were performed with a fine Ni mesh between the sample and the ionizer. The mesh openings were 6 μm square and yielded a net "transparency" of 25%. The presence of the grid had little if any effect on the number of observed bursts, but did reduce the average intensity. These observations are consistent with atomic emissions, but do not rule out the presence of ejecta smaller than 1 μm.

To unambiguously rule out the possibility that the detected emissions were due to small Ge fragments, Ge emitted during fracture was deposited on an alumina substrate and subsequently thermally desorbed in front of the QMS ionizer. The substrate was a thin-walled alumina ceramic tube heated with a Mo filament running through its center. Temperature estimates were obtained by fixing an Alumel-Chromel thermocouple to the substrate during a separate experiment and applying a heating cycle identical to that used in the desorption runs. For comparison purposes, thermal desorption of Ge evaporated onto the substrate from a Knudsen cell was also performed. The QMS filter was again tuned to 74 amu and the detected signal digitized at regular time intervals. Figure 2 shows typical desorption-induced emissions for Ge deposited by fracture and by evaporation. The approximate temperature is noted along the horizontal (time) axis. The desorption of fracture-deposited Ge shows a peak at the same temperature and with time behavior similar to the desorption of Knudsen-cell–deposited Ge. This is strong evidence for the atomic (or molecular) nature of the fracture-related emission. The low temperature at which desorption takes place is further evidence for atomic or molecular Ge. The vapor pressure of Ge in this temperature range is exceedingly low, totally ruling out evaporation of captured ejecta as a source of these emissions.

A final test for atomic and molecular emission utilized the setup shown in Fig. 3, where the emission was detected using *two* mass spectrometers at distances of 3 and 9 cm from the sample. Figure 3 shows the leading edges of two sequential bursts acquired at mass 74. The time difference at half maximum shown here is −100 μs; an average value of 85 μs was observed. A time delay of 85 μs indicates that atoms in this portion of the emission curve have a velocity of about 700 m/s, which corresponds to a kinetic energy of 0.2 eV. Interpreting the data as a shift in the leading edge of a Maxwellian time-

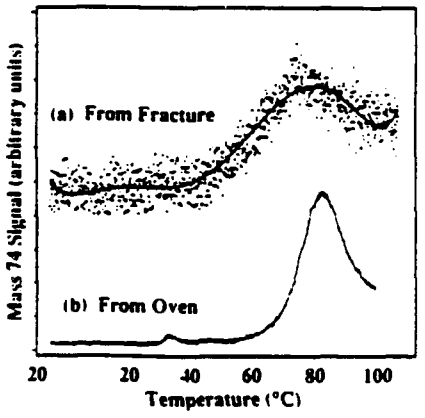

FIG. 2. Thermal desorption of Ge (mass 74) from alumina deposited by (a) fracture and (b) evaporation from a Knudsen cell. The temperature scale along the horizontal axis was established in a separate experiment with a thermocouple attached to the alumina substrate. The peaks heights have been normalized for presentation purposes. The peak electrometer currents were (a) 20 pA and (b) 400 pA.

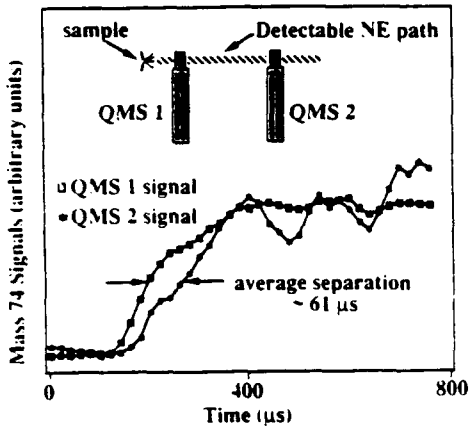

FIG. 3. Mass-selected emissions at 74 amu (principally Ge atoms) detected by two consecutive quadrupole mass spectrometers. The experimental geometry is shown in the inset, showing two quadrupole mass spectrometers (QMS1 and QMS2) tuned to the same mass (mass 74) at different distances from the sample. Because of the long duration of the signals on this faster time scale, only the leading edges of the signals are shown.

of-flight distribution, the corresponding temperature is about 750 K. This is consistent with a nonthermal-emission mechanism, since reasonable vapor pressures of Ge require $T > 1200$ K.

The velocity associated with this peak shift is far greater than that expected for particles ejected from the surfaces. Upper limits for ejecta translational speeds are given by the maximum particle speed associated with a longitudinal wave incident on the fracture surface, Δu. The most intense longitudinal waves would be associated with stress oscillations equal in magnitude to the tensile stress at fracture, Δp. Under these conditions, $\Delta u = \Delta p/\rho c$, where c is the longitudinal sound speed in Ge.[5] In this work $\Delta p < 360$ MPa, so that $\Delta u < 14$ m/s. Thus, the observed mass-74 bursts are traveling far too fast to be attributed to ejecta. We therefore conclude that the observed bursts seen in the QMS tuned to masses 74 and 148 are due to principally Ge atoms and Ge_2 molecules.

Similar emission bursts of atomic and molecular species accompanying the fracture of single-crystal NaCl and LiF were attributed to the emergence of dislocation structures (e.g., loops, pileups, and slip bands) at the fracture surface.[1] Dislocations are produced in the fracture of alkali halides and are readily observed by etching the fracture surfaces.[6,7] Shallow dislocations and dislocation structures are attracted to the surface by the image force which decreases as 1/(distance from the surface). Dislocations are readily generated during the fracture of alkali halides, being driven into the bulk by the high-stress field near the crack tip. After fracture, mobile dislocations close to the surface will be accelerated back to the surface. Numerical models of dislocation motion in LiF suggest that shallow dislocation loops $\lesssim 2$ μm from the surface take long enough to reach the surface to explain significant delays from fracture (on the order of ms to s).[1] The kinetic energy delivered by such a dislocation loop at "popout" can be high, on the order of several keV. Because of the great number of atoms and molecules observed in a typical emission burst from the alkali halides, we proposed that dislocation structures, such as dislocation pileups and slip bands, are involved.

However, dislocation motion at room temperature in Ge is severely hindered relative to the alkali halides. The activation energy for "low-temperature" dislocation motion is on the order of 1.4–1.7 eV,[8,9] due to the energy required for the nucleation of double kinks. In the absence of kinks, dislocation motion would require stresses on the order of the Peierls stress, which is estimated to be 2–3 GPa.[10] Fracture stresses in excess of this (at least 3.8 GPa) have been observed in carefully prepared, chemically etched Ge samples.[11,12] Stresses at the crack tip can be up to twice this high before reaching the limit imposed by crack branching.[13] These stresses are sufficient to create large numbers of dislocations and to move them into the bulk material, as shown by etch-pit studies of fracture surfaces of very strong samples.[11] However, the image stresses driving dislocations back to the surface are well below the Peierls stress at depths greater than a few lattice spacings, implying that long, *straight dislocations in the bulk would be trapped.*

However, curved dislocations geometrically require high kink densities to accommodate their curvature. These kinks are quite mobile, even at room temperature. (The activation energy for kink motion in Ge is on the order of 0.04 eV.) TEM observations indicate that curved dislocations are *much* more mobile than straight segments in Ge.[9] Since dislocations produced by fracture must begin and end on the surface and therefore require curvature, we expect dislocations produced by fracture to be similarly mobile. The geometry of such a loop is shown in Fig. 4. If a curved dislocation is not pinned, these kinks provide a low-stress mechanism for motion toward the surface which is not available to long, straight segments.

In the alkali halides, numerical models indicate that dislocations may arrive at the surface with substantial kinetic energies in addition to their nominal line energy.[1] Similar models of dislocation motion in Ge may be difficult to construct, given the "nonequilibrium" density

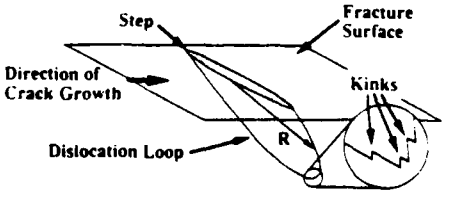

FIG. 4. Geometry of a dislocation loop of radius R relative to the fracture surface. The curvature of the loop requires kinks along its length, as shown in the inset.

of kinks along a dislocation loop. However, the elastic strain energy associated with dislocations in Ge is quite high; the energy of a dislocation loop 1 μm in radius is in excess of 100 keV, which corresponds to -5.1 eV per atomic length (estimated from $E \approx Gb^3$).[10] This is well in excess of the sublimation energy of Ge, about 3.6 eV/atom.[14] Additional energy may be available in the form of dangling or strained bonds in the dislocation core (about 0.5 eV per dangling bond for Si). Although it is overly optimistic to assume that all this energy will be available for emission, this is sufficient for the emission of perhaps 10^4 Ge atoms. As in the case of the alkali halides, the intensity of the observed emissions requires the participation of many dislocations in any given emission event. We suggest that *the concerted emergence of such dislocations is responsible for the bursts in neutral Ge and Ge_2 emission described above*, where the required energy is supplied by release of both lattice strain and kinetic energies associated with moving dislocations.

Localized plastic deformation may result from rapid crack growth in a number of brittle materials. X-ray line-broadening measurements and selected-area electron-channeling measurements on alumina fracture surfaces have shown features attributed to plastic deformation.[15,16] Similar evidence for plastic deformation at cleavage surfaces of Ge formed in compression is provided by x-ray diffraction.[17] This deformation need not represent slip *per se*, but perhaps deformation twinning[17] or imperfect healing of microcracklike structures.[18] Although the popout of dislocation pileups may be the most likely source of the observed emissions, a number of other structures can be produced by inelastic deformation during rapid crack growth. Again, *catastrophic* relaxation of such deformation, e.g., via dislocation popout or a related process, could yield bursts of neutral emission.

To conclude, we have presented evidence that accompanying the fracture of single-crystal Ge under flexure loading, low-energy Ge atoms and Ge_2 molecules are released from the fracture surface at times ranging from 10 to 100 ms after fracture. We have attributed this emission to the emergence of dislocations from the fracture surface, where these dislocations are created by dynamic crack growth. Our results strongly suggest that production of dislocations from dynamic crack growth in Ge is more extensive than might be expected. Measurements of atomic and molecular emission serve as a useful probe of these processes, particularly in light of the time scales (ms) that are involved.

We wish to thank John Hirth and Richard Hoagland, Department of Mechanical and Materials Engineering, Washington State University, for helpful discussions. This work was supported by the Ceramics and Electronics Materials Division of the National Science Foundation under Grant No. DMR 8912179, Office of Naval Research under Contract No. N00014-87-K-0514, and the Washington Technology Center.

[1]J. T. Dickinson, L. C. Jensen, S. C. Langford, and J. P. Hirth, J. Mater. Sci. **6**, 112 (1991).

[2]S. C. Langford, L. C. Jensen, J. T. Dickinson, and L. R. Pederson (to be published).

[3]J. T. Dickinson, in *Non-Destructive Testing of Fibre-Reinforced Plastic Composites*, edited by J. Summerscales (Elsevier Applied Science, London, 1990), Vol. 2, pp. 429–482.

[4]J. E. Kingcade, H. M. Nagarathna-Naik, I. Shim, and K. A. Gingerich, J. Phys. Chem. **90**, 2830 (1986).

[5]E. E. Donaldson, J. T. Dickinson, and S. K. Bhattacharya, J. Adhes. **25**, 281 (1988).

[6]J. J. Gilman, C. Knudsen, and W. P. Walsh, J. Appl. Phys. **29**, 601 (1958).

[7]S. J. Burns and W. W. Webb, Trans. Metall. Soc. AIME **236**, 1165 (1966).

[8]O. W. Johnson, J. Appl. Phys. **36**, 3247 (1965).

[9]F. Louchet, D. Cochet Muchy, and Y. Brechet, Philos. Mag. A **57**, 327 (1988).

[10]H. Alexander and P. Haasen, in *Solid State Physics*, edited by F. Seitz and D. Turnbull (Academic, New York, 1968), Vol. 22, pp. 27–158.

[11]O. W. Johnson and P. Gibbs, in *Fracture of Solids*, edited by D. C. Drucker and J. J. Gilman (Interscience, New York, 1963), pp. 315–338.

[12]T. L. Johnson, R. J. Stokes, and C. H. Li, Acta Metall. **6**, 713 (1958).

[13]H. P. Kirchner and J. P. Conway, Jr., in *Fracture Mechanics of Glasses and Ceramics*, edited by J. R. Varner and V. D. Frechette (American Ceramic Society, Westerville, OH, 1986), pp. 187–213.

[14]E. G. Rochow, *Comprehensive Inorganic Chemistry* (Pergamon, Oxford, 1973), Chap. 16.

[15]R. W. Guard and P. C. Romo, J. Am. Ceram. Soc. **48**, 7 (1965).

[16]J. Lankford and D. L. Davidson, J. Mater. Sci. **17**, 1501 (1982).

[17]H. Suzuki and K. Kamada, J. Phys. Soc. Jpn. **21**, 571 (1966).

[18]O. W. Johnson, J. Appl. Phys. **37**, 2521 (1966).

V. Alkali emission accompanying fracture of sodium silicate glasses

S. C. Langford, L. C. Jensen, and J. T. Dickinson
Physics Department, Washington State University, Pullman, WA 99164-2814

L. R. Pederson
Pacific Northwest Laboratory, Richland, WA 99352

Measurements of atomic Na emission accompanying the fracture of sodium trisilicate glass and a soda lime glass in vacuum were made by quadrupole mass spectroscopy and surface ionization techniques. Peak Na° emission intensities occur some 3-6 ms after the fracture event and decay over tens of milliseconds. This behavior is attributed to the diffusion of Na^{+} ions into a layer of damaged material at the surface where the ions are subsequently neutralized and thermally emitted as Na°. Charge carriers generated during fracture and subsequently trapped at defect sites apparently play important roles in charge compensating Na^{+} diffusion and in neutralizing Na^{+}. During the first 300 ms following fracture, we also observe intense, short lived (400 μs) bursts in Na° emission which may be associated with catastrophic relaxation of residual stresses. The kinetics of Na emission suggest that the relaxation of newly formed glass surfaces involves rather complex surface physical and chemical processes.

I. INTRODUCTION

Deformation and fracture of many materials is accompanied by the emission of photons, electrons, ions, and neutral particles.[1-7] We refer to these emissions collectively as fracto-emission. Fracto-emission is a result of chemical and electronic relaxation of the surface from the nonequilibrium state produced by fracture. Electronic excitations on newly formed fracture surfaces during dynamic crack growth can result in particularly intense emission of charged particles and light. Some fracture surfaces apparently display nonequilibrium stoichiometry which

relaxes over periods of ms or seconds depending on the environment. (Observations of the slowest relaxations require vacuum.) As surface structure often has important chemical and mechanical consequences, the processes by which these deviations from "ideal" structures relax are of considerable practical importance. They also have implications in the interpretation of the results of surface analysis of fracture surfaces. To the degree that atomic rearrangements may occur at the crack tip itself, such relaxations may also affect fracture behavior, particularly at intermediate and high crack velocities.

Significant deviations from bulk compositions have been observed in surface analyses of silicate glasses, of which sodium silicate glasses and various commercial soda lime glasses are the among most extensively studied. Specifically, an excess of alkali is often found in the first few monolayers of a fractured surface.[8,9] Molecular dynamics simulations of alkali silicate glass surfaces have demonstrated a tendency of heavier alkali atoms to accumulate at surfaces,[10,11] accounting at least qualitatively for the observed excess alkali. Alkali composition gradients in the near surface region of silicate glasses have important consequences in the degradation of mechanical properties by water and thus in the suitability of glass as a matrix in which to confine radioactive alkalis in the long term storage of nuclear waste.[12] Furthermore, the transport of alkali at the earth's surface and along moving geological faults could be influenced by alkali release accompanying fracture and grinding of minerals such as feldspars. Emission of alkali containing species has been recently reported from the fracture of NaCl and LiF single crystals and was attributed to a dislocation-related mechanism.[7]

We have previously reported measurements of alkali emission following the fracture of sodium trisilicate glass suggesting that surface formation and equilibration may involve significant changes in surface stoichiometry.[1] The present work reports more detailed measurements of the rate of neutral sodium (Na°) emission indicating that significant amounts of alkali diffuse to the surface following fracture and are subsequently emitted. We have extended the work to commercial soda lime silicate glasses, and have taken special measures to rule out artifacts caused by the ejection of small glass fragments created in fracture (ejecta).

II. EXPERIMENT

The emission of neutral alkali atoms was measured by quadrupole mass spectrometry and surface ionization techniques. Detection efficiencies on the order of unity can be attained with surface ionization, which takes advantage of the charge transfer accompanying adsorption of an alkali metal atom on a high work function metal. At elevated temperatures, the alkali can be desorbed as an ion with a probability given by the Saha-Langmuir equation.[13] Figure 1(a) shows schematically a surface ionization detector.[14] In this work, the ionizing surface was a 50 μm x 8 mm x 20 mm Pt ribbon. A dc current of ~32 A was passed through the ribbon, heating it to 1300-1600 C. At these temperatures, clean Pt has an 80% efficiency for ionization of Na metal atoms,[13] with typical alkali residence times on the surface of ~1 μs. However, the surface employed in this work was somewhat contaminated, so that lower ionization efficiencies were obtained. Pt temperatures were determined by optical pyrometry through a Pyrex window viewing the back surface of the ribbon. The ion collector was connected to the input of a Keithley 602 electrometer floated 20 V below ground potential; this potential appears on the collector and thus attracts positive ions. Although the detection efficiencies are somewhat reduced for alkali atoms in polyatomic molecules or clusters, the resulting signals nevertheless represent the collective alkali atom content of the emission. No discrimination of Na from atomic and molecular sources is possible using surface ionization. We note that the ionization energy of Ca and other nonalkali components of the plate glass used in this study are significantly higher than that of Na, and thus are not readily ionized on the Pt surface.

Discrimination between atomic and molecular species is often possible using quadrupole mass spectroscopy. To determine origin of a given signal, simultaneous measurements of emission intensities at two or more masses are quite valuable. Mass selected intensity measurements could be made simultaneously at two masses using the dual quadrupole apparatus shown schematically in Fig. 1(b).[7] The electron impact ionizer was symmetrically situated between

two identical quadrupole mass filters (UTI Model 100C). A sample injection system positioned the samples 1 cm from the ionizer, providing a reasonable solid angle for neutral detection. The electric fields within the ionizer favored the detection of ions created near mass filter 1 by mass filter 1, and conversely for ions created near mass filter 2. The two focus plate voltages and the average positive potential inside the ionizer ("ion energy") were adjusted to maximize sensitivity and mass resolution (~1 amu). The resulting ion currents were amplified by electron multiplication and monitored by identical electrometers. In this geometry, the detected particles can safely be identified as neutrals rather than ions. Ions entering the ionizer from the outside would need an energy of at least 15 eV to overcome the potential on the energy grid and pass into the mass filter; yet ions of this energy would not be able to "turn the corner" required for passage through the mass filter. The time response of the neutral emission signals was limited by the 25-50 μs rise times and 25-100 μs decay times of the electrometers.

Another arrangement of quadrupole mass spectrometers was used to estimate the velocity distributions of the emitted particles. Two mass spectrometers were arranged sequentially as shown in Fig. 1(c). The distances from the sample to the centers of the ionizers were 3 cm and 9 cm, respectively. The signal strength measured 9 cm from the sample is typically quite low, so that comparable signal pairs were obtained for only the most intense signals.

The load at fracture was monitored with a Kistler 9202 quartz load transducer. The output of the transducer was digitized at 10 μs intervals, simultaneously with the neutral emission signals. The frequency response of the load transducer allowed the time of fracture to be determined to within about 20 μs.

Samples were prepared from commercial soda lime glass rod and from sodium trisilicate glass. The soda lime glass samples were cut to 12 mm lengths from 3.4 and 4.1 mm diameter rods. Electron microprobe analysis of the soda lime glass yielded the following composition, expressed in terms of the weight percent of the components in their oxide form: Na_2O 12.7%, CaO 4.4%, MgO 3.8%, Al_2O_3 2.6%, 72.5% SiO_2, with traces of Fe, K, and Ba. The sodium trisilicate glass was prepared from stoichiometric quantities of either sodium carbonate or sodium

metasilicate and quartz powder. The resulting glass was cut into rectangular samples, 2.5 x 6 x 13 mm^3, with a diamond saw and mechanically polished to 3 μm diamond grit. The samples were mounted in an ultrahigh vacuum system with a base pressure below 1 μPa and loaded across a support span of 6.3 mm at a rate of about 70 μm/s.

The fracture of glassy materials often results in the ejection of fragments (ejecta) with typical dimensions ranging from mm down to at least μm. As even μm-sized glass fragments can volatilize Na upon striking a hot filament, great care was taken to prevent such fragments from reaching the filaments. We found that a stainless steel shield with a 2 x 0.5 mm aperture located midway between the sample and the surface ionization filament was sufficient to protect the surface ionization filament. The shield blocked not only most line-of-sight paths to the filament, but also eliminated most arcing and bouncing trajectories. As noted below, careful electron microprobe analysis of a Pt filament after three fracture events showed no sign of ejecta despite significant Na signals accompanying fracture. The spatial resolution of the probe was at least 500 nm, although somewhat smaller particles should have yielded measurable Si signals. Many (>100) submicron particles would be required to explain the observed signals. It is highly unlikely that so many submicron particles would appear in the absence of larger particles.[15, 16]

Measurements of photon emission (phE), electron emission (EE), and positive ion emission (PIE), accompanying the fracture of the soda lime glass were carried out under similar conditions in a separate vacuum system.[1] phE was detected by an EMI Gencom 9924QB photomultiplier tube with a quartz window and bialkali phosphor. EE and PIE were detected with a Galileo Electro-optics 4039 Channeltron electron multiplier. The photon and charged particle detectors were operated in a pulse-counting mode. The resulting pulses were counted and summed in a multichannel scaler over 1-ms intervals.

III. RESULTS

III.A Surface Ionization Measurements

The Na emission following fracture typically displays intense, transient bursts superimposed on and following a relatively weak, long-lived emission. These features are evident in the surface ionization current accompanying the fracture of a soda lime glass rod shown in Fig. 2(a). The integrated current is equivalent to at least 1.2×10^{11} alkali atoms, presumably due to Na°. This is a substantial number of alkali atoms, about 1×10^{12} atoms per cm^2 of (nominal) fracture surface area. As this emission was collected through a small aperture (~1 mm^2 in area positioned about 1 cm from the sample), the number of emitted atoms is clearly some orders of magnitude *higher*. Unfortunately, larger apertures allowed small glass fragments to reach the filament. Because of the highly anisotropic distribution of Na° emission as it escapes a narrow crack, we are hesitant to make a more precise estimate of the total amount of Na° emitted from the surface. We can safely conclude that: (a) our measurements are a modest lower limit, and (b) the large number of observed alkali atoms suggest that diffusion of alkali from the subsurface region plays an important role in the alkali emission process.

The long slow decay of the surface ionization current, here in excess of 1 s, is an artifact due to the relatively low temperature of the Pt filament (~1430° C). At these lower filament temperatures, a substantial portion of the incident Na° is re-emitted as neutrals. Most of these neutrals are deposited onto the nearby sample shield and cooler portions of the filament support structure. The shield is sufficiently close to the filament that some of these neutrals are subsequently desorbed from the shield and ionized by the filament, resulting in a long slow decay. One of the most remarkable features of these data is the frequent transients observed. The emission shows strong bursts, some with their own tails, many milliseconds after fracture. Bursts with similar time distributions were observed in the quadrupole mass spectrometer measurements, where better time resolution was obtained (discussed below).

The nature of the emission tail is readily verified by raising the temperature of the Pt filament. The fraction of the incident Na° ionized by the filament is a strong function of temperature in this temperature range with our filament preparation, so that data taken at high temperatures more accurately reflects the intensity of the incident Na° as a function of time. However, premature filament failure was a problem at higher filament temperatures due to local melting at inhomogenieties in the Pt foil. Figure 2(b) shows the surface ionization current measured at a filament temperature of ~1580° C. The major portion of the peak is confined to a 60-80 ms period following fracture, which we take to reflect the actual duration of emission from the sample. Figure 2(b) still has a long, slow decay, but its amplitude is substantially reduced relative to the tail of Fig. 2(a). Even at the higher filament temperatures, a small portion of the incident Na° is desorbed in the neutral state. However, the total integrated emission is not much different from that measured at lower filament temperatures.

The tail of Fig. 2(b) also slows a substantial shoulder, which we attribute to ejecta striking the filament. The evaporation of Na° from glass melted on the filament is expected to proceed rapidly until very low Na concentrations are reached, at which point a sharp drop in the detected Na signal should be observed. (Under these conditions, Na evaporation should approximate a "zeroth order" process.) This is appears to be the best explanation for the observed shoulder. Such shoulders were most often observed without a shield between the sample and the filament, but were rarely observed when the small aperture was used. From the size of the observed shoulder, a crude estimate of the size of the glass fragment may be made. Extrapolating from the shoulder back to zero time and assuming that virtually all the Na from the melted glass was detected, the volume of the original glass fragment was ~0.1 μm^3, i.e. equal to the volume of a cube 500 nm on a side. Although the shoulder contributes substantially to the total emission intensity, its time behavior distinguishes it from the other emission components.

Two other conspicuous features of the surface ionization current are the relatively slow rise to the peak emission intensity and the time required after the fracture event before the onset of emission. These features are evident in Fig. 3. The onset of measurable emission typically occurs

400-700 μs after fracture. The rise to maximum emission intensity usually requires 3-6 ms, often showing several shoulders or bumps, as shown in Fig. 3(b). Although the amount of data at higher filament temperatures is limited, both the delay and the rise time are apparently independent of filament temperature. The delay and rise time were also independent of load at fracture. Most fracture related emissions (e.g. photon, electron, and ion emission) peak during the relatively short time interval defined by the fracture event. The slow rise in alkali emission is far to long to be due to atomic or molecular time-of-flights (~40 μs, assuming an atom of mass 23 amu at room temperature). We expect that the crack is fully open in ~40 μs, when the measured load reaches its minimum value. Therefore, the geometry for the escape of atoms and molecules from the opening crack is certainly good if not optimal long before peak emission is reached.

Similar results for sodium trisilicate glass were obtained with the surface ionization detector with slightly less Na° emission intensities/sample cross-section as compared to the soda lime glass.

III.B Quadrupole Measurements

The general features of the surface ionization current are confirmed by quadrupole mass filter measurements which also unambiguously determine the masses of the emitted species. Figure 4 shows emission measurements made at mass 23 (Na°) accompanying the fracture of sodium trisilicate glass. Although few quadrupole measurements showed the relatively weak, long-lived (continuum) component of Fig. 2, we present one of them to allow comparison with the more sensitive surface ionization current measurements. Estimates of the quadrupole mass filter sensitivity suggest that relatively intense signals are required for the detection of the continuum component. Again the peak in the continuum is delayed 6-7 ms from the fracture event, and persists some tens of ms. Sharp bursts are also observed in the emission decay.

The bursts show a great deal of variety in intensity and timing. They were delayed from the fracture event, usually following the load drop by at least 10-40 ms. The bursts are quite narrow, with typical full-width-at-half-maxima of about 200 μs. Since the electric fields

surrounding the quadrupole ionizer oppose the entrance of externally generated ions into the detection region, the signal at mass 23 can be confidently attributed to an initially neutral species. Simultaneous measurements made with the dual quadrupole system [Fig. 1(b)] described above indicate that most of the bursts are atomic rather than molecular in composition. Occasionally small bursts were observed with a component at mass 39 (NaO).

To rule out ejecta as a source for the mass 23 bursts, further measurements were made with two quadrupoles arranged sequentially [Fig. 1(c)]. The ionizer of the first quadrupole was centered 3 cm from the sample and the ionizer of the second 9 cm from the sample. From the difference in arrival times at the two quadrupoles the velocity of the particles making up the burst can be estimated. An example of mass 23 measurements made through sequential quadrupoles appears in Fig. 5. The separation of the peaks in Figs. 5(a) and (b) is about 200 μs, corresponding to a velocity of 300 m/s. This velocity is *significantly* higher than any expected for ejecta leaving the sample,[15] and is only slightly lower than the average thermal velocity of a room temperature particle at mass 23 (470 m/s).

We can summarize the overall behavior for the neutral alkali emission accompanying fracture of sodium silicate and soda lime glasses:

- The neutral emission is principally Na°.
- The Na° emission is delayed. Measurable emission begins hundreds of microseconds after the fracture event and builds to a peak over a few milliseconds.
- Intense, delayed bursts of Na° occur long after fracture, with average velocities consistent with atomic particles as opposed to macroscopic ejecta.

III.C. Photon and Charge Particle Emission

Measurements of photon emission (phE), electron emission (EE), and positive ion emission (PIE) accompanying the fracture of fused silica and sodium trisilicate glass have been reported previously.[1] Here we report phE, EE, and PIE measurements on the soda lime glass rod used in much of this work. Figure 6 shows typical emissions recorded from three separate fracture events. Each signal rises to a peak immediately after fracture on the time scale shown (1 ms/channel). This contrasts with the Na° emission, which requires a few milliseconds to rise to a peak. Both EE and PIE decay rapidly over a few tens of milliseconds; sharp bursts in emission follow as long as 100 ms after fracture. This behavior *is* comparable with the decay of the continuum component in Na° emission and the associated bursts. The phE displays a significantly longer tail, lasting a few hundred milliseconds, without significant spiking. However, the intensity of the phE tail would make the observation of most bursts of magnitudes comparable to those in the EE and PIE difficult to observe. These emissions suggest a rather high degree of electrical activity related to the recombination of trapped electrons and holes on the freshly formed fracture surface.

III.D. Ejecta

As the ejection of small glass particles constituted a potential source of "artifacts" in our measurements of atomic emissions accompanying fracture, a brief discussion of their nature is appropriate here. The detection and prevention of ejecta are of some technological importance as well, having important ramifications in the fracture of window and eyeglass materials.

Although some fracture events yielded significant quantities of ejecta, the problem was minimized by its angular dependence. Virtually all ejecta had significant velocity components parallel to the fracture surface, along the direction of crack growth. This accounts for our ability to stop essentially all ejecta by placing a small aperture directly between the sample and the filaments.

The shoulder in Fig. 2(b) which we attribute to ejecta was actually rare with the aperture in place. After a series of three fracture events in which no shoulder was observed, a electron microprobe was used to scan the filament surface for evidence of Si, which would remain on the filament surface at the temperatures employed. No Si was found, despite a spatial resolution of about 500 nm. We expect that excess Si would be observed even if particles less than 500 nm in diameter were present. Thus we are confident that surface ionization measurements without shoulders in their tails are not due to small numbers of ejecta. Of course, a large number of sufficiently small ejecta could yield smoothly varying emissions; however, it is not likely that a large number of small particles would be produced without at least a few larger particles. At some point, the distinction between molecular and particulate emission (clusters??) becomes fuzzy. One might expect to see Si-containing ionic fragments from electron bombardment of very small clusters, but none were observed.

Glass fracture *without* the aperture, but with a fine mesh rectangular grid positioned between the sample and the Pt filament (grid openings: 5 x 5 μm^2, transmission: 25%), generally yielded all of the features attributed to atomic emission as well as ejecta, including shoulders in the tail of the emission decay. This is consistent with the ejection of micron-sized or smaller glass fragments, such as that inferred from shoulder in the tail of Fig. 2(b) (assuming cubic geometry, 50 nm on an edge).

Further evidence for the atomic/molecular character of emission passing through the aperture was provided by flash desorption measurements. The Pt surface was held at a temperature of <100 °C during fracture and allowed to collect the emitted particles. Then, a few seconds after fracture, the temperature of the Pt was raised at a rate of approximately 100 °C/s while monitoring the emitted ion current. If atomic/molecular particles are residing on the Pt surface, this current should resemble a flash desorption curve, i.e., showing a fairly narrow peak in time and temperature. A typical result is shown in Fig. 7(a). Figure 7(b) shows a second flash desorption measurement made after dosing the Pt filament with Na° from a commercial effusive Na source. The Na dose provided by the source was quite high and spatially diffuse, so that nearby

surfaces were coated with Na° despite the presence of the aperture. This tends to broaden the desorption peaks, including the first peak of Fig. 7(b). As noted above, Na° on nearby surfaces is responsible for long emission tails; in the flash desorption measurements this appears as a rapidly growing emission as these surface warm. This is the source of the second, offscale peak in Fig. 7(b). The significant result here is that the temperature of the first peaks from the fracture and dosing events agree to within 30 °C; the peak widths are also quite similar. This is strong evidence for the atomic or molecular character of this portion of the emission. Na associated with ejecta should be more tightly bound within the glass network, yielding diffusion limited emissions. Thus, desorption peaks due to ejecta would be very broad (due to diffusion to the glass surface) and would appear at somewhat higher temperatures.

Some material was occasionally ejected during fracture in the form of readily visible, macroscopic particles. In the absence of the grid and the aperture, a macroscopic piece of glass (volume ~1 mm^3) would occasionally strike the surface ionization or quadrupole filament. Then the Na° signal would usually go *slowly* off-scale. The return to background values could take hours, consistent with the huge amount of Na in a piece of glass this large. When such ejecta stuck to the Pt filament, it would soon cease to function as a surface ionizer due to the thin layer of molten silica which would cover the surface. The apertured signals, however, *never* showed these attributes.

Thus, we can safely say that although small glass fragments were occasionally emitted during fracture, the effect of these particles on the observed signals is understood and their presence minimized. We therefore conclude that the fast decaying continuum and the accompanying rapid, but delayed, bursts observed with both types of detectors (by surface ionization and electron impact ionization) are not due to ejecta, but due to atomic Na emission.

IV. DISCUSSION

The emission of substantial amounts of Na° following fracture is evidence for some remarkable surface chemistry. We attribute this emission to the diffusion of Na^{+} to the surface under the influence of its excess "free volume" relative to that in the glass network. This diffusion should be rate limited by the availability of mobile charge (trapped holes) to charge compensate the ion current. At the surface, Na^{+} can be neutralized by trapped electrons, at which point thermal energies are sufficient for emission into the vacuum. As the glass fracture surface is characterized by high defect densities, including high densities of electron and hole traps, competition for available charge, as well as depletion of Na^{+} in the subsurface region, may be rate limiting steps. Although the origin of emission bursts is not clear, we suspect that catastrophic relaxation of localized residual stresses may be important.

Sodium has been shown to preferentially occupy surface sites in silicate glasses. Ion scattering spectroscopy (ISS) measurements on sodium trisilicate glass fractured in vacuum have been made by Pantano, Kelso, and Suscavage.[9] They found that O peaks from sodium trisilicate glass were reduced 50% relative to those from fused silica (SiO_2) despite the fact that the oxygen concentrations of these materials differ only 12%. In both cases the samples were analyzed within 5 minutes of fracture, minimizing the effect of adsorbed gases. Interestingly, the ISS Na/O signal ratio measured on sodium trisilicate glass fractured in vacuum appears to be somewhat higher than that measured on surfaces annealed in vacuum at temperatures above the glass temperature.[17] This is consistent with the hypothesis that surface damage or broken bonds play a role in the accumulation of sodium at the surface. Evidence for sodium accumulation at the surface of alkali glasses fractured in vacuum also appears in Auger electron spectroscopy measurements by Lacharme, et al.[8] Silicon and oxygen peak heights in the sodium silicate and soda lime glasses were consistently lower than that expected on the basis of the bulk oxygen concentration and the peak heights observed from fused silica and was attributed to a possible enrichment of alkali in the fracture propagation zone.

A similar preference for alkali occupation of surface positions was shown in molecular dynamics simulations of sodium trisilicate fracture surfaces. Garofalini and Levine[11] modeled the fracture of a sodium trisilicate glass by removing periodic boundary conditions along one direction in a three dimensional glass network composed of 394 atoms. The positions of the lowest 192 atoms were fixed to represent the effect of the underlying bulk glass. The resulting Na^+ density profiles show a definite tendency to relax toward the outer surface of the glass. This relaxation is more pronounced if fracture is simulated at elevated temperatures (1500 K) and then quenched to room temperature, but is still observed in room temperature simulations. This is of interest because of evidence for elevated temperatures at the tip of a moving crack.[18,19] At elevated temperatures, Na^+ tends to migrate away from the surface into the "vacuum," suggesting that longer simulations might show the evaporation of Na, perhaps as Na_2O. These simulations extended over times of 6-12 ps, times long relative to that required for crack growth through such an assembly, but short relative to the duration of the emissions observed in our work.

The diffusion of Na^+ to the surface is driven by its excess free volume in the glass network and by the presence of broken and strained bonds in the surface region. The positive free volume of Na^+ in the silicate glass implies that its free energy depends on pressure,[20] i.e. $G_{Na} = V_{Na}dP$ where V_{Na} ~2.2 Å^3. Pressure gradients therefore drive Na^+ into regions of low pressure, such as regions under tensile stress. Michalske and Smith[21] have shown that alkali diffusion in the strain field of a growing crack can account for a significant fraction of the fracture energy of alkali containing glasses. This diffusion is limited by the intense electric fields that accompany Na^+ concentration gradients. However, these fields can be minimized if mobile trapped charge is available for charge compensation, as indicated by the observed photon and charged particle emission. In particular, holes trapped at nonbonding oxygens appear to be fairly mobile. Wang et al. have attributed the slow onset of Na^+ emission in electron stimulated desorption from sodium trisilicate glass to the trapping of mobile holes at nonbonding oxygens.[22]

Localization of Na^+ at the surface could also be enhanced by the presence of broken and strained bonds. Fracture inherently produces a high density of broken and strained bonds.

Molecular dynamics simulations of alkali atom adsorption on silica surfaces indicate that alkali atoms preferentially adsorb at sites of nonbonding oxygens and strained bonds.[23] Heavier alkali, such as K, do not diffuse into the lattice until these defect sites are saturated. (Lighter alkalis, such as Li, can diffuse into the lattice before saturation occurs.) High resolution X-ray photoelectron spectroscopy measurements of K adsorbed on fused silica indicate that K is indeed preferentially adsorbed at defect sites localized at the surface.[24] The presence of nonbonding oxygens and strained bonds at fracture surfaces may help explain the absence of emission immediately after fracture. The first Na^+ to reach the surface would react with surface defects and be unavailable for emission processes. Many of these surface defects also serve as hole and electron traps.

The density of these surfaces defects would be enhanced markedly by the presence of deformed material at the fracture surface. Molecular dynamics simulations of fracture in sodium trisilicate glass fibers reported by Soules and Busbey indicate that significant plastic deformation accompanies fracture despite failure in a brittle mode.[25] The depth of the deformed layer is necessary quite small, perhaps ~1 nm. Such a deformed layer would have a density lower than that of the bulk glass and a high defect density. Given time scales much longer than those probed in molecular dynamics simulations, much of this damage could heal, eventually reducing the defect density. Thus the dynamic properties of this process zone would have significant effects on the kinetics of alkali emission. The depth or degree of surface damage could easily vary along the fracture surface due to changes in local stress intensity during crack growth. These variations may be responsible for the shoulders or bumps in the leading edge of the surface ionization current shown in Fig. 3(b). We note that the alkali content within the volume of this process zone is $\sim 10^4$ times higher than the detected emission.

The distribution and diffusion of Na^+ at the fracture surface will also be affected by any Na^+ clustering or other medium range order in the glass network. Greaves et al. have performed extended X-ray absorption fine structure measurements on sodium disilicate and soda lime glasses which indicate that the coordination of Na^+ is well defined and varies with glass composition.[26] They describe the glass network in terms of two continuous, interpenetrating, random sublattices

composed of a SiO_2 network and intercalated Na_2O. The continuity of the alkali sublattice is supported by isotopic diffusion measurements on alkali glasses.[27,28] In silicate glasses with at least 10 mol% alkali oxide, diffusion involves the *correlated* motion of alkali ions. Fracture would naturally be favored along the alkali sublattice, where Na^+ concentrations are naturally high. As noted above, immediate emission of Na° would still be hindered by the presence of stable defect sites at the surface.

Release of the alkali neutrals from the surface is most likely a thermally stimulated process. The principal alternative to thermal emission is electron stimulated desorption (ESD),[22] but this appears to be unlikely given the extremely low observed electron and ion emission intensities ($\sim 10^5$ particles per fracture event) relative to the observed neutral emission intensities ($\sim 10^{12}$ alkali atoms per fracture event). It is not likely that the charged particle emission would be so weak if the neutral emission were stimulated by bombardment of the surface. More convincing, the neutral and charged particle emissions grow differently with time; the neutral emission requires some milliseconds to rise to a peak while the charged particle emission peaks at fracture (to within the resolution of the measurement, 1 ms). However, the durations of the charged particle and neutral emissions are roughly similar, suggesting the proposed connection.

The emission of charged particles and photons is strong evidence for significant quantities of trapped charge at or near the fracture surface which can provide charge compensation for Na^+ as it diffuses toward the surface. The diffusion of holes into the bulk compensates the negative charge left behind by departing Na^+, converting the remaining $Si\text{-}O^-$ to nonbonding oxygen defects. The electron traps may be related to oxygen vacancy–peroxy defects. Vigouroux et al. suggest that electrons may be trapped at metastable oxygen vacancy–peroxy defects in fused silica.[29] These defects are readily created by low energy electron bombardment (< 200 eV). Although other electron traps may be operative in the sodium silicate glasses, we note that electrons in Na levels (i.e. in normal O^--Na^+ structures) are not localized and are therefore not trapped.[30] Thus, the neutralization of Na^+ is not very probable while either localized holes or electron traps are abundant. We suggest that the density of metastable electron traps is an important parameter in

determining the rate of Na° emission. As the trap density decreases due to the healing of surface damage, charge would become available to neutralize Na^{+}, yielding a weakly adsorbed Na° which would be readily desorbed at thermal energies.

We therefore attribute the continuum component of the Na° emission to the thermal emission of Na° formed by the neutralization of surface Na^{+} by electrons released during the decay of metastable electron traps. The surface excess Na^{+} may arise from fracture along an alkali sublattice structure, but is also expected on the basis of free volume effects which result in the diffusion or relaxation of Na^{+} toward the surface. Na^{+} diffusion is readily charge compensated by the counter-diffusion of holes into the bulk. In the first moments after fracture, the surface Na^{+} tends to be bound at defect sites, including strained and dangling bonds. The gradual relaxation of residual stresses in the deformed surface layer (the process zone), results in the re-establishment of many network bonds. The decay of the metastable electron traps would provide free charge for the neutralization of Na^{+}, which is subsequently emitted thermally. In this scenario, the surface Na^{+} excess is maintained by diffusion from the bulk.

The observed Na° emission spikes also appear to be thermal in origin, perhaps accompanying a localized, catastrophic relaxation process. Fracture along an alkali rich sublattice may well leave a metastable surface which eventually becomes unstable and relaxes catastrophically. Such damage need not be limited to the fracture surface per se. Localized shear can result in the formation of "shear bands," similar to those formed during the indentation of soda lime glasses.[31] Interestingly, delayed fracture can be initiated at or near shear bands seconds after pulsed indentation of soda lime glass, as radial cracks "pop in" under the influence of residual stresses. Shear bands are not unlike healed cracks. Formation of shear bands could easily be favored along alkali rich regions of the glass. In any event, they may quickly develop excess Na^{+}. Viscous relaxation of the stresses which formed the shear band, accompanied by diffusion of Na^{+} and further disruption of the silica network in the region, may result in delayed failure along the band. As charge migration and Na^{+} neutralization should be fairly complete prior to failure,

exposing the surface of such a region to vacuum could result in a brief, intense spike of Na° emission.

In support of this mechanism, we note that plastic deformation of sodium silicate and soda lime glasses is readily seen around indentations.[32,33] Beneath the indentations, features reminiscent of slip lines (shear bands) are observed. Structurally these feature are analogous to healed cracks. Because they are regions of reduced cohesion in the glass network, they are not observed in tensile fracture. However, they may be important in the onset of tensile fracture. This is supported by the agreement between effective yield stresses and ultimate tensile stresses of glass fibers.[34] Fractographic observations of soda lime glass indicate that the fracture initiation sites are often much larger than the the size of the actual fracture initiating flaws even at liquid nitrogen temperature; at liquid nitrogen temperature, slow (water-assisted) crack growth is ruled out as a source of the fracture initiation features.[35,36] Although it is not clear that shear deformation plays a role in the onset of crack growth, decohesion across the interface of a shear band or crack nucleation in the vicinity would explain this puzzling result.[31] Further, shear bands or related features would be available for the production of intense Na° bursts.

V. CONCLUSION

The intense Na° emission following fracture of sodium trisilicate glass indicates that the chemical and electronic state of the fracture surface requires at least tens of milliseconds for equilibration after fracture. The interaction of Na^{+} ions with the free surface in the presence of trapped holes and electrons, also produced in fracture, yields a net diffusion of Na^{+} to the surface, followed by neutralization and thermal emission. The amount of Na° emitted can be substantial, in excess of 10^{12} atoms/cm^2 of fracture surface area. The driving force for the diffusion of Na^{+} to the surface is most likely the excess free volume of Na^{+} in the silica network. Charge compensation of diffusing Na^{+} by mobile holes would allow diffusion to the surface without significant long-range changes in the stoichiometry of the near surface bulk glass. However, the

expected structural defects on the fracture surface still allow for greater "equilibrium" surface concentrations of Na^+ than are observed on well annealed (and quenched) fracture surfaces.

Since glass fractured in vacuum provides one of the most "pristine" surfaces available for surface studies, an understanding of how they are formed may have important implications with regard to glass surface chemistry. For instance, a well annealed (and quickly cooled) surface may have a composition more closely related to the bulk than either fractured or ion-etched surfaces, due to the potential effect of surface defects on the "equilibrium" surface Na^+ concentration. The charge transfer processes involved in neutral emission from silicate glasses are similar to those taking place in electron and ion beam stimulated desorption of Na^+ and in dissolution of glass in aqueous solutions. An understanding of charge transfer in any one environment will have implications concerning charge transfer in other environments. It should also be clear that the interpretation of surface analysis studies of fractured alkali glass surfaces needs to include a careful consideration of the neutral emission phenomena reported here. In fact, due to their transient nature, the high time resolution of our fracto-emission techniques provide one of the few probes of these effects.

VI. ACKNOWLEDGMENTS

We wish to thank Delbert Day for helpful discussions. This work was supported by the Ceramics and Electronics Materials Division of the National Science Foundation under Grant DMR 8912179, the Office of Naval Research under Contract No. N00014-87-K-0514, and the Washington Technology Center.

REFERENCES

1. J. T. Dickinson, S. C. Langford, L. C. Jensen, G. L. McVay, J. F. Kelso, and C. G. Pantano, J. Vac. Sci. Technol. A 6, 1084 (1988).

2. J. T. Dickinson, L. C. Jensen, and A. Jahan-Latibari, J. Vac. Sci. Technol. A 2, 1112 (1984).

3. S. C. Langford, J. T. Dickinson, and L. C. Jensen, J. Vac. Sci. Technol. A 7, 1829 (1989).

4. J. T. Dickinson, L. C. Jensen, and M. R. McKay, J. Vac. Sci. Technol. A 4, 1648 (1986).

5. J. T. Dickinson, L. C. Jensen, and M. R. McKay, J. Vac. Sci. Technol. A 5, 1162 (1987).

6. S. C. Langford, J. T. Dickinson, and L. C. Jensen, J. Appl. Phys. 62, 1437 (1987).

7. J. T. Dickinson, L. C. Jensen, S. C. Langford, and J. P. Hirth, J. Mater. Res., in press.

8. J. P. Lacharme, P. Champion and D. Léger, Scanning Electron Microsco. 1981, Part I, pp. 237-243 (1981).

9. C. G. Pantano, J. F. Kelso, and M. J. Suscavage, in *Advances in Materials Characterization*, (*MRS Vol. 15*) edited by D. R. Rossington, R. A. Condrate, and R. L. Snyder, (Plenum Press, New York, 1983), pp. 1-38.

10. J. F. Kelso, C. G. Pantano, and S. H. Garofalini, Surf. Sci. 134, L543 (1983).

11. S. H. Garofalini and S. M. Levine, J. Am Ceram. Soc. 68, 376 (1985).

12. L. L. Hench and D. E. Clark, J. Non-Cryst. Solids 28, 83 (1978).

13. E. Ya. Zandberg and N. I. Ionov, *Poverkhnostnaya ionizatsiya*, (Nauka, Moscow, 1960) [*Surface Ionization*, translated by E. Harnik, (Israel Program for Scientific Translations, Jerusalem, 1971)].

14. S. Datz and E. H. Taylor, J. Chem. Phys. 25, 389 (1956).

15. E. E. Donaldson, J. T. Dickinson, and S. K. Bhattacharya, J. Adhesion 25, 281 (1988).

16. E. E. Donaldson, M. H. Miles, and J. T. Dickinson, J. Mater. Sci. 24, 4453 (1989).

17. J. F. Kelso and C. G. Pantano, J. Vac. Sci. Technol. A 3, 1343 (1985).

18. R. Weichert and K. Schonert, J. Mech. Phys. Solids 22, 127-133 (1974).

19. R. Weichert and K. Schonert, J. Mech. Phys. Solids 26, 151-161 (1978).

20. Neill Weber and Martin Goldstein, J. Chem. Phys. 41, 2898 (1964).

21. T. A. Michalske and W. L. Smith, Bull. Am. Phys. Soc. 36, 1035 (A) (1991).

22. Y. X. Wang, F. Ohuchi, and P. H. Holloway, J. Am. Vac. Sci. Tech. A 2, 732 (1984).

23. S. H. Garofalini and D. M. Ziri, J. Vac. Sci. Technol. A 6, 975 (1988).

24. R. Caracciolo and S. H. Garofalini, J. Am. Ceram. Soc. 71, C-346 (1988).

25. T. F. Soules and R. F. Busbey, J. Chem. Phys. 78, 6307 (1983).

26. G. N. Greaves, A. Fontaine, P. Lagarde, D. Raoux, and S. J. Gurman, Nature 293, 611 (1983).

27. Chung Lim and D. E. Day, J. Am. Ceram. Soc. 60, 198 (1977).

28. J. E. Kelly III, J. F. Cordaro, and M. Tomozawa, J. Non-Cryst. Solids 41, 47 (1980).

29. J. P. Vigouroux, J. P. Duraud, A. Le Moel, C. Le Gressus, and D. L. Griscom, J. Appl. Phys. 57, 5139 (1985).

30. R. A. Murray and W. Y. Ching, J. Non-Cryst. Solids 94, 144 (1987).

31. B. R. Lawn, T. P. Dabbs, and C. J. Fairbanks, J. Mater. Sci. 18, 2785 (1983).

32. K. W. Peter, J. Non-Cryst. Solids 5, 103 (1970).

33. A. Arora, D. B. Marshall, B. R. Lawn, and M. V Swain, J. Non-Cryst. Solids 31, 415 (1979).

34. D. M. Marsh, in *Fracture of Solids*, edited by D. C. Drucker and J. J. Gilman, (Interscience Publishers, New York, 1963), pp. 143-155.

35. R. H. Doremus and W. A. Johnson, J. Mater. Sci. 14, 2236 (1979).

36. R. H. Doremus and J. F. Kay, J. Mater. Sci. 13, 855 (1978).

FIGURE CAPTIONS

FIG. 1. Apparatus for the detection of neutral emission during fracture. (a) Surface ionization detector. (b) Dual quadrupole mass filter for the simultaneous detection of emission at two different masses. (c) Sequential quadrupole mass filters for estimating velocity distribution of neutral emission.

FIG. 2. Surface ionization current measurements accompanying fracture at two filament temperatures: (a) ~1430 °C and (b) ~1580 °C.

FIG. 3. (a) Onset of the surface ionization signal and (b) load drop accompanying the fracture event of Fig. 2(b). The Pt filament temperature is ~1580 °C.

FIG. 4. (a) Load and (b) quadrupole mass selected emission at 23 amu accompanying the fracture of sodium trisilicate glass.

FIG. 5. Emission bursts detected by consecutive quadrupoles tuned to 23 amu and positioned (a) 3 cm and (b) 9 cm from the sample, a soda lime glass rod.

FIG. 6. (a) Photon emission, (b) electron emission, and (c) positive ion emission accompanying fracture of soda lime glass. These signals were obtained from three separate fracture events.

FIG. 7. Flash desorption of alkali adsorbed on cold Pt filaments due to (a) fracture of a soda lime glass rod and (b) an effusive Na° source. Temperature vs time was measured by a low thermal mass (80 μm dia. wire) W/W-Rh thermocouple spot welded to the back of the Pt filament.

Neutral Emission Detectors

(a) Surface Ionization Detector

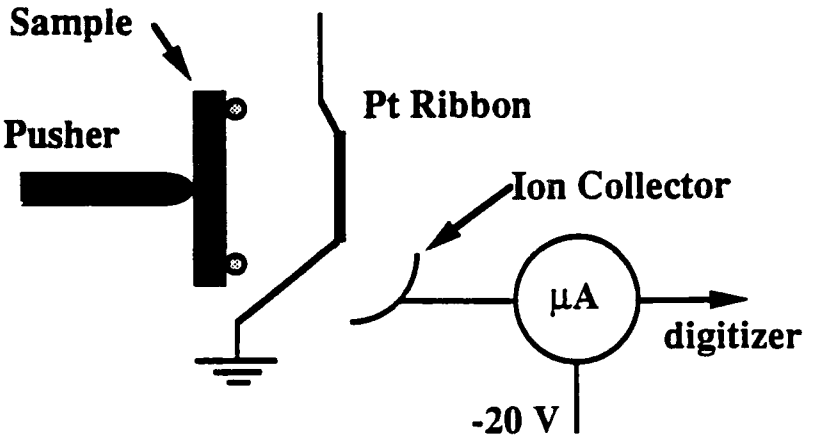

(b) Two Quadrupole Mass Spectrometers With A Shared Ionizer

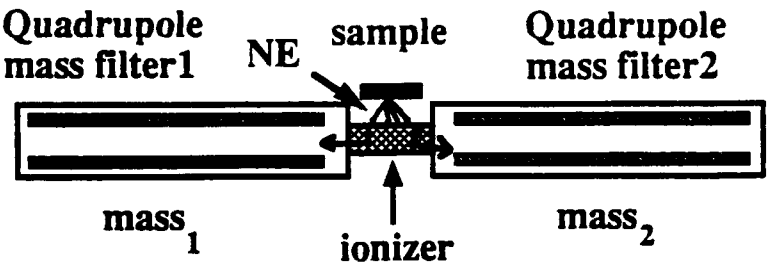

(c) two ionizers -- spatially separated

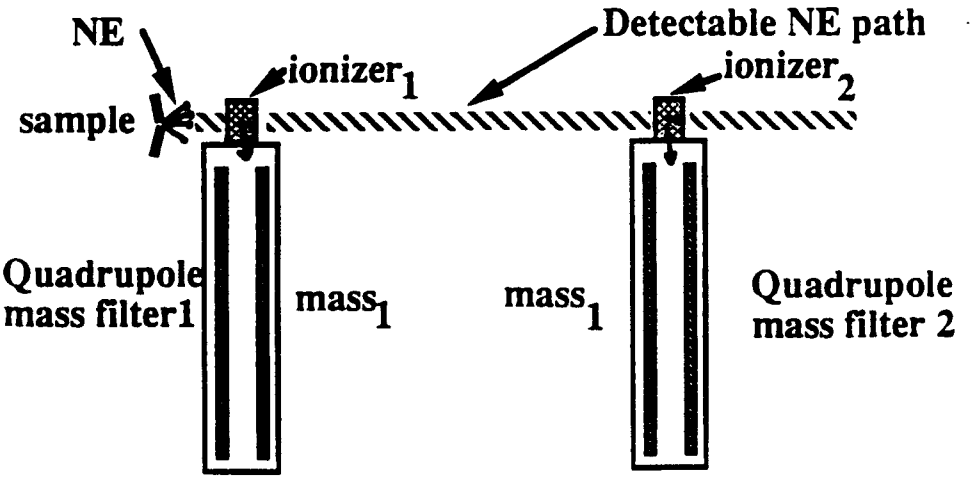

Fig. 1

50

Surface Ionization of Na° from Fracture

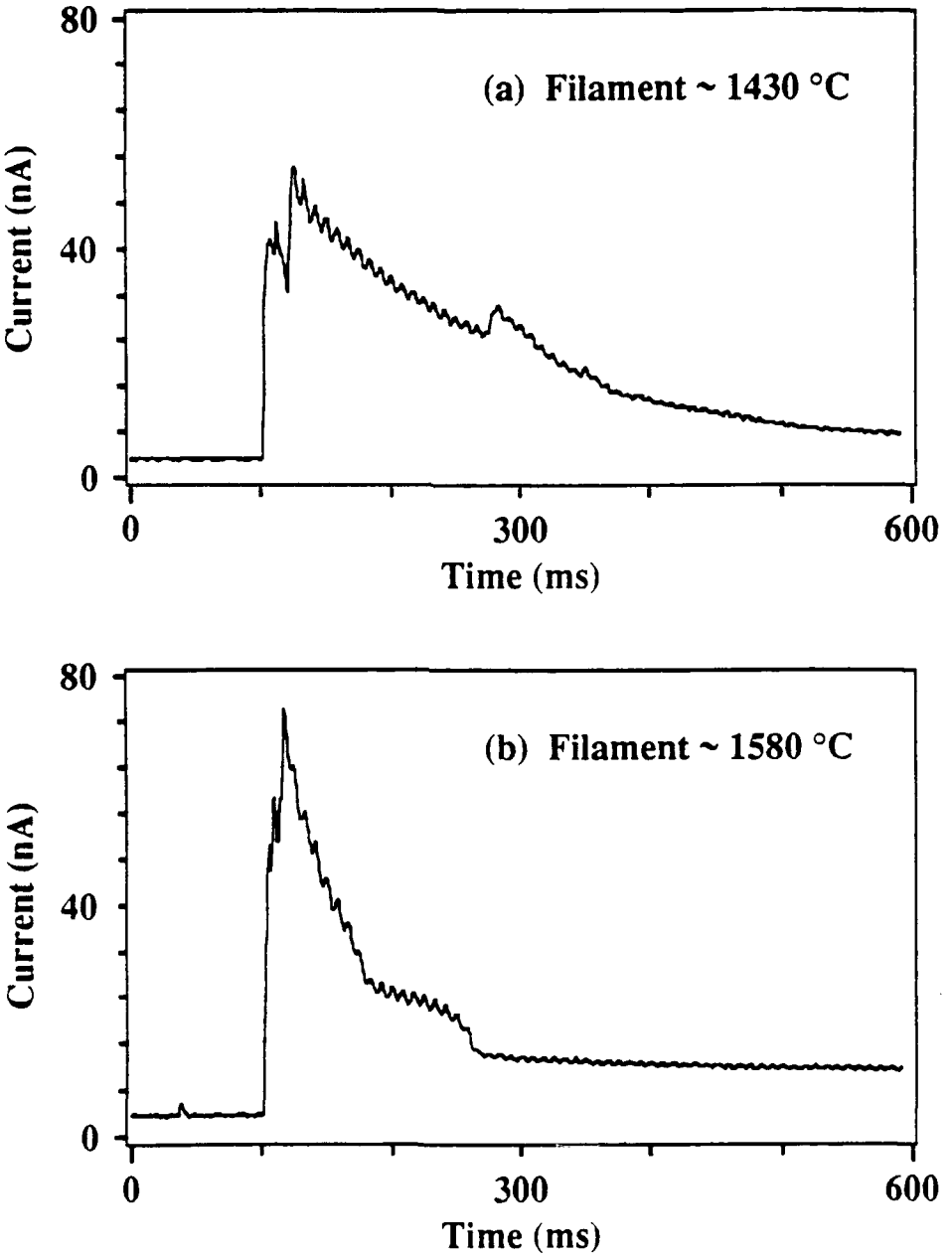

Fig. 2

Onset of Surface Ionization Current and Load Drop

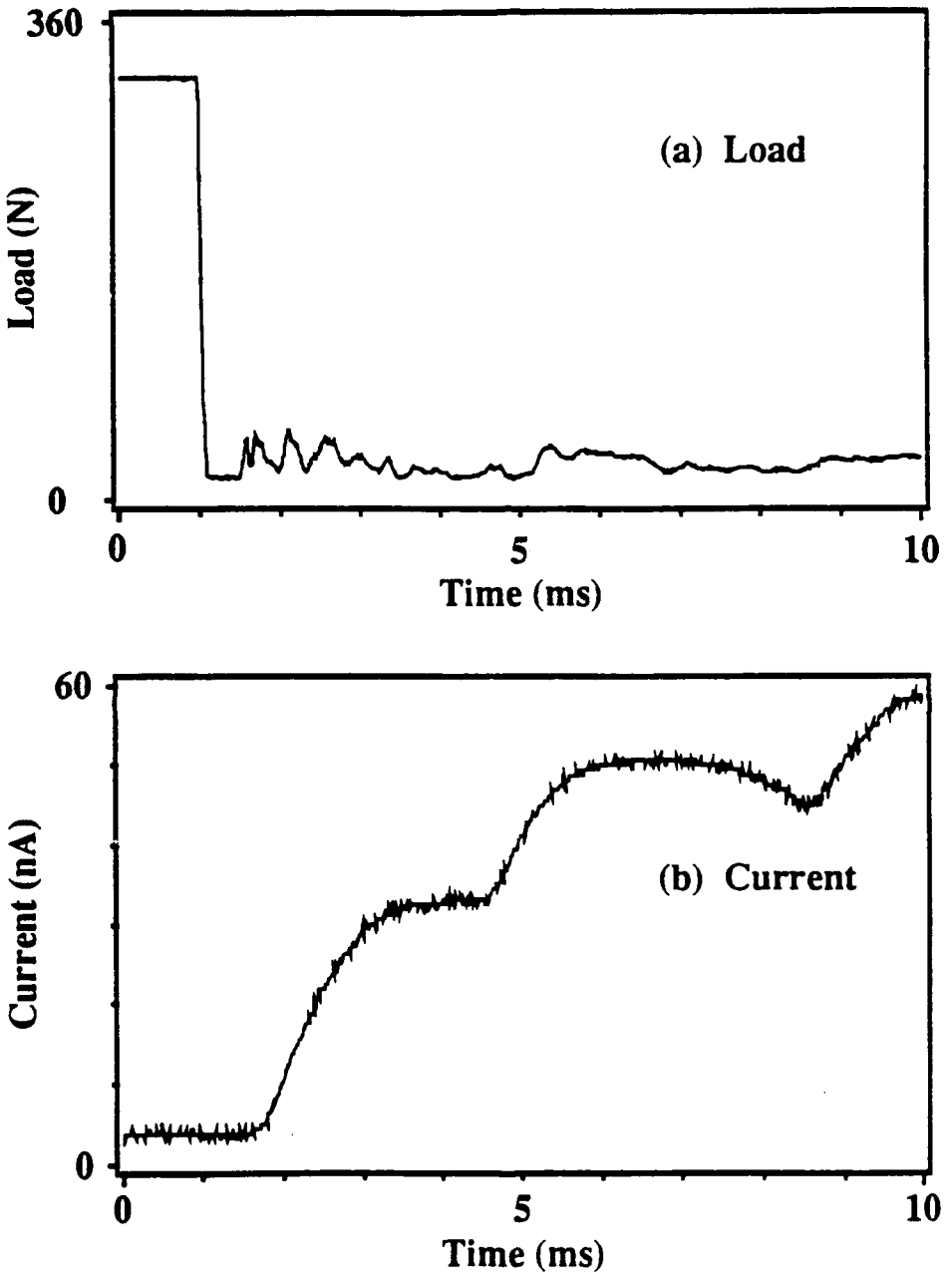

Fig. 3

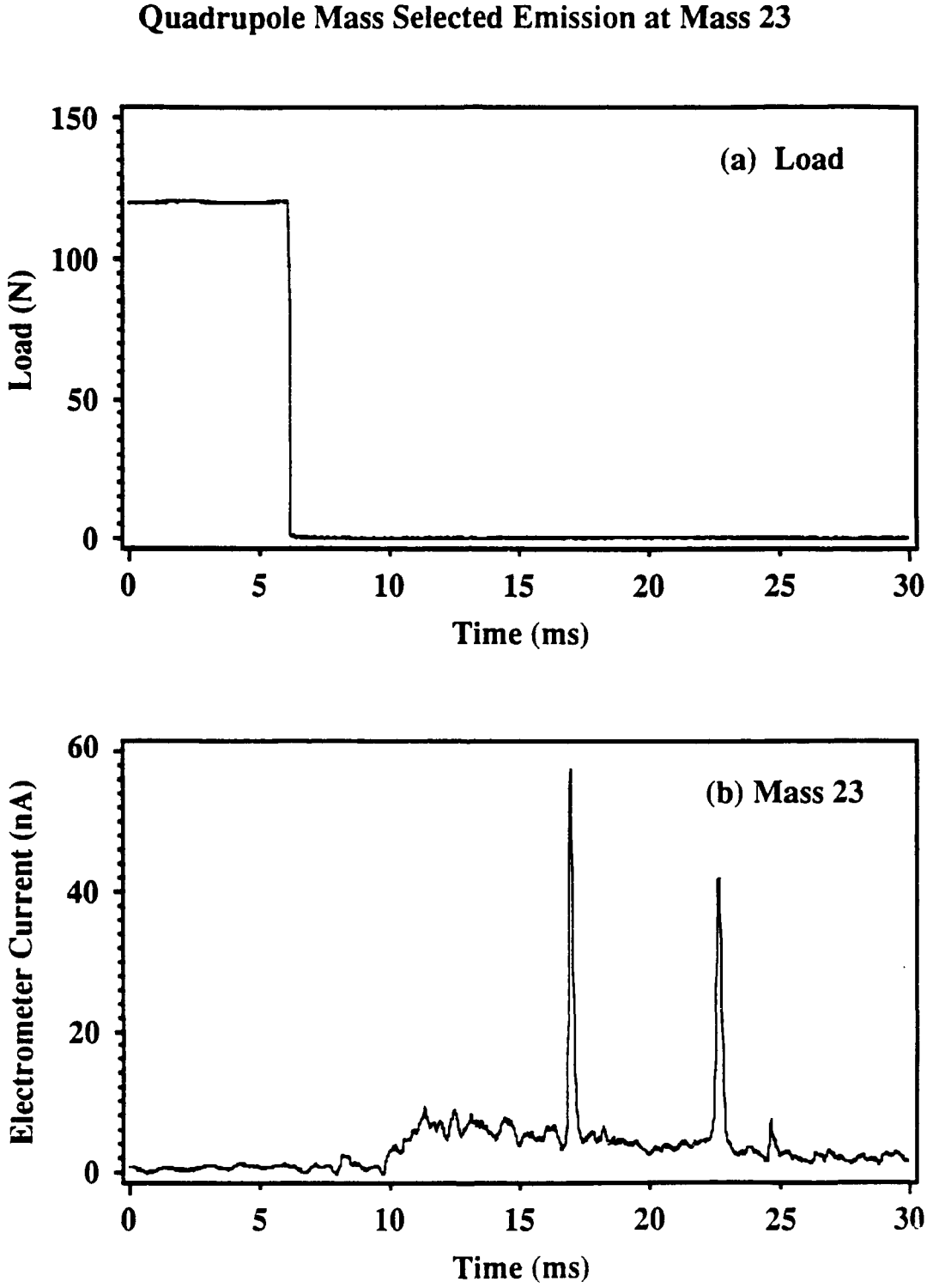
Quadrupole Mass Selected Emission at Mass 23
(a) Load
Load (N)
150
100
50
0
0
5
10
15
20
25
30
Time (ms)
(b) Mass 23
Electrometer Current (nA)
60
40
20
0
0
5
10
15
20
25
30
Time (ms)

Fig. 4

Bursts at Mass 23 through Sequential Quadrupoles

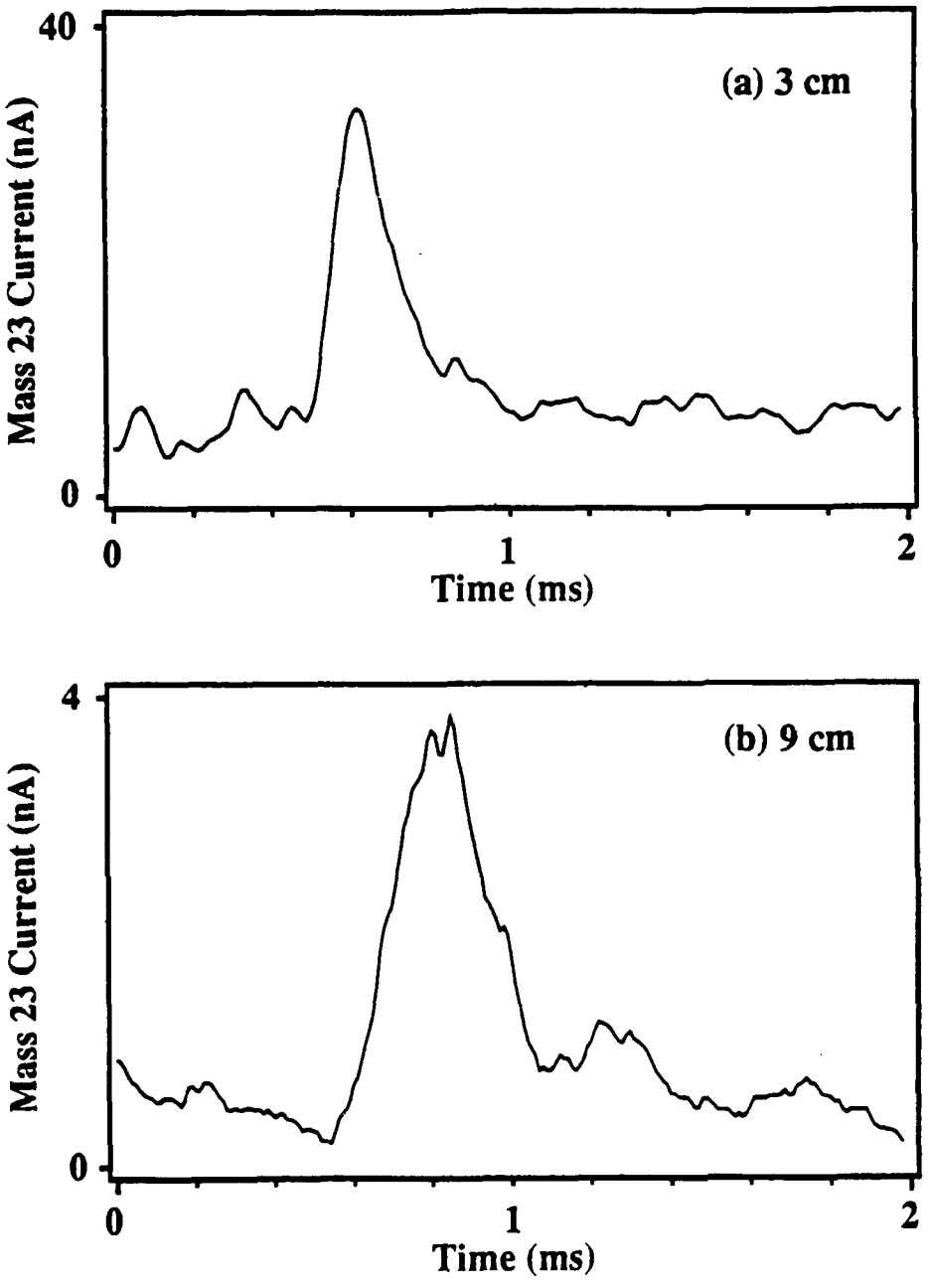

Fig. 5

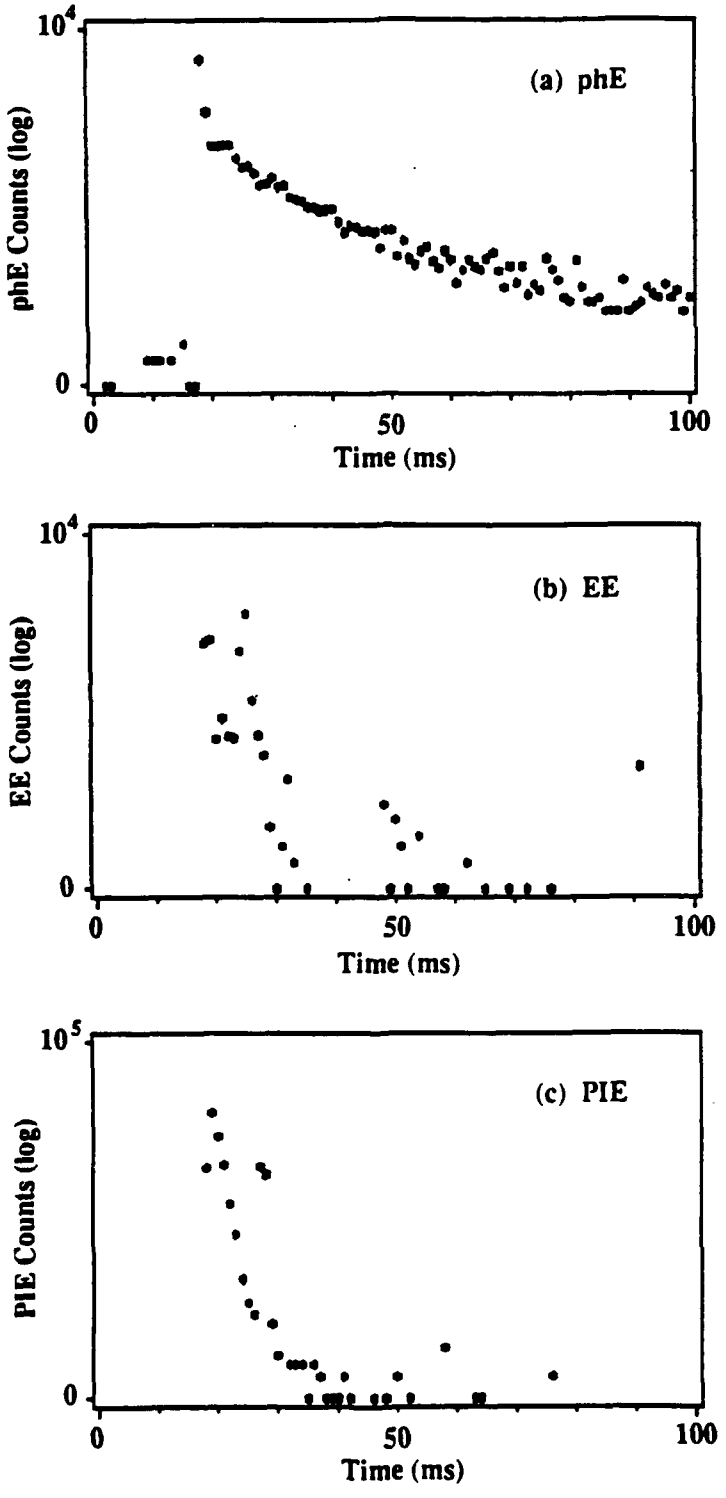
phE, EE, and PIE from Fracture of Soda Lime Glass
(a) phE
phE Counts (log)
10^4
0
0
50
100
Time (ms)
(b) EE
EE Counts (log)
10^4
0
0
50
100
Time (ms)
(c) PIE
PIE Counts (log)
10^5
0
0
50
100
Time (ms)

Fig. 6

Surface Ionization of Adsorbed Alkali

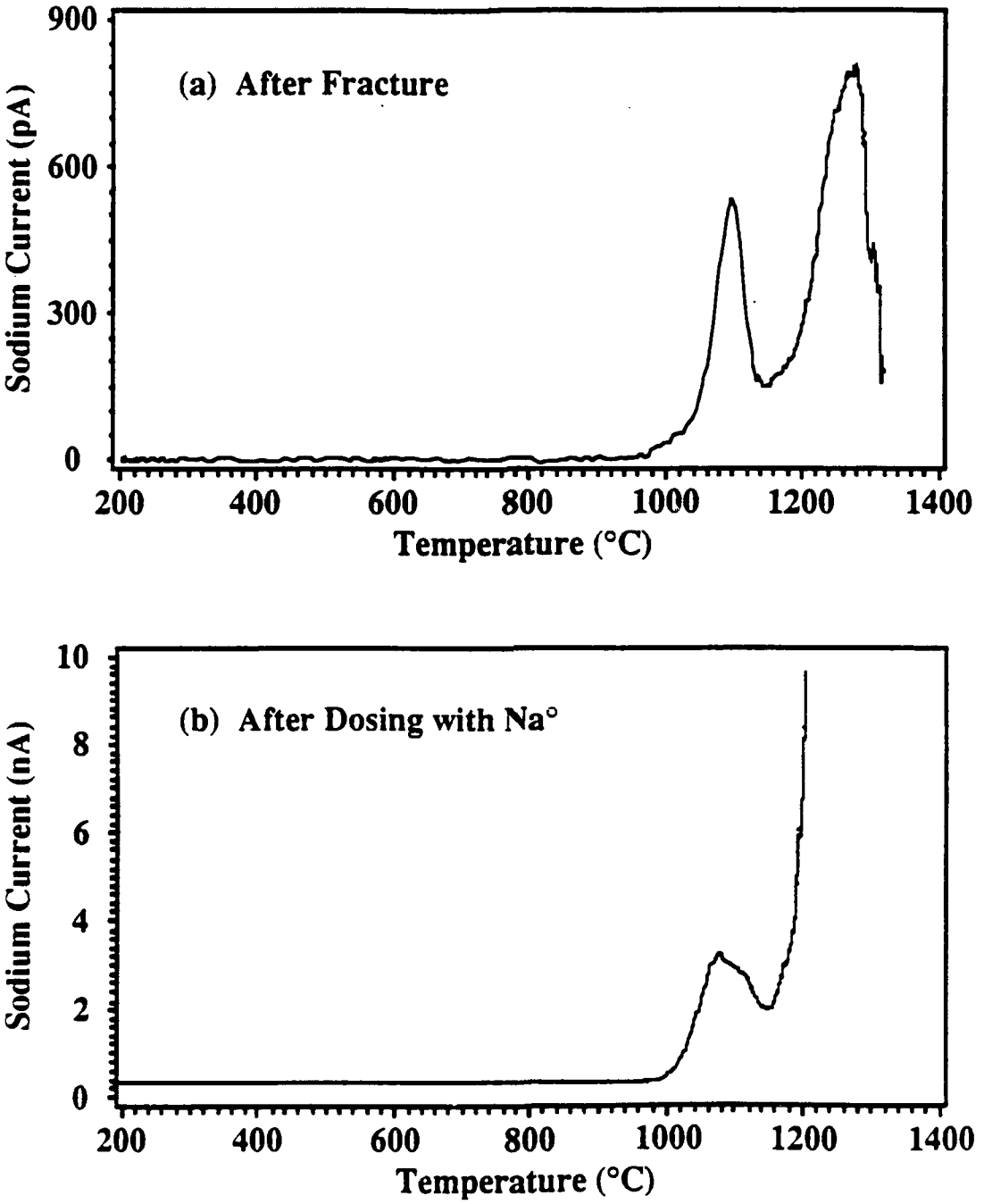

Fig. 7

VI. Fractal character of crack propagation in epoxy and epoxy composites as revealed by photon emission during fracture

Ma Zhenyi, S.C. Langford, and J.T. Dickinson
Physics Department, Washington State University, Pullman, Washington 99164-2814

M. H. Engelhard and D. R. Baer
Molecular Science Research Center, Pacific Northwest Laboratories, Richland, Washington 99352

(Received 6 April 1990; accepted 4 October 1990)

We examine the photon emission accompanying rapid crack growth in an unfilled epoxy resin and in the same resin filled with alumina particles. The alumina particles substantially increase the toughness of the material and increase the photon emission intensities at least tenfold. We attribute the increased photon emission in the filled material to high densities of broken bonds near the alumina particles. The photon emission signals from both filled and unfilled materials show nonintegral (fractal) dimensions which are insensitive to the presence of the particles at the level of precision employed. Fractal dimension measurements of the fracture surfaces are likewise relatively insensitive to the presence of the filler, despite marked variations in apparent surface roughness. The photon emission signals were examined for the presence of chaos. Computations of the correlation exponent of Grassberger and Procaccia indicate that the photon emission fluctuations are not noise-like in character, and suggest deterministic chaos. Lyapunov exponent estimates on photon emission signals confirm the presence of chaotic processes. X-ray photoelectron spectroscopy and electron microscopy of the fracture surface indicate very little interfacial failure; i.e., fracture proceeds predominantly through the epoxy matrix in both filled and unfilled materials. Consequently, the character of the polymer matrix dominates the fracture process and therefore determines the fractal nature of the surface and the chaotic nature of the photon emission intensities in each material.

I. INTRODUCTION

The fracture of many materials in vacuum is accompanied by the emission of photons and particles. In particular, photon emission intensity is readily sampled on ns time scales and can provide a great deal of information concerning rapid (km/s) crack growth. In previous work, we showed that fluctuations in photon emission (phE) intensities during the fracture of a neat epoxy resin reflect variations in crack velocity and surface roughness.[1] Further study indicated that these phE fluctuations are chaotic in nature, reflecting chaos in the process of rapid crack growth in this material.[2] As pointed out by Goldberger, Rigney, and West,[3] chaotic nonlinear dynamics often produce fractal structures, but the relations between the nonlinear dynamics and the resulting fractal structures are not easily established. These fractal structures include abstract elements of system dynamics such as the "path" of fracture in a suitable phase space (e.g., involving time and/or derivatives with respect to time) but also physical fractal objects, such as the resulting fracture surface. Empirical relations between fractal dimension measurements on fracture surfaces and material properties, such as fracture toughness, have been established for some materials systems[4,5] and provide motivation for study of systems in which toughness can be varied. As the addition of alumina particles to epoxy is known to increase both the fracture toughness[6] and the resulting emission intensities,[7-9] we speculated that fast photon intensity measurements during the fracture of alumina-filled epoxy might reflect the possible influence of filler material on the chaotic dynamics of epoxy fracture.

In this paper we present measurements and analyses of the photon emission (phE) intensities during fracture of alumina-filled and unfilled epoxy resin. Power spectra and fractal "box dimension" measurements of the phE signals were made to compare the phE *fluctuations* during fracture. The fractal and chaotic features of the data, which we believe reflect temporal fluctuations in crack growth, were further investigated by performing estimates of Grassberger and Procaccia's correlation dimension as well as the maximum positive Lyapunov exponent. To investigate possible correlations between the locus of failure and phE intensities, typical fracture surfaces were also examined by scanning electron microscopy and x-ray photoelectron spectroscopy. In addition, fractal dimension measurements of the fracture surfaces were undertaken to allow com-

 © 1991 Materials Research Society

parisons with the phE fluctuations. We present evidence that the photon signals from both unfilled and filled epoxy are indeed fractal, consistent with chaotic processes. Likewise, the resulting surfaces are fractal. However, the presence of the alumina particles has little effect on the measured fractal dimensions of the phE signals *and* of the physical fracture surface. We attribute these somewhat surprising results to the fact that interfacial failure is minimal in the filled materials, as demonstrated below. Therefore, fracture in these materials proceeds almost entirely in the epoxy resin matrix; thus, the properties of the polymer matrix control the dynamics of crack progress in each of these materials on the time/length scales probed by the phE/surface fractal dimension measurements. We suggest that statistical variations in the microstructure of the polymer network along the crack path are common to these three materials and determine the fractal nature of crack growth over a fairly large range of scales.

II. EXPERIMENTAL

The epoxy used in this investigation is Epon 828-Z (Shell Chemical Corporation), made from Epon 828, a condensation product of epichlorohydrin and bispenol-A with no dilutants, cured with Hardener Z, a eutectic mixture of methylenedianaline, metaphenylenediamine, and phenylglycidyl ether. The mean particle size of the alumina filler is about 8 μm, with a few particles as large as 100 μm. Samples were prepared with three alumina concentrations: 0%, 20%, and 40% by volume. Dried alumina was added to preheated resin (70 °C), mixed, and allowed to sit for 3 h at 70 °C. The resin and preheated curing agent were then mixed, outgassed, and poured into silicone rubber molds. The material was cured for 4 h at 55 °C and postcured for 16 h at 95 °C. The samples had a dog-bone shape with a gauge cross section of 3.7 × 13 mm^2 and a length of 50 mm.

The samples were notched to a depth of 3 mm from one direction only with a saw blade, leaving a crack path length of about 10 mm. The specimen was loaded in tension under vacuum at a pressure of about 10^{-6} Pa. The phE was detected with a EMI Gencom 9924QB photomultiplier tube (PMT). The output of the PMT was amplified and recorded by a LeCroy TR8828 digitizer at 5 ns time intervals. Load measurements were made on a much slower time scale. The phE data were acquired continuously during loading by successively overwriting old data with new until the load drop at fracture was detected.

A rough estimate of the total neutral particle emission from filled and unfilled epoxies was made by measuring the total pressure change accompanying fracture. This was done by breaking specimens in three-point bend in front of the ionizer of a UTI Model 100C quadrupole mass spectrometer (QMS). For the total pressure measurements, the QMS rods were grounded, disabling the mass filter. The samples were cut to 12 × 6.4 × 3.2 mm^3 from tensile specimens and mounted in a carousel sample holder which rotated samples successively into place between the loading nose and the quadrupole ionizer. The tensile face of each sample was about 2 cm from the ionizer during loading. The vacuum system was maintained at pressures below 2 × 10^{-5} Pa. The time scale of the pressure changes we could monitor was limited by the time constant of the QMS electrometer, about 10 μs. Thus the QMS output was digitized at a much slower rate than the phE signal, i.e., at about 50 μs intervals. Mass scans during the abrasion of the neat epoxy were made to identify likely fracture-related emission products.

III. phE INTENSITIES AND FRACTAL CHARACTER

Figure 1 presents typical phE signals versus time from (a) unfilled, (b) 20% filled, and (c) 40% filled epoxy. The phE signal from the unfilled epoxy was acquired at higher detector and amplifier gain because of lower phE intensity from the unfilled material. These differences increased the amplitude of the recorded signal for the unfilled sample by a factor of about eight relative to the signals from the filled samples. The higher gain used in (a) resulted in a higher noise level evident in the early portion of (a) relative to (b) and (c); this higher noise level did not appear to affect the results of the subsequent analysis. Simultaneous phE and crack position measurements (timing strip) confirm that the intense part of the phE signal corresponds to the duration of the fracture event itself. This strongly implies that the bulk of the phE is from the region of the advancing crack tip. Each of the signals fluctuates rapidly with no apparent periodicity (i.e., the signal *looks* chaotic). Previous analysis indicated that the magnitude of these fluctuations was well in excess of that expected on the basis of photon counting statistics, and thus must be attributed to the emission, rather than the detection process.

The true difference in phE intensities from the three materials is somewhat greater than the factor of eight difference in gains noted above. The transparency of these three materials varies markedly, the filled materials being quite opaque and the unfilled material being translucent. The poor transparency of the filled materials hinders the detection of phE originating deep within the sample interior. An intense light source was used to estimate the ability of white light to penetrate these materials. The ratio of the penetration depths was found to be about 20:5:4, in the order unfilled:20%-

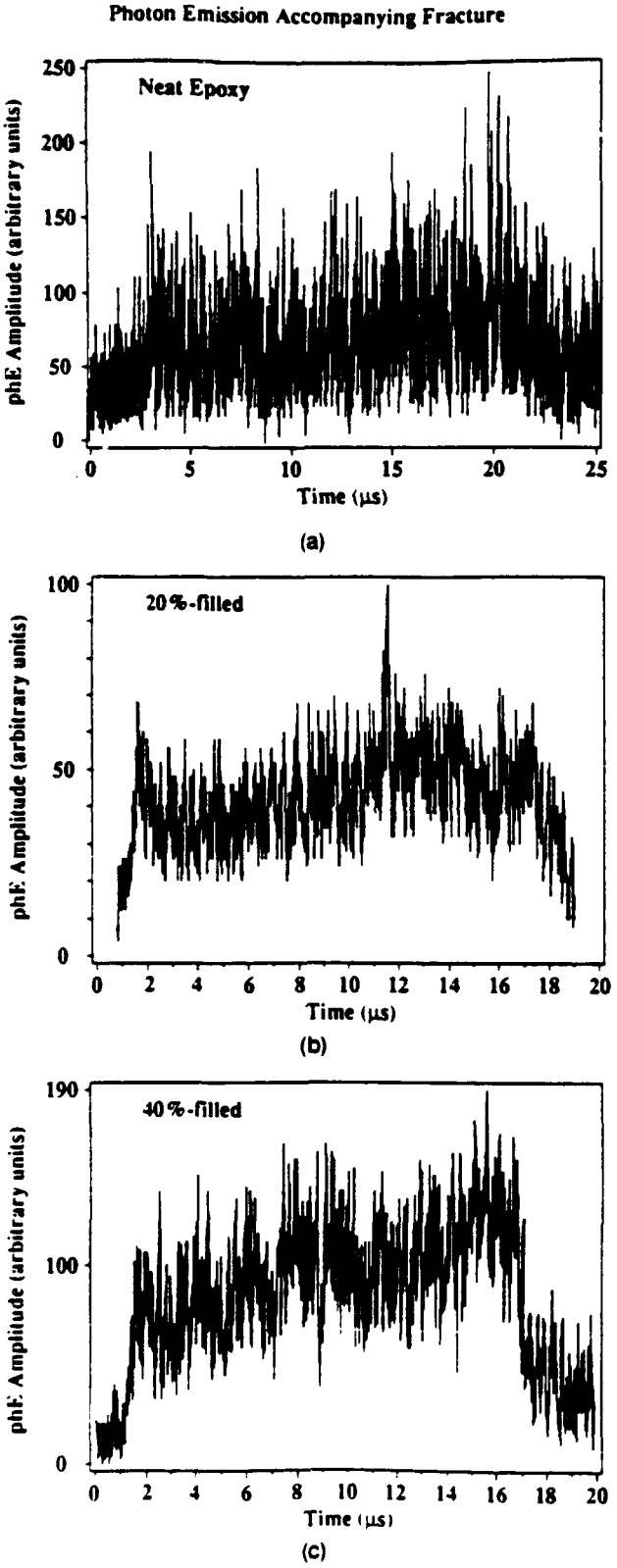

FIG. 1. Photon emission intensity during the fracture of (a) the neat epoxy resin, (b) 20%-alumina filled epoxy resin, and (c) 40%-alumina filled epoxy resin.

filled:40%-filled. The volume of the material from which phE is detectable must vary in about the same ratio. Using average intensities during fracture, we estimate the actual difference in phE intensities per unit area of sample cross section to vary in the ratio 1:16:20, unfilled:20%-filled:40%-filled. Since phE generally involves the recombination or relaxation of electronic excitations, this difference in emission indicates that substantially greater number of defects are being created in the filled materials. Previous experience with other composites led us to suspect that a substantial portion of this emission was due to electrical breakdown resulting from charge separation across the alumina-epoxy interface.[9,10] This motivated experiments described later where we searched for evidence of interfacial failure. As noted below, we concluded that little interfacial failure was present. As the alumina particles themselves are quite strong and not likely to fail, we attribute the observed differences in phE intensities to different numbers or concentrations of electronic defects (probably radicals due to broken bonds) in the epoxy matrix.

Depending on the phE mechanism, high emission intensities may result from either high absolute numbers of broken bonds, or merely by concentrating the broken bonds into smaller regions of the matrix. For instance, if the phE is a first order decay of excited states (as in radioactive decay), higher emission intensities require higher numbers of broken bonds. However, if the emission involves defect recombination (as in a second order peak in thermally stimulated luminescence) higher *initial* emission intensities can be had by merely concentrating a given number of defects in a small region. Previous measurements on time scales of seconds indicate that the phE decay is definitely higher order, suggesting that defect concentration might be sufficient to explain the observed intensities. Although we cannot presently rule out first order processes in the intense emissions *during* fracture, the most likely source of electronic defects in this material appears to be bond breaking, and relaxation of these defects would appear to require a recombination process. Locally high concentrations of defects may occur in the epoxy matrix at regions of high stress concentrations near the alumina particles. Studies of luminescence mechanisms in epoxies may help resolve this point and perhaps allow quantitative comparisons of the free radical density or distribution between the filled and unfilled materials.

Some insight into the nature of the fluctuations is given by the power spectra of the signals, shown in Fig. 2. The power spectra are plotted on log-log scales. Each of the power spectra is relatively flat in the low frequency portion of the spectrum and falls off at frequencies above about 4 MHz. The region between 5 and 35 MHz is fairly linear on the log-log plot in each case.

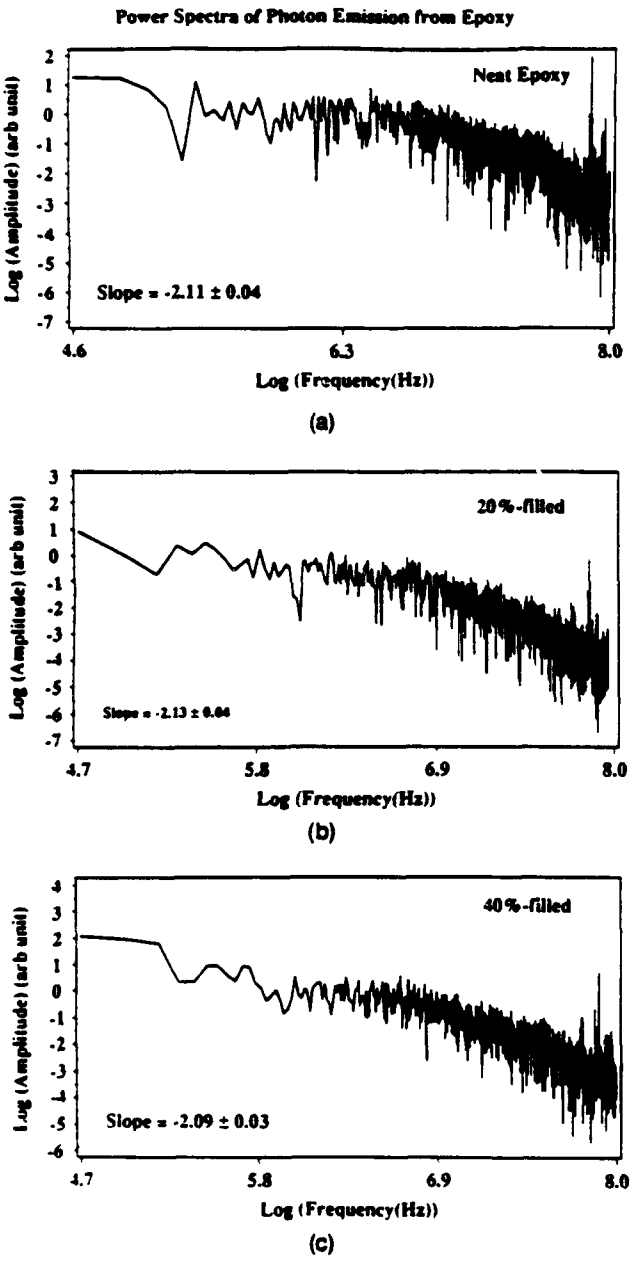

FIG. 2. Power spectra of the phE signals shown in Fig. 1: (a) the neat epoxy, (b) the 20%-alumina filled epoxy resin, and (c) the 40%-alumina filled epoxy resin.

indicating a power law dependence at high frequencies ($1/f^{\beta}$ behavior). At still higher frequencies, the finite, 20 ns pulse width of the photomultiplier tube attenuates the signal, so we expect little power at these higher frequencies. This is most evident in the neat epoxy spectrum which shows a definite shoulder at about 35 MHz. This shoulder is not evident in the spectra from the filled materials, indicating additional high frequency components in these signals. The spikes above 50 MHz are due to noise from a pre-amplifier. We expect the power spectra at frequencies below 50 MHz to be unaffected by aliasing of very high frequency components (greater than the Nyquist frequency of the spectra, 100 MHz).

The relatively strong high frequency components of the spectra from the filled materials may result from crack pinning events associated with the filler. The increased toughness of the filled materials is attributed to crack pinning, in which the filler particles pin the crack front in much the same way as defects pin a dislocation.[6,11] An effective frequency of pinning or shadowing events can be estimated from the average interparticle spacing. Assuming a uniform array of "average" particles, 8 μm in diameter, the center-to-center interparticle spacing is about 12 μm in the 20%-filled material and 9.4 μm in the 40%-filled material. At typical crack velocities (500 m/s), particles would be encountered at roughly 20 ns intervals. This would modulate the phE at frequencies on the order of 50 MHz and thus explain the relatively intense components in this region of the power spectra from the filled materials.

$1/f^{\beta}$ behavior has been associated with the fractal character of certain time series records (e.g., Brownian motion displacement versus time) and with spatial profiles of various fracture surfaces.[12-15] In describing the time series records and fracture surfaces as fractal, we distinguish these self-affine structures from self-similar structures, to which the term fractal is generally applied. The relevant dimensions of a time series record are not strictly equivalent (e.g., displacement versus time), so that no natural scaling can be applied to both dimensions simultaneously for comparisons at different scales. However, by examining the scaling behavior in certain limits, one can often establish fractal character (a self-affinity).[13] Several common measures of fractal character are not appropriate to self-affine structures, and even the appropriate measures apply only in the high frequency limit. Typically, a structure associated with a $1/f^{\beta}$-like power spectrum is described by (Fourier) fractal dimension, D_f, of[14,16]

$$D_f = 2.5 - \beta/2. \quad (1)$$

As noted in Fig. 2, the slopes of these plots (plotted $\log_{10}$-$\log_{10}$) in the region of $1/f^{\beta}$-like behavior all lie in the range 2.09–2.13. The reported errors in the slopes are those derived from the curve fitting process and do not account for errors in defining the linear portion of the curve or due to sample-to-sample variations. Given these uncertainties, these slopes are indistinguishable. The corresponding fractal dimension is $D_f = 1.44 \pm 0.02$. As noted below, the actual uncertainty in the analysis is somewhat greater, perhaps as large as 10–20% of the fractional part of the fractal dimension, due to errors introduced by applying this method to discrete, digital measurements.[17]

To ensure that the similarity between these power spectra was not an artifact of the detection process, light from a pulsed LED of approximately the same intensity was digitized and analyzed in the same fashion. The power spectrum displayed a linear portion in the high frequency limit much like the spectra above. However, the slope of this region was about 3.0, corresponding to a fractal dimension of −1.0; i.e., light from the LED shows little, if any, fractal character. Thus our phE detection and signal amplification system is capable of distinguishing fractal and nonfractal behavior.

To check our interpretation of the power spectra, fractal dimensions of the phE data were also estimated with a box counting method.[13] B. Dubuc *et al.* found that the box counting method underestimated the fractal dimension of a variety of digitized fractal figures even with larger data sets than those available in this work.[17] Nevertheless, it provides a check on the assumptions made in applying the power series method. The box dimension is found by superimposing a rectangular grid upon the curve defined by the phE data and counting the number of grid cells intersected by the curve, $N(r)$, as a function of the grid cell size, r. In the limit of small box size, $N(r)$ is proportional to r^{-D_b} for fractal data. Thus the fractal box dimension, D_b, is given by the slope of the linear portion of the graph of $N(r)$ vs $(1/r)$ on a log-log plot. Figure 3 shows the $N(r)$ plots corresponding to the phE data of Fig. 1. The oscillations in these plots are largely due to the fact that the grids employed in the calculation often "overflow" on one end of the data or the other. This results in an uncertainty in the slope determination, because the oscillations obscure the deviations from linearity expected at large and small scales due to the data collection process. Using all the points in each plot one finds D_b = 1.42, 1.24, and 1.31 for the phE data from the unfilled, 20%-filled, and 40%-filled material, respectively. The value of 1.24 for the 20%-filled epoxy was somewhat anomalous. Typically, D_b measurements on phE from both 20%- and 40%-filled samples were about 1.31. The box dimension measurements provide strong supporting evidence to the conclusion that the phE data are fractal, and suggest a lower bound on the dimension of about 1.3.

Box dimension measurements were also undertaken on subsets of the phE data (4 μs time intervals) in order to investigate the possibility that the dimension was a function of time during rapid crack growth. We found that $D_b(t)$ was constant within the accuracy of the measurement for all three materials for the duration of high phE intensity (during fracture). This indicates that the character of the phE fluctuations during fracture is fairly stable and therefore that the aspects of fracture associated with the phE fluctuations do not vary over the duration of crack motion down, at least down to time intervals of about 4 μs, where total crack propagation times were about 20 μs.

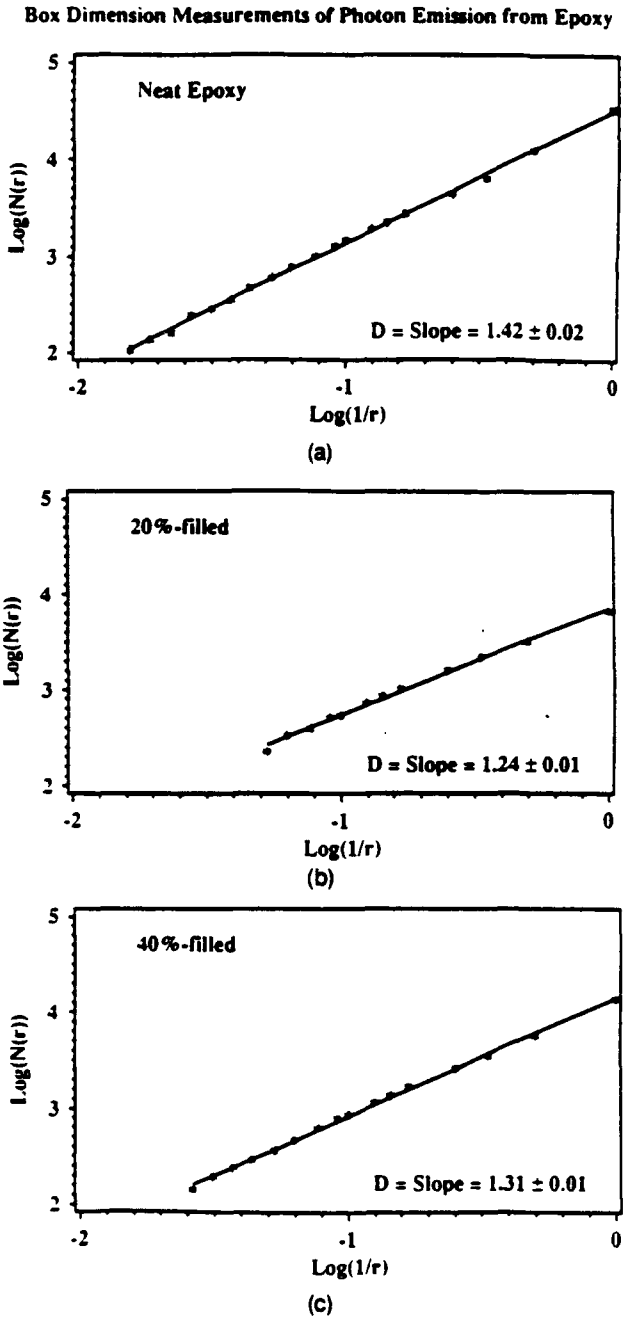

FIG. 3. Fractal box dimension plots of $N(r)$ vs $(1/r)$ on log-log scales for the phE signals shown in Fig. 1: (a) the neat epoxy, (b) the 20%-alumina filled epoxy resin, and (c) the 40%-alumina filled epoxy resin. The reported uncertainty is that due to the curve fitting process.

IV. CHAOTIC DYNAMICS OF FRACTURE PROCESS

A one-dimensional probe of a multi-dimensional chaotic process, such as measurements of one compo-

nent of velocity at a point in a turbulent fluid, often contains sufficient information to reconstruct a (locally) topologically correct model of the multiple-dimensional process.[18-20] This is accomplished by "reconstructing" a phase space trajectory of the appropriate dimension from the measured values. In our case, we have a set of N intensity measurements $\{I_j : j = 1 \ldots N\}$ made at 5 ns intervals which we assume reflect the progress of crack growth, perhaps the rate of production of new crack surface area (area/s). We define a sequence of D-dimensional vectors $\mathbf{X}_j$ whose components are intensity measurements made at intervals Δt, the phase space delay time, where Δt is a multiple of 5 ns (n times 5 ns).

$$\mathbf{X}_j = \{I_j, I_{j+n}, I_{j+2\cdot n}, \ldots, I_{j+(m-1)\cdot n} : j = 1 \ldots (N - nD)\} \quad (2)$$

Provided the measurements $\{I_j\}$ adequately reflect the system dynamics and given a sufficiently high phase space dimension, the trajectory defined by $\mathbf{X}_j$ will have the same topological form as the "true" phase space trajectory in most physical systems.[20] Procedures to measure various generalized dimensions and entropies on similar reconstructed trajectories have yielded valuable information on the dynamics of chaotic processes, such as turbulence.

The correlation dimension of Grassberger and Procaccia[19] probes the fractal structure of the reconstructed phase space trajectory by forming a "correlation integral," $C(r)$, defined as the fraction of point pairs $(\mathbf{X}_i, \mathbf{X}_j)$ separated by a distance less than r, i.e.,

$$C(r) = \frac{1}{N(N-1)} \sum_{i,j=1}^{N-nD} H(r - |\mathbf{X}_i - \mathbf{X}_j|), \quad (3)$$

where $H(r) = 1$ when $r > 0$ and $H(r) = 0$ otherwise. In the limit of small r, $C(r)$ typically scales with r^{D_c}, where D_c is the correlation dimension, provided the phase space dimension is greater than the correlation dimension ($D > D_c$). If $D < D_c$, or if the "noise" in $\{\mathbf{X}_j\}$ is larger than r, $C(r)$ scales with r^D in the small r limit.[21] Log-log plots of $C(r)$ vs r for fractal signals typically display portions of constant, nonintegral slope equal to D_c when $D > D_c$, and slopes equal to D when $D < D_c$. In the presence of noise, the slopes increase to D as r approaches the noise level. If $C(r)$ scales with r^{D_c}, with $D_c < D$, we have strong evidence that the signal fluctuations result from deterministic chaos rather than random noise.

Log-log plots of $C(r)$ vs r for the phE of Fig 1 are shown in Fig. 4 for several values of D. The phase space delay time was 20 ns, i.e., about the width of a single photon pulse from the photomultiplier tube. The noise limit of $r \sim 2$ is evident in each set of data. The slopes shown were computed from the linear portion of each curve. Care was taken in slope computations to avoid the noise limited region ($r < 2$), as well as the region of poor counting statistics [$C(r) < 10^{-5}$]. As D increases, the slopes begin to saturate at $D = 3$ or 4 in all the plots. Although the slopes continue to rise with D, the increase is much slower than the increase in phase space dimension. This is often attributed to inhomogeneity in the local fractal dimension of the phase space trajectory.[22] The saturation of slopes with D is a strong evidence that these fluctuations have fractal character; therefore the phase space trajectory can be said to lie on a strange attractor as the result of chaotic processes accompanying fracture. Further, the saturation at a relatively *low* phase space dimension suggests that the underlying dynamics may be described by a small number of variables, perhaps three or four. This suggests that a reasonably simple physical theory might exist that would relate a measured phE intensity-time sequence to a detailed description of the fracture process.

Another measure of chaos in dynamic systems is the Lyapunov exponent, λ. λ is a measure of the exponential rate of divergence or convergence of nearby trajectories in phase space along a given coordinate direction. Chaotic processes are characterized by an exponential divergence of nearby trajectories and thus at least one positive Lyapunov exponent. We have employed an algorithm constructed by Wolf *et al.* to estimate the maximum Lyapunov exponent associated with the phE data.[23] It takes advantage of the fact that most chaotic processes are somewhat cyclic; i.e., their trajectories display orbits in phase space. The distance between two nearby points on different phase space trajectories can be approximated by the distance between two nearby points from different orbits. One defines a fiducial trajectory and follows its distance from a selected nearby trajectory as time proceeds. As the distance between two points in phase space is bounded from above by the diameter of a typical orbit, large separations fail to show the interesting divergences. "Folds" in the trajectory introduce a similar problem at somewhat smaller separations. These problems can be minimized by periodically replacing the "nearby" orbit with another, closer orbit. The maximum Lyapunov exponent is estimated by the time average of the separation rates as measured over the intervals between replacements. Let the distance between two nearby orbits in phase space be $L'(t)$, where time is measured along the fiducial trajectory. Then periodically replace the nearby trajectory at times $\{t_i\}$ (equal intervals), and compare the separation immediately before one replacement, $L(t_i)$, with that just after the prior replacement, $L(t_{i-1})$. The largest Lyapunov exponent, λ_{max}, is then estimated by

$$\lambda_{max} = \frac{1}{t_f - t_0} \sum_{i=1}^{P} \mathrm{Log}_2\left(\frac{L'(t_i)}{L'(t_{i-1})}\right), \quad (4)$$

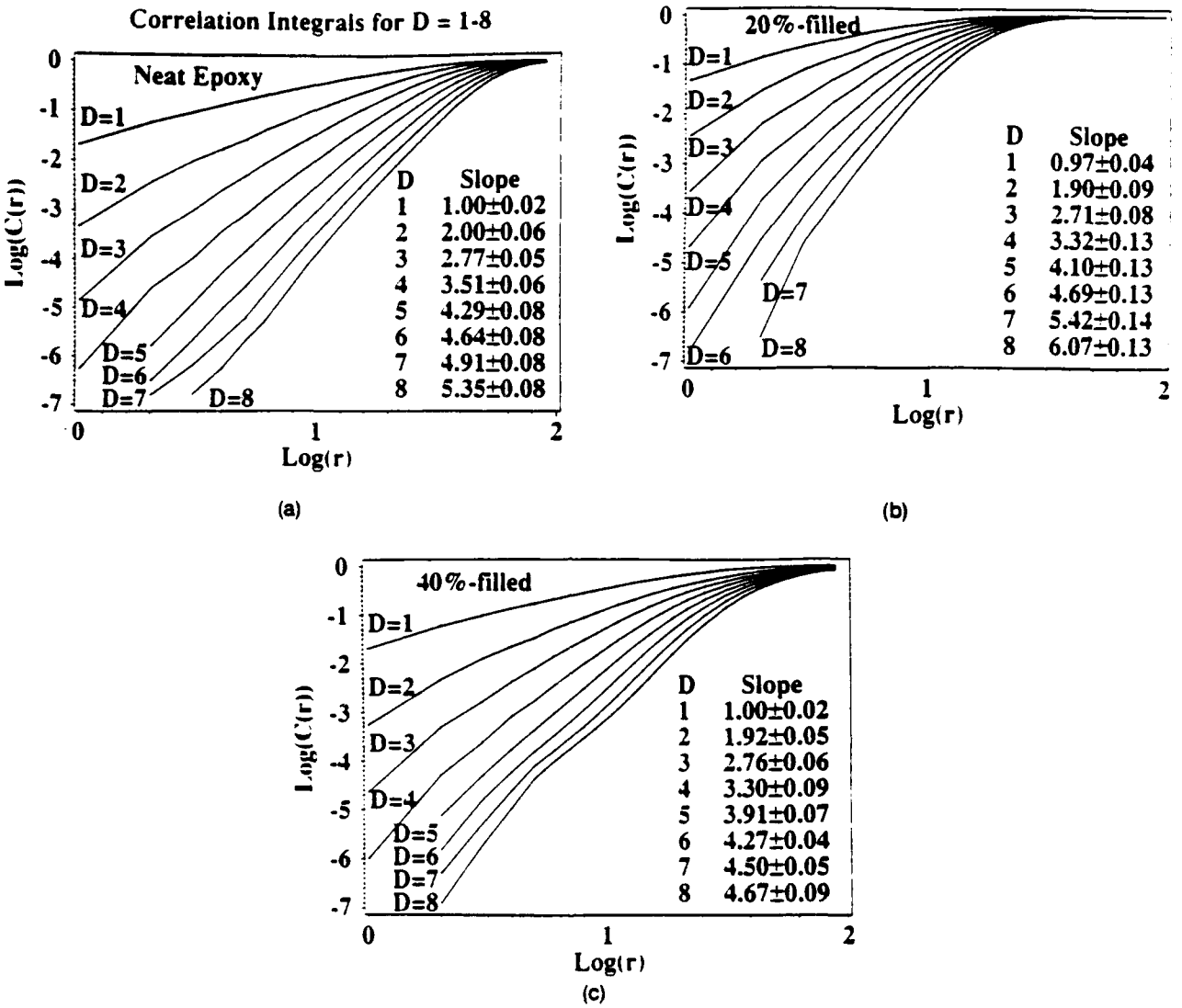

FIG. 4. Correlation integral computations for phase space dimensions D = 1 through 8 for the phE signals shown in Fig. 1: (a) the neat epoxy, (b) the 20%-alumina filled epoxy resin, and (c) the 40%-alumina filled epoxy resin. The phase space trajectory was reconstructed using a delay time of 20 ns.

where t_f and t_0 are the final and initial times associated with the fiducial trajectory. The units of λ_{max} computed with the base 2 logarithm are bits per unit time.

λ_{max} estimates made from experimental data generally depend on the replacement time in long and short time limits. If the replacement time is too long, the separation becomes an appreciable fraction of the orbit diameter and thus ceases to grow exponentially. Folds in the trajectory have a similar effect. When the data are significantly affected by noise, errors resulting from replacement operations can significantly increase λ_{max} estimates at short replacement times. This occurs because the replacement process favors nearby points in phase space, and most often such points are especially close together because of a noise-induced fluctuation. This problem can be minimized by setting a "small-distance cutoff" in the selection procedure. By employing an appropriate cutoff, the probability of choosing points which are "accidentally" near is small. Other errors are introduced in the replacement process, but these generally average out. Typical plots of λ_{max} versus replacement time show a drop or rise to a plateau, followed by a slow decline to zero at large replacement times.

Figure 5 shows a series of λ_{max} estimates for data from each of the three materials as a function of replacement time. The λ_{max} estimates fall in roughly the same range for all three materials, with a plateau evident at about 0.02 bits per sampling interval (4 bits/μs) before falling off at high evolution times. In general, the noise cutoff was consistent with our impression of the background noise in the phE data. A cutoff of 40 mV was used for the neat epoxy data and a cutoff of

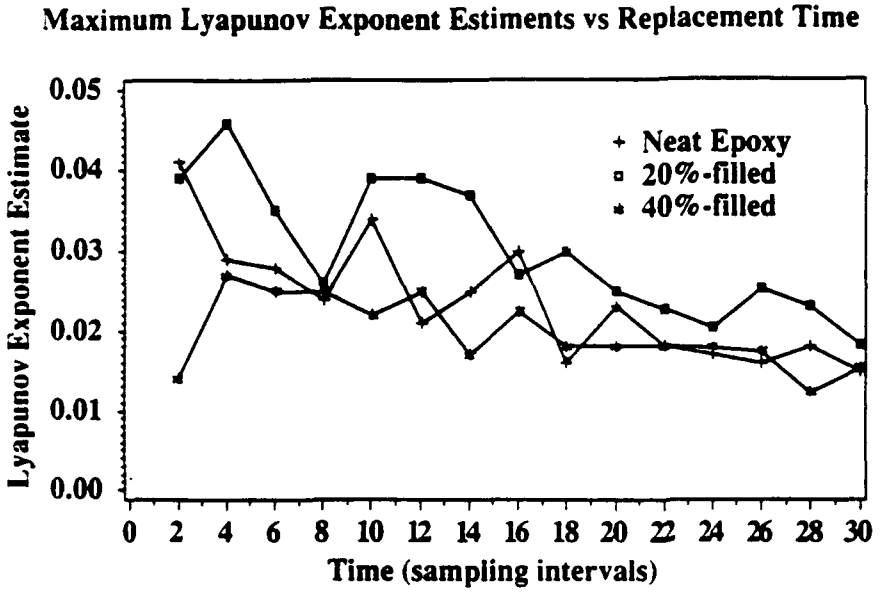

FIG. 5. Lyapunov exponent estimates as a function of replacement time for the three phE signals of Fig. 1. A phase space dimension of four and a delay time of 20 ns was used in reconstructing the phase space trajectory. The units of λ_{max} shown are bits per sampling interval (bits per 5 ns).

10 mV for the 20%-filled epoxy data. However, we found that a cutoff of about 30 mV was required for the 40%-filled data to avoid a spurious peak at low replacement times. This leads us to suspect that an additional noise (stochastic) component was present in the signal from the 40%-filled epoxy. This signal was unusually intense (a factor of two above the others); i.e., this extra fluctuating signal is *not* due to counting statistics and arises from a very subtle influence of the filler particles on the fracture process.

Most importantly, the fact that these λ_{max} estimates all fall in the same range and plateau at a positive value is strong evidence for chaos in the fracture process. Further, the similarity in the λ_{max} estimates made from these phE signals suggests that the *chaotic* component of the fracture dynamics is basically the same in all three materials.

V. TOTAL PRESSURE CHANGE DURING FRACTURE

Given the lack of evidence for interfacial failure (discussed in more detail below), we expected that the especially intense phE from the filled material was most likely due to additional damage and/or bond breaking in the filled material. Local damage processes in epoxide materials often result in the emission of neutral atoms and molecules; therefore we measured the total pressure change in our vacuum system during the fracture of these materials. Typical results for unfilled and 20%-filled samples of comparable strength are shown in Fig. 6. These pressure rises are quite significant, some orders of magnitude above the background. The difference between the peak emissions of the two materials is not great, perhaps due to detector saturation. However, the *decay* of the pressure changes accompanying fracture differs markedly. The pressure change from the filled material is sharper and decays much faster. As time passes, the difference between the two materials increases. After about 3 s, the total pressure change from the filled material is typically 1/2 to 1/3 that from the unfilled material. Although we are reluctant to compare the peak emissions, the delayed emissions from the filled material are markedly weaker than those from the unfilled material.

The identities of the products produced during fracture of this particular epoxy are not known with certainty at this time. Preliminary experiments indicate that water is the major component of the total pressure rise. Fracture experiments with other epoxy materials confirm that the desorption of materials entrained in the epoxy network are major emission components.[24] Although we expect additional emission components due to bond breaking processes during the fracture itself, the diffusion of entrained species to the surface and subsequent evaporation is responsible for the large majority of emission at later times. Since the exposed fracture surface is nearly all epoxy, we expect little difference in emission decays due to differences in surface composition. However, variations in the total amount of fracture surface area and the dimensions of arrested cracks are expected to affect the emission intensities and decays significantly.

The escape of volatile gases from an arrested crack depends exponentially on the square of its depth. Thus gases will escape much more rapidly from an array of short cracks than an array of long, deep cracks. This suggests that the surface of the filled material is characterized by numerous short crack branches while the sur-

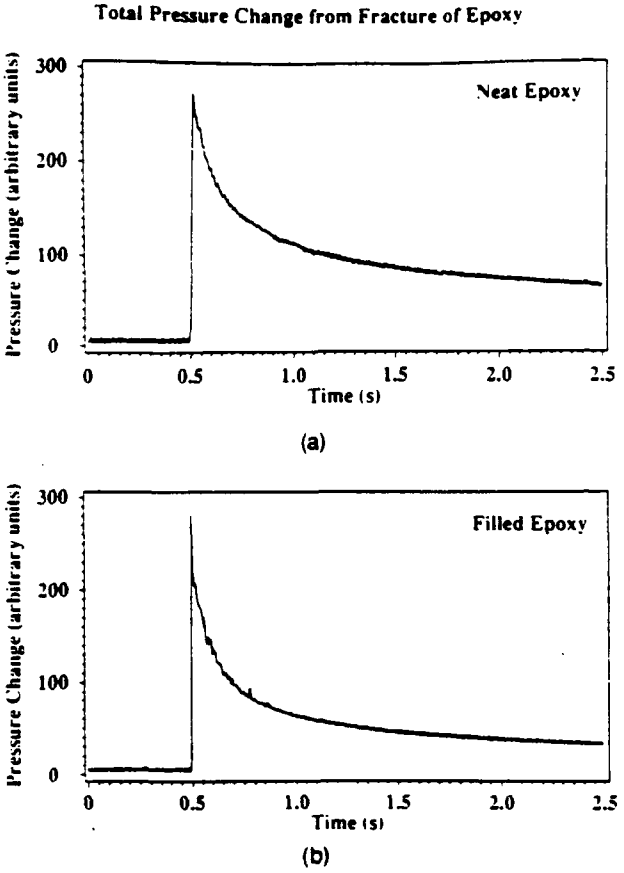

FIG. 6. Total pressure change accompanying the fracture of (a) the neat epoxy resin and (b) the 20%-filled epoxy resin in vacuum. On the time scale shown, fracture is simultaneous with the peak pressure.

face of the neat epoxy is characterized by relatively long crack branches. This impression is confirmed by inspection of the fracture surfaces with optical microscopy. The neat epoxy surface is typically quite rough, with branches extending well into the bulk. These long cracks may be the source of the long tails in the pressure measurements accompanying fracture. The filled epoxy surface is smoother, with less vertical relief. This apparent smoothness may result from the dissipation of the available fracture energy in large numbers of small crack branches. These small branches could be created as the crack front passes around the filler particles as branches on either side of a particle seldom mate. This activity would be consistent with the enhanced high frequency components in phE observed in the filled materials.

VI. CHARACTERIZATION OF FRACTURE SURFACES

In order to relate the properties of the phE studied above to parameters of the fracture surface, two investigations of the fracture surfaces were undertaken. First, fractal dimension measurements were made of the fracture surfaces which may be directly compared with the fractal dimensions of the phE signal. Second, fractography and x-ray photo-emission spectroscopy were employed to determine the degree of interfacial failure accompanying fracture. As previous studies had indicated that high phE intensities from composite materials often accompany interfacial failure, this determination was critical in our interpretation of the intense phE emissions from the filled epoxies.

Fractal dimension measurements of fracture surfaces of each of the studied materials were made by the slit island technique. This method compares area and perimeter measurements of the "slit islands" defined by the contours of the fracture surface. First, the fracture surfaces are coated with an opaque, 30 nm thick gold film and mounted in a clear epoxy. The samples are then polished parallel to the fracture surface until the polished surface intersects the fracture surfaces. This intersection defines the "island" contours, which are then photographed. The perimeter and area of the resulting islands are then calculated from a digitized trace of the perimeter of each island. The average fractal dimension of the island perimeters can be found by plotting the island areas as a function of island perimeter for a series of such measurements. The fractal dimension, D_{si}, is found by the slope of this function on a log-log plot β, using the relation,[5,12]

$$D_{si} = 2/\beta. \tag{5}$$

Consistent measurements require that polishing does not proceed to the point at which the islands become connected, so that the perimeters actually define "lakes" rather than islands.[25] Further, the measured value of D_{si} can depend on the effective "ruler length" used in the perimeter measurements.[26]

A series of these area versus perimeter plots for the three kinds of samples appear in Fig. 7. The corresponding fractal dimensions are $D_{si} = 1.22 \pm 0.05$, 1.28 ± 0.03, and 1.24 ± 0.04, for the unfilled, 20%-filled, and 40%-filled materials, respectively. Again, the reported uncertainties are due to the slope measurements and do not reflect sample-to-sample variation. The differences in the measured D_{si} values are barely significant, if at all. Lung and Mu argue that an unfortunate choice of ruler length can result in failure to detect a trend (or in the detection of a wrong trend) in a series of dimension measurements.[26] However, it is interesting to note a possible correlation between D_{si} and the fracture surface energy (G_{IC}) of the alumina-epoxy system. G_{IC} peaks at about 20% alumina,[6] near the weak maximum in D_{si}. In spite of the uncertainty in the dimension measurements, it appears that the surface fractal dimensions are somewhat lower than the phE

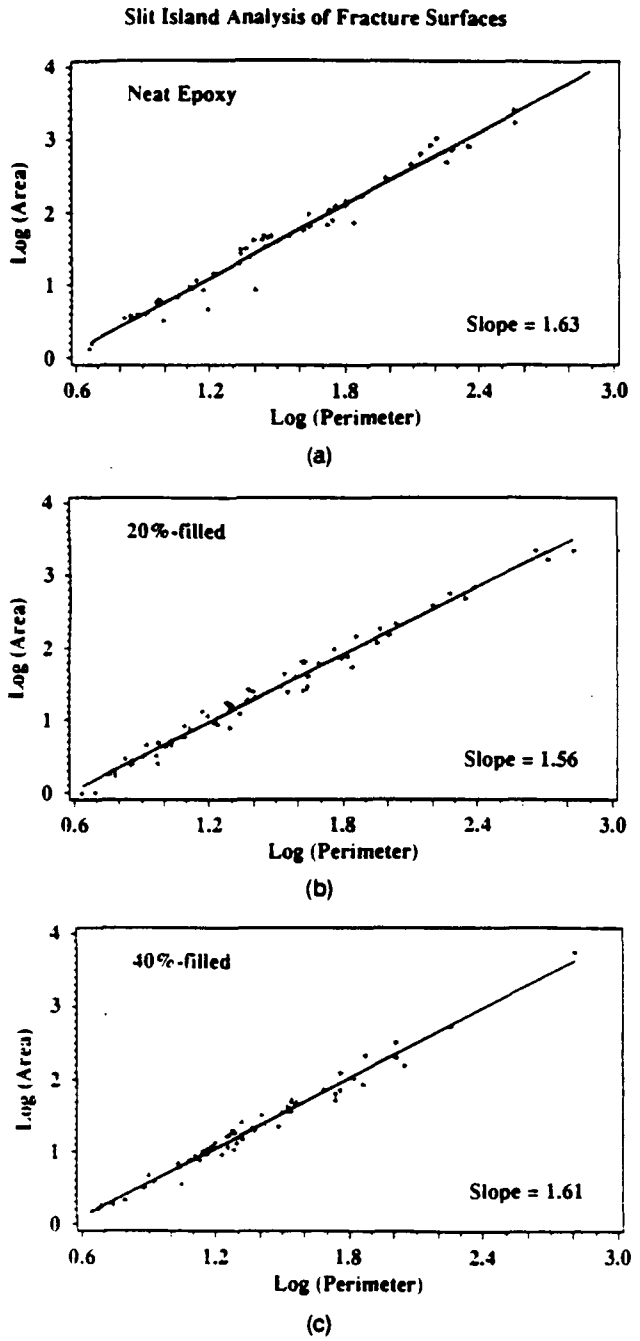

FIG. 7. Slit island analyses of the fracture surfaces yielding the emissions shown in Fig. 1: (a) the neat epoxy, (b) the 20%-alumina filled epoxy resin, and (c) the 40%-alumina filled epoxy resin.

dimensions (comparing the fractional part of these dimensions).

The typical island sizes observed in the three materials correlate well with visual impressions of surface roughness. The filled materials display both smaller island sizes and smoother surfaces, but only slightly higher fractal dimensions. This contrasts with the general correlation between the "roughness" of a geometric figure and its fractal dimension. We attribute this to the effect of vertical relief on visual impressions of surface roughness. As noted above, the fracture surface of the filled material appears to be smoother than that of the neat material on large distance scales, but is quite rough on small distance scales. Some of the variation in surface roughness is due to variations in the load at fracture. Weaker samples show both smoother surfaces and less intense phE.[1] However, some of the variation in the vertical relief appears to be due to other factors, especially in the 40%-filled material; even the surfaces of strong samples displayed little vertical relief. Despite the great variation in vertical relief for filled and unfilled samples, their fractal dimensions were quite similar.

To probe the extent of interfacial failure in the alumina-epoxy systems on phE intensities, we first looked for radio frequency emissions accompanying fracture. These emissions usually accompany electrical discharge events resulting from strong charge separation during high velocity interfacial fracture.[24] Near-field radio frequency emissions are readily detected with coil positioned a few mm from the sample during fracture, and are observed during interfacial failure of many composite systems.[10] No significant radio frequency emissions were observed during fracture of the filled epoxy, implying little interfacial failure.

SEM photographs of the fracture surfaces were also examined for evidence of interfacial failure. Although some regions of some fracture surfaces did show exposed particles, most of the surface area of the filled samples were covered by epoxy. If interfacial failure were common, one would expect to see a high density of exposed particles on the surface. Assuming a close-packed array of 8 μm diameter particles, the center-to-center particle spacing would be 12 μm in the 20%-filled material and 9.4 μm in the 40%-filled material. If the crack intersected and exposed particles at random, regions in the SEM fractographs without particles would be quite small However, the fracture surfaces typically showed few exposed particles.

Further evidence for the lack of significant interfacial failure was provided by x-ray photoelectron spectrometry (XPS) measurements on the fracture surfaces. These measurements were made in a Perkin-Elmer 560 XPS AES system using Mg K_α radiation. Atomic compositions of fracture surfaces were calculated using peak areas obtained from 25 eV pass energy multiplex data and typical atomic sensitivity factors. The data were collected after a short 5 keV Ar^+ ion etch to remove surface contaminates due to exposure to air and specimen handling. We estimate that the etching process removed about 150 Å of epoxy. Further etching did not significantly affect the observed signal intensities. The estimated atomic percentages of the major surface

atoms are shown in Table I. The surface percentage of Al is far below that expected if fracture along the alumina-epoxy interface were at all favored over fracture through the epoxy matrix. The Si detected in the filled material is most likely due to a silane coupling agent applied to the alumina particles, as the position of the Si peak was consistent with a chemical environment with less binding energy than quartz. Thus we conclude that fracture proceeded largely through the epoxy matrix, leaving the great majority of alumina grains in the near surface region covered with a layer of epoxy material. This implies that the intense phE from the filled materials relative to the neat material is due to the creation of substantially greater numbers of primary electronic defects during the breaking of polymer bonds.

VII. DISCUSSION AND CONCLUSION

The phE accompanying fracture generally results from electronic excitations produced during fracture. Radio frequency emission measurements, fractographic observations, and XPS analysis of the fracture surfaces rule out interfacial failure as a major source of phE in the filled materials. Therefore, these excitations are formed by bond breaking in the epoxy matrix. In epoxies and most polymers, the molecular physics of such mechanically stimulated excitations is quite complicated and ill-described. Nevertheless, we can say that there are very fast processes (the bursts in Fig. 1 decay in less than 100 ns) which are consistent with localized molecular excitations such as Frenkel excitons, and longer lived excitations (the decay curve following fracture lasts typically seconds) consistent with spatially separated charge transfer types of excitations. The latter generally involves thermally stimulated mobile carriers where the motion of the carriers toward a recombination center forms the rate limiting step in the emission process. In terms of the fast decaying emission observed only during fracture, the presence of filler particles greatly increases the phE intensities, reflecting higher concentrations of these excitations. This enhanced concentration of excitations may be due to additional bond breaking at high stress regions concentrations in the bulk near the particles. The instantaneous phE intensity would therefore reflect the rate of bond breaking, with relatively small contributions from the slowly decaying components of phE. We expect the rate of bond breaking to be simply related to the rate of volume damage production in the matrix.

TABLE I. Estimated surface concentrations (atomic percent) of main XPS peaks.

	O	C	Al	Si
Neat	6	94		
20%-filled	7.2	90	1.1	1.3
40%-filled	18	73	5.4	3.2

Analysis of the phE signals shows strong evidence of chaotic dynamics. Chaotic dynamics characterize a number of nonlinear, dissipative systems. These systems are characterized by phase space trajectories which define abstract fractal structures (strange attractors) after sufficient time has passed for the decay of any initial transients. The geometry of a strange attractor, including its fractal dimension, can often be reconstructed from any one phase space variable associated with the system. Correlation integral computations on the phE data from all three materials suggest that the dynamics of crack growth can be described in terms of such a fractal structure and that a relatively small number of variables will be required to describe the system. The attractor appears to be fairly inhomogeneous, perhaps lacking a readily computed fractal dimension. The largest Lyapunov exponent associated with the phE data is clearly positive, confirming the presence of chaotic dynamics. The similarity of the correlation integrals and exponent estimates for filled and unfilled epoxies suggests that fracture displays similar chaotic dynamics in all three materials. This is reasonable on the grounds that fracture in each material takes place largely in the epoxy matrix, so that the resin properties control any chaotic dynamics associated with fracture. The phE measurements on faster time scales thus have the potential to probe fluctuations on the scale of individual crack/particle interactions and should reflect the effects of the filler. As mentioned above, only hints of these interactions appear in the high frequency portions of the power spectra of phE from the filled materials.

The fractal dimensions of the fracture surfaces of the unfilled and the two filled materials are not significantly different, despite significant differences in material toughness (critical stress intensity). Substantial correlations between fracture toughness and surface dimension have been observed in maraging steel,[4] where the surface dimension decreases with toughness, as well as in certain ceramic and ceramic-glass systems,[5] where the surface dimension increases with toughness. This contrasting behavior may reflect variations in measurement technique, which can affect trends in slit island dimension measurements.[25,26] However, different toughening mechanisms may well affect surface topology, including fractal dimension, in different ways. Multifractal models may be required to model realistically the effects of competing fracture mechanisms on surface dimensions and toughness.[27] Our measurements suggest that the surface dimension depends only weakly on toughness in this set of materials, if K_{IC} is the appropriate measure of toughness. The critical stress intensities (K_{IC}) of these three epoxy materials should be roughly proportional to the filler content.[6] However,

their fracture surface energies ($G_{IC} \propto K_{IC}^2/E$, where E is Young's modulus) display less variation, peaking at about 20% filler content by volume. This is due to the complex dependence of Young's modulus on filler concentration.[6] If the relevant parameter is the fracture surface energy, less variation in the surface dimension would be expected. Further refinements in fractal dimension measurement techniques and interpretation may resolve the nature of correlations between toughness and surface fractal dimension.

The origin of the fractal character of fracture surfaces is not yet clear. Simple numerical models of quasistatic bond-breaking in two-dimensional triangular lattices result in fractal surfaces.[28,29] In these models, bonds are typically broken with probabilities based on bond energy or stress. The structures defined by the set of broken bonds often resemble those observed in experiments and numerical models of diffusion limited aggregation. These models suggest that the fractal nature of fracture surfaces is due to the probabilistic nature of bond breaking. The resulting numerical equations formally resemble those describing diffusion processes,[29] which often yield fractal structures.[16] Analysis of crack growth as a function of time (i.e., the dynamics of crack growth) using these models has not yet been performed; but by analogy with the related viscous fingering problem,[30] one may expect that fluctuations in local crack velocity will require multifractal descriptions. Similar models may elucidate the connections between the fluctuations in the rate of crack growth, the fractal properties of the resulting surfaces, and the energy required for crack propagation.

Fractal structures in the polymer network of the epoxy resin may also influence the course of crack growth by perturbing the crack in a chaotic fashion. The formation of fractal structures in branched epoxies has been observed in the early stages of the curing process.[31,32] The statistical variations in the microstructure of the polymer network along the crack path are common to all three materials described above, which would account for the similar dynamics of crack growth and the similar fractal dimensions of the fracture surfaces.

The nature of energy dissipation during crack propagation is perhaps fairly well understood on the continuum level. However, the existence of fractal fracture surfaces and empirical correlations between surface fractal dimension and material toughness suggests that fluctuations in the progress of crack growth associated with crack branching can substantially affect the energy required for crack propagation. These fluctuations, whether due to crack branching and fingering or to void nucleation and coalescence, are difficult to model. phE accompanying fracture is a useful probe of the dynamics of these fluctuations over a wide range of time scales and is experimentally quite simple to acquire. The mode of fracture often strongly affects the phE intensity, which thus provides information on competing fracture mechanisms in composite materials. The ability of phE to reflect the dynamics of crack growth on ns times scales is especially important in probing the dynamics of rapid crack growth, including the study of possible chaotic processes.

ACKNOWLEDGMENTS

This work was supported by the Dow Chemical Co., the Office of Naval Research under Contract No. N00014-87-K-0514, the Ceramics and Electronics Materials Division of the National Science Foundation under Grant DMR 8912179, and the Washington Technology Center. The PNL activities were supported by the United States Department of Energy (BES-DMS) and through internal Exploratory Research of the Molecular Science Research Center funds under Contract DE-AC06-76RL0-1830.

REFERENCES

[1] J.T. Dickinson, L.C. Jensen, and S. Bhattacharya, Die Makromolekulare Chemie: Macromolecular Symposia 7, 129 (1987).
[2] S.C. Langford, Ma Zhenyi, and J.T. Dickinson, J. Mater. Res. 4, 1272 (1989).
[3] A.L. Goldberger, D.R. Rigney, and B.J. West, Sci. Am. 262, 42 (1990).
[4] B.B. Mandelbrot, D.E. Passoja, and A.J. Paullay, Nature 308, 721 (1984).
[5] J.J. Mecholsky, D.E. Passoja, and K.S. Feinberg-Ringel, J. Am. Ceram. Soc. 72, 60 (1989).
[6] A.C. Moloney, H.H. Kausch, and H.R. Stieger, J. Mater. Sci. 18, 208 (1983).
[7] J.T. Dickinson, Proceedings of the ACS Division of Polymeric Materials: Science and Engineering 56, 264 (1987).
[8] J.T. Dickinson and A.S. Crasto, in *Cross-linked Polymers: Chemistry, Properties and Applications*, edited by R.A. Dickie, S.S. Labana, and R.S. Bauer, ACS Symposium Series 367 (American Chemical Society, Washington, DC, 1988), pp. 145–168.
[9] J.T. Dickinson and L.C. Jensen, Proceedings of the International Society for Optical Engineering (SPIE): Fluorescence Detection I 743, 68 (1987).
[10] J.T. Dickinson, L.C. Jensen, and A. Jahan-Latibari, J. Vac. Sci. Technol. A 2, 1112 (1984).
[11] A.C. Moloney, H.H. Kausch, T. Kaiser, and H.R. Beer, J. Mater. Sci. 22, 381 (1987).
[12] B.B. Mandelbrot, *The Fractal Geometry of Nature* (W.H. Freeman, New York, 1983).
[13] B.B. Mandelbrot, Physica Scripta 32, 257 (1985).
[14] B.B. Mandelbrot and R.F. Voss, in *Noise in Physical Systems and 1/f Noise*, edited by M. Savelli, G. Lecoy, and J-P. Nougier (Elsevier Science Publishers, Amsterdam, 1983), p. 31.
[15] S.C. Langford, Ma Zhenyi, L.C. Jensen, and J.T. Dickinson, J. Vac. Sci. Technol. A 8, 3470 (1990).
[16] Paul Meakin, in *Phase Transitions and Critical Phenomena*, edited by C. Domb and J.L. Lebowitz (Academic Press, London, 1988), Vol. 12, p. 335.
[17] B. Dubuc, J.F. Quiniou, C. Roques-Carmes, C. Tricot, and S.W. Zucker, Phys. Rev. A 39, 1500 (1989).

[18]N. H. Packard, J. P. Crutchfield, J. D. Farmer, and R. S. Shaw, Phys. Rev. Lett. **45**, 712 (1980).
[19]Peter Grassberger and Itamar Procaccia, Physica **9D**, 189 (1983).
[20]H. G. Schuster, *Deterministic Chaos* (VCH Verlagsgesellschaft, Weinheim, FRG, 1988).
[21]Avraham Ben-Mizrachi and Itamar Procaccia, Phys. Rev. A **29**, 975 (1984).
[22]R. S. Shaw, *The Dripping Faucet as a Model Chaotic System* (Aerial Press, Santa Cruz, CA, 1984).
[23]Alan Wolf, J. B. Swift, H. L. Swinney, and J. A. Vastano, Physica **16D**, 285 (1985).
[24]J.T. Dickinson, "Fracto-emission from adhesive failure," to appear in *Adhesive Bonding*, edited by L. H. Lee (Plenum Publishers, New York, 1990).
[25]Z. H. Huang, J. F. Tian, and Z. G. Wang, Scripta Metall. Mater. **24**, 967 (1990).
[26]C.W. Lung and Z. Q. Mu, Phys. Rev. B **38**, 11781 (1988).
[27]R. E. Williford, Scripta Metall. **22** (11), 1749–1754 (1988).
[28]Yves Termonia and Paul Meakin, Nature **320**, 429 (1986).
[29]E. Louis and F. Guinea, Europhys. Lett. **3**, 871 (1987).
[30]M. J. Blunt and P. R. King, Phys. Rev. A **37**, 3935 (1988).
[31]Benjamin Chu, Chi Wu, Danqing Wu, and J. C. Phillips, Macromolecules **20**, 2642 (1987).
[32]Wenli Wu, B. J. Bauer, and Weijie Su, Polymer **30**, 1384–1388 (1989).

VII. Fracto-emission from deuterated titanium: Supporting evidence for a fracto-fusion mechanism

J.T. Dickinson, L.C. Jensen, and S.C. Langford
Washington State University, Pullman, Washington 99164-2814

R.R. Ryan and E. Garcia
Los Alamos National Laboratory, Los Alamos, New Mexico 87545

(Received 14 July 1989; accepted 31 August 1989)

Measurements of the emission of charged particles, photons, and radio frequency signals accompanying the deformation and fracture of polycrystalline Ti metal and deuterated Ti are described. Preliminary evidence for charge separation created by crack propagation is presented which supports a proposed fracture mechanism to explain neutron bursts observed during treatment of deuterated metals.

I. INTRODUCTION

The reported observations of fusion accompanying electrochemical loading of deuterium into Pd and Ti by Fleischmann and Pons[1] and by Jones *et al.*[2] stimulated experiments involving the detection of neutrons during treatment of both gas loaded and electrochemically loaded specimens of these metals. Scaramuzzi *et al.*[3] and Menlove *et al.*[4] showed that heating and/or cooling metal specimens exposed to high pressure D_2 frequently resulted in statistically significant bursts of neutrons. We,[5] Cohen and Davies,[6] Mayer *et al.*,[7] Furth,[8] and Segre *et al.*[9] have independently proposed a mechanism leading to a D + D fusion reaction involving crack propagation in the embrittled material. A schematic of the model is shown in Fig. 1. We suggest that crack growth results in charge separation on the newly formed crack surfaces, which act like a miniature "linear accelerator;" i.e., D^+ ions are accelerated in the electric field across the crack tip to kinetic energies of $10–10^4$ eV or more, sufficient to raise significantly the D + D fusion probability. An important requirement of this model is that during fracture and because of fracture, D^+ exists as a free ion in the volume of the crack. We refer to this proposed fracture-induced fusion mechanism as *fracto-fusion*. It should be noted that Deryagin *et al.* have published the observation of neutron bursts accompanying impact loading of LiD and described a similar crack acceleration model.[10,11]

In previous work on particle emission accompanying fracture (so-called fracto-emission) we have observed that a number of materials (see Refs. 12–19) exhibit intense charged particle and photon emission as well as bursts of radio frequency signals upon fracture, indicating charge separation across the crack (i.e., separating charge patches are equivalent to rapid current variations), sometimes accompanied by small but consistent microdischarges which produce broad band, far field electromagnetic radiation. Strong charge separation effects are most often observed in piezo- or ferro-electric materials, layered structures, and in adhesively bonded interfaces where bond breaking occurs in a state of high polarization. Examples of each are fracture of single crystal quartz, electrically polarized lead zirconate titanate, mica, and polymer-metal interfaces. All of these materials produce intense fracto-emission and easily detected radio frequency emission. Note that all of these systems involve components that are good insulators so that separated charge is not readily neutralized on timescales of at least several microseconds (duration of fracture). In addition to emission during fracture, these materials exhibit sustained emission, sometimes for as long as 2 h following fracture, due to excitations resulting from charged particle bombardment of the insulating fracture surfaces. Very similar "tails" in the emission can be generated by bombarding insulator surfaces with energetic electrons.[19] This process is analogous to the thermally stimulated luminescence and electron emission observed following exposure of insulators to radiation.[20]

In the case of metals, we have observed that polycrystalline Al, when freed of surface oxide and fractured in ultrahigh vacuum, yields little or no emission.[21,22] Although metallic bonds are being broken and stochastic distributions of charge on the fracture surfaces are possible, high conductivity should result in decay times on the order of 10^{-14} s, making charge acceleration in the crack unlikely. Mayer has suggested that longer decay times might result from crack geometry.[7] Perhaps more importantly, impurity segregation and the existence of inclusions in commercial metals and alloys may result in interfaces and insulating surface layers that simultaneously induce strong charge separation and inhibit reneutralization at separating fracture surfaces for considerably longer times. Because of the current interest in these effects, we felt it appropriate to make a preliminary study of the fracto-emission from deuterated Ti. In this paper, we present measurements of negative and

 © 1990 Materials Research Society

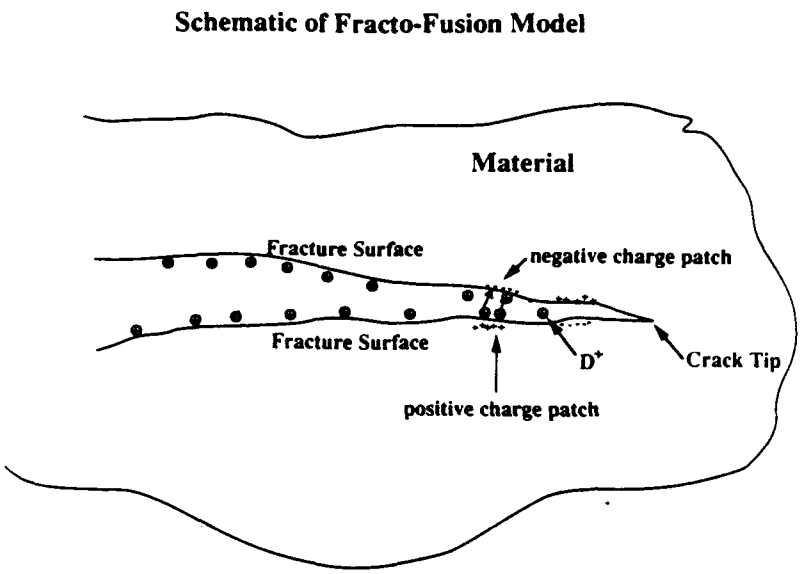

FIG. 1. Schematic diagram of the fracto-fusion model where a propagating crack produces separation of charge and releases D^+ which accelerates in the resulting **E** field, thereby enhancing the D + D fusion reaction.

positive charge emission, visible photon emission, radio frequency emission, and preliminary mass spectroscopy of a single neutral species emitted during and following deformation and fracture of deuterated Ti. A number of these observations provide supporting evidence for a fracto-fusion mechanism.

II. EXPERIMENTAL

Details of our experimental arrangements can be found in Refs. 12–19. The majority of the experiments shown here were performed in vacuum at 10^{-6} Torr in a system containing a large O-ring in a removable top. We discovered after the completion of these experiments that there may have been a small leak associated with this seal during these studies, implying that there might have been a small partial pressure of molecular oxygen in the background. Charge particles were detected with Galileo Electro-optics Corporation Channeltron electron multipliers, which produce fast (10 ns) pulses with high detection efficiency for both electrons and $\pm$ ions. Background noise count rates typically ranged from 1 to 10 counts/s. The detectors were positioned 1–2 cm from the sample, with the bias voltage on the front cone chosen to attract the charged particles of interest. It should be noted that in a number of fracto-emission studies, we have shown that the principal particles detected for positive and negative bias on the Channeltron front cone are electrons and positive ions, respectively.

Photons were detected with a Thorn-EMI 9924QB photomultiplier tube also mounted inside the vacuum system. This photomultiplier responds to photons of wavelengths from about 600 nm to 200 nm, with a maximum quantum efficiency of 25%. Within the vacuum system cooling the photomultiplier was not practical, resulting in relatively high backgrounds of typically 1000 counts/s.

Radio frequency emission was detected with coil antennas placed a few mm from the sample. Such an antenna couples to a changing B field. It should be emphasized that with the antenna only a few mm from the sample, one detects the *near-field* electromagnetic "emission" because of the close proximity of the coils to the source. Thus, moving charge (e.g., due to charge separation) can be detected by such a probe. Simultaneous emission of visible photons and radio frequency bursts is indicative of actual microdischarges occurring in the crack. The most unambiguous fracture experiments where discharges have been detected are in systems involving interfacial failure.

Neutral particles were detected with a UTI 100C quadrupole mass spectrometer, tuned to a single mass peak. The spectrometer is equipped with an ionizer, in which neutrals are ionized by electron impact at an energy of 70 eV. Mass spectrometry was performed in an ultra-high vacuum system with base pressures on the order of 5×10^{-9} Torr.

Samples were cut to $12 \times 6 \times 1.6$ mm^3 from commercial Ti sheet and degassed by heating in vacuum to 750 °C for 1 h. The chamber was then backfilled with the appropriate gas (H_2 or D_2) at 100 Torr and the samples slowly cooled to 400° over a period of an hour and a half, maintaining the 100 Torr. The samples were finally quenched to room temperature. The degree of loading was determined from the weight increase which occurred during hydration/deuteration. The resulting

H:Ti ratio was about 1.0. The D:Ti ratio was typically somewhat lower, about 0.8, due to the lower diffusivity of D relative to H in the Ti lattice. The process of hydration/deuteration yielded quite brittle samples which were readily fractured in three-point bend using devices compatible with high or ultra-high vacuum. Typical loading rates were 10–50 μm/s. Unhydrated/undeuterated "dogbone" samples were prepared from 0.5 mm commercial Ti sheet subjected to the same thermal cycling as the hydrated/deuterated samples, but without backfilling the vacuum system during the cooling step. These samples were notched to ensure that fracture occurred near the detectors and loaded in tension at an elongation rate of $\sim$40 μm/s ($\sim$0.60%/s). The tension geometry can accommodate the much larger plastic deformation associated with unhydrated/undeuterated samples.

Figure 2(a) shows a schematic of the detector arrangements for simultaneous photon and charged particle detection. When better collection geometry was desired, the sample holder was rotated 90° so that the crack opened directly in front of a single detector, as shown in Fig. 2(b), where the "single detector" = photomultiplier, Channeltron, or quadrupole mass spectrometer. In the case of charged particle detection, this orientation increased the electric field at the sample surface and consequently greatly improved the collection efficiency of the Channeltron cone. An acoustic emission transducer (Acoustic Emission Technology Corp. AC1500L) was attached to the breaker to provide a time marker and trigger pulse associated with the fracture event. Signals were either pulse counted with a multichannel scaler or digitized at 10 ns/channel.

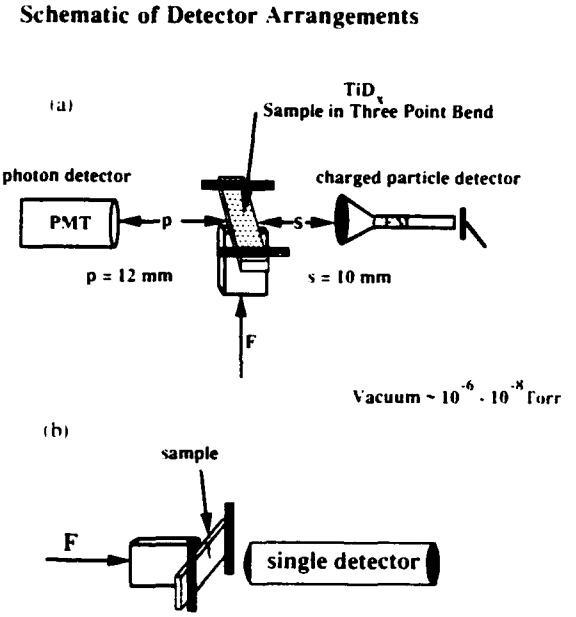

FIG. 2. Schematic of detector arrangement for simultaneous measurements on charged particle and photon emission. When improved sensitivity was desired, the breaker could be rotated 90° so that the crack opened directly toward the chosen detector, shown in (b).

III. RESULTS AND DISCUSSION

Weight measurements made before and after fracture showed no evidence of weight loss at the 0.1 mg level due to exposure to the vacuum and/or fracture; thus, the TiD_x and TiH_x compounds formed were quite stable on this macroscopic level.

Figure 3 shows the detected signals (counts/10 ms time interval) for a TiD_x specimen (where $x \sim 0.8$). The Channeltron cone was biased at +300 V and the Channeltron and photomultiplier were positioned as shown in Fig. 2(a). Similar samples tested in the same geometry but with higher positive cone voltages showed significant increases in count rate; this strongly suggests that negatively charged particles are indeed being collected. We do not know for certain that these are electrons and therefore refer to these emissions as negative charge emission; however, for a large number of other materials, negative charge emission is dominated by electron emission and we suspect that this is also the case for these samples. Of several samples fractured in this manner, the basic time dependence for both the negative charge and photon emissions was similar to the data shown in Fig. 3: a distinct peak at fracture (shown by the arrows) is followed by what appears to be a relaxation-type tail lasting several seconds. Note that despite the high noise level in the photon emission prior to fracture, the photon emission appears to parallel the negative charge emission for some time after fracture.

Figure 4 represents a similar experiment with the front cone of the Channeltron at −2200 V. Such voltage should repel all but the most energetic negatively charged particles. In this particular data set, the photon emission returned to the noise level very rapidly after fracture.

To be absolutely sure that positive ions are indeed emitted, we arranged the Channeltron in the configuration shown in Fig. 5(a), where a metallic disk at ground potential shadowed the Channeltron from line of sight of the crack. Any excited neutral particle would be stopped by the disk, any negatively charged particle would be deflected away from the detector, and any positively charged particle would be detected if it could be drawn around the disk due to the −2200 V on the Channeltron cone. Although the resulting detected emission was small due to constraints, we see in Fig. 5(b) a significant peak at fracture with a few channels of after-emission. We therefore have strong evidence that positive ion emission is produced by fracture of this material. If D^+ is indeed a component of this positive charge emission, then a crucial requirement for the fracto-fusion model, namely free D^+ in the crack, would be met.

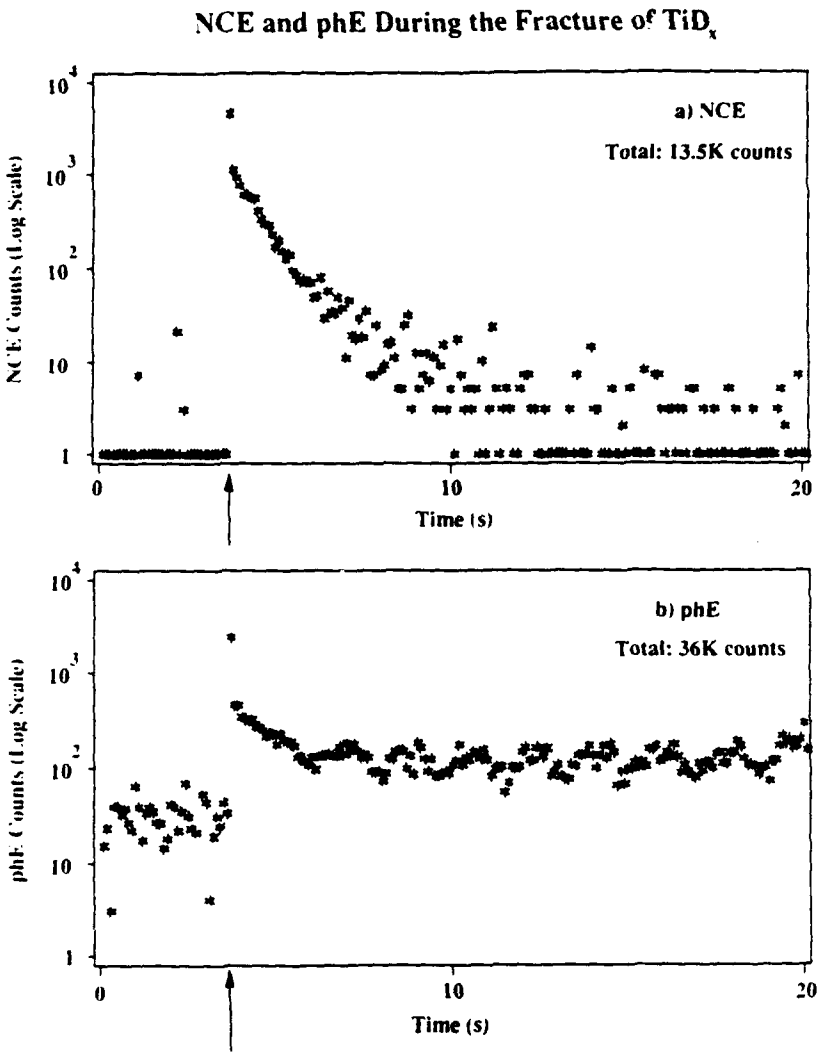

FIG. 3. Simultaneous measurements of (a) negative charge emission (NCE) and (b) photon emission (phE) from the fracture of a TiD_x sample broken in three point bend [Fig. 2(a) geometry].

When the specimen is rotated so as to break directly facing the Channeltron, considerably more negative charge and positive ion emissions are collected. Figure 6 shows the resulting counts/channel (10 ms/channel) versus time for this geometry (no beam block in position) with the Channeltron front cone biased at (a) +300 V, thus attracting negative charge, and (b) −2200 V, thus attracting positive charge. The negative charge emission [Fig. 6(a)] at fracture begins to decay immediately, reaches a minimum, then grows to a broad peak in a few seconds, followed by a nearly exponential decay (similar to Fig. 3) lasting many tens of seconds (the inset shows 80 s of the same data taken at 160 ms/channel). The positive charge emission [Fig. 6(b)] has multiple peaks at and following failure, possibly due to crack arrest and resumed crack growth. The tail after fracture was weak, lasting a few seconds, and appeared to be unrelated to the negative charge emission.

The behavior of the negative charge emission appears suspiciously like a phenomenon known as chemisorptive electron emission[23-26] where a clean metal surface with relatively low work function reacts with gases such as O_2, halogens, and perhaps H_2O during chemisorption. This reaction induces nonadiabatic electronic transitions that result in both chemisorptive luminescence and electron emission. Models developed by Norskov *et al.*,[27] Kasemo *et al.*,[28] and Prince *et al.*[29] describe a strong work function dependence and predict that as coverage increases, the emission rate decreases. Born and Linke[30] have reported dramatic work function decreases on Al surfaces, for example, due to H_2O adsorption. H_2O is a significant component of the background gases in our vacuum system.

In our case, deformation and fracture would produce an increasing number of clean metal sites (recall that not all of the Ti metal has reacted with D). After fracture,

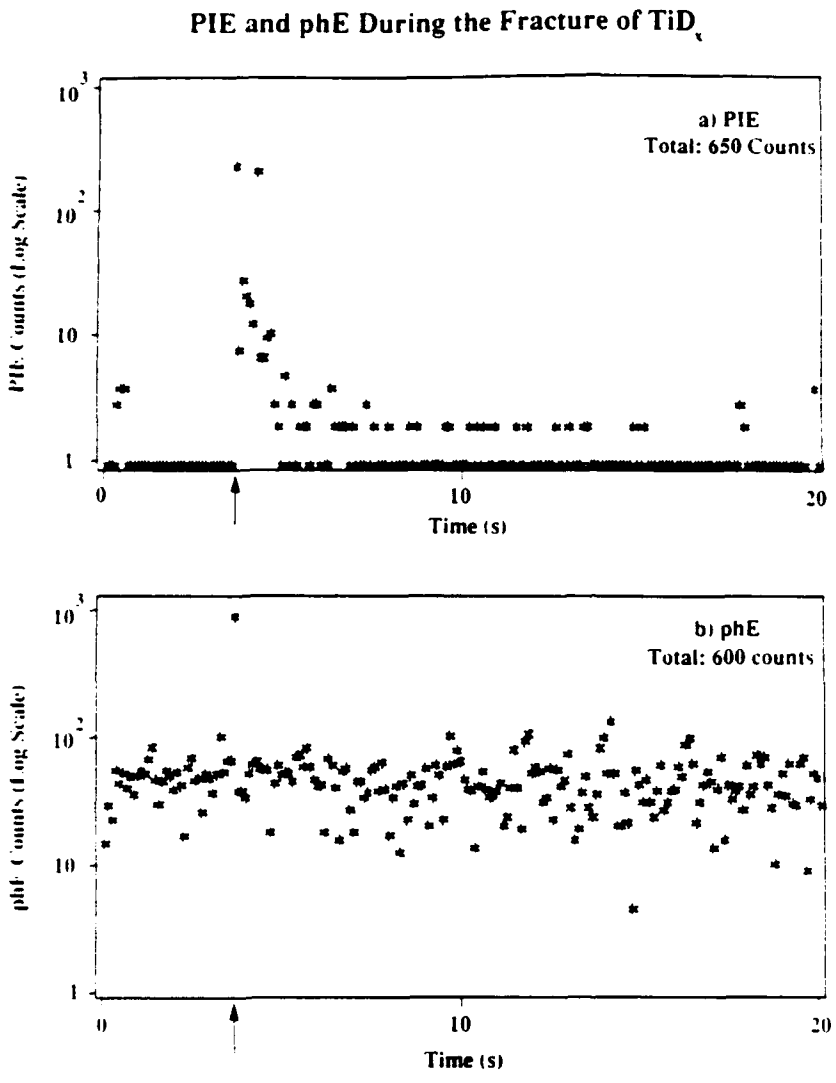

FIG. 4. Simultaneous measurements of (a) positive ion emission (PIE) and (b) photon emission (phE) from the fracture of a TiD_x sample broken in three point bend (Fig. 2(a) geometry).

chemisorption begins on the clean metal sites as soon as the gas can reach the surface. Assuming the reaction probability is proportional to the number of remaining clean metal sites, an exponential decay in emission rate would be observed, consistent with the *later* times (after a few seconds) in the observed emission. If at low coverages, chemisorption decreases the work function of the surface, the emission rate would in fact increase at the onset, thus explaining the observed secondary maximum emission rate following fracture. Several deuterated specimens showed photon emission after fracture which paralleled the negative charge emission, consistent with a parallel chemisorptive luminescence mechanism.

To test this hypothesis, we performed tensile tests on undeuterated Ti tensile specimens in background vacuum and during exposure to O_2 at a pressure of $\sim 10^{-7}$ Torr. O_2 is known to induce chemisorptive luminescence and electron emission on a number of metals, including Ti. If a significant change in the photon and electron emissions is observed during elongation and fracture, this would indicate that chemisorptive luminescence and electron emission could explain these after-emission curves. Figure 7 compares the negative charge and photon emissions for these two atmospheres. We first note that the undeuterated Ti in background vacuum still emits both negative charge and photons at fracture; furthermore, the total emission was of the same order of magnitude as the brittle deuterated Ti broken in three point bend. The O_2 atmosphere is associated with much more intense negative charge and photon emissions than the background vacuum, particularly in the case

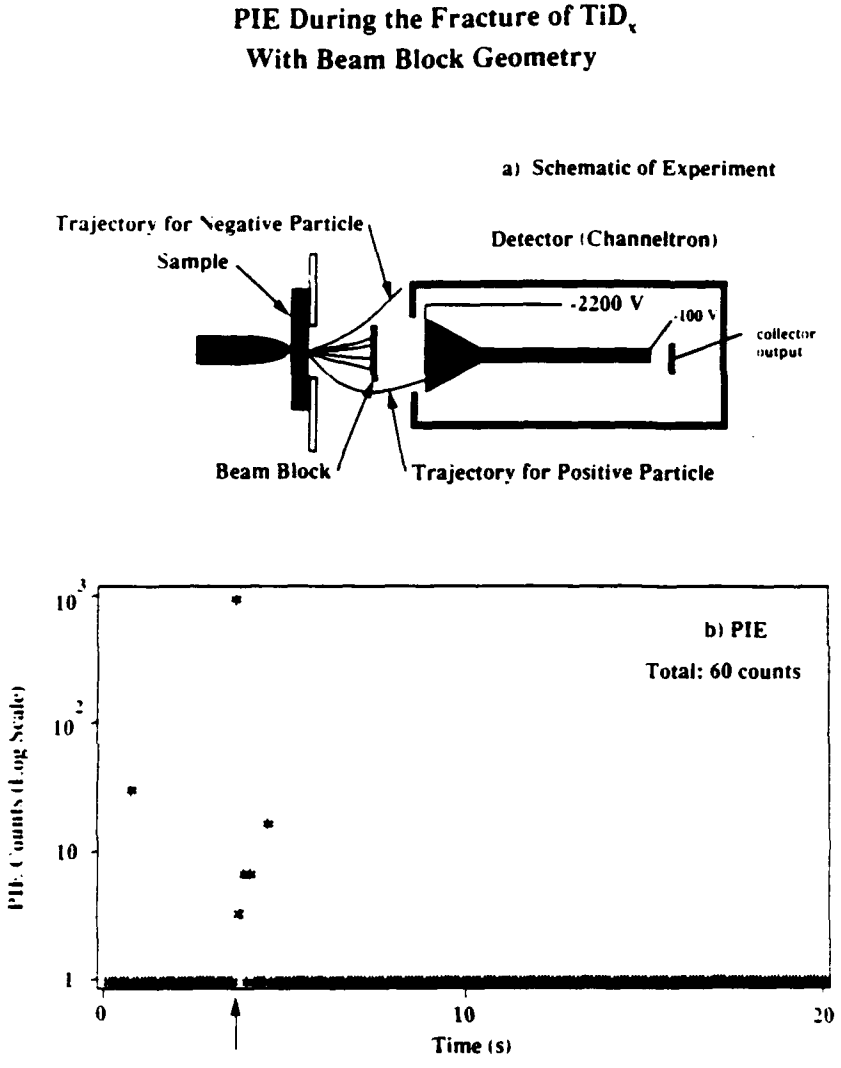

FIG. 5. (a) Experimental configuration for verification of emission of positively charged particles by use of a beam block mounted between the specimen and the detector. (b) The resulting positive ion emission (PIE) from TiD_x.

of negative charge emission. The secondary maximum observed in the negative charge emission (and to some extent in the photon emission) immediately after fracture in the background vacuum is not observed in the O_2 atmosphere. The partial pressure of active gases is at least 2 orders of magnitude higher in the O_2 ambient than in the background vacuum, greatly reducing the time required for establishing intense chemisorptive emissions. Thus, the time to form this secondary peak is too small to be resolved by the rate of data acquisition employed in Fig. 7. The negative charge emission prior to fracture is evident in both background and the O_2 atmosphere, where it is greatly enhanced. These emissions are due to plastic deformation (extensive in the undeuterated material) which brings clean Ti metal (via step formation) to the surface where it reacts with the active gases. The resulting chemisorptive electron emission rate depends on the rate at which fresh Ti reaches the surface and the rate of chemisorption (which is often strongly dependent on gas surface coverage). For the two specimens shown, the negative charge emission intensities can be divided in time as follows:

	Counts during 80 ms time interval including fracture event	Integrated counts in tail ~30 s time interval
In background	13 K	95 K
In O_2	50 K	23 K

The total counts for these two negative charge emission curves are approximately the same; assuming that the surface areas of clean Ti metal created are equal in the two samples, then the total chemisorptive electron emissions would be expected to be nearly equal.

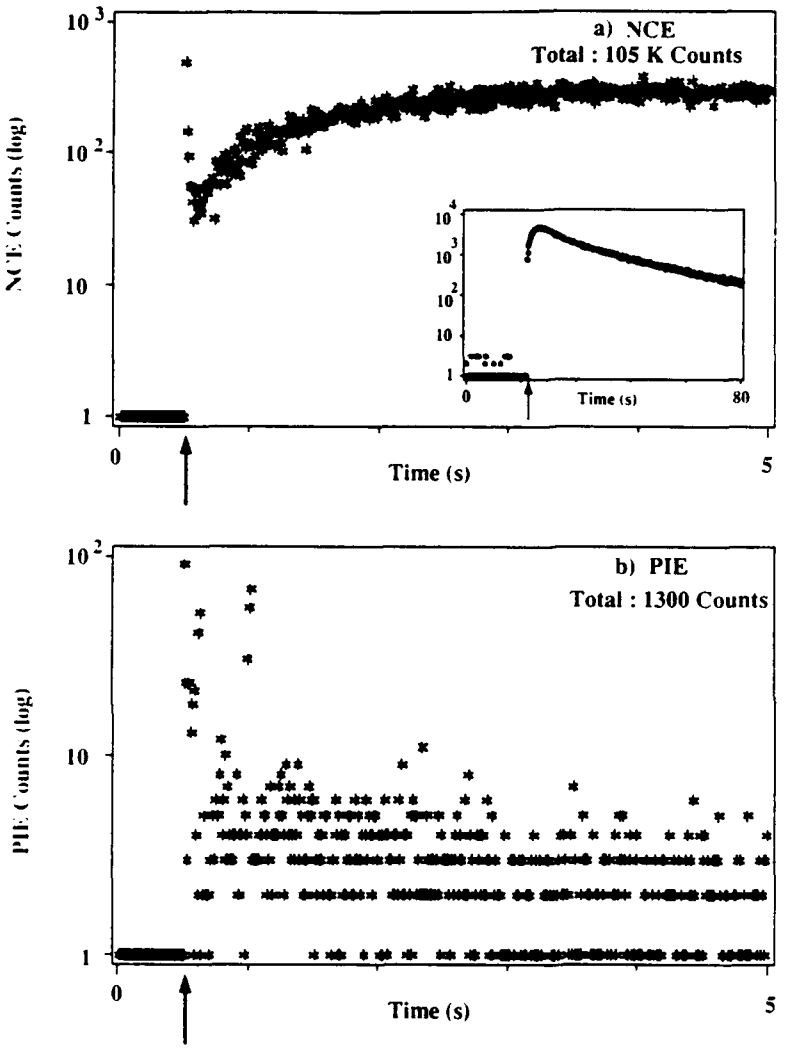

FIG. 6. The charged particle emission for two different TiD_x samples where the specimen is loaded in three point bend [Fig. 2(b) geometry]. The Channeltron electron multiplier is biased for (a) detection of negative charge emission (NCE) and (b) detection of positive ion emission (PIE). The inset displays the negative charge emission data over a longer time interval.

One characteristic of almost all of the negative charge emission data presented so far is the two types of kinetics controlling the after-emission (following the secondary maximum): (i) a first order decay (in background: $\tau \sim 8$ s; in 10^{-7} Torr O_2: $\tau \sim 0.05$ s), and (ii) a nearly steady, low count rate emission. The decay represents chemisorptive electron emission responding in a first order fashion to a fixed number of available chemisorption sites in two different partial pressures of reactive gas; the ratio of the time constants is inversely proportional to the partial pressure (about a factor of 160), which predicts a quite reasonable value for the O_2 partial pressure in the background vacuum, if we assume that O_2 in the background gas is due to a small leak. The nearly constant emission is consistent with a steady state process wherein O chemisorption sites are made continuously available, e.g., through replacement of $O_{(chemisorbed}$ by reaction and desorption with background CO or H_2. The products (CO_2 or H_2O) would desorb, leaving a clean adsorption site. Obviously, many of these questions can be resolved by moving the experiment into ultrahigh vacuum, which we plan to do in the near future.

A very important question in relation to the fracto-fusion mechanism is: Are there negative charge and photon emission components unattributable to chemisorp-

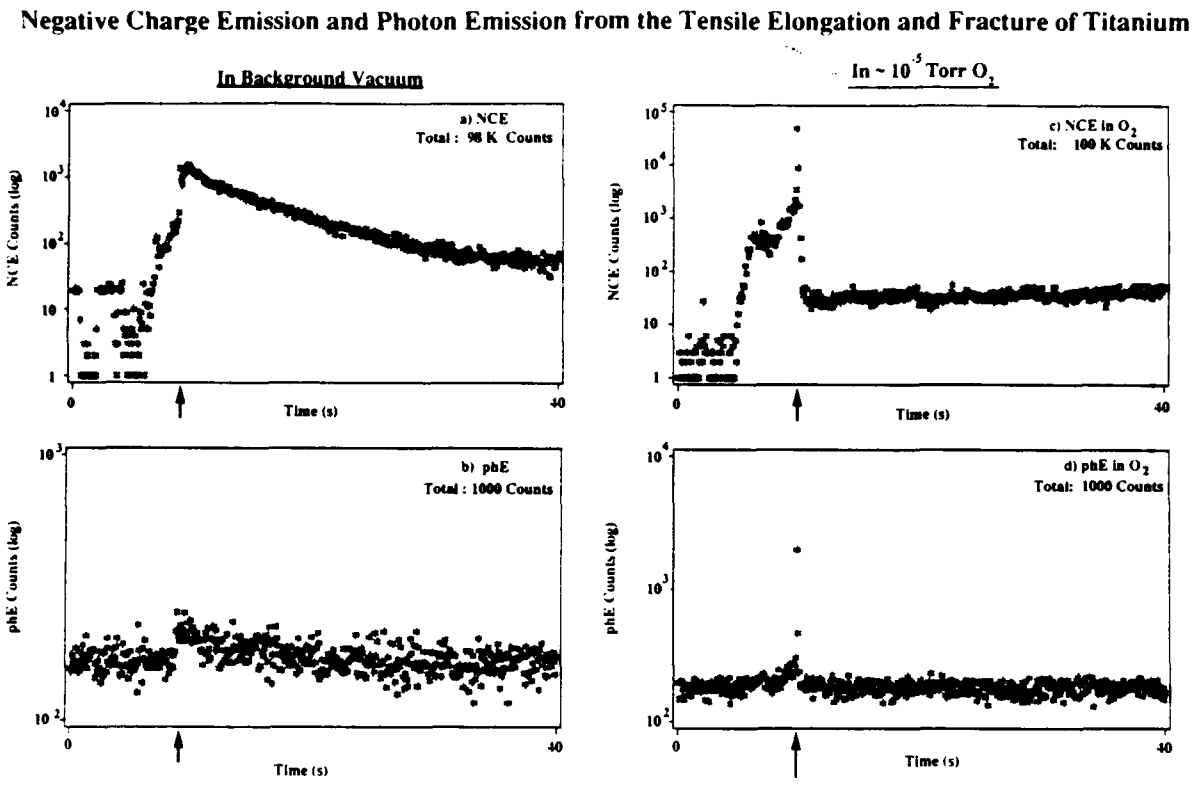

FIG. 7. A comparison of fracto-emission signals from tensile deformation and fracture of commercial Ti in background vacuum: (a) negative charge emission (NCE) and (b) photon emission (phE); and in ~10^{-5} Torr O_2: (c) negative charge emission and (d) photon emission.

tive electron emission and luminescence? Such emission should be most readily apparent during and shortly after fracture, while chemisorptive electron emission and luminescence processes are still quite weak. Examples of this faster emission are shown in Figs. 8(a) (negative charge emission) and 8(b) (positive ion emission) for two different deuterated Ti specimens fractured in three point bend, where we display the digitized Channeltron output. The data were acquired at 10 ns/channel over a total time of 800 μs and integrated over successive 1 μs time intervals; the location of the first fracture event as determined from the acoustic emission trigger pulse is indicated by the arrow. One sees that in both cases the emission was relatively concentrated in two bursts with approximately the same duration and time between the bursts. The smaller, more scattered signals seen at other times correspond to single particles striking the detector. Similar behavior (two bursts) was frequently observed in the photon emission. One is tempted to attribute these bursts to multiple fracture events (crack arrest), although the time interval between the bursts is rather long. These emissions decay rapidly (1–2 ms) and merge into the chemisorptive emission which is at a much lower rate and gradually increases with time, as described above, on time scales of 0.01–1 s. Thus, the processes responsible for chemisorptive electron emission long after fracture are not likely responsible for these bursts of emissions during and shortly after fracture.

As a preliminary test of possible electrostatic activity accompanying these fast fracto-emission features, we placed a small coil around the end of the photomultiplier so that radio frequency and photon emissions could be detected simultaneously. The response of this "antenna" to a burst of radio frequency B-field consists of a damped ringing signal resonating at the resonant frequency of the LCR circuit associated with the coil and amplifier (264 kHz). In the past, such correlations have served as a test for either charge separation or microdischarges accompanying fracture. Radio frequency and photon emissions accompanying the fracture of TiD_x in vacuum are shown in Fig. 9. Note the different timescales for the two signals; the time of fracture is marked by the arrows. The existence of such a radio frequency signal strongly supports the presence of charge separation. In past work, supporting evidence for microdischarges accompanying fracture involved intense photon emission *during* fracture accompanying such radio frequency signals. Relative to other materials which dis-

Charged Particle Emission During the 3 Pt-Bend Fracture of TiD_x

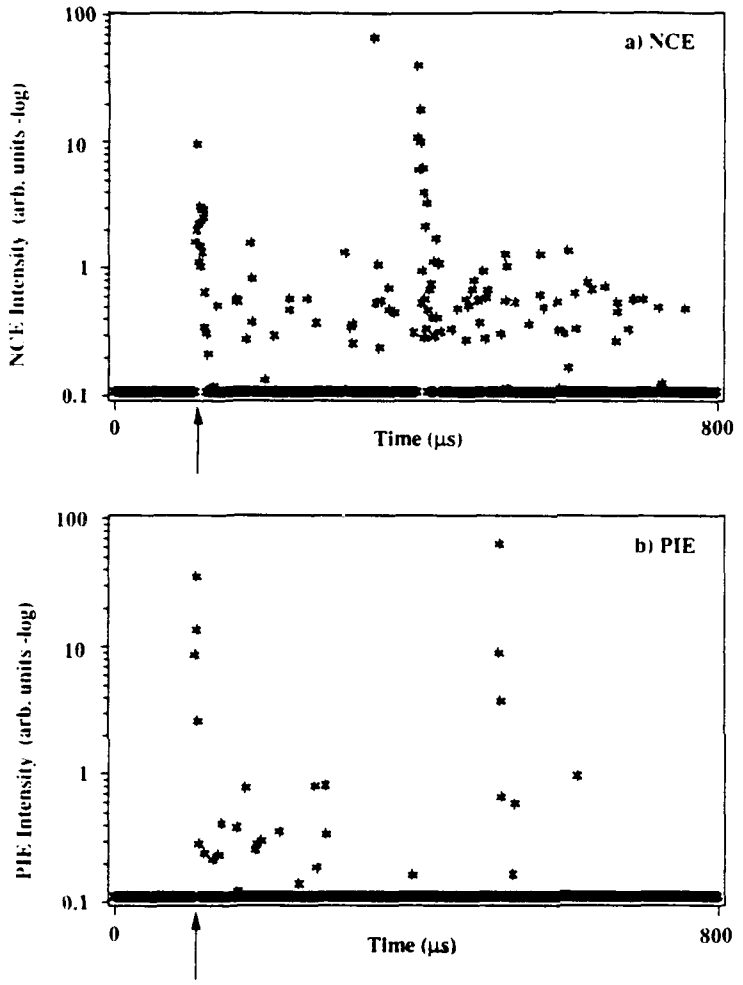

FIG. 8. Charged particle emission acquired on a faster timescale from the fracture of two different TiD_x samples in three point bend. The resulting (a) negative charge emission (NCE) and (b) positive ion emission (PIE) show two fairly intense bursts which may be due to multiple fracture events.

play microdischarges, the photon emission burst at fracture in Fig. 9 is quite small and seems to be spread out over several hundred μs. Although the radio frequency signal is clear evidence for electrical activity, the observed radio frequency and photon emissions are probably not due to microdischarges in the crack.

The nature of this electrical activity was further investigated by testing for the generation of electrical currents during and following fracture. The sample was electrically isolated from the three point bend apparatus and wired in series with the 50 Ω input resistor of an amplifier so that fracture would cut the circuit between one end of the sample, connected to ground, and the other end of the sample, tied to the amplifier input resistor (see diagram of the circuit shown in the inset of Fig. 10). It is important to note that initially both ends of the sample were at ground potential, and no external potential or field was applied to the circuit during the course of the experiment. Figure 10 shows the digitized amplifier output, converted to current (i = V/R), during the fracture of a TiH_x sample (used in place of TiD_x due to sample availability at the time). At or soon after fracture, as determined by an accompanying acoustic emission source, a rapidly fluctuating voltage is recorded. The fluctuations are consistent with variations in the charge balance across the crack tip during fracture. After ~15 μs, a sharp drop in signal (negative current) is observed, followed by a slow decay toward zero. Any charge imbalance remaining across the crack following failure is expected to yield a rapid falling (or rising) current followed by a super-exponential decay as the two sides of the crack accelerate away from each other.

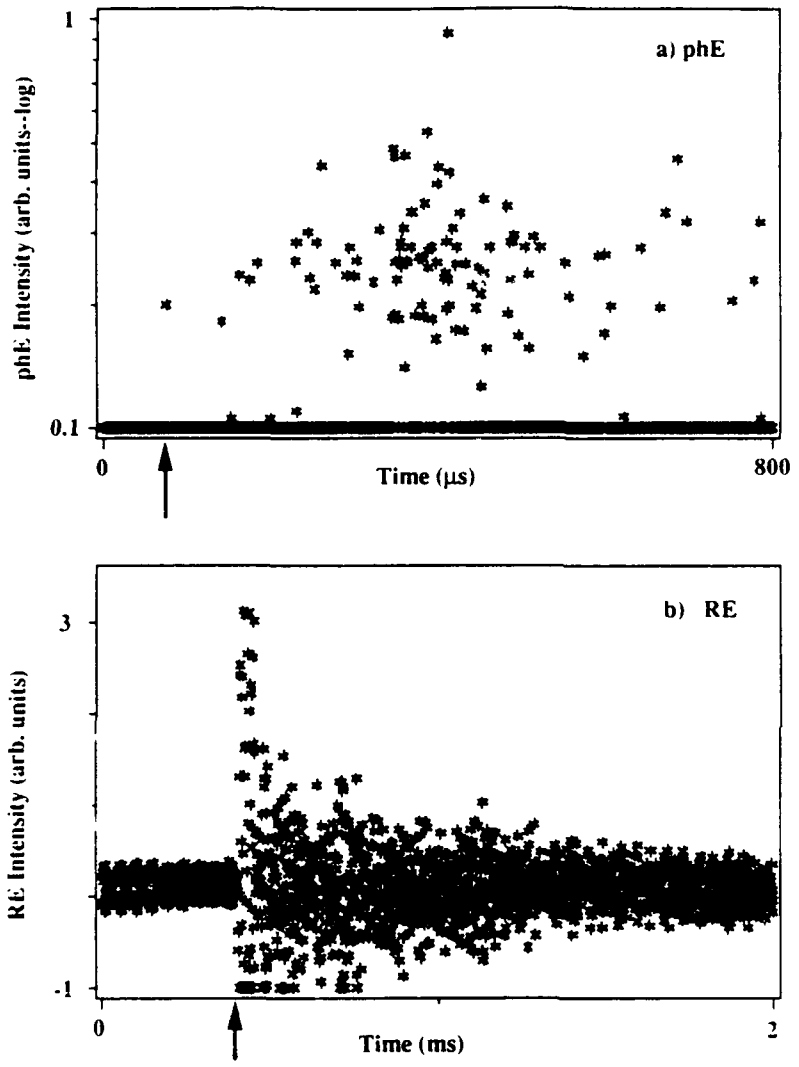

FIG. 9. Simultaneous measurements of (a) photon emission (phE) and (b) radio frequency emission (RE) produced by fracture of TiD$_x$ in vacuum. The radio frequency signal is a damped, ringing signal responding to an "impulse" of changing **B** *field at fracture.*

The decay is punctuated by occasional ringing signals, perhaps due to the influence of reflected acoustic waves on the path of the separating pieces of sample. Although we cannot absolutely rule out the presence of artifacts in this signal, our attempts to explain these signals on the basis of anything other than fracture induced currents have failed. We therefore interpret these current measurements as evidence for charge separation across the crack tip during and following fracture. Note that for such currents to be sustained for any length of time during fracture, the circuit must contain relatively high resistance conduction paths. Impurity segregation at grain boundaries and crack branching into the sample bulk may contribute to the effective resistance of the near surface region.

In our investigation of the possible role of chemistry on the emissions during the fracture event itself, we performed photon and radio frequency emission measurements on deuterated and hydrogenated Ti samples in air. Figure 11 shows typical results for TiD$_x$. The radio frequency emission in air was essentially the same as in vacuum, but the photon emission was much larger, saturating the photomultiplier for approximately 100 μs. A rough estimate of the ratio of intensities of the fast photon emission in air versus vacuum is 10^3. Similar tests performed in N_2 and O_2 atmospheres resulted in very

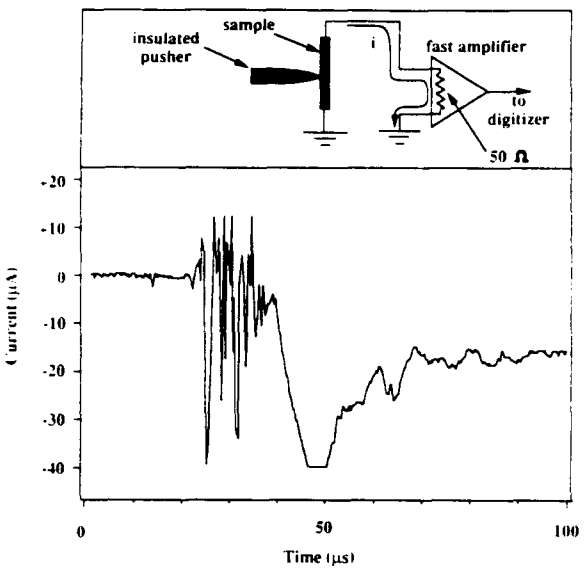

FIG. 10. Fracture-induced current produced in a TiH_x specimen fractured in three point bend. Schematic of circuit is shown in inset.

weak photon emission in N_2 and very strong photon emission in O_2. Tests of undeuterated Ti tensile specimens in an O_2 atmosphere displayed much weaker photon emission during fracture than the deuterated Ti. Suspecting that D_2 would be the dominant species in the crack during fracture, we fractured three point bend deuterated specimens in vacuum near the ionizer of a quadrupole mass spectrometer tuned to mass 4. The background pressure in the vacuum system before fracture was 3×10^{-9} Torr. Figure 12 shows the resulting mass 4 signal. (The ion detector output has passed through a fast electrometer undergoing some integration; thus a smooth curve.) This is a very strong signal (total detected mass 4 corresponds to $\sim 10^{15}$ molecules) which we attribute to D_2 emission (*not* ^{4}He!). Much of this D_2 would be available for a catalytic reaction with O_2 from the air. Thus, it appears that the intense photon emission from TiD_x (and TiH_x) during fracture in air is chemical in origin, not associated with discharges, but due to the catalytic reaction of D_2 from the sample and O_2 from the atmosphere. The highly exothermic nature of the $D_2 + O_2$ reaction, coupled with high reaction rates due to the catalytic nature of the surface, produce intense photon emission in the visible region, possibly black body radiation. (This effect was utilized in the so-called "Doebereiner cigarette lighter".[31]) Using an optical multichannel analyzer, we were able to detect a weak spectrum from one TiD_x sample fractured in air; it appears to be band-like starting up at ~350 nm and extending toward the red to ~650 nm.

SEM photographs of the fracture surface of a TiD_x specimen are shown in Fig. 13. There appears to be evidence of platelet formation of the deuteride phase and intergranular fracture similar to that described by Boyd in Ti–Al alloys.[32] Livanov *et al.*[33] describe the fracture of embrittled Ti as involving the interface between metallic Ti and the hydride including formation of Griffith cracks at the interface whose growth is facilitated by a smaller surface energy compared to the original metal.

Impurity segregation at grain boundaries is a well-known phenomenon and could contribute to the charge separation and inhibition of reneutralization. Mayer *et al.*[7] have also suggested that other mechanisms, including crack branching, could increase the conduction path lengths and resistivity and therefore increase the resistance to charge flow. In the photographs of Fig. 13, one can also see evidence of a few cracks normal to the fracture surface which may also represent interfacial failure at the boundaries of the deuteride platelets.

It was our assumption (and still is) that the phenomena presented so far resulting from TiD_x fracture should be reproduced by similar TiH_x samples. The TiH_x samples (where $y \sim 1.0$) were found to be considerably weaker and more brittle than the TiD_x specimens. We attribute this difference to the higher loading of hydrogen (20% higher). The differences in the fracto-emission between these two types of specimens were astounding. The intensities were dramatically reduced in the TiH_x samples. For example, Fig. 14 shows negative charge emission from the fracture of TiH_x under conditions comparable to Fig. 6(a). The photon emission from the TiH_x samples was barely detectable above the noise. No chemisorptive electron emission or luminescence of a magnitude comparable to that from deuterated Ti was seen. Finally, most surprising was the lack of any detectable mass 2 (H_2) when the TiH_x was fractured in the mass spectrometer system. We are somewhat puzzled by these results although sample strength and the mode of failure may indeed be primary differences. The very small chemisorptive electron emission and luminescence signals suggest that in $TiH_{1.0}$, Ti metal sites are not produced in significant numbers relative to $TiD_{1.5}$. Furthermore, the lack of H_2 emission from $TiH_{1.0}$ suggests that the mass 4 signal (which we attribute to D_2) is not due to molecular deuterium trapped in voids in the metal, but rather from the decomposition of TiD_x during crack propagation. The weaker TiH_x may not release sufficient energy at the crack tip to free the H from its bond with Ti.

IV. CONCLUSION

This preliminary study has shown that both negative and positively charged particles, visible photons, and long wavelength emission are emitted during and fol-

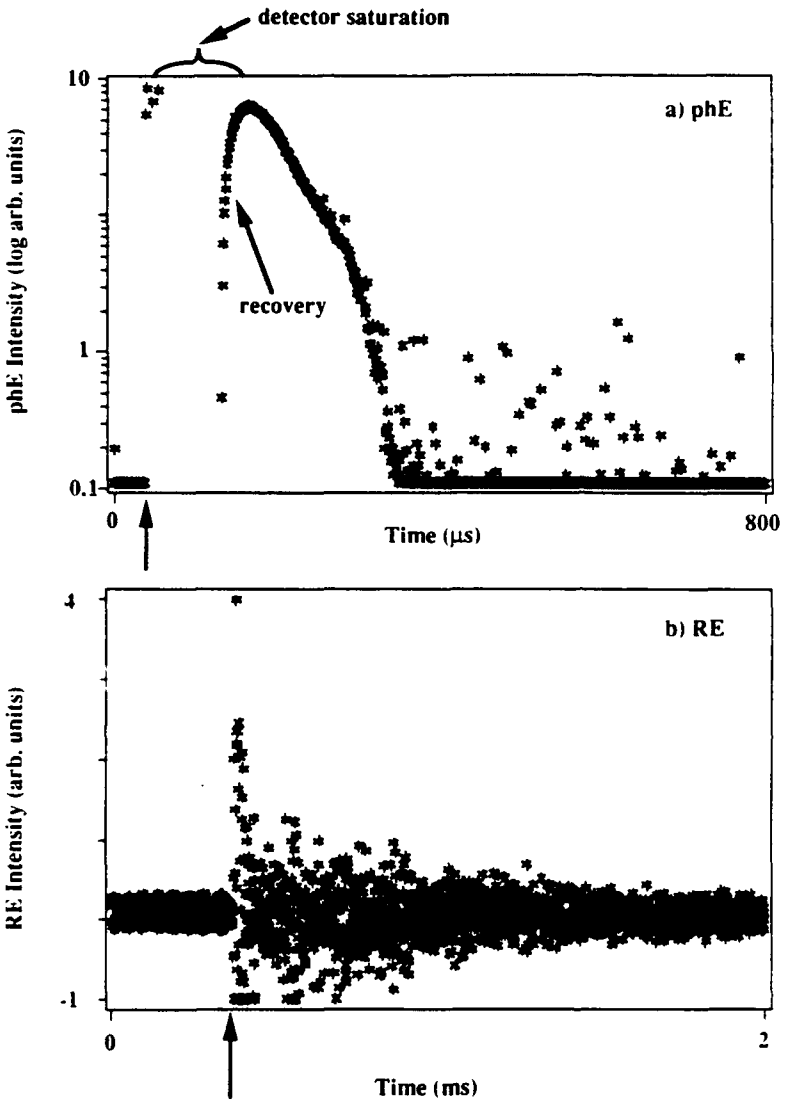

FIG. 11. Simultaneous measurements of the (a) photon emission (phE) and (b) radio frequency emission (RE) produced by fracture of TiD_x in air. The photon emission is three orders of magnitude or more greater in air than in vacuum.

lowing fracture. Surface reactions of freshly exposed Ti with active background gas(es) result in chemisorptive emission of negative and positive charge as well as photons on timescales of seconds. These slow emissions appear to have little relevance to questions of charge separation. The origin of the fast emissions accompanying fracture is not yet clear. However, the behavior of the measured radio frequency emission and fracture-generated currents strongly suggest charge separation during fracture. Further studies will concentrate on determining the identity of the emitted species (e.g., electrons, ±ion and neutral masses), the energy of the charged particles, and spectra of the photon emission in vacuum and in controlled gaseous environments (N_2, O_2, H_2). Most relevant to fracto-fusion mechanisms are (a) the identification of D^+ in the positive charge emission and (b) energy measurements of the charged particles. Electrostatic acceleration would be the only reasonable source of charged particle kinetic energies of several eV or higher. Finally, the dependence of the fracto-emission behavior on materials properties [nature of grain boundaries, locus of fracture, impurity concentrations, D (or H) concentrations] should also be investigated, in particular regarding the observed dif-

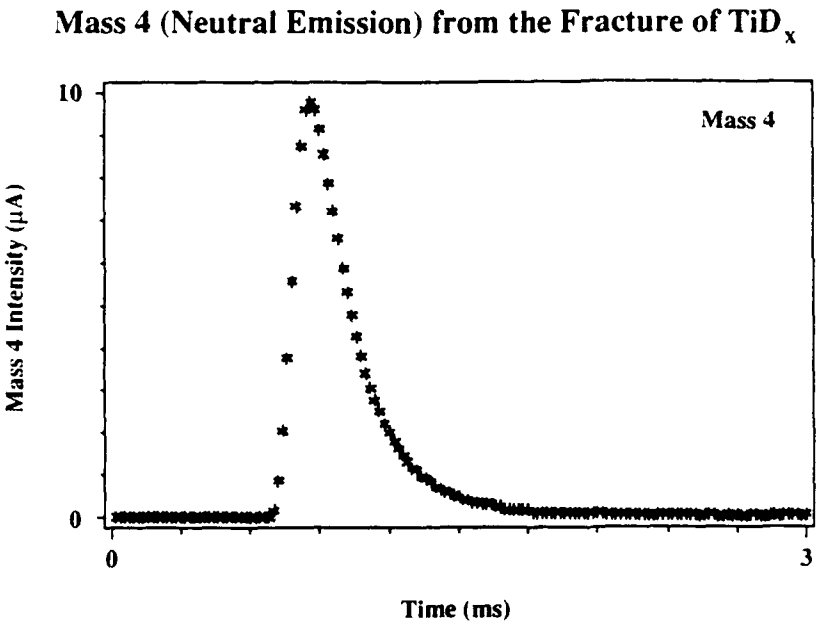

FIG. 12. The quadrupole mass spectrometer output at mass 4 due to the fracture of TiD_x. We attribute this signal to the emission of D_2.

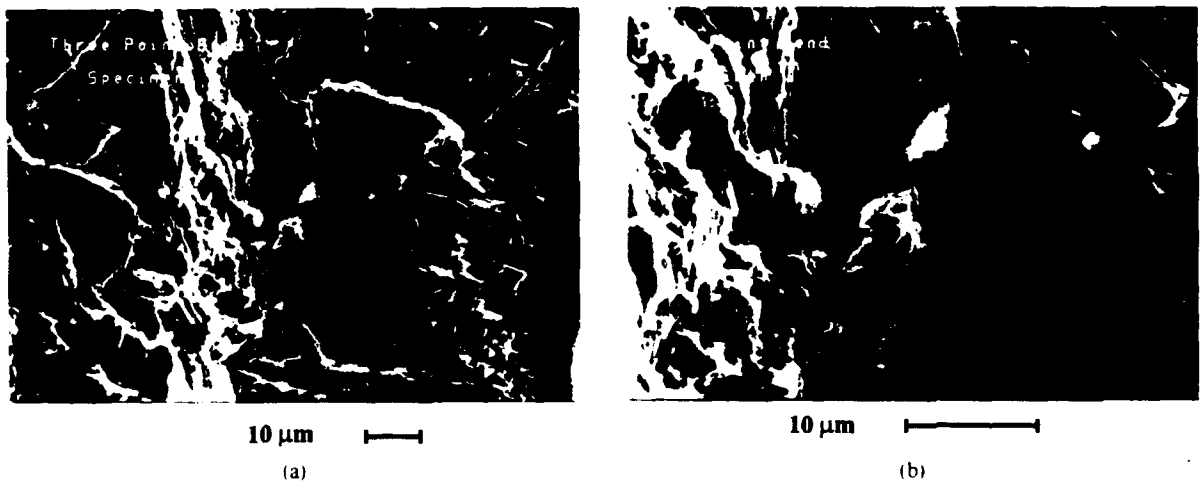

FIG. 13. SEM photographs of the fracture surface of a TiD_x sample broken in three point bend.

ferences in emission from the $TiD_{0.8}$ and $TiH_{1.0}$. When possible, these studies should be made in conjunction with neutron emission experiments, including correlation experiments between fracture, fracto-emission, and neutron emission. Obviously, if the fracto-fusion mechanism is valid, it would not be a cold fusion process due to the necessary electrostatic acceleration provided by charge separation. Energetically, this charge separation is driven by mechanical forces transmitted to the crack tip via elastic deformation of the lattice.

ACKNOWLEDGMENTS

This work was supported by the Ceramics and Electronics Materials Division of the National Sciences Foundation DMR-8601281, the Office of Naval Research Contract No. N00014-87-K-0514, and the Washington Technology Center. The authors wish to thank Gary Collins, Washington State University, for useful discussions. We also thank M. Stout and A. Geltmacher, Los Alamos National Laboratory, for taking the SEM micrographs of the TiD_x fracture surfaces.

NOTE ADDED IN PROOF

Another discussion of the fracto-fusion mechanism has recently been published: "Fracto-Fusion Mechanism", Tatsuoki Tekeda and Tomonori Takizuka, J. Phys. Soc. Japan **58**, 3073 (1989).

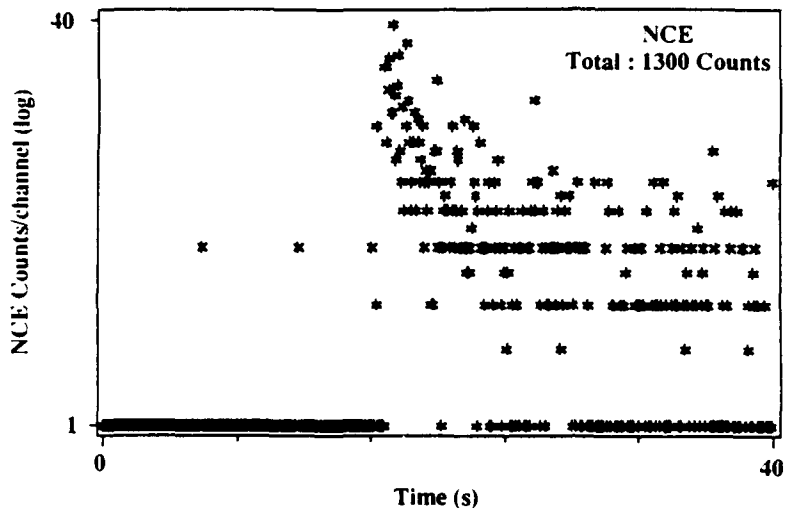

FIG. 14. The negative charge emission from the much weaker, more brittle TiH_y fracture. This emission should be compared with Fig. 6(a) for TiD_y.

A recent experiment has been reported by B.V. Derjaguin, A.G. Lipson, V.A. Kluev, Dm. M. Sakov, and Yu. P. Toporov, Nature **341**, 492 (1989), claiming low levels of neutron emission above background during ball-milling of Ti and deuterium containing compounds. This emission is attributed to a fracto-fusion mechanism.

REFERENCES

[1]M. Fleischmann and S.J. Pons, J. Electroanal. Chem. **261**, 301 (1989).
[2]S.E. Jones, E.P. Palmer, J.B. Czirr, D.L. Decker, G.L. Jensen, J.M. Thorpe, S.F. Taylor, and J. Rafelki, Nature **338**, 737 (1989).
[3]A. De Ninno, A. Frattolillo, G. Lollobattista, L. Martinis, M. Martone, L. Mori, S. Podda, and F. Scaramuzzi, Europhysics Letters **9**, 221 (1989).
[4]H.O. Menlove, M.M. Fowler, E. Garcia, A. Mayer, M.C. Miller, R.R. Ryan, and S.E. Jones, submitted to Nature.
[5]R. Ryan, M. Fowler, E. Garcia, H. Menlove, M. Miller, A. Mayer, J. Wilhelmy, C. Orth, S. Schmidt, D. Moore, A. Voter, and J.T. Dickinson, presented at Santa Fe Workshop on Cold Fusion Phenomena, Santa Fe, NM, May 23–25, 1989.
[6]J.S. Cohen and J.D. Davies, Nature **338**, 705 (1989).
[7]F.J. Mayer, J.S. King, and J.R. Reitz, presented at Santa Fe Workshop on Cold Fusion Phenomena, Santa Fe, NM, May 23–25, 1989.
[8]H. Furth, S. Bernabei, S. Cowley, and R. Kulsrud, Bull. Am. Phys. Soc. **34**, 1860 (A) (1989).
[9]S.E. Segre, S. Atzeni, S. Briguglio, and F. Romanelli, "A Mechanism for Neutron Emission from Deuterium Trapped in Metals" (to be published).
[10]V.A. Klyuev, A.G. Lipson, Yu. P. Toporov, B.V. Deryagin, V.I. Lushchikov, A.V. Strelkov, and E.P. Shabalin, Pis'ma Zh. Tekh. Fiz. **12**, 1333 (1986) [Sov. Tech. Phys. Lett. **12**, 551 (1987)].
[11]B.V. Deryagin, V.A. Klyuev, A.G. Lipson, and Yu. P. Toporov, Kolloidnii Zhurnal **48**, 12 (1986).
[12]J.T. Dickinson, E.E. Donaldson, and M.K. Park, J. Mater. Sci. **16**, 2897 (1981).
[13]J.T. Dickinson, L.C. Jensen, and A. Jahan-Latibari, J. Vac. Sci. Technol. **A2**, 1112 (1984).
[14]J.T. Dickinson, W.D. Williams, and L.C. Jensen, J. Am. Ceram. Soc. **68**, 235 (1985).
[15]J.T. Dickinson, in *Adhesive Chemistry — Developments and Trends*, edited by L.H. Lee (Plenum Publishers, New York, 1984), pp. 193–243.
[16]L.A. K'Singam, J.T. Dickinson, and L.C. Jensen, J. Am. Ceram. Soc. **68**, 510 (1985).
[17]J.T. Dickinson and E.E. Donaldson, J. Adhesion **24**, 199 (1987).
[18]J.T. Dickinson, to appear in *Advances in Adhesion*, edited by L.H. Lee (Plenum Press, New York).
[19]J.T. Dickinson and L.C. Jensen, J. Polym. Sci.: Polym. Phys. Ed. **23**, 873 (1985).
[20]R. Chen and Y. Kirsch, *Analysis of Thermally Stimulated Processes* (Pergamon Press, Oxford, 1981).
[21]J.T. Dickinson, P.F. Braunlich, L.A. Larson, and A. Marceau, Appl. Surf. Sci. **1**, 515 (1978).
[22]D.L. Doering, T. Oda, J.T. Dickinson, and P. Braunlich, Appl. Surf. Sci. **3**, 196 (1979).
[23]B. McCarroll, J. Chem. Phys. **50**, 4758 (1969).
[24]B. Kasemo, Phys. Rev. Lett. **32**, 1114 (1974).
[25]I.V. Krylova, *Proc. 5th Int. Symp. on Exoelectron Emission and Dosimetry*, edited by A. Bohun and A. Scharmann, 40 (1976).
[26]M.A. Loudiana, J. Bye, J.T. Dickinson, and D.A. Dickinson, Surf. Sci. **157**, 459 (1985).
[27]J.K. Norskov, D.M. Newns, and B.I. Lundqvist, Surf. Sci. **80**, 179 (1979).
[28]B. Kasemo, E. Tornqvist, and L. Wallden, Mater. Sci. Eng. **42**, 23 (1980).
[29]R.H. Prince, R.M. Lambert, and J.S. Foord, Surf. Sci. **107**, 605 (1981).
[30]D. Born and E. Linke, *Proc. 5th Int. Symp. on Exoelectron Emission and Dosimetry*, edited by A. Bohun and A. Scharmann, 265–269 (1976).
[31]Cited on BITNET, April 26, 1989, SCHWARTZ_GERHARD at FRANKFT.
[32]J.D. Boyd, in *The Science, Technology, and Application of Titanium*, edited by R.I. Jaffee and N.E. Promisel (Pergamon Press, Oxford, 1970), pp. 545–555.
[33]V.A. Livanov, B.A. Kolachev, and A.A. Buhanova, in *The Science, Technology, and Application of Titanium*, edited by R.I. Jaffee and N.E. Promisel (Pergamon Press, Oxford, 1970), pp. 561–576.

VIII. Fracto-emission from embedded interfaces

Ma Zhen-Yi and J. T. Dickinson

Department of Physics, Washington State University, Pullman, Washington 99164-2814

Abstract

Fracto-emission (FE) is the emission of particles and photons during and after fracture of materials. The observed emissions include electrons, ±ions, neutral species in both ground states and in excited states, and visible photons. Here we examine primarily photon and electron emission during failure of axially loaded stainless steel fixtures (e.g., rods) embedded in epoxy. The observed signals provide time resolved information on the sequence of events involving interfacial fracture proceeding pullout. In addition, we examine the emissions during frictional pullout following debonding. Over a large range of strain rates this pull-out exhibits stick-slip behavior. These effects model the processes of fiber/matrix debonding and fiber pullout in a brittle matrix composite.

Introduction

The term fracto-emission (FE) refers to the release of photons, electrons, ions, and molecules from a material under stress prior to, during, and after ultimate failure.[1-5] FE is useful for examining failure mechanisms in polymers, ceramics, and composites. When reinforcing particles or fibers are placed in a matrix such as an epoxy, deformation frequently leads to debonding along the interface between the two dissimilar materials. When this occurs internally, it is often difficult to determine when and where these processes take place. Semi-transparent and transparent matrix materials often allow sufficient light transmission for measurements of photons emitted from internal interfaces and escaping through the matrix to the detector.[6] In addition,

separation of dissimilar materials is often accompanied by strong charge separation which can lead to detectable radio frequency emission (RE). Furthermore, comparison of photon emission (phE) signals with simultaneous electron emission (EE) measurements allow us to distinguish between interfacial failure at embedded interfaces and failure which communicates with the surface. As electrons cannot penetrate the matrix to any significant degree, EE is observed only from failure events at external surfaces.

In the case of fiber reinforced epoxy, a poor bond between the fibers and the matrix can lead to detectable emission. In a study of E-glass fibers (10 μm in diameter) embedded in an Epon 828/Jessamine Hardener matrix (a clear, flexible epoxy) strained in tension, clear phE signals resulting from internal failure of fibers and subsequent debonding were observed.[6] When the fibers were coated with an epoxy-compatible sizing to enhance fiber/matrix adhesion, very little phE was observed before failure due to the absence of interfacial failure. In similar experiments on single boron-carbon filaments (100 μm in diameter) embedded in the same matrix material, the application of a release agent (silicone oil) to the fiber before embedding it in the resin was shown to lead to pre-failure debonding when strained under a microscope. Identical samples strained in the presence of a photomultiplier tube yielded intense pre-failure phE at strains known to yield debonding. Without the release agent, the boron-carbon filament adhered very well to the epoxy, and no pre-failure phE was observed.

In an earlier study we reported fracto-emission measurements during the peel of gold thin films from Si substrates.[7] The detachment of the gold was accomplished by means of an epoxy pad attached to the gold film; the head of a steel pin was embedded in the epoxy (see Fig. 1) and pulled perpendicular to the substrate. Usually, no pre-failure emission was observed (normal failure was a peel of the Au from the substrate). However, as shown in Fig. 1, the failure of very strongly adhering Au films always yielded copious photon emission (phE) a few hundred milliseconds *before* the peel event (indicated by the arrows). On the basis of the above mentioned studies, it was not difficult to provide a partial interpretation of these results: the pre-failure photons were coming from debonding at the embedded interface between the metal pin and the

86

epoxy. In vacuum, the creation of an metal/epoxy debond is known to produce intense electron emission (EE).[8] *No* electron emission (EE) is seen before final failure because the debonding is inside the epoxy–the electrons cannot escape to reach the detector. The intense phE and EE accompanying and following failure were from the Au-Si detachment event which eventually occurred and finally exposed the emitting surfaces to the vacuum, thus allowing the electrons to escape and be detected.

In this paper we present more detailed studies of the internal interfacial failure between metal and epoxy utilizing a simplified geometry, namely that of a model fiber (i.e., a cylindrical metal rod) partially embedded into an epoxy matrix and loaded in tension. Depending on the ratio of the fiber or rod diameter to the embedded depth, the matrix will either fail cohesively or the rod will debond and pull out, the latter being most probable in the case of shallow embedding depths. Atkinson *et al.*[9] have discussed the fracture mechanics of this problem and have indicated a strong tendency for tensile debonding at the embedded *end* or *tip* of the rod. Subsequently, debonding via shear deformation (Mode II) is predicted to occur along the sides of the rod, starting from the upper, free surface and moving down towards the tip. In this work, we report measurements of several fracto-emission components and use these signals to help clarify the sequence of events accompanying debonding and pullout, showing slight differences from the predicted order of events. In addition, we examine the emissions during frictional pullout following debonding. The latter is of interest as a model for fiber pullout in composites, particularly in crack bridging fibers in brittle matrices. In our system, this pull-out exhibits stick-slip behavior over a large range of loading parameters. Interestingly, such phenomena show striking similarities to the slip occurring in geologic faults.[10,11]

Experimental

Two epoxies were used in this investigation, Devcon 5-Minute epoxy and Ciba-Geigy Araldite 502. 5-Minute epoxy is a bisphenol A based resin with a mixture of polymercaptans as hardner. Fixtures were placed immediately into the mixed resin/hardner. Araldite 502 is a low

viscosity epoxy resin based on bisphenol A and epichlorohydrin and modified with dibutyl phthalate; the curing agent is HY 956, an alkoxylated triethylene tetramine. The resin and hardner were mixed and poured into cylindrical silicone rubber molds. Highly polished, stainless steel rods, nominally 2.5 mm in diameter, were then inserted into the resin and supported externally while the epoxy cured. The length of rod embedded in the epoxy was about 5 mm in the 5-Minute epoxy and 50 mm in the Ciba-Geigy epoxy. Some 5-Minute epoxy samples were prepared with a 1/2 inch box nail instead of the rod, for comparison with the embedded pin [Au-Si peel] results discussed above. This nail has a broad, flat head 3 mm in diameter and a stem 1.2 mm in diameter, which is comparable in form to the head of the pin used in the peel study. The 5-Minute epoxy was cured for 24 hours at room temperature; the Ciba-Geigy epoxy samples were cured at 100 °C for 3 hr and cooled overnight. Both epoxies are quite transparent so that visible photons created at the rod-epoxy interface pass readily through the matrix to the detector. The samples were mounted in a tensile loading apparatus and tested in vacuum at pressures of 10^{-5} Pa. The sample geometry and detector arrangement is shown in Fig. 2.

Electrons were detected with a Galileo Electro-Optics Channeltron electron multiplier (CEM), which produces fast (10 ns) pulses with high detection efficiency. Background noise counts typically ranged from 1 to 10 counts/s. The CEM was positioned within 1 cm of the sample and its front cone biased positive for the detection of negatively charged particles. In previous studies of organic polymers we have shown that the principle particles detected with a positive bias voltage on the CEM front cone are electrons and not negative ions.

Photons were detected with a Thorn-EMI 9924QB photomultiplier tube with a bialkali phosphor and quartz window. Background count rates were typically about 1 kHz. Some data were acquired with a cooled photomultiplier tube (PMT) and thus much lower background. A second, uncooled PMT, a Bendix BX754A, with an S-20 cathode and a much smaller photosensitive surface (1 mm in diameter) was sometimes used to acquire spatial information about the phE.

88

Low-frequency electromagnetic waves (RE--for radiowave emission) were detected with a coil antenna placed a few mm from the sample. The resonant frequency of the detection circuitry was 48 kHz. More sensitive measurements could be made at much lower time resolution with the ferrite core antenna of an AM-band radio. Both antennae couple to a changing B field, which in this case is a *near-field* electromagnetic "emission" because of the close proximity of the antenna to the source. Simultaneous bursts of visible photons *coincident* with the observed RE bursts reinforces the interpretation that these signals are caused by microdischarges.

The CEM and PMT were mounted approximately 1 cm on either side of the sample. The detector outputs were amplified, discriminated, and pulse counted with a LeCroy multichannel analyzer. Load transducers, such as a Sensotec Model 31/1432-08, were used to measure the load accompanying deformation. The output of the load transducer was digitized and recorded concurrently with the CEM and PMT outputs. Counting/digitizing intervals were typically 1 ms/channel. For very fast time measurements of phE and/or EE, the detector outputs were coupled directly to LeCroy TR8828 digitizers and recorded at 5 ns intervals.

Results and Discussion

Short Fixtures in "5-Minute" Epoxy.

As a follow-up of the results shown in Fig. 1, we examined a number of stainless steel fixtures embedded in bulk epoxy. Microscopic examination of stressed samples showed that for the pin, the "head"of the pin was debonding first from the matrix. Using a 1/2 in steel box nail which has a large flat head, one could readily observe optically the initial debonding from the flat face by means of interference fringes.

The resulting (a) phE, (b) EE, and (c) applied force near the time of failure are shown in Fig. 3. Although the details of the internal failure are not observable, no drop in load is observed prior to the onset of significant phE activity. The phE starts with an abrupt jump in intensity, believed to be due to the tensile debonding of the head. The drop in the load (labeled "pullout"

marks final failure, where the nail was pulled out of the epoxy accompanied by some cohesive failure. The resulting fracture produces exposed surfaces capable of releasing electrons, thus yielding the observed EE burst, coincident with an intense phE burst. The decaying phE and EE following failure originates from the epoxy matrix; the loading arrangement was such that the nail was removed immediately from the vicinity of the detectors after failure.

We next examined the pullout of a smooth cylindrical rod to eliminate the complications of the "head" of the nail. Figure 4 shows the phE, EE, and load accompanying the failure of a 2.5 mm diameter rod embedded 4 mm into a 5-Minute epoxy matrix. This particular failure event was somewhat unusual in that the load showed a small drop nearly in coincidence with the first appearance of phE (in the time interval marked A-B). We believe that this first burst of phE is due to the debonding of the embedded rod tip and that the rise in emission after the time marked C is due to debonding along the edges of the rod. At time D, debonding is complete and the rod is rapidly pulled out, yielding *both* phE and EE. The phE between times B and C is significantly above background while the force is fairly constant, suggesting that portions of the interface are failing during this time, with other portions hanging on until D.

A sample similar to that used in Fig. 4 was prepared with mold release applied to the flat end of the rod to minimize metal-epoxy adhesion in this region. The resulting phE and EE is shown in Fig. 5. Note that the load shows no downward deviation until pullout. Most importantly, the phE shows no characteristic burst at the onset of phE activity, consistent with the interpretation that the initial phE bursts seen in Figs. 1, 3, and 4 are indeed due to "tip" or "head" debonding (The level count rate prior to B in Fig. 5(b) is due to an abnormally high noise level).

The effect of debonding at the tip of the rod can also be minimized by employing rods with small diameters. Figure 6 shows the results of phE, EE and load measurements with a rod 0.25 mm in diameter embedded into the epoxy a distance of 5 mm. The resulting phE shows no characteristic burst at the onset of phE activity. No indication of a load drop is observed until pullout. However, a small EE signal does accompany the strong phE signal in the time interval between B and C. This indicates the presence of fracture activity at the top surface of the epoxy,

90

presumably associated with the region where the rod leaves the epoxy. Pullout occurs at C, and strong burst of EE from the epoxy is again observed.

To test the sensitivity of EE to fracture activity at the exposed epoxy surface, we loaded a embedded rod (2.5 mm diameter) in torsion. In torsion, interfacial failure is expected to begin at or near the exposed epoxy surface and quickly force a crack to the exposed surface. Figure 7 shows the resulting phE and EE signals. Just prior to the first drop in torsional load in the time interval A-B, the phE signal builds up and a slight indication of EE is observed. At B, the torsional load drops slightly over a few ms, indicating interfacial failure along a significant portion of the length of the rod. Accompanying EE is observed. At C, after a large burst of EE, the load begins to rise slowly while the phE is sustained. Finally, the remaining interface fails. No burst of EE is observed at this point, because the remaining interface is not exposed to the vacuum--the metal rod still plugs the hole. Therefore the EE signal appears to be quite sensitive in discriminating between surface damage exposed to vacuum and embedded interfacial failure. We conclude the initial failure of the short metal fixtures (rods/pins/nails) loaded in tension (Fig. 1, 3-6) takes place *below* the surface prior to any activity at the free surface.

Long Rods in Ciba-Geigy Epoxy.

To more carefully determine the sequence of failure events accompanying rod pull out we increased the size of the sample. The diameter of the polished stainless steel rod was increased to 5 mm and the length of the rod embedded into the epoxy was increased to 50 mm. The ratio of dimensions more closely models fibers embedded in brittle matrices. In our case, the principal limitation on the size of the samples was the load required to initiate fracture. The load at failure of these samples was typically 5000 N, approaching the capacity of the loading apparatus used in these experiments.

The phE and EE accompanying an initial debonding event is shown on a slow time scale in Fig. 8. Logarithmic scales are used for the phE and EE scales to accommodate their large dynamic range. On this relatively slow time scale intense phE and EE bursts appear in coincidence with

fracture. Although the rod remains nominally inside the epoxy, we note that a strong EE signal is still observed that is sustained for several seconds. Observation of the specimen after failure shows that ~4 mm of the debonded rod has been pulled out of the epoxy and the interfacial crack extends completely out to the free surface. Thus electrons can escape the top of the exposed interface crack and reach the electron detector.

Tests of planar surfaces of stainless steel and epoxy showed that the post-separation emission was all coming from the epoxy surfaces. Thus, the tails in both the phE and EE indicate that the epoxy surfaces are still "active" in terms of electronic excitations for several seconds after the debond. The nonlinearity of these decays on the semilogarithmic plot of Fig. 8 indicates that the phE decay is not "first order." This is characteristic of phE signals following adhesive failure of a number of composite systems[12] and is due to the kinetics of recombination of mobile charge and recombination centers (e.g., mobile electrons and + ion sites). The energy available from the recombination can either result in photon *or* electron emission. Although the kinetics of the phE and EE decays look different in Fig. 8, the phE descends into the background noise after only a few seconds, masking the long tail.

The sequence of events during and following the onset of the debond can be examined much more closely by using fast transient digitizers with a common trigger pulse, capturing several signals simultaneously. To more precisely indicate the onset of fracture and pullout, a resistive strain gauge was attached to the top of the rod (see Fig. 2). Tests utilizing brittle fracture showed that the minimum time response of the strain gauge electronics to a sub-microsecond drop in load was about 10 μs. RE (radio frequency emission) measurements which are sensitive to electrostatic activity (charge separation/microdischarges) were also made. Strong evidence for charge separation and microdischarges has been found during failure of a number of interfaces[13] and composite systems.[14] Prior to the tests presented here, intense RE was shown to accompany failure of the rod-epoxy system by using an AM broadcast band transistor radio; unfortunately, the time resolution of this circuit was not adequate for correlation with transient signals.

In Fig. 9 we show simultaneous measurements of strain in the metal rod, phE, EE, and RE. At the arrow marked (1), we see simultaneously a small drop in the strain indicating the onset of the debonding process, accompanied by small phE signals. A few μs later, between arrows (1) and (2), we see a few, fast bursts of EE and phE, with a small burst of RE. As was the case for the short metal fixtures described above, delayed EE indicates that interfacial failure has begun *beneath* the free surface, except now the time scales involved are much faster (μs vs ms) due to the much higher energy failure. Postmortem inspection of the sample showed a small "quarter-penny" crack normal to the free surface with one edge along the rod-epoxy interface; this may have been the first crack to reach the free surface. At arrow (2) the strain in the rod begins to drop rapidly, and all the other signals show very large amplitude bursts. The phE and EE signals show large clusters off-scale bursts throughout the remaining drop in the strain to arrow (3). During this time interval, debonding is completed along the bulk of the rod-epoxy interface. If displacement is stopped at this point, a portion of the rod is found to have been extracted from the matrix, typically 4 mm; i.e., at the instant of completion of the debond crack, the rod is released.

The strain actually shows oscillations following the debonding (compression--elongation) which damp out over several cycles. [Only ~2.5 cycles are shown in Fig. 9(a).] During these oscillations, rapid phE and EE (and to some extent RE) bursts can be seen, suggesting that the damped vibrational motion of the rod in the epoxy socket leads to additional emission both inside the sample and at the free surface. The frequency of these oscillations agree with the calculated translational mode of vibration of the rod.

Comparisons of the onset of phE vs the onset of EE were made for several samples. Over 80% of the time, the phE preceded the EE with an average delay time of 120 μs. Thus, most specimens appear to have a debond crack originating *beneath* the free surface. In many cases, the onset of EE coincided with the onset of rod pullout and in all cases, pullout was accompanied by intense EE and phE.

The direction and approximate velocity of interfacial crack growth along the rod can be established using two PMT's viewing different regions of the rod, as shown schematically in Fig.

2. Light shields were attached to the outer epoxy cylinder to limited the field of view of each PMT: PMT A was arranged to favor the detection of photons produced near the top (free surface) and PMT B (which has a much smaller photocathode) was positioned to favor the detection of photons produced near the tip (bottom) of the rod. In Fig. 10, we see that the leading edge of the signal from PMT A precedes that from PMT B by 102 μs. This confirms that interfacial crack growth starts originates at or near the top (free surface) of the sample and propagates *towards* the embedded tip. The time interval between signals corresponds to an average crack speed of about 500 m/s, which is a reasonable interfacial crack velocity in this system. Contrary to the results for short rods in 5-Minute epoxy, no photon emission corresponding to a tip debond event preceding the fracture along the sides of the rod was seen in the long rod experiments.

In addition to the two PMT's, we added a CEM positioned near the epoxy-surface region as shown in Fig. 2. The resulting signals are shown in Fig. 11. The arrows indicate the onset of significant emission for each of the three detectors. The onset of the signal from PMT A proceeds that of PMT B by ~68 μs, indicate crack motion from near the free end (top) of the rod towards the embedded end. This corresponds to an average crack velocity of ~700 m/s. The leading edge of the large burst in the signal from PMT A (actually off scale several times) coincides with the onset of emission from PMT B and with the drop in load accompanying rod pullout, as discussed above. The the onset of EE is delayed from the leading edge of the signal from PMT A by 150 μs. With the onset of EE, the debonding fracture event is nearly complete, and a surface crack finally forms which allows EE detection. Again, no evidence of a tip debond event prior to the fracture along the sides of the rod is observed.

We therefore conclude that the normal sequence of events for the tensile loading of the long stainless steel rod embedded in epoxy is as follows:

- debond crack formation at the metal/epoxy interface near the top but *below* the free surface; (For the shorter rods discussed above, failure initiated at the embedded tip.)

94

- crack propagation along the metal/epoxy interface towards the embedded tip of the metal rod; (Tip debond occurs only after the debonding crack has run down the sides of the rod.)

- arrival of the debonding crack at the free surface (and therefore electron emission), followed by rapid rod pullout. The duration of the initial pullout motion is typically ~50 μs.

Our conclusion that debond crack nucleation occurs below the surface is contrary to the fracture mechanics analyses of Atkinson et al.[9] and by Karbhari and Wilkins,[15] where the nature of the maximum in shear stress at the point where the fiber enters the matrix is discussed. Our results may be a result of sample geometry and/or inhomogeneous residual stresses within the epoxy due to thermal mismatches during the cure/cooling cycle.

Stick-Slip.

After the debond crack is complete, the applied load drops to zero. Continued loading to about 400 N typically results in further rod pullout via stick-slip. The behavior is quite similar to the pullout of debonded Cu rods from epoxy reported by Cook et. al.[17] Two typical load vs elongation curves for stainless steel rods embedded in epoxy *after debonding* are shown in Fig. 12. The sample of Fig. 12(a) displayed the stick-slip behavior at a relatively low load, while the sample of Fig. 12(b) displayed this behavior at a relatively high load. In the stick slip region, the rod "sticks" to the matrix until the load on the rod reaches a critical value, at which point the rod suddenly slips to a new position, where it is "grabbed", thereby sticking again. The load does not go to zero, and the oscillations tend to be quasi-periodic. Note that the pattern of stick-slip cycles (particularly Fig. 12(b) appears "chaotic".

Eventually, the pullout exhibits a frictional force nearly proportional to the embedded length and therefore decreases linearly with pullout. From the slope of the stress strain curve in this region, we can calculate the effective shear strength of the interface; i.e.:

$$\tau = \frac{\frac{dP}{dL}}{2\pi R} \qquad (1)$$

where P is the applied load, L is the length of the embedded epoxy, and R is the radius of the rod. This effective shear strength of the debonded interface varied considerably, from 0.4–4 MPa. The average embedded length over which linear slip was observed was ~16 mm. Like Cook et al.,[10] we observe that the frequency and amplitude of the load oscillations depend dramatically on the strain rate, which suggests that the frictional forces are v-dependent (as opposed to Coulombic friction).[16] It should be noted that in our samples the areas under the stress-strain curves during pullout are actually equal to or larger than the areas prior to the debonding event, so that for at least this ideal system, pull-out can contribute significantly to the total energy of failure.

Figure 13 showed the applied force, phE, and EE vs time, acquired simultaneously on a slow time scale during stick-slip. The particle signals were acquired by pulse counting. The average pullout distance for a single stick-slip event was about 150 μm. On this time scale, the phE and EE bursts appear in coincidence with the drop in load, i.e. when the rod *slips*.

To establish the correlation between fracto-emission and the stick-slip motion on a much faster time scale, phE and RE were digitized at 5 ns intervals. Figure 14 shows simultaneous phE and RE measurements during a single stick-slip event. The digitizer was triggered by the load drop corresponding to slip; the onset of the load drop is indicated by the arrows in Fig. 14(a) and 14(b). Note that the phE actually starts before the onset of the load drop, indicating that there is interfacial activity prior to catastrophic release of the rod. Seldom was any RE seen accompanying the onset of slip.

In this particular stick-slip event, a large (off-scale) photon burst was observed in coincidence with a RE burst near the end of the traces shown in Figs. 14(a) and (b). We show these events on expanded time scales in Figs.14(c) and (d), illustrating the alignment of the onset of the two signals. [The RE ringing is the response of LCR circuit to an impulse in **B** field]. Analyzing a large number of phE/RE records from stick-slip events, two emission patterns were observed. One pattern consisted of isolated single photons (no RE) with an onset slightly before

96

the load drop and continuing a few milliseconds afterwards. The other pattern was that of Fig. 14, which includes 1-2 intense phE and RE bursts in coincidence . The latter pattern, with large phE and RE bursts, occurred in ~15% of the slip-events. These large bursts were delayed from the load drop by anywhere from several μs to several ms, with a "most probable" delay of 100 μs. Every time we observed an RE signal, a large, intense phE burst was observed in coincidence. This coincidence indicates that these large bursts are produced by microdischarges between the metal and epoxy surfaces due to highly charged surfaces, probably generated during the slip process. The relative motion of the epoxy and metal surfaces during the slip portion of the cycle follows local adhesive failure where interfacial contact has been established. The interplay between highly charged surfaces and the gases that are emitted subsequent to failure therefore frequently results in electrical breakdown.

Stick-slip motion involving solid on solid normally is associated with local instabilities in contact between surfaces, where "stick" is a consequence of static frictional forces being larger than during sliding. Ohara[13] attributed stick-slip motion to surface deformation at points of frictional contact; using optical interferometry, he found that stick-slip motion along a glass-polymer interface was accompanied by the collective deformation of a multitude of semi-macroscopic contact regions. Schematically, one might envision these contact regions to involve asperities, as shown in Fig. 15(a). As the rod is displaced, asperities on the epoxy surface deform, resisting the rod displacement and exerting this resistance via static friction. Locally, microscopic slip between the two surfaces eventually results, causing rapid variations (jittering) in the increasing shear stress as shown schematically in Fig. 15(b). Finally, a series of asperities slip, leading to a catastrophic "lunge" of the rod. Repositioning and new alignment of asperities on both the metal and epoxy surfaces results in the recapture of the moving rod before zero stress is reached and the cycle begins again. It is the during the lunge that rapid detachment and high velocity "rubbing" between regions of the surface occur , resulting in local charge separation and excitation of the polymer surface, which in turn yields phE. When the conditions for

microdischarges are met (sufficient charge density and appropriate gaseous atmosphere), then discharges occur, producing intense, phE and RE bursts like those in Fig. 14.

Scanning electron microscopy (SEM) was used to compare epoxy surfaces which had not experienced stick slip with surfaces having experience extensive stick slip. The epoxy matrix was cut along the rod axis after failure to expose the rod-epoxy interface. The rod was removed (if necessary) and the epoxy surface gold coated for viewing. Fig. 16(a) shows a 60 μm^2 region of a surface which has not experienced stick slip. Although the surface was relatively smooth, a number of narrow striations aligned along the rod axis can be seen. Debonding was always followed by a small displacement of the rod (~4 mm), and any asperities in the rod surface would tend to scratch the epoxy. We therefore attribute these striations to surface scratches formed when the rod moved in its initial jump following debonding. Other surface features were often observed on the epoxy surface, presumably due to surface features of the rod surface molded into the epoxy. These larger surface features on the rod probably play an important role in the subsequent stick-slip activity.

In Fig. 16(b) is shown a 0.06 mm^2 region of an epoxy surface having experienced extensive stick-slip, i.e., the rod has been pulled all of the way out of the epoxy. Herringbone-like fracture patterns aligned with the rod axis occupy a good portion of the fracture surface. The surface also shows occasional deep gouges, and some evidence of particulate matter gouged from the epoxy surface. The herringbone structure appears to have been formed as an asperity on the rod surface dragged across the epoxy, which was alternately gripped and released by the epoxy matrix, causing fracture in the form of the V-shaped markings which make up the herringbone pattern. To ensure that the damage was not induced by edge effects or bending induced by misalignment in the loading apparatus, we also examined epoxy surfaces formed after partial rod pullout (about 25 mm of the 50 mm embedded length of the rod). Similar microcracks were observed along the entire length of the metal-epoxy interface, indicating that this phenomenon is definitely associated with stick-slip.

98

As mentioned previously, considerable energy is consumed during stick-slip motion (area under force-elongation plots of Fig. 12). The relatively high force required for pullout indicates considerable compression of the epoxy gripping the rod, such that the passage of asperities through the epoxy produces significant plastic deformation of the epoxy, as well as fracture, both dissipating significant energy. In many instances, enhanced matrix cracking during fiber pullout could be very beneficial in a composite. Additional amounts of energy are dissipated in the acoustic/thermal bursts which accompany each slip event, possibly associated with the deacceleration or "catching" part of the cycle when the rod motion is stopped. Our work on neutral particle emission (gases) released during cohesive failure of epoxies and other polymers would provide a useful tool for monitoring the growth of the microcracks during stick slip. These gases would have to leak out of the interface crack into the vacuum; if they are non-reactive species such as N_2, this would not be difficult and given the dimensions of the specimen would occur on time scales of $\sim 10^{-5}$ s.

Conclusion

We have shown that for a variety of geometries and two epoxies, we can detect photon emission generated at embedded metal/polymer interfaces undergoing adhesive failure, transmitted through the matrix to external detectors. These signals along with other time resolved measurements (e.g., strain in the metal, radiowave emission, and electron emission) provide details on the sequence of failure events such as the direction and speed of debonding crack propagation, the onset of pullout, and the arrival of cracks to the matrix surface. In addition, we observed readily detectable fracto-emission signals accompanying the subsequent pullout process, which accompanied repetitive stick-slip activity. It is of some significance that the time-sequence and the force law dictating the rate of energy dissipation during pullout are both highly unpredictable. Thus, modeling the bridging of cracks with fibers or the latter stages of failure of embedded fixtures in glassy materials must obviously be done carefully. Fracto-emission can provide details of the failure to help our understanding of both the debonding and pullout

processes. We note that all of our emission experiments involve non-contact detection of events so that the testing of fragile specimens (e.g., single fibers) or testing materials at high temperatures can be done routinely.

Useful future work will be to use these probes to examine the role of mixed mode and frictional stresses at the interface (discussed by Hutchinson and Jensen[19]) in crack propagation along that interface. Also, it is possible that this simple system might serve as a mechanical analog for fault motion in the earth; we point out that stick-slip plays an important role in fault dynamics and can lead to chaotic behavior in terms of spatial and frequency of slip in both nature and model systems.[10,11] Furthermore, during the time interval when the external force on the rod is increasing, the sequence of events leading up to the slip event appears to be an example of self-organized criticality,[10,20] wherein small failure events (localized slip) "mushroom" into catastrophic failure (massive slip). The photon emission prior to slip, shown in Fig. 14(a), may be a useful probe for examining on fast time scales these precursors to catastrophe in order to study in more detail the chain of events resulting in failure. As an example, it would be of interest to determine possible correlations between the duration and total intensity of these precursors and the magnitude of the drop in force at slip, analogous to the *magnitude* of the earthquake. It is obvious that as a "sentinel of failure" [Fig. 14(a)], 0.1 ms is a short time, although scaling to dimensions of the San Andres Fault would certainly result in significantly longer times.

Acknowledgments

We wish to thank Les Jensen, Kurt Zimmerman, and Brian Mielke for their assistance in this study and Robert Cook, IBM Yorktown for helpful discussions. This work was supported by the the Dow Chemical Co., the Ceramics and Electronics Materials Division of the National Science Foundation, DMR 8912179, the Office of Naval Research under Contract No. N00014-87-K-0514, and the Washington Technology Center.

100

References

1. J. T. Dickinson, M. K. Park, E. E. Donaldson, and L. C. Jensen, J. Vac. Sci. Technol. 20, 436 (1982).
2. J.T. Dickinson, L.C. Jensen, and A. Jahan-Latibari, J. Vac. Sci. Technol. A 2, 1112 (1984).
3. S. C. Langford and J. T. Dickinson, in *Spectroscopic Characterization of Minerals and Their Surfaces*, edited by L. M. Coyne, S. W. McKeever, and D. F. Blake, ACS Symposium Series Publication 415, pp. 224-244, (1990).
4. S. C. Langford, Ma Zhenyi, and J. T. Dickinson, J. Mater. Res. 4, 1272 (1989).
5. J. T. Dickinson, "Fracto-Emission from Adhesive Failure", to appear in *Adhesive Bonding*, edited by L. H. Lee, Plenum Press, New York.
6. A. S. Crasto, R. Corey, J. T. Dickinson, R. V. Subramanian, and Y. Eckstein, Composites Sci. Technol. 30, 35 (1987).
7. D. L. Doering, J.T. Dickinson, S. C. Langford, and P. Xiong-Skiba, J. Vac. Sci. Technol. A 8, 2401 (1990).
8. J. T. Dickinson, L. C. Jensen, and S. Bhattacharya J. Vac. Sci. Technol. A3, 1398 (1985).
9. C. Atkinson, J. Avila, E. Betz, and R.E. Smelser, J. Mech. Phys. Solids 30, 397 (1982).
10. J. M. Carlson and J. S. Langer, Phys. Rev. Lett. 62, 2632 (1989).
11. J. Huang and D. L. Turcotte, Nature 348 (234 (1990).
12. J. T. Dickinson and L. C. Jensen, J. Poly. Sci.: Poly. Phys. Edition 23, 873 (1985).
13. E. E. Donaldson, J. T. Dickinson, and X. A. Shen, "Time and Size Correlations of Photon and Radiowave Bursts from Peeling Pressure Sensitive Adhesives in Air," J. Adhesion 19, 267 (1986).

14. J. T. Dickinson, "Fracto-Emission", in *Non-Destructive Testing of Fibre-Reinforced Plastic Composites II,* J. Summerscales, ed. Elsevier Applied Science, London (1990), pp. 429-482.

15. V. M. Karbhari and D. J. Wilkins, Scripta Metallurgica and Materialia 24, 1197 (1990).

16. A. W. Adamson, *Physical Chemistry of Surfaces*, 5th Ed., John Wiley & Sons, New York (1990), pp. 464-465.

17. R. F. Cook, M. D. Thouless, D. R. Clarke, and M. C. Kroll, Scripta Metall. 23,1725 (1989).

18. K. Ohara, Wear 50, 333 (1978).

19. J. W. Hutchenson and H. M. Jensen, to be published.

20. P. Bak and K. Chen, Sci. Am 264(1) 46 (1991).

102

Figure Captions

Fig. 1. a) phE and b) EE acquired during a peel test of a Au-Si interface. The phE observed before failure of the interface under test is from the *internal* failure of the metal "pin" – epoxy interface.

Fig. 2. Experimental arrangement for the debonding and pullout tests. The length and diameter of the stainless steel rods were varied. Most of the tests were done with a single PMT positioned to view as much of the rod-epoxy interface as possible. Where noted, two PMTs were used, as shown here.

Fig. 3. (a) phE, (b) EE, and (c) applied force accompanying the pullout of a 0.5 in box-nail from a 5-Minute epoxy cylinder. Time of pullout (with some cohesive failure of the epoxy) is indicated by the dashed line.

Fig. 4. (a) EE, (b) phE, and (c) applied force accompanying the pullout of a short polished metal rod from 5-Minute epoxy. . Final pullout of the rod is indicated by the drop in the force at the time marked D.

Fig. 5. FE measurements during pullout of a stainless steel rod with mold release applied to the tip end, thus the the rod-epoxy adhesion at the tip end is very poor. "A" marks the onset of phE and "B" indicates the pullout event.

Fig. 6. FE during the pullout of a short, thin rod (wire). "A" marks the onset of phE. A small amount of EE precedes pullout in the time interval B-C.

Fig. 7. Simultaneous EE and phE from a short rod tested in torsion. This forced fracture to occur at the free surface.

Fig. 8. (a) phE and (b) EE accompanying interfacial failure of a long stainless steel rod in epoxy on a slow time scale.

Fig. 9. (a) strain gauge output, (b) phE, (c) EE, and (d) RE during and following debonding between a stainless steel rod and an epoxy matrix.

Fig. 10. Photon emission acquired on a fast time scale during the propagation of the debond interface crack between the stainless steel rod embedded in epoxy. (a) phE detected by PMT A located near the free surface; (b) phE detected by PMT B viewing the lower portion (tip region) of the metal rod.

Fig. 11. phE *and* EE accompanying interfacial failure of stainless steel rod in epoxy on a fast time scale. (a) phE detected by PMT A located near the free surface; (b) phE detected by PMT B viewing the lower portion (tip region) of the metal rod; and (c) EE.

Fig. 12. Load vs elongation during the frictional pullout of the stainless steel rod from the epoxy after the completion of debond fracture. (a) low load sample, (b) high load sample. Both exhibit extensive regions of stick slip behavior.

Fig. 13. (a) load, (b) phE and (c) EE during stick-slip motion of stainless steel rod pullout from epoxy matrix.

Fig. 14. (a) phE and (b) RE on a fast time scale. Expanded views of (a) and (b) appear in (c) and (d), respectively.

Fig. 15. Schematic of a stick-slip mechanism and the local shear stress vs deformation in the vicinity of an asperity.

Fig. 16. SEM micrographs of epoxy debonded surfaces (a) after the debond but any stick-slip pullout; (b) after stick-slip pullout of the stainless steel rod. Considerable fracture in the epoxy matrix is evident in (b) produced during repeated stick-slip events.

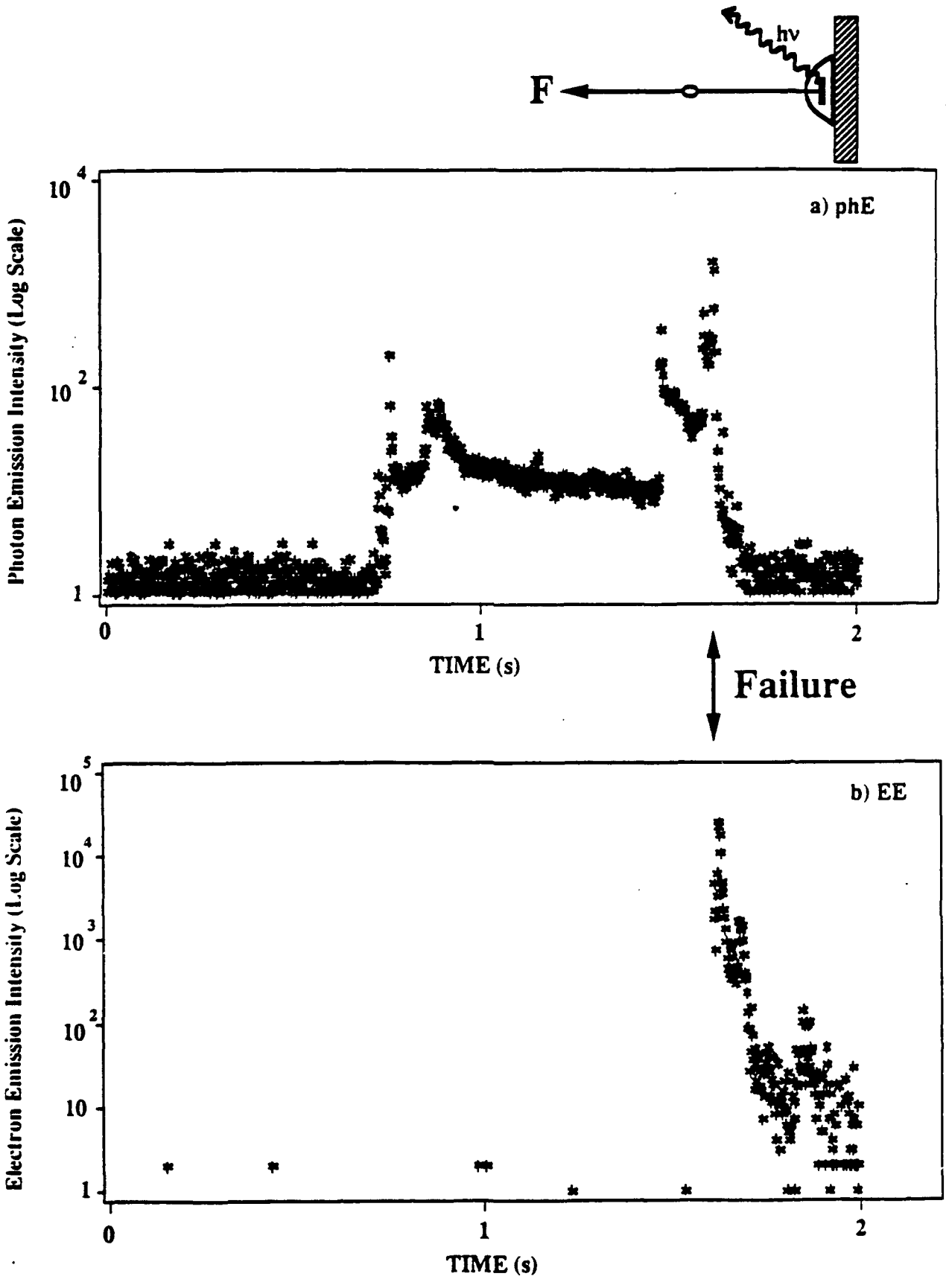
phE and EE During Adhesive Test (Strong Bond)
hν
F
a) phE
Photon Emission Intensity (Log Scale)
10 4
10 2
1
0
1
2
TIME (s)
Failure
b) EE
Electron Emission Intensity (Log Scale)
10 5
10 4
10 3
10 2
10
1
0
1
2
TIME (s)

Fig. 1

106

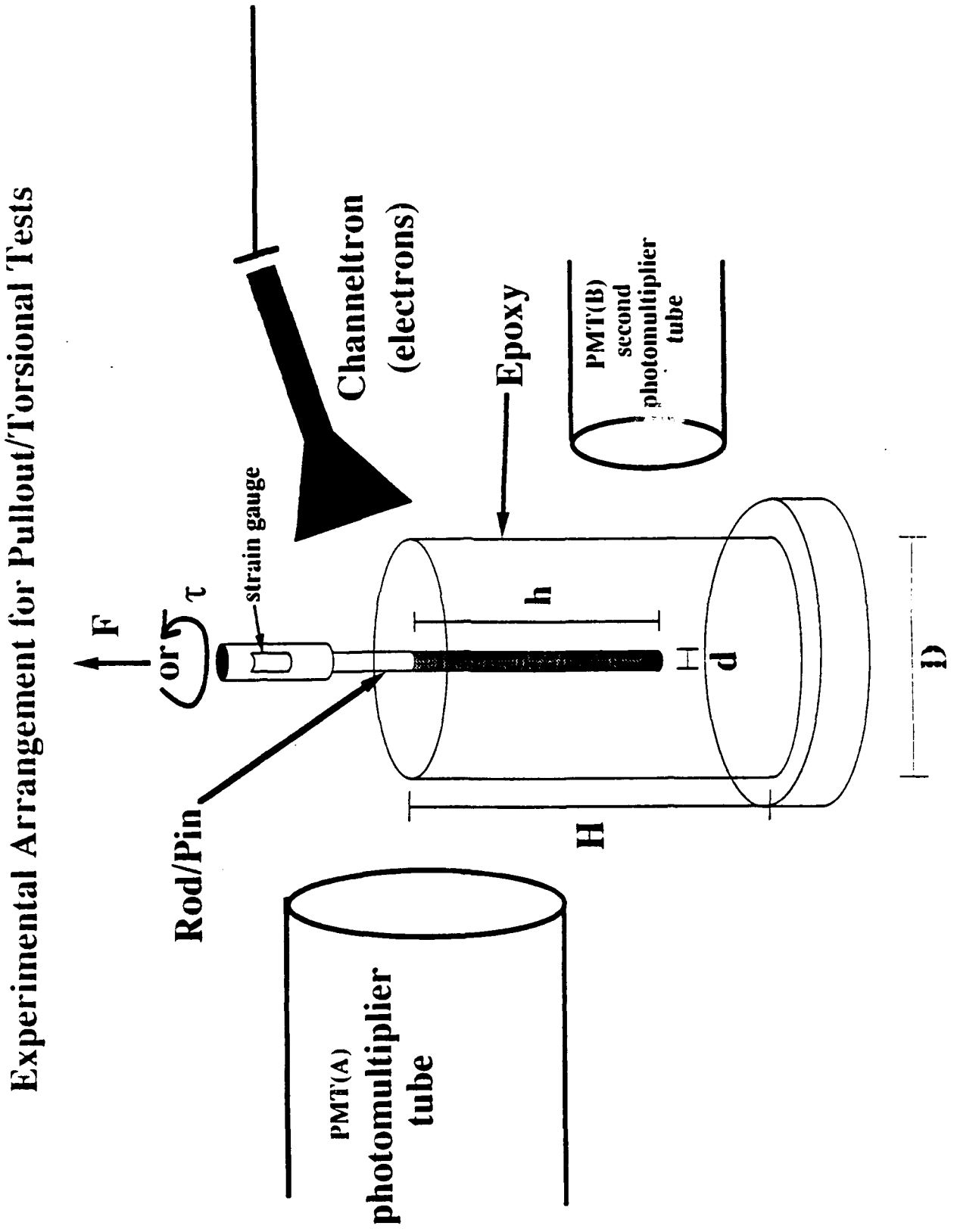
Experimental Arrangement for Pullout/Torsional Tests
F
or
τ
strain gauge
Channeltron
(electrons)
Epoxy
PMT(B)
second
photomultiplier
tube
h
H
d
D
Rod/Pin
PMT(A)
photomultiplier
tube

Fig. 2

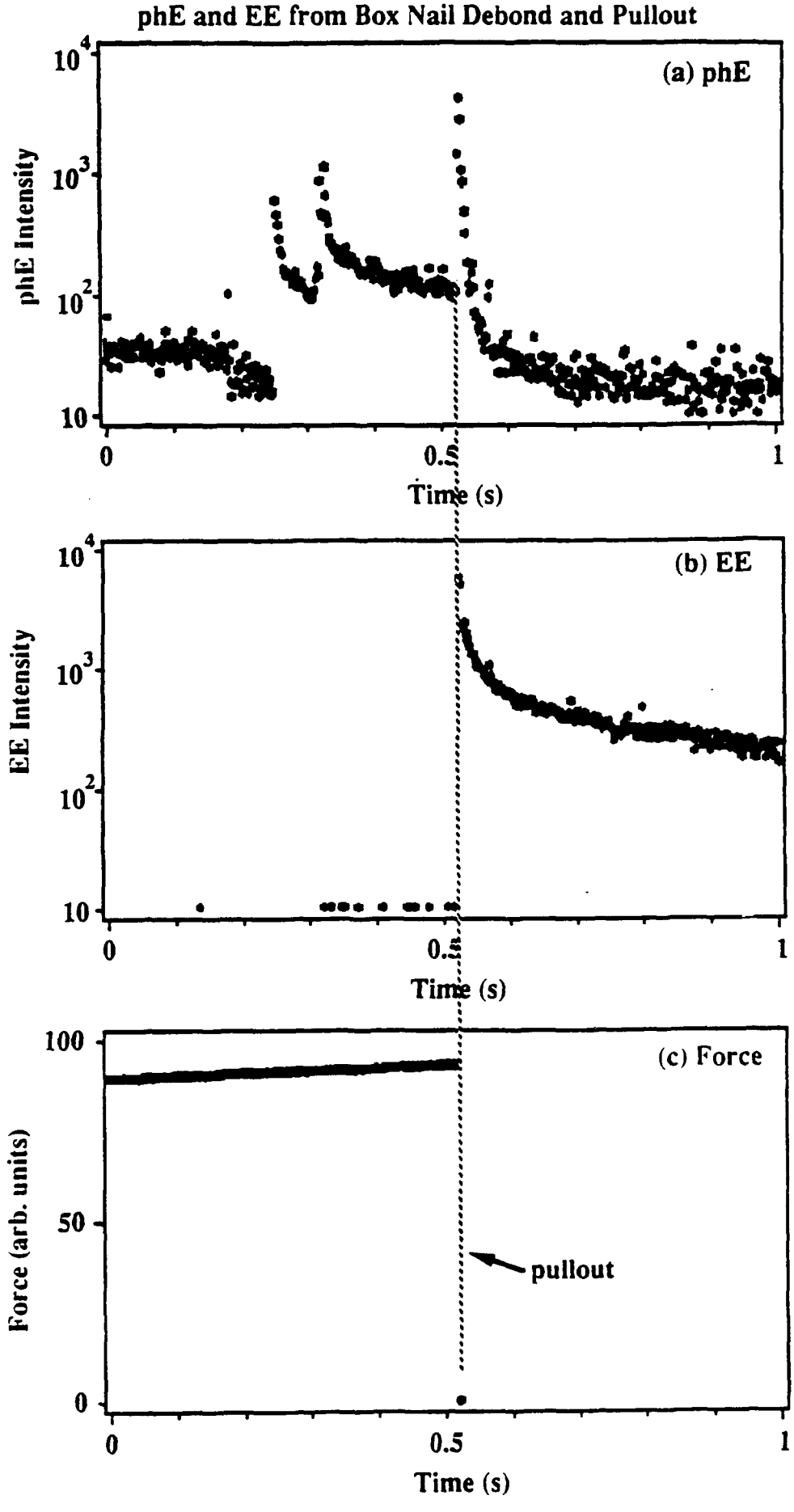
phE and EE from Box Nail Debond and Pullout
(a) phE
phE Intensity
10^4
10^3
10^2
10
0
0.5
1
Time (s)
(b) EE
EE Intensity
10^4
10^3
10^2
10
0
0.5
1
Time (s)
(c) Force
Force (arb. units)
100
50
0
pullout
0
0.5
1
Time (s)

Fig. 3

108

phE and EE During Tensile Loading of Metal Rod/Epoxy

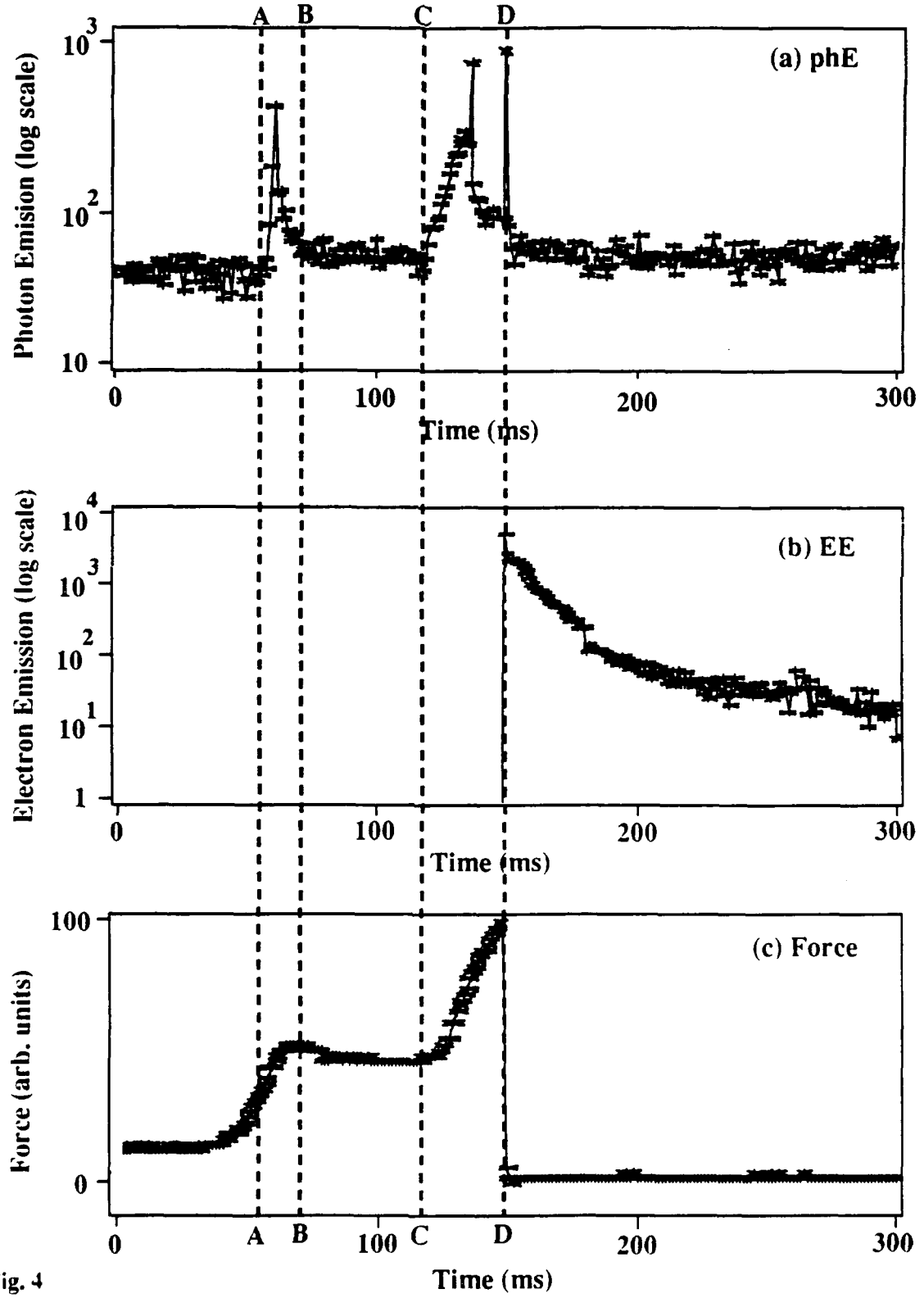

Fig. 4

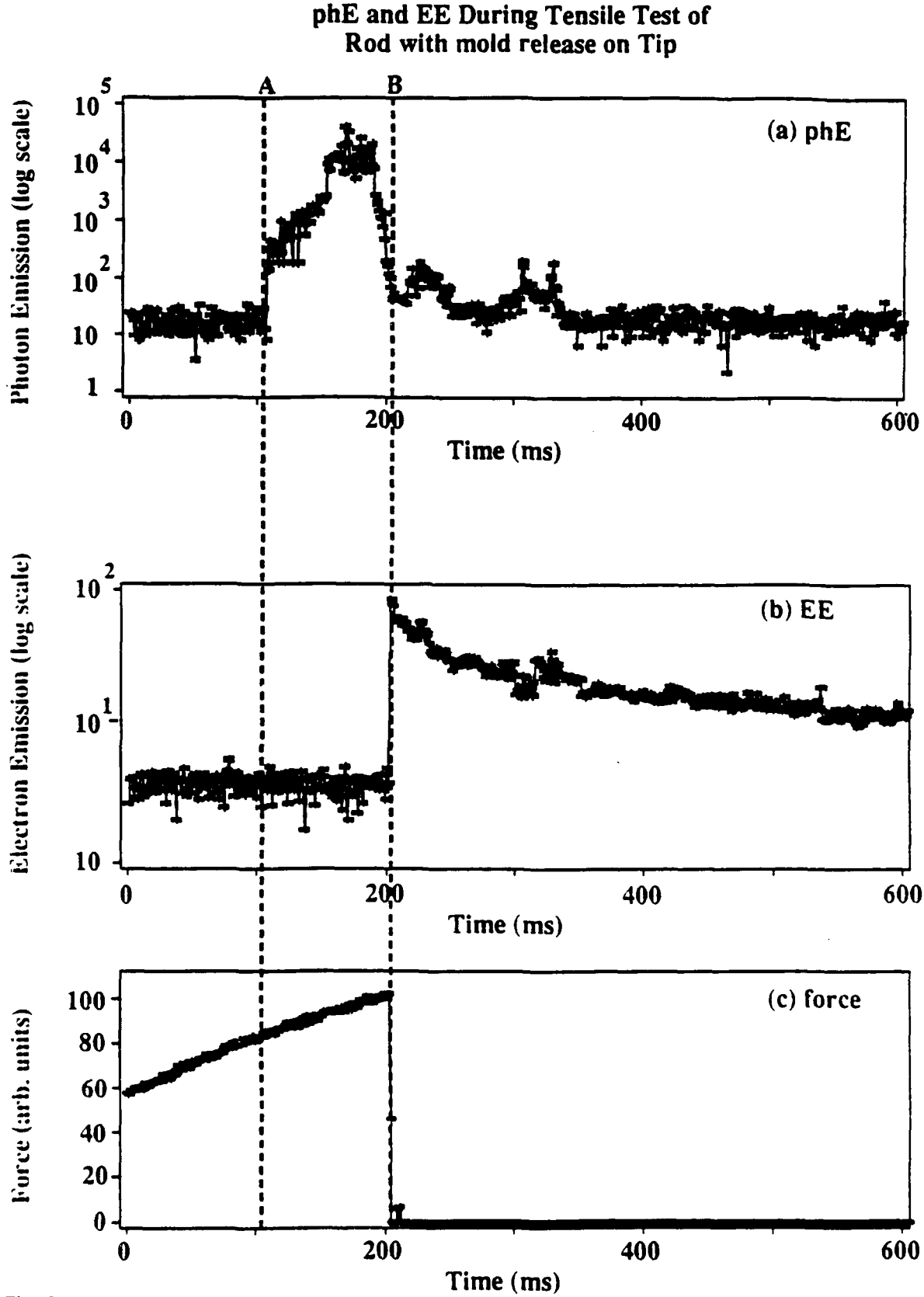
phE and EE During Tensile Test of
Rod with mold release on Tip
A
B
(a) phE
Photon Emission (log scale)
Time (ms)
(b) EE
Electron Emission (log scale)
Time (ms)
(c) force
Force (arb. units)
Time (ms)

Fig. 5

110

phE and EE During Tensile Loading of Metal/Epoxy (d = 0.25 mm h = 5 mm)

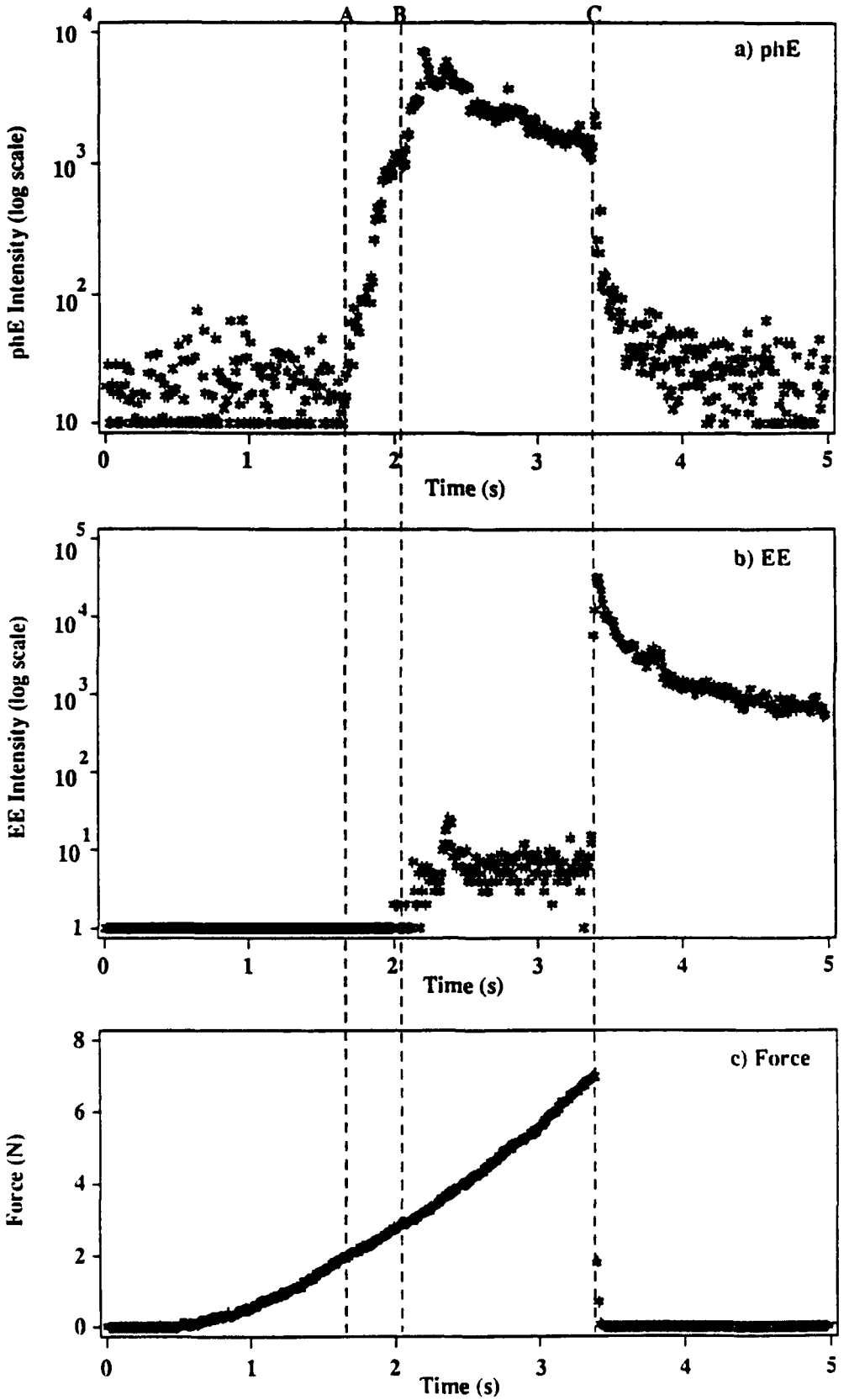

Fig. 6

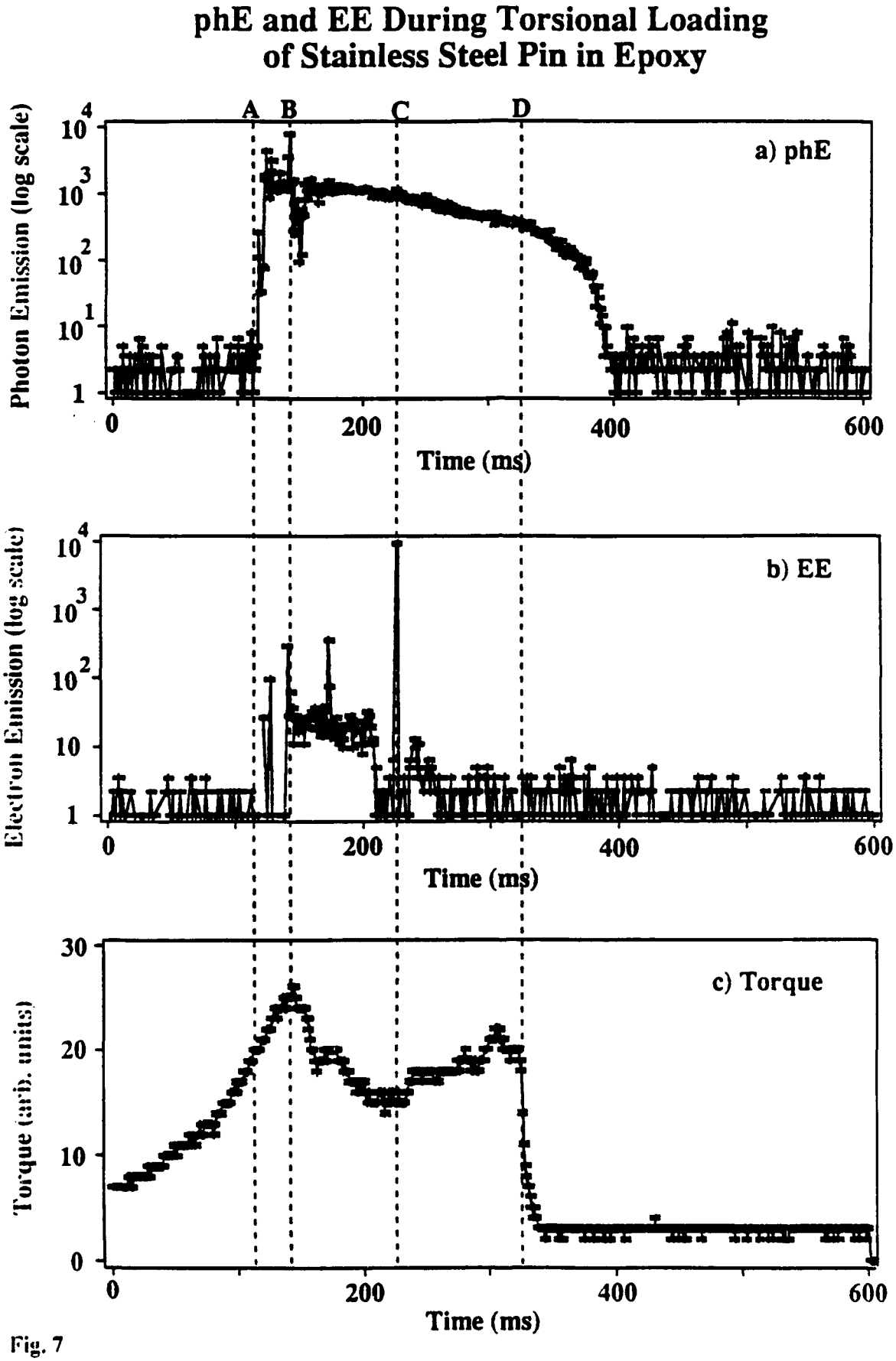
phE and EE During Torsional Loading
of Stainless Steel Pin in Epoxy
A
B
C
D
a) phE
Photon Emission (log scale)
Time (ms)
b) EE
Electron Emission (log scale)
Time (ms)
c) Torque
Torque (arb. units)
Time (ms)

Fig. 7

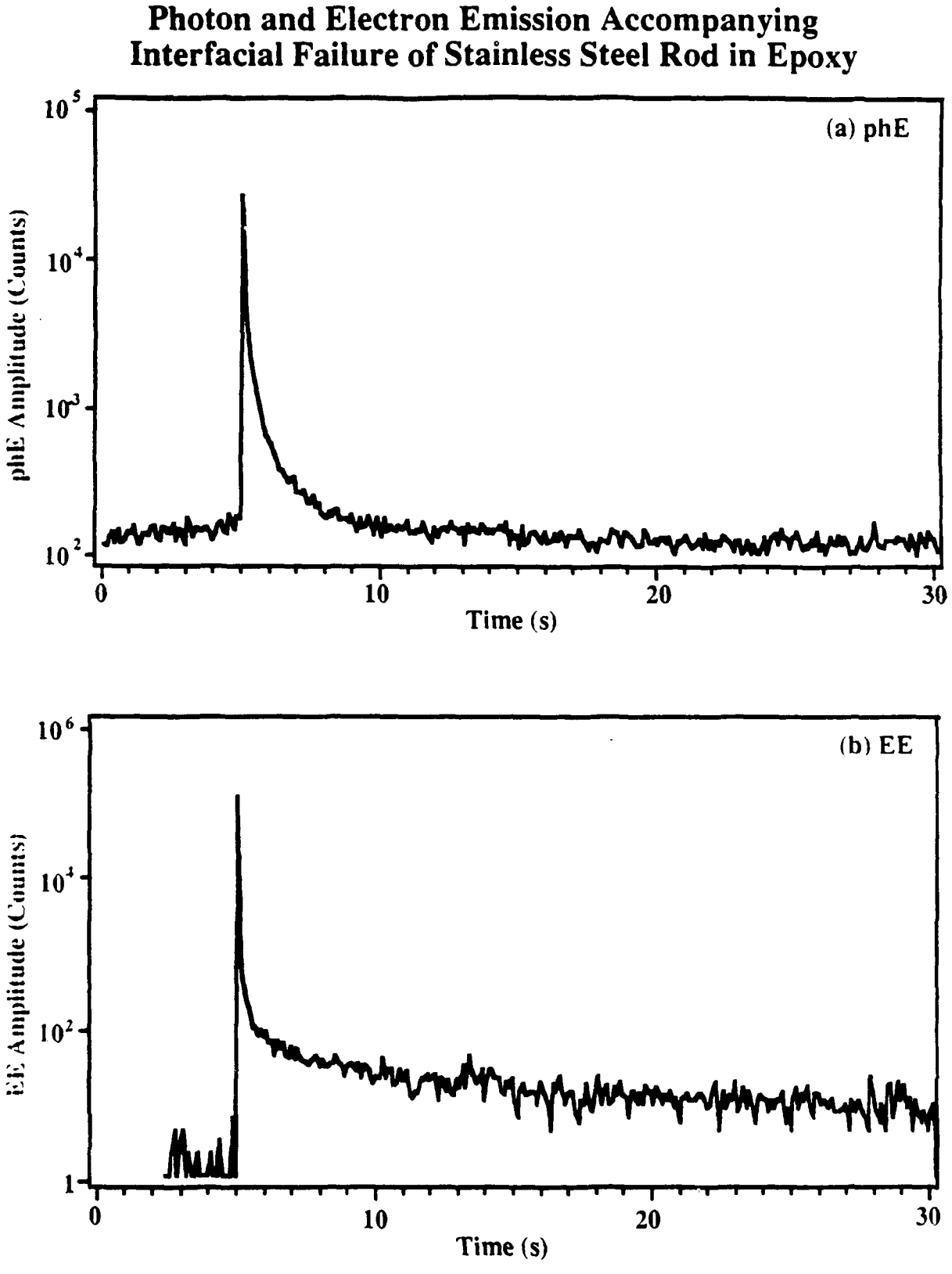
Photon and Electron Emission Accompanying
Interfacial Failure of Stainless Steel Rod in Epoxy
(a) phE
phE Amplitude (Counts)
10^5
10^4
10^3
10^2
0
10
20
30
Time (s)
(b) EE
EE Amplitude (Counts)
10^6
10^4
10^2
1
0
10
20
30
Time (s)

Fig. 8

Strain, phE, EE, and RE During Debonding and Pullout

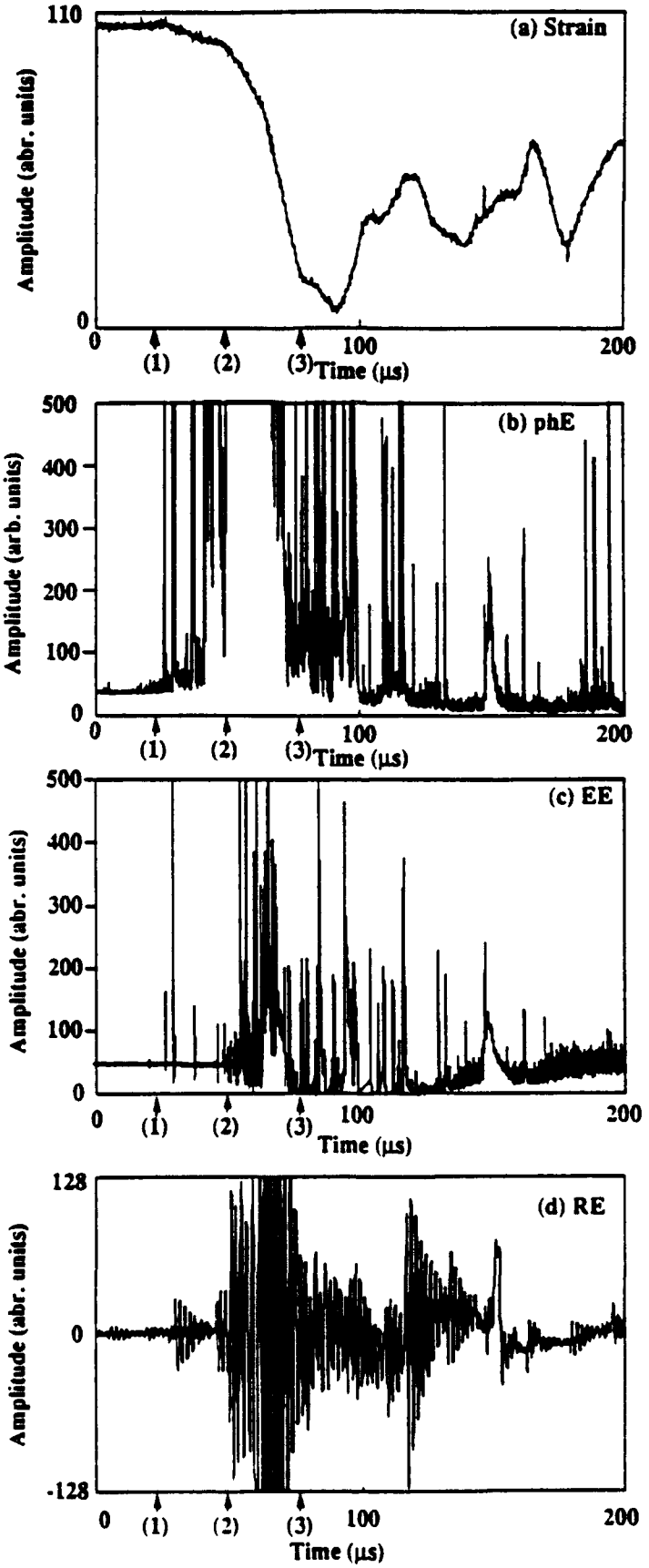

Fig. 9

114

Two PMT Measurement During Debonding

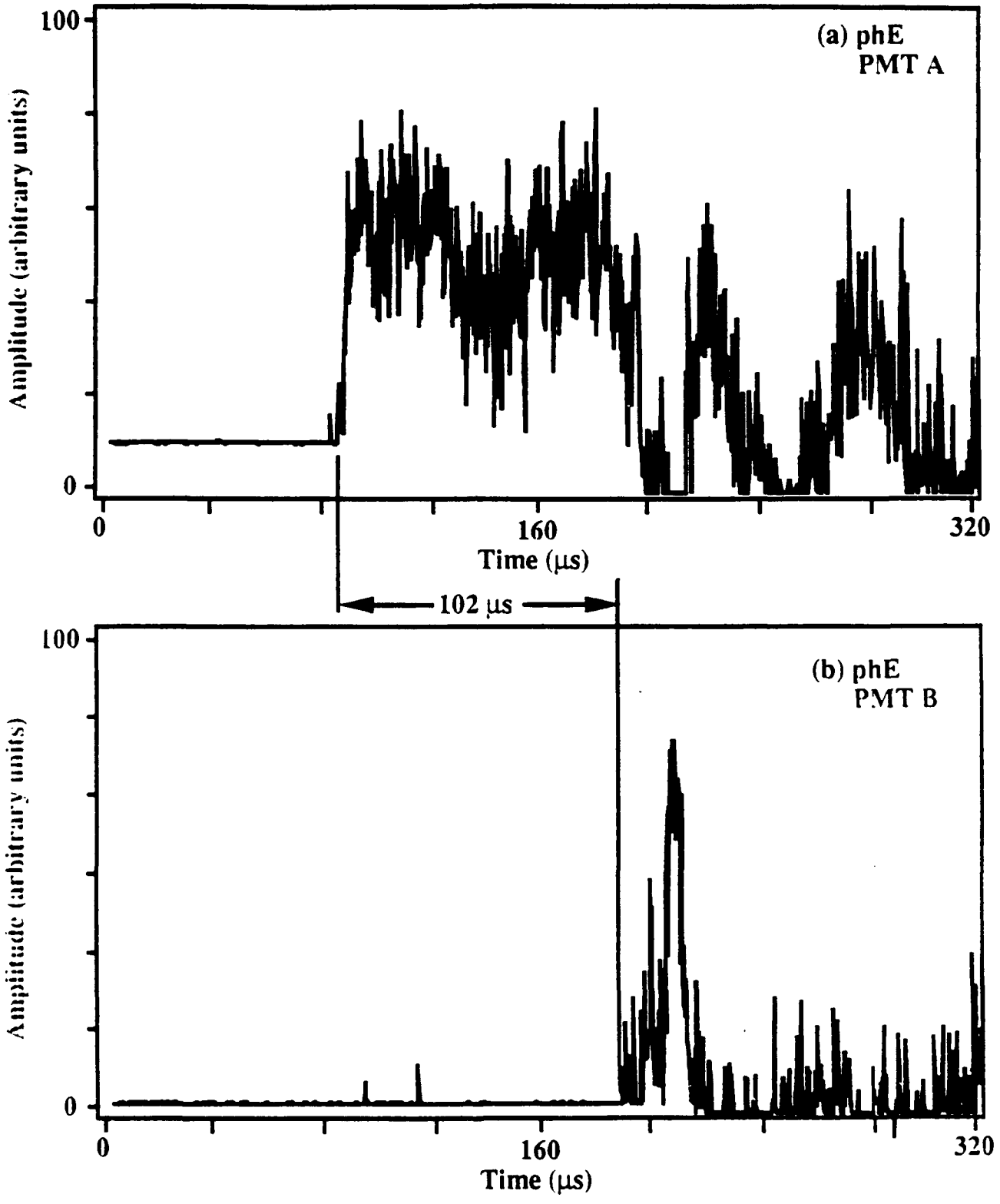

Fig. 10

Two PMT Measurement During Debonding -- With Electrons

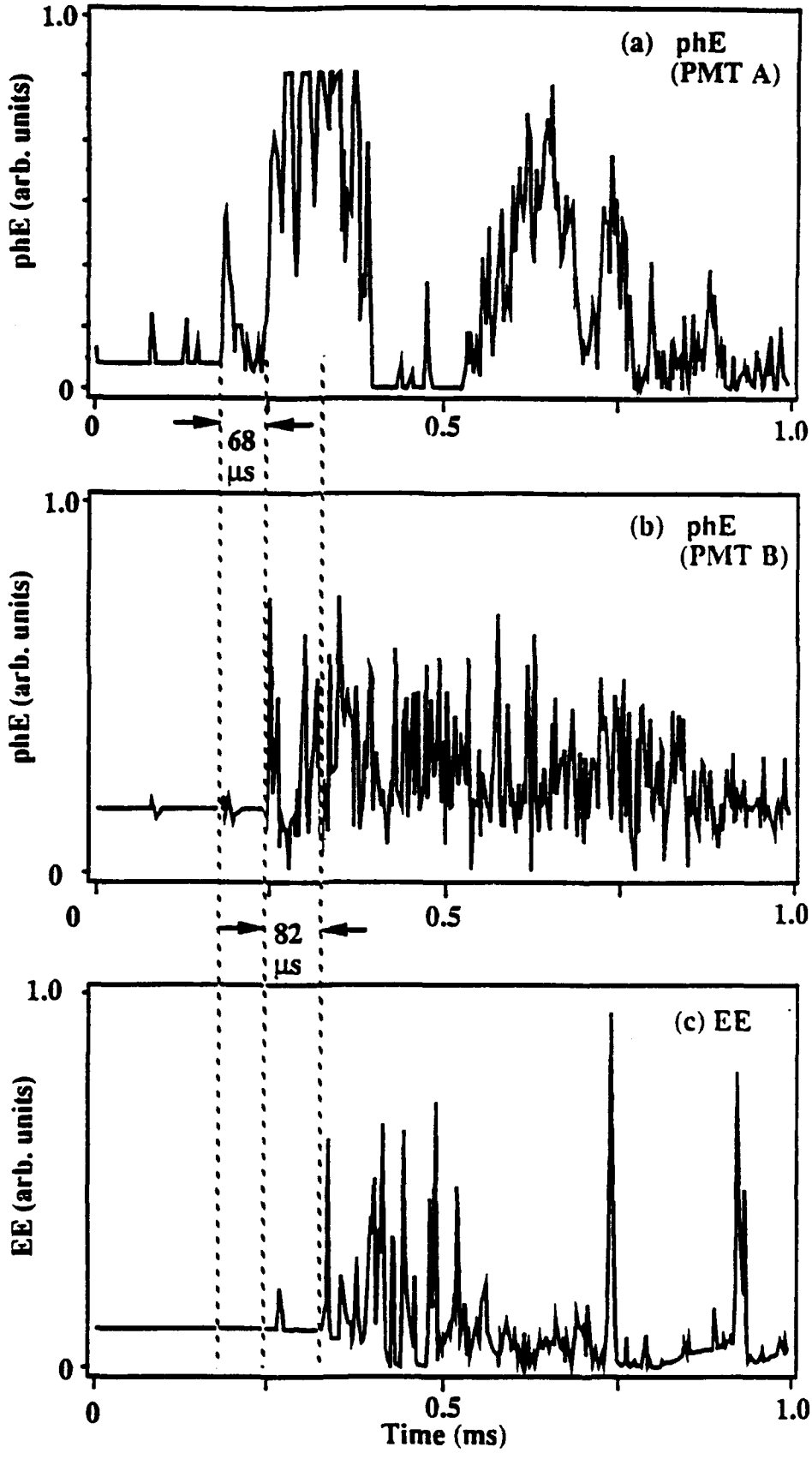

Fig. 11

116

Pullout vs Strain During Stick-Slip -- Stainless Steel Rod in Epoxy

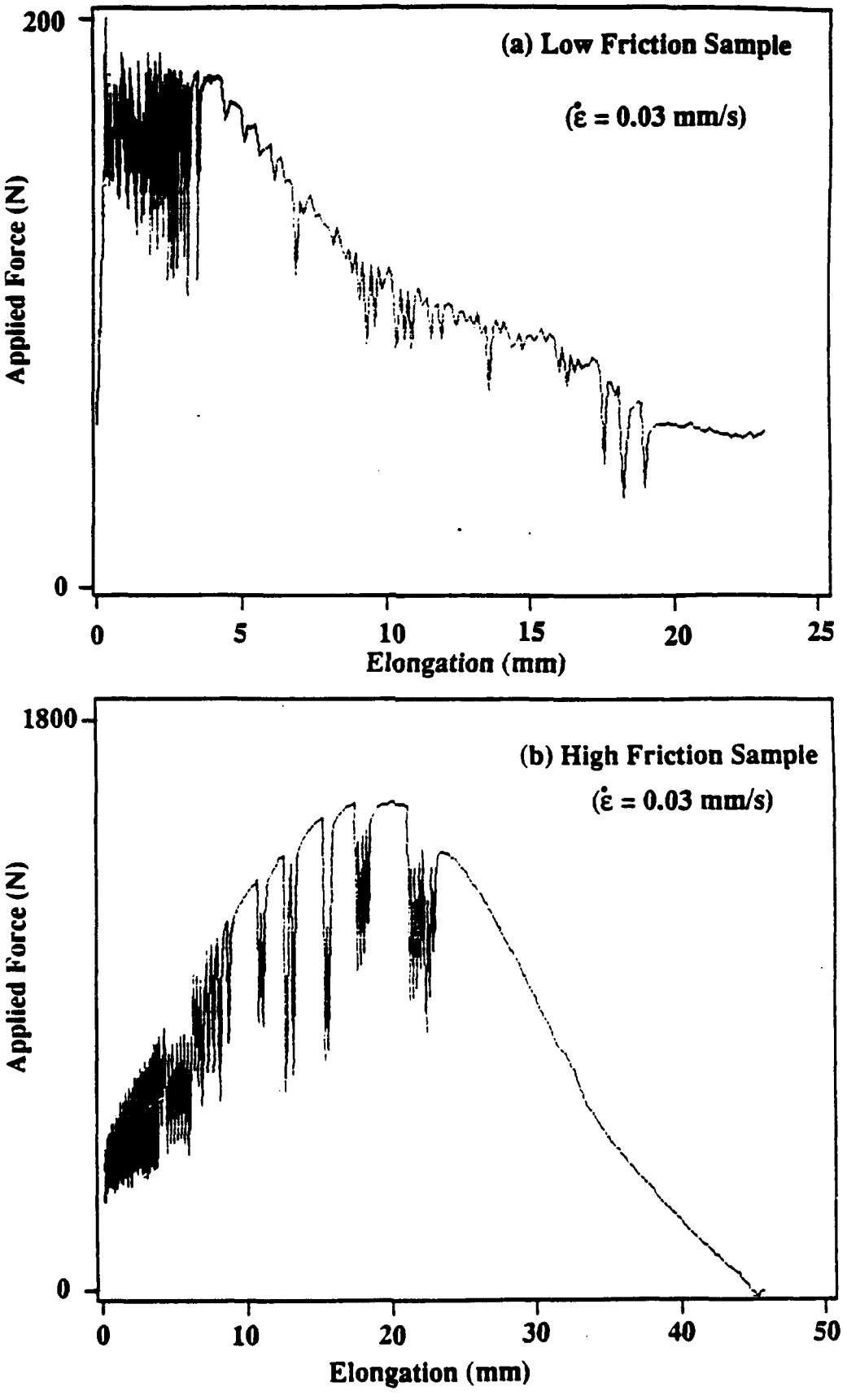

Fig. 12

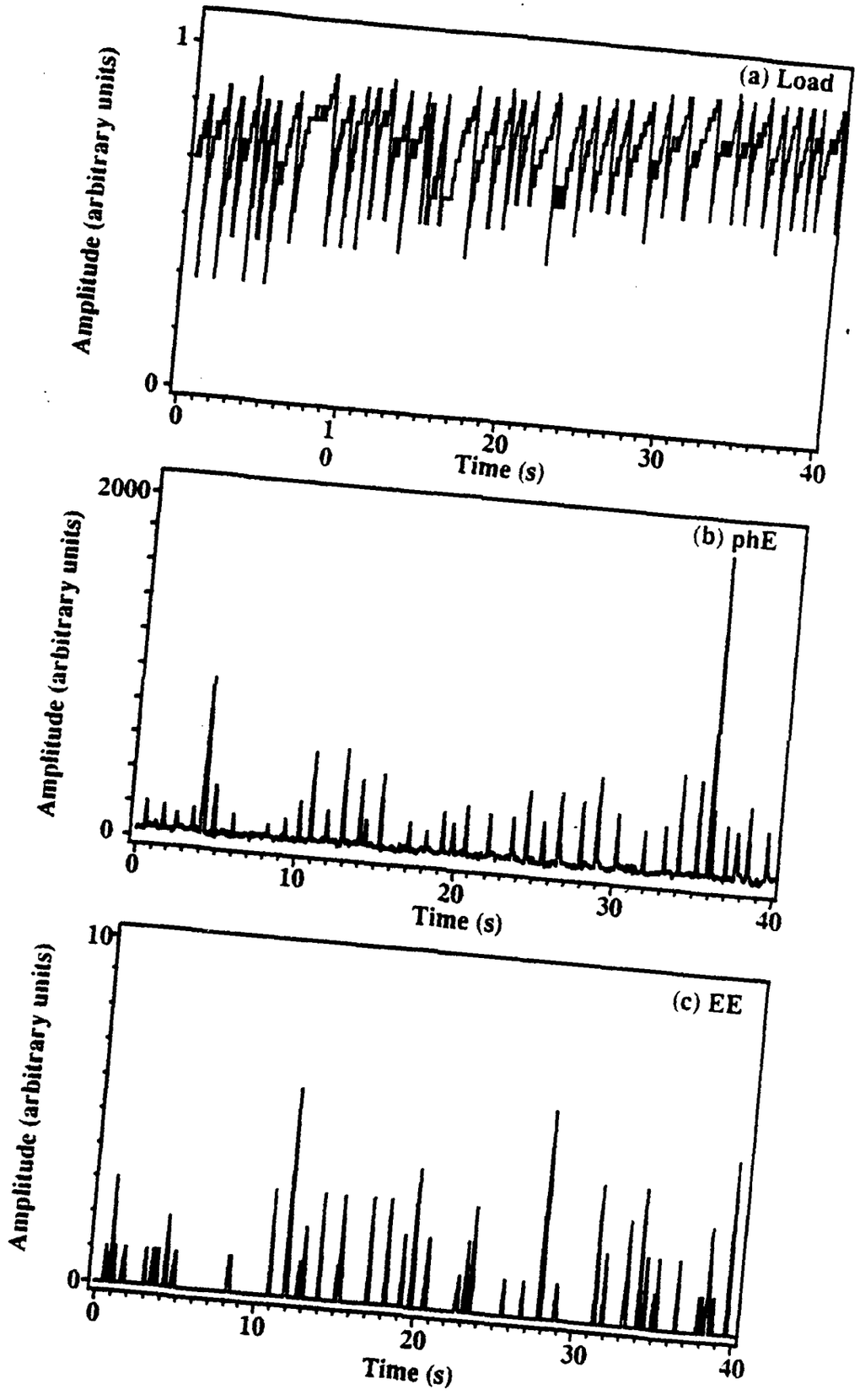
(a) Load
Amplitude (arbitrary units)
1
0
0
1
0
20
30
40
Time (s)
(b) phE
Amplitude (arbitrary units)
2000
0
0
10
20
30
40
Time (s)
(c) EE
Amplitude (arbitrary units)
10
0
0
10
20
30
40
Time (s)

Fig. 13

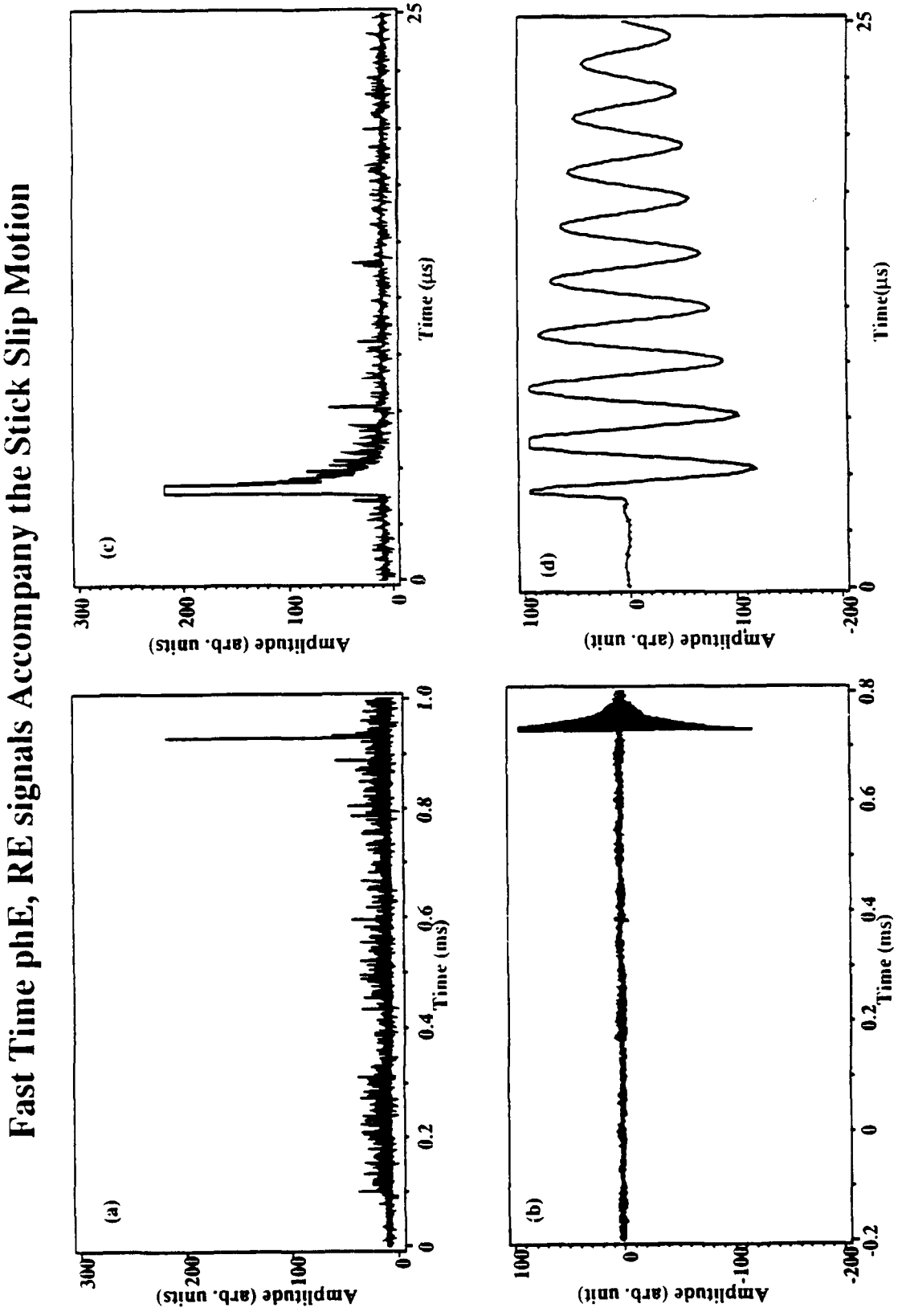
Fast Time phE, RE signals Accompany the Stick Slip Motion
(a)
(b)
(c)
(d)
Amplitude (arb. units)
Amplitude (arb. unit)
Time (ms)
Time (μs)

Fig. 14

Schematic of Stick-Slip

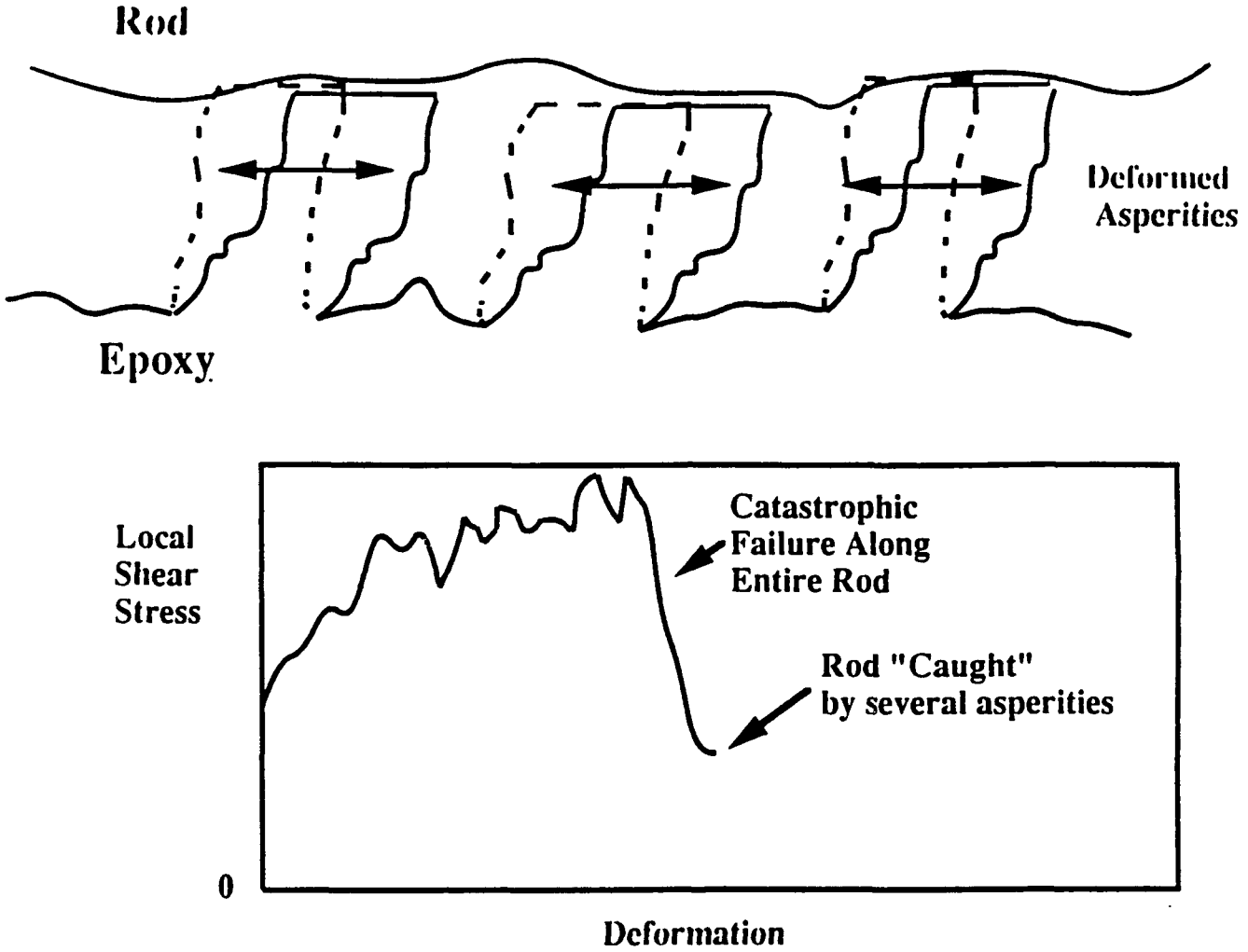

Fig. 15

SEM Photographs of Epoxy Surface Before and After Stick-Slip Pullout

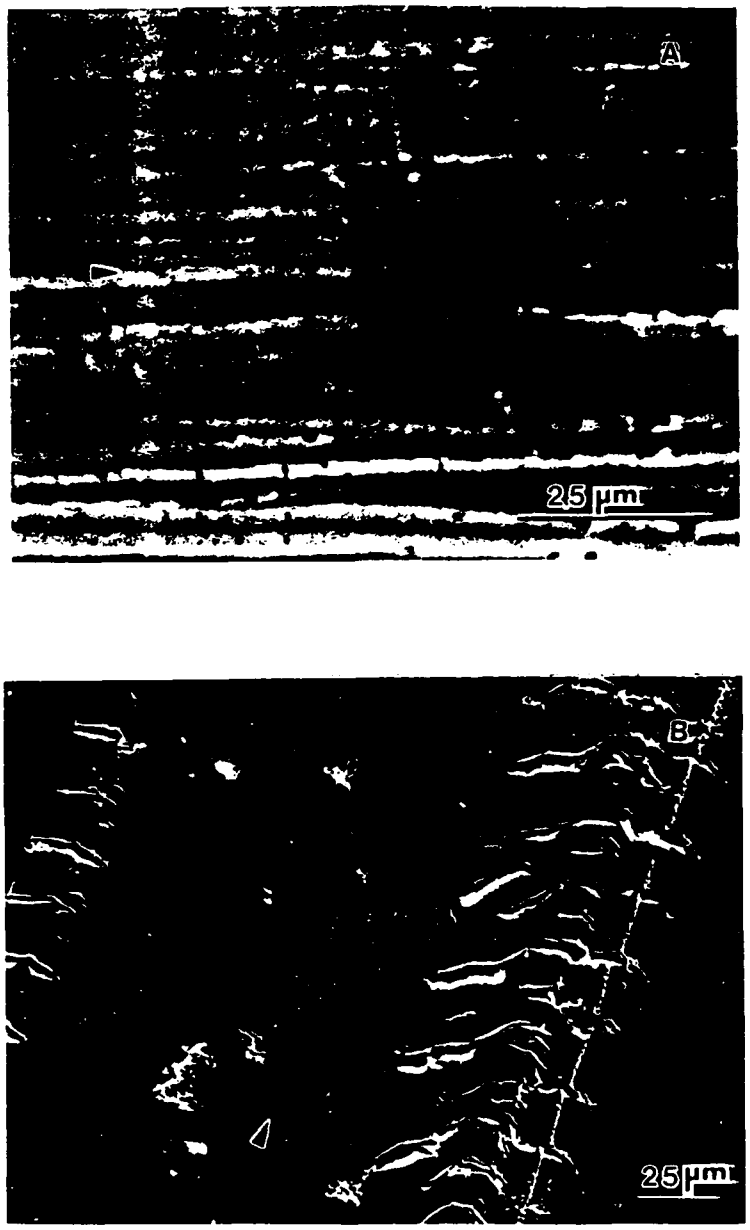

Fig. 16

IX. Electrical transients during interfacial debonding and pullout of a metal rod from an epoxy matrix

K. A. Zimmerman, S. C. Langford, and J. T. Dickinson

Department of Physics, Washington State University, Pullman, WA 99164-2814

Abstract

We examine electrical transients which are produced during the propagation of a debonding crack along the interface of an axially loaded stainless steel rod embedded in epoxy. Correlations with fracto-emission signals and tensile strain in the rod are made to assist interpretation. These experimental data provide time-resolved information on the sequence of events leading to interfacial fracture and initial pullout of the rod from the epoxy.

failure, the oscillating strain is accompanied by further phE, EE, and RE, indicating electrical activity accompanying the slip of the rod along the cavity in the epoxy matrix. The presence of RE and intense phE accompanying interfacial failure is especially significant in that these often mark the occurrence of electrical discharges.[3]

These fracto-emission signals accompanying the failure of a conductor-insulator interface suggest that significant electrical transients may be generated in the conducting phase. In this work, we examine these currents and interpret them in terms of contact charging between the two dissimilar materials followed by charge separation and redistribution of charge during interface formation and pullout. By comparing the resulting currents with fracto-emission signals and strain measurements, we may characterize the relationship between these currents and the sequence of events associated with interfacial failure at an embedded interface. We point out that the geometry we have chosen mimics the debond and pullout of crack bridging fibers in a brittle matrix composite. The methods we develop here may be applicable to studies of failure events in materials with conducting phases including cermets, metal reinforced dielectrics, carbon-dielectric, and carbon-carbon composites.

II. EXPERIMENT

Stainless steel rods 3.1 mm in diameter were polished and imbedded 50 mm into an epoxy matrix. The epoxy was Ciba Geigy Araldite 502, modified with dibutyl phthalate, and cured with Hardener HY956, an alkoxylated triethylene teramine. The resin and hardener were mixed and degassed in vacuum to remove bubbles. The mixture was then poured into silicone rubber molds into which the rods were subsequently inserted. The epoxy was cured at 100 °C for three hours and slowly cooled overnight, producing a clear matrix. Any sample showing a debonded region at the metal/epoxy interface was rejected.

All tests were performed in air. The samples were loaded in tension using an Applied Test Systems Universal Testing Machine. One grip of the testing machine was attached to the

I. INTRODUCTION

The term fracto-emission (FE) refers to the emission of photons, electrons, ions, and molecules from a stressed material prior to, during, and after ultimate failure.[1-6] FE can provide useful information on failure mechanisms in polymers, ceramics, and composites. In particular, FE is often strongly affected by the presence and nature of interfacial failure in composite materials, e.g., the photon and electron emissions accompanying interfacial failure are typically much stronger than when failure is largely cohesive. Charged particle energy distributions also tend to be very high due to strong **E** fields associated with charge separation.[5] Given composite materials of sufficient transparency, photon emission (phE) can provide information on failure events interior to the sample, indicating both the location and the nature of the failure events.[6-8] Because of the rapid response and high sensitivity of commercially available photomultiplier tubes, this information can be provided in real time with considerable time resolution. In some cases, intensities are sufficient to image the phE[9,10] and the EE.[11]

In a recent study,[5] we have examined the following time resolved signals: the rod strain, photon emission (phE), electron emission (EE), and long wavelength electromagnetic signals (RE, for radio emission) accompanying the failure of axially loaded rods with one end embedded in a semi-transparent epoxy matrix. Typical signals accompanying failure[5] correlated with fracture events involving time scales shown in Table I. Thus, phE transmitted through the epoxy from the interface and the RE provides information on the progress of the debond and pullout of the rod. Because electrons require an unobstructed path to the detector in order to produce a signal, the onset of EE indicates the time when the interfacial crack communicates with the "outside world." This time can be precisely ascertained relative to the progress of the interfacial crack. We also demonstrated[5] that the approximate position and velocity of the interfacial crack can be determined by focusing light from two separate regions of the rod-epoxy interface onto two different photomultiplier tubes. Following interfacial

stainless steel rod, and the other grip was attached to a yoke which fit over the epoxy portion of the sample, as shown schematically in Fig. 1(a). As noted below, the compressive stresses in the epoxy near the intersection of the epoxy surface and the rod represent a departure from the typical rod/fiber pullout geometry. The rod grip employed in most tests did not constrain rod motion in the direction of the applied force; this allowed for significant rod pullout after debonding. The sample was loaded in tension at a displacement rate of 2 mm/min. The load at the debonding fracture event ranged from 5000 N to 7500 N. The strain in the rod was monitored with a resistive strain gauge (Omega 3/120LY41), attached as shown in Fig. 1(a). The gauge resistance was placed in an initially balanced Wheatstone bridge. The bridge output was amplified by a differential amplifier, and digitized with a Lecroy 9450 Dual 350 MHz Digital Oscilloscope at 500 ns time intervals. The time response of the strain gauge circuit was ~10 μs.

The testing machine was enclosed in a light-tight, grounded aluminum box to minimize background levels in the current, phE, and RE measurements. The metal rod was insulated from the grips and a wire was attached for the transient current measurement. The epoxy sample was enclosed in a grounded brass cylinder which provided the "return" path for current from the rod, as shown in Fig. 1(b). The brass cylinder was slotted along the side toward the photomultiplier tube to allow light detection. An aluminum foil liner between the brass cylinder and the epoxy increased the phE signal by reflecting light into the slot.

Photon emission measurements were made with an EMI Gencom 9816QB photomultiplier tube (PMT) with bialkali phosphor and a quartz window mounted 5 cm from the sample axis. The PMT was cooled to -40 C, which reduced the PMT dark current. The PMT output was amplified by a preamplifier and fast filter amplifier with 500 ns integration time. Integration was necessary because of the fast time response of the PMT. Single photon pulse widths were typically 20 ns << 500 ns. Stretching the signal by integration allowed digitization at 500 ns intervals using a LeCroy 6810 Digitizer. With 64K of memory, a total

acquisition time interval of 32 ms was then available. Some measurements were made without a preamplifier to avoid signal overshoot and other low frequency artifacts.

Current measurements were made by connecting the electrically isolated rod to the input of a Keithley 602 Electrometer [as shown in Fig. 1(b)]. The electrometer output was then digitized at 10 μs intervals by a Lecroy 8210 Digitizer. Higher time resolution could be obtained at somewhat reduced sensitivity by connecting the rod directly to the 1 MΩ input of the LeCroy 6810 Digitizer. The RC time constant of the sample-coax-digitizer circuit was ~5 μs, consistent with the estimated sample capacitance of 5 pF. The resulting signal was then digitized at 500 ns intervals, simultaneous with the phE intensity measurements.

Low-frequency electromagnetic signals (RE) were simultaneously monitored by a coil antenna approximately 3 cm from the sample axis. This antenna couples to a changing **B** field and probes the *near-field* electromagnetic signal due to its proximity to the source. Such signals often result from the changing **B** field accompanying electrical breakdown, an interpretation which is reinforced by simultaneous bursts in the phE signals. The output of the coil was differentially amplified (1 MHz bandpass) and digitized at 500 ns intervals with the Lecroy 9450 Dual 350 MHz Digital Oscilloscope. Data acquisition of all signals was triggered by the onset of the RE signal.

III. RESULTS

The sign of the net charge remaining on the stainless steel and epoxy surfaces after interfacial failure was determined by examining a failed planar steel-epoxy interface with a charge probe connected to a Keithley electrometer. The stainless steel was found to have a net positive charge and the epoxy a net negative charge following separation.

A display of simultaneous measurements of (a) rod strain, (b) phE, (c) current (made with the electrometer), and (d) RE are shown in Fig. 2. In Fig. 2(c), a positive-going signal corresponds to a positive current from the rod (a flow of electrons *to* the rod). The four arrows

labeled A-D indicate the various stages in the progress of fracture. The first two arrows (A, B) mark the onset of phE and current, respectively. A very small drop in strain occurs with the onset of phE, and a somewhat larger drop in strain with the onset of the current signal. These two events are attributed to two stages of crack growth along the rod-epoxy interface. The delay (~35 μs) between the onset of phE and current is not typical. In most experiments, the first phE coincided with the onset of current. We suspect that the initial debonding event in this sample was not sufficiently strong to yield detectable current on the electrometer scale used.

Between the arrows marked B and C, interfacial crack growth initially appears to be continuous in the region where the strain drops linearly. The bump in the strain midway between the arrows is consistent with the passage of a reflected stress wave. From this point on, the strain is strongly influenced by reflected stress waves. During crack propagation, the current rises dramatically to about 0.55 μA. The phE in this region is weak but continuous, showing a modest burst during the steepest portion of the current rise. An RE signal is also observed in this region, but this was not the case for all samples in this study, as well as those reported in Ref. 5.

At arrow C the load drops sharply to zero over about 20 μs: at this point, interfacial failure along the length of the rod is complete and rod pullout begins, associated with the first wave of stress relaxation along the rod/epoxy interface. A very large phE signal, an additional positive jump in the current, and a very large RE signal accompany this load drop. The coincident large phE and RE signals indicate electrical discharges accompanying relative motion of the rod and epoxy surfaces, again, a correlation noted in Ref. 5. The current does not begin to drop until arrow D, ~20 μs after the onset of pullout. Normally, the current would begin to drop within ~5 μs of the onset of pullout. The delay shown here may be due to a small portion of intact interface which finally detached; a sharp phE burst coincident with the leading edge of the current drop supports this interpretation.

Following arrow D, the strain oscillates at ~20 kHz and strong phE and RE signals occur in coincidence with each *drop* in strain. 20 kHz is approximately the frequency of a

standing longitudinal wave in the 13 cm steel rod with both ends free. Due to the manner in which the loading apparatus is coupled to the specimen, both ends of the rod are effectively free following debonding so that stress waves can reflect from the rod ends and oscillate in a longitudinal direction. It should be noted that although the rod/epoxy surfaces are essentially separated, there is considerable contact between the two surfaces at asperities along the interface,[5] most likely due to significant plastic deformation of the epoxy. The observed signals therefore result from small displacements of the rod in the direction of pullout accompanying successive stress waves as they pass through the rod. After several milliseconds these oscillations dampen to a background level of strain. Note that the small noise-like variations in the current after the main pullout event do not follow the 20 kHz oscillations in strain. This is consistent with a transient current source related to interfacial failure rather than rod displacement. Due to a discharging capacitance in the electrometer circuitry, the phE and current signals drop below zero after fracture; this particular behavior is thus an artifact of the detection circuitry.

Higher time resolution (with some loss of sensitivity) could be obtained for the current measurement by connecting the rod directly to the input of the digitizer, which is DC coupled to ground through a 1 MΩ input resistor. Figure 3 shows the four signals with both phE and current digitized at 500 ns intervals. In this sample, the total time between initial debonding and the completion of interfacial failure was rather long, almost 500 μs. Here, the first arrow (A) marks the first observed phE signal, which coincides with both a small drop in rod strain and a rise in current. This initial current rises rapidly, then falls linearly over ~300 μs. phE is observed during the current rise, but not the fall, implying that phE is not always sustained during slow crack motion. Both signals are consistent with an initial rapid acceleration of the interfacial crack followed by slow crack growth. During the time interval from B to C, where the current is substantial, both phE and current are active for ~150 μs, followed by an abrupt, intense burst in both signals.

If we expand this time interval as in Fig. 4, the phE activity during this slower rise in current is more evident. Both signals are quite reproducible from sample to sample. From the associated strain data, we conclude that the debond crack is completed during the first part of this time interval and that the onset of pullout results in the large, coincident phE and current burst. The pullout event is also accompanied by an RE signal [Fig. 3(d)], suggesting microdischarges. Post-failure examination of samples strained in this geometry showed considerable displacement of the rod out of the epoxy cavity (~4 mm). The positive current after debonding is consistent with the decrease in capacitance associated with the net displacement of the rod. In addition to it's outward displacement, the rod oscillates in the epoxy socket generating the observed oscillations in strain, phE, and RE, probably due to triboelectric interactions between the two surfaces which touch at asperities during these oscillations.

A rather large pullout displacement of the rod was possible because the grips employed were not rigidly attached to the rod, allowing the rod to move "freely" upon the completion of interfacial failure. To test if the resulting relative motion was the origin of this sustained current, the grips were modified to hold the rod securely after the removal of tensile stress. Resulting strain, phE, and current records are shown in Fig. 5. (RE was not attainable in this configuration). As expected, the signals prior to the completion of interfacial failure are similar to those observed without the grip modification. The regions associated with the debond and onset of pullout are marked. The duration of interfacial failure is about 300 μs. The onset of current appears to be a more sensitive indicator of the onset of crack propagation than the rod strain. The phE is rather weak or absent at the onset of debonding, presumably due to the low crack velocity at this point.

Note that the phE bursts during rod pullout are much narrower, the current oscillates less and at a lower frequency, and the strain quickly rings up to constant level. The current signal suggests that the rod continued its contraction ~170 μs following failure, then stopped rather abruptly in two "arrest events." Strong phE bursts accompany these arrest events and

are coincident with decreasing rod strain. Peak rod strain corresponds to the position of maximum rod extension in its oscillation; at this point the relative velocity of epoxy and rod is zero, assuming the epoxy matrix is still at rest. Since the epoxy has accelerated somewhat, one of these maxima would be the most likely point of arrest. Post-failure examination of the sample confirmed that rod pullout was much reduced in these constrained samples (typically, 1 mm of pullout). In addition, the new boundary conditions on longitudinal waves in the rod (one end now fixed, the other free), halved the frequency of the oscillations in the strain and phE signals during pullout (from 20 kHz to 10 kHz) as expected.

IV. DISCUSSION

The mechanics of a rod embedded in a large matrix and loaded in tension have been well studied and have important implications with respect to fiber matrix composites. Experimental and theoretical work by Atkinson et al. suggest that interfacial failure initiates at the intersection of the rod with the epoxy surface, then proceeds along the length of the rod toward the embedded tip.[12] These simulations assume a geometry in which the epoxy surface near the rod is free of applied stresses. Simultaneous measurements of photon and electron emission in our laboratory[5] on samples identical to those employed in the rod current work indicate that interfacial failure initiates somewhat below the epoxy surface and proceeds both toward the embedded tip and towards the epoxy surface. We attribute the difference to our loading geometry, which yields compressive stresses near the intersection of the rod with the epoxy surface (see Fig. 1a).

Interfacial failure is accompanied by several electronic processes, including the emission reported in this work. Much of the electronic activity is a consequence of contact charging created during sample preparation.[13] The conventional interpretation would be that the rod and epoxy have different effective "work functions," which result in a flow of charge across the interface until the Fermi levels of the two materials are aligned. Lowell and Rose-Innes[13] have discussed alternative processes whereby charge carriers, usually electrons, can

flow in *both* directions, with a net flow generally in one direction. Adopting the latter possibility, we propose that the epoxy *loses* some electrons (creating positive ions), but accepts many more electrons which occupy high electron affinity sites (creating negative ions). Although the charge in the metal is very mobile, the charge in the epoxy tends to be localized at these sites, often defect sites, and is thus relatively immobile. Initial separation of the two surfaces tends to drive charge back to its original "owner." (Recall above: contact charging involved transfer of excess electrons *to* the epoxy).

In the first stages of separation, small displacements of the two surfaces produce a *redistribution* of electrons between the two surfaces resulting in de-excitation events (e.g., electron-positive ion recombination) occurring in the polymer surface/near surface region, yielding phE. If the separation were such as to provide access to the outside (e.g., vacuum), and if the de-excitation transition is sufficiently energetic, detectable electron emission can also occur from the epoxy surface. This redistribution/recombination mechanism is the origin of the phE seen during debonding (in the absence of electrostatic discharges).

As interfacial failure progresses, charge transfer is greatly hindered after the surfaces are separated by a few nm, so that the greater portion of the charge separation occurs under conditions of *constant charge*. The work done (supplied by strain energy) on this charge as the surfaces separate increases the potential difference between the surfaces. Diffusion of charge to asperities on the rod and epoxy surfaces can then result in locally very intense electric fields and breakdown. After interfacial failure the rod and epoxy surfaces make contact only at asperities, generally making up only a small fraction of the interfacial area. Breakdown may be triggered by the motion of asperities past one another upon completion of interfacial failure. Electrical discharges/breakdown are therefore responsible for the intense phE and RE bursts observed during and after failure.

To examine the origin of the current created during the debonding event, consider the geometry of the sample during fracture shown in Figures 6(a) and 6(b), where we show the crack propagating from left to right. Assuming that interfacial failure occurs under conditions

of constant charge, the opening of the gap between the rod and epoxy results in a change in the potential across this gap. In the region where no debonding has occurred, we assume the metal/epoxy interface has a separation of δ_o (very small) which increases to a constant width $\delta = \delta_o + \Delta\delta$, where $a >> \Delta\delta >> \delta_o$. If we integrate the electric field from the surface of the rod to the outer conductor, we obtain the potential difference between the rod and outer cylinder; because of the connection through the resistor R, shown in Fig. 6(b), this value is zero before and after charge flow. For cylindrical geometry, ignoring edge effects, the radial components of the E fields in the separation region and in the epoxy at radial distance r are:

$$E(r) = \frac{\rho^+}{2\pi\varepsilon_o r} \qquad a < r < a+\delta \qquad (1)$$

$$E(r) = \frac{1}{2\pi\kappa\varepsilon_o}\left[\frac{\rho^+ + \rho^-}{r}\right] \qquad a+\delta < r < c \qquad (2)$$

where ρ^+ and ρ^- are the charge/length on the metal rod and on the epoxy surfaces, respectively. ρ^- is the constant, free charge on the epoxy and κ is the relative dielectric constant of the epoxy. Before the crack is opened, the potential difference is given by

$$V = \int_a^{a+\delta} \frac{\rho^+}{2\pi\varepsilon_o r}\,dr + \frac{1}{2\pi\kappa\varepsilon_o}\int_{a+\delta}^{c}\left[\frac{\rho^+ + \rho^-}{r}\right]dr \qquad (3)$$

or:

$$V = \frac{\rho^+}{2\pi\varepsilon_o}\ln\left(1+\frac{\delta}{a}\right) + \frac{(\rho^+ + \rho^-)}{2\pi\kappa\varepsilon_o}\ln\left[\frac{c}{a+\delta}\right] \qquad (4)$$

Before any crack growth, $V = 0$, $\rho^+ = \rho^+_o$, and $\delta = \delta_o$, so that:

$$\rho_o^+ = \frac{\frac{\ln\left[\frac{c}{a+\delta_o}\right]}{\kappa}}{\left\{\ln\left(1+\frac{\delta_o}{a}\right) + \frac{\ln\left[\frac{c}{a+\delta_o}\right]}{\kappa}\right\}} \rho^- = K_o \cdot \rho^- \qquad (5)$$

where K_o is the collection of constants shown. If a annular region debonds and opens to a width $\delta = \delta_o + \Delta\delta$, then to keep V=0, charge will flow, changing the local charge/length in the debonded region: i.e., $\rho^+_o \dashrightarrow \rho^+_f$, where ρ^+_f is given by:

$$\rho_f^+ = \frac{\frac{\ln\left[\frac{c}{a+\delta_o+\Delta\delta}\right]}{\kappa}}{\left\{\ln\left(1+\frac{\delta_o+\Delta\delta}{a}\right) + \frac{\ln\left[\frac{c}{a+\delta_o+\Delta\delta}\right]}{\kappa}\right\}} \rho^- = K_f \cdot \rho^- \qquad (6)$$

where K_f represents the new collection of constants.

Thus, for an increment of length in the crack, Δx, the net charge that would flow (through R) would be:

$$\Delta q = (\rho_o^+ - \rho_f^+) \cdot \Delta x = (K_o - K_f) \cdot \rho^- \cdot \Delta x \qquad (7)$$

For an increment of crack length Δx in time Δt ($v_c = \Delta x/\Delta t$), the current generated is:

$$i = (K_o - K_f) \cdot \rho^- \cdot v_c \qquad (8)$$

We assume the time constant associated with R and the (sample + coax) capacitance is << time of fracture, which for R = 1 MΩ and C~5 pF is satisfied. Values of ρ^- for metal/polymer interfaces have been measured[14] and are typically ~10^{-4} C/m^2 From the observed durations of the photon emission and strain decrease, we obtain average crack velocities of 200 m/s. We estimate $\Delta\delta$ to be ~1 μm. This spacing is consistent with Ohara's optical interferometer measurements[15] on polymer/glass structures undergoing shear deformation. Using known values of a, c, and κ (~4), Eq. 8 yields an estimated current of 0.2 μA and a total charge transfer of 60 pC. This is in good agreement (somewhat fortuitous, considering the approximations) with measured values for i (which ranged from 0.1 - 1 μA during debonding)

and Δq (~50 pC). Furthermore, the predicted direction of charge transfer is electron flow *to* the rod, which is also in agreement with experiment.

As mentioned above, immediately after debonding, the constrained rod undergoes an initial, fast pullout due to the response of the rod and epoxy to the sudden stress release at the interface; this is followed by a damped longitudinal oscillation of the rod. Additional charge transfer occurs during this fast pullout because rod pullout shortens the length of the capacitor formed by the rod and shield. To maintain the charge density (i.e., constant charge/length, ρ^+_f of equation 6 above), to maintain zero potential difference between the rod and outer shield, additional charge must flow during pullout. Again, electrons will flow *to* the rod. Ignoring fringe fields and letting ΔL be the pullout distance and Δt be the duration of pullout, then the current generated during this event will be:

$$i = \frac{\Delta q}{\Delta t} = \rho_f^+ \cdot \frac{\Delta L}{\Delta t} \qquad (9)$$

For ΔL ~ 1.5 mm, Δt = 170 μs, and ρ^+_f = 1 μC/m, this yields a current of 8 μA. We observe peak currents of 1-5 μA (corresponding to electron flow to the rod, as predicted) in good agreement with Eq. 9.

The time dependence of the current and phE during debonding may be due to changes in crack speed. phE intensities accompanying the fracture of neat epoxies depend strongly on crack velocity.[2] A similar dependence of EE intensities on crack velocity has been observed during the failure of filled elastomers[16,17] and Au-SiO_2 interfaces.[4] This is consistent with the relatively intense phE and the rapidly rising current immediately prior to the completion of interfacial failure. In the final stages of crack growth, the stress intensity at the crack tip should be quite high and the crack velocity correspondingly high. Some of the phE in these final stages may be due to electrical discharges, but we note that phE bursts were also observed at small jumps in current long before the completion of debonding (e.g., see Fig. 5). The most natural interpretation of the initial phE bursts is that the initial

debonding event involves localized, rapid crack growth at a stress concentrating defect. The new crack often relaxes the local stress, slowing subsequent crack growth and temporarily reducing the phE intensity.

The current and phE signals indicate that the epoxy surfaces are electrically charged during interfacial failure. The large, aligned phE and RE signals accompanying the completion of interfacial failure are attributed to electrical discharges between epoxy and rod surfaces as the surfaces are displaced with respect to one another. This displacement brings asperities on the two surfaces in close proximity, allowing the discharge of accumulated charge. phE and RE bursts after failure accompany additional displacements of the rod with respect to the epoxy as it oscillates with its natural frequency which depends on the clamping arrangements. The total charge involved in phE and RE events is a small fraction of the total charge on the two surfaces, as the large bursts following fracture do not affect the current signal significantly.

V. CONCLUSION

Interfacial failure in the steel rod-epoxy matrix system is accompanied by distinctive voltage and current signals which are correlated with interfacial failure events inferred from small changes in rod strain. These electrical transients are accompanied by phE signals which are sensitive indicators of the onset of interfacial crack growth. In the final stages of interfacial failure, intense phE and RE bursts reflect electrical discharges which are associated with the relative motion of rod and matrix accompanying pullout. Subsequent bursts are correlated with oscillations in rod strain which accompany further displacement.

The intense FE signals which generally accompany interfacial failure can provide important information on the fracture event, often with extremely good time resolution. By appropriately modifying the detection conditions one can readily extract information on the initial locus of debonding and its subsequent course. It might be useful, for example, to use these probes to examine the role of mixed mode and frictional stresses at the interface (discussed by Hutchinson

and Jensen[18]) in crack propagation along that interface. Observations on macroscopic samples may eventually prove useful in understanding the fracture of fiber-based composites, where pullout contributes substantially to material toughness. We note that in principle, these measurements could also be carried out on fragile specimens (e.g., small, single fibers) and/or at high temperatures as long as electrical contact can be maintained.

VI. ACKNOWLEDGMENTS

The authors wish to thank Ma Zhen-Yi and Les Jensen for their assistance in this study, and Robert Cook, IBM Yorktown, for helpful discussions. This work was supported in part by the Dow Chemical Corporation, the Ceramics and Electronic Materials Division of the National Science Foundation under Grant DMR 8912179, the Office of Naval Research under Contract No. N00014-87-K-0514, and the Washington Technology Center.

REFERENCES

1. J. T. Dickinson, L.C. Jensen, and S.K. Bhattacharya, J. Vac. Sci. Technol. A 3, 1398 (1985).
2. J. T. Dickinson, L. C. Jensen, and S. K. Bhattacharya, Makromol. Chem., Macromol. Symp. 7, 129 (1987).
3. J. T. Dickinson, L.C. Jensen, and A. Jahan-Latibari, J. Vac. Sci. Technol. A 2, 1112 (1984).
4. S. C. Langford, D. L. Doering, and J. T. Dickinson, Phys. Rev. Lett. 59, 2795 (1987).
5. J. T. Dickinson, "Fracto-Emission", in *Non-Destructive Testing of Fibre-Reinforced Plastic Composites II*, edited by J. Summerscales, (Elsevier Applied Science, London, 1990), pp. 429-482. (see cited references).
6. Ma Zhen-Yi and J. T. Dickinson, "Fracto-emission from embedded interfaces," submitted to J. Mat. Res.
7. J. T. Dickinson and A. S. Crasto, in *Cross-linked Polymers: Chemistry, Properties and Applications*, edited by R. A. Dickie, S. S. Labana, and R. S. Bauer, ACS Symposium Series 367 (American Chemical Society, Washington, D.C., 1988), pp. 145-168.
8. A. S. Crasto, R. Corey, J. T. Dickinson, R. V. Subramanian, and Y. Eckstein, Composites Sci. Technol. 30, 35 (1987).
9. J. T. Dickinson and E. E. Donaldson, J. Adhesion 24 , 199 (1987).
10. E. E. Donaldson and J. T. Dickinson, J. Adhesion 30, 13 (1989).
11. J. T. Dickinson, "Fracto-Emission Accompanying Adhesive Failure," in *Adhesive Chemistry: Developments and Trends*, edited by L. H. Lee, (Plenum Press, New York, 1985).
12. C. Atkinson, J. Avila, E. Betz, and R. E. Smelser, J. Mech. Phys. Solids 30, 397 (1982).
13. J. Lowell and A. C. Rose-Innes, *Contact Electrification*, Adv. Phys. 29, 947 (1980).

14. D. K. Davies, J. Phys. D 2, 1533 (1969).

15. Keiji Ohara, Wear 50, 333 (1978).

16. J. T. Dickinson and L. C. Jensen, J. Polymer Sci., Polymer Phys. Ed. 20, 1925 (1982).

17. J. T. Dickinson, L. C. Jensen, and A. Jahan-Latibari, Rubber Chem. and Tech. 56, 927 (1984).

18. J. W. Hutchenson and H. M. Jensen, to be published.

FIGURE CAPTIONS

Fig. 1. Experimental setup for rod pullout and related measurements. (a) Loading arrangement for most of the tests. (b) Detector arrangements: Coil for RE (radiofrequency emission), photomultiplier tube (PMT) for photon emission, and electrometer or fast digitizer for measurement of current *i*.

Fig. 2. Signals for (a) strain, (b) phE, (c) rod current, and (d) RE. The current was measured with an electrometer. Insert in (b) shows phE in initial debond region.

Fig. 3. Typical (a) strain, (b) phE, (c) current, and (d) RE signals during debonding and pullout of rod. The current from the rod was digitized directly by a high input resistance digitizer (no electrometer).

Fig. 4 . (a) phE and (b) current signals of Fig. 3 shown on an expanded time scale.

Fig. 5. Typical (a) strain, (b) phE, and (c) current signals accompanying the debonding and pullout of a rod from an epoxy matrix. Both rod and epoxy have been rigidly attached to the grips, preventing free motion of the rod upon relaxation of the tensile stress. Insert in (b) shows phE in initial debond region.

Fig. 6. Schematic of electrical aspects of sample. (a) End view of debonded region. Nominal dimensions are a = 1.5 mm, c = 14 mm, and L = 50 mm. We estimate the gap between the metal and epoxy surfaces after failure to average about 1 μm. (b) Side view showing partially debonded sample and external circuit.

Table I.

Signal	Correlated Event	Time Scale (μs)
Initial drop in strain	Onset of debonding between rod and epoxy	0
Onset of phE	Onset of debonding between rod and epoxy	0 [sometimes < 0]
Onset of EE	First appearance of a surface crack--follows onset of debonding	$10\text{-}10^2$
Onset of RE	Onset of pull-out of rod from epoxy	10^2
Most intense EE, phE, RE	Rapid pull-out of rod from epoxy	10^2
Oscillations/bursts in all signals	Oscillations of debonded in epoxy socket accompanying/following pullout	$10^2\text{-}10^3$

Table Captions

Table I. Fracto-emission signals, failure events, and relevant time scales for rod/epoxy debonding and pullout.

(a) Loading Arrangement

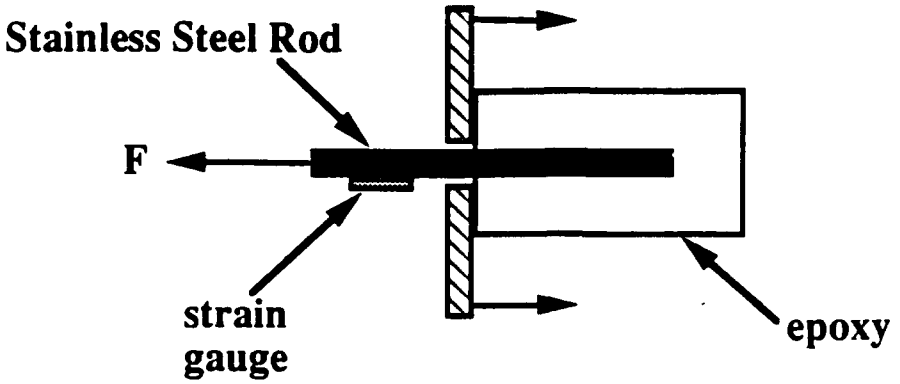

(b) Schematic of i, phE, and RE Measurements

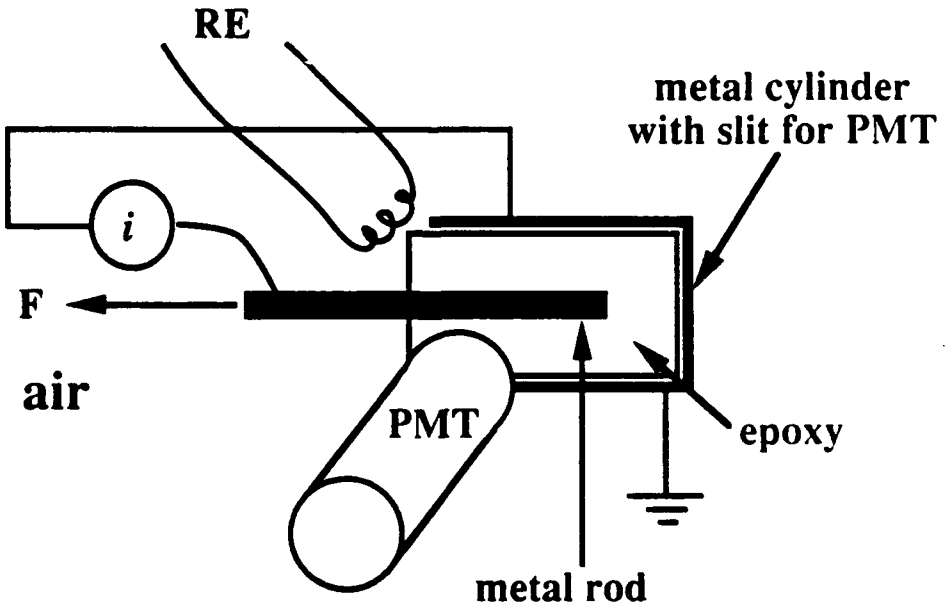

Fig. 1

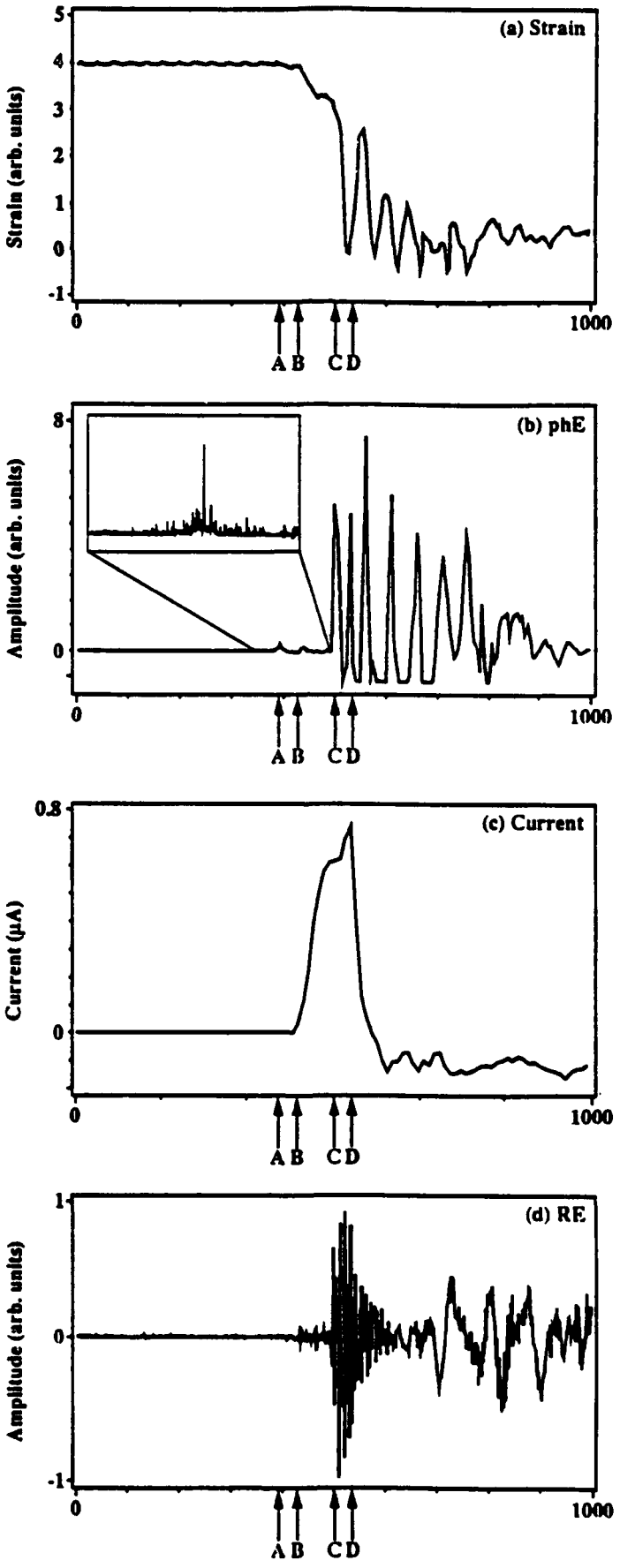
(a) Strain
Strain (arb. units)
5
4
3
2
1
0
-1
0
1000
A B C D
(b) phE
Amplitude (arb. units)
8
0
0
1000
A B C D
(c) Current
Current (μA)
0.8
0
0
1000
A B C D
(d) RE
Amplitude (arb. units)
1
0
-1
0
1000
A B C D
Time (μs)

Fig. 2

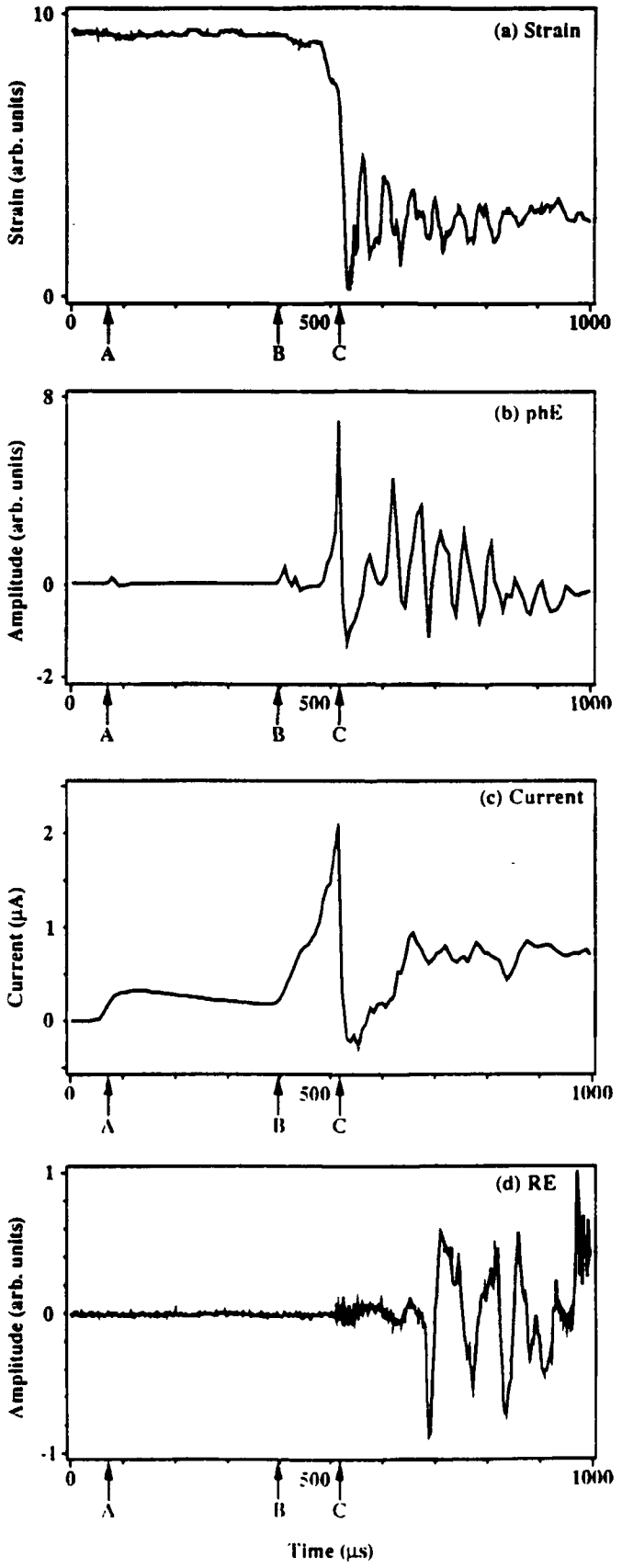
(a) Strain
Strain (arb. units)
10
0
(b) phE
Amplitude (arb. units)
8
0
-2
(c) Current
Current (μA)
2
1
0
(d) RE
Amplitude (arb. units)
1
0
-1
0
500
1000
A
B
C
Time (μs)

Fig. 3

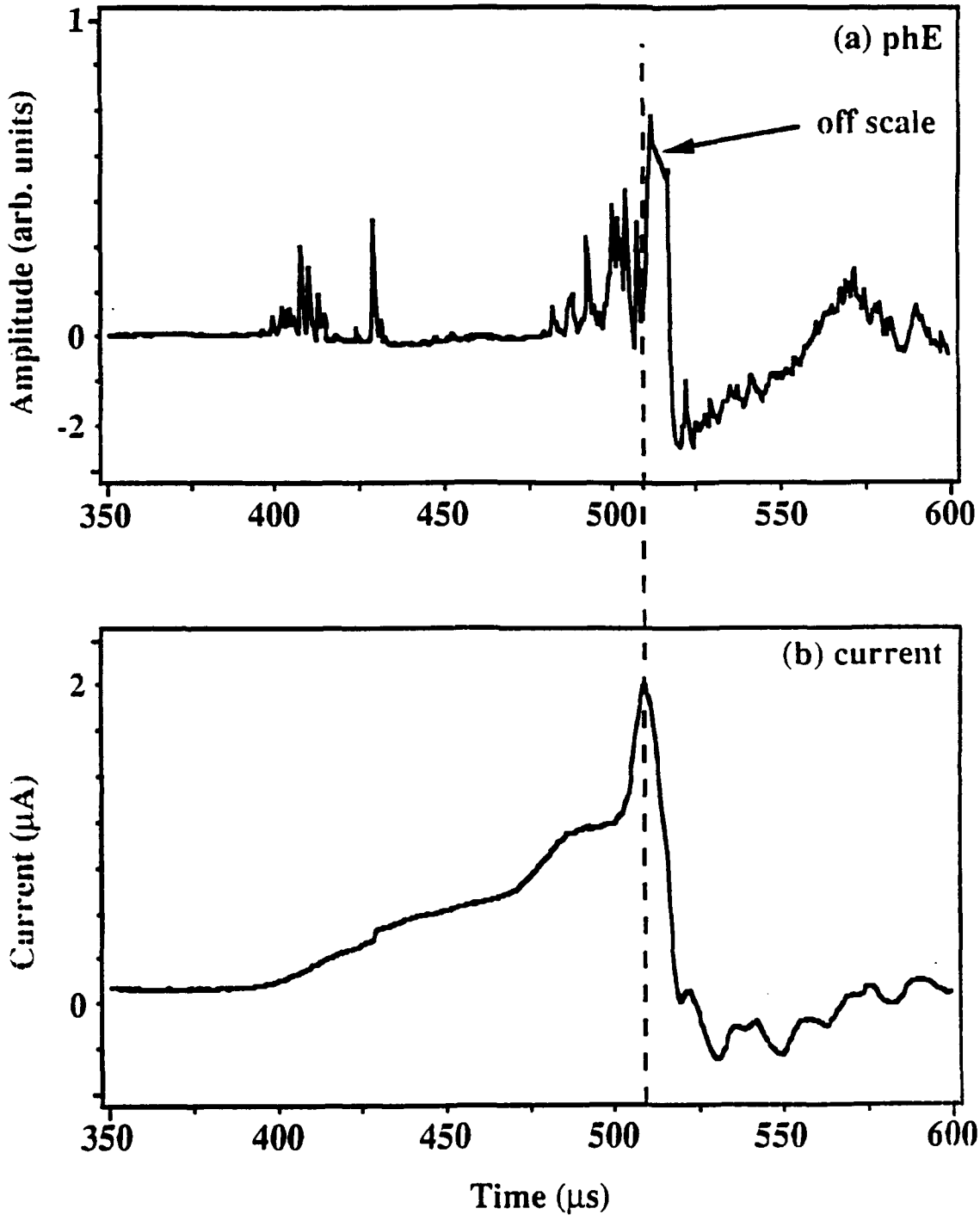
(a) phE
off scale
Amplitude (arb. units)
1
0
-2
350
400
450
500
550
600
(b) current
Current (μA)
2
0
350
400
450
500
550
600
Time (μs)

Fig. 4

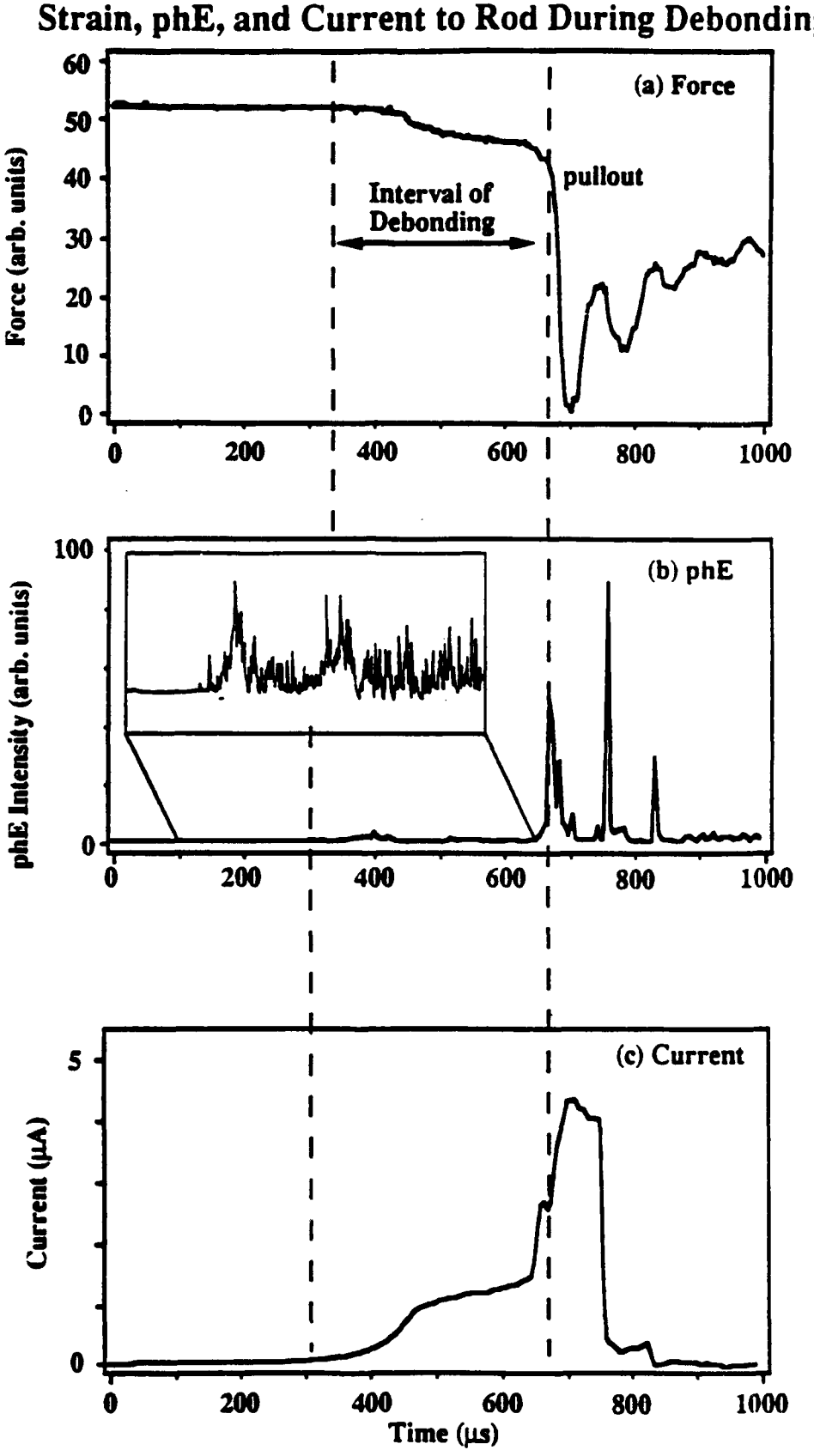
Strain, phE, and Current to Rod During Debonding
(a) Force
pullout
Interval of Debonding
Force (arb. units)
60
50
40
30
20
10
0
0
200
400
600
800
1000
(b) phE
phE Intensity (arb. units)
100
0
(c) Current
Current (μA)
5
0
Time (μs)

Fig. 5

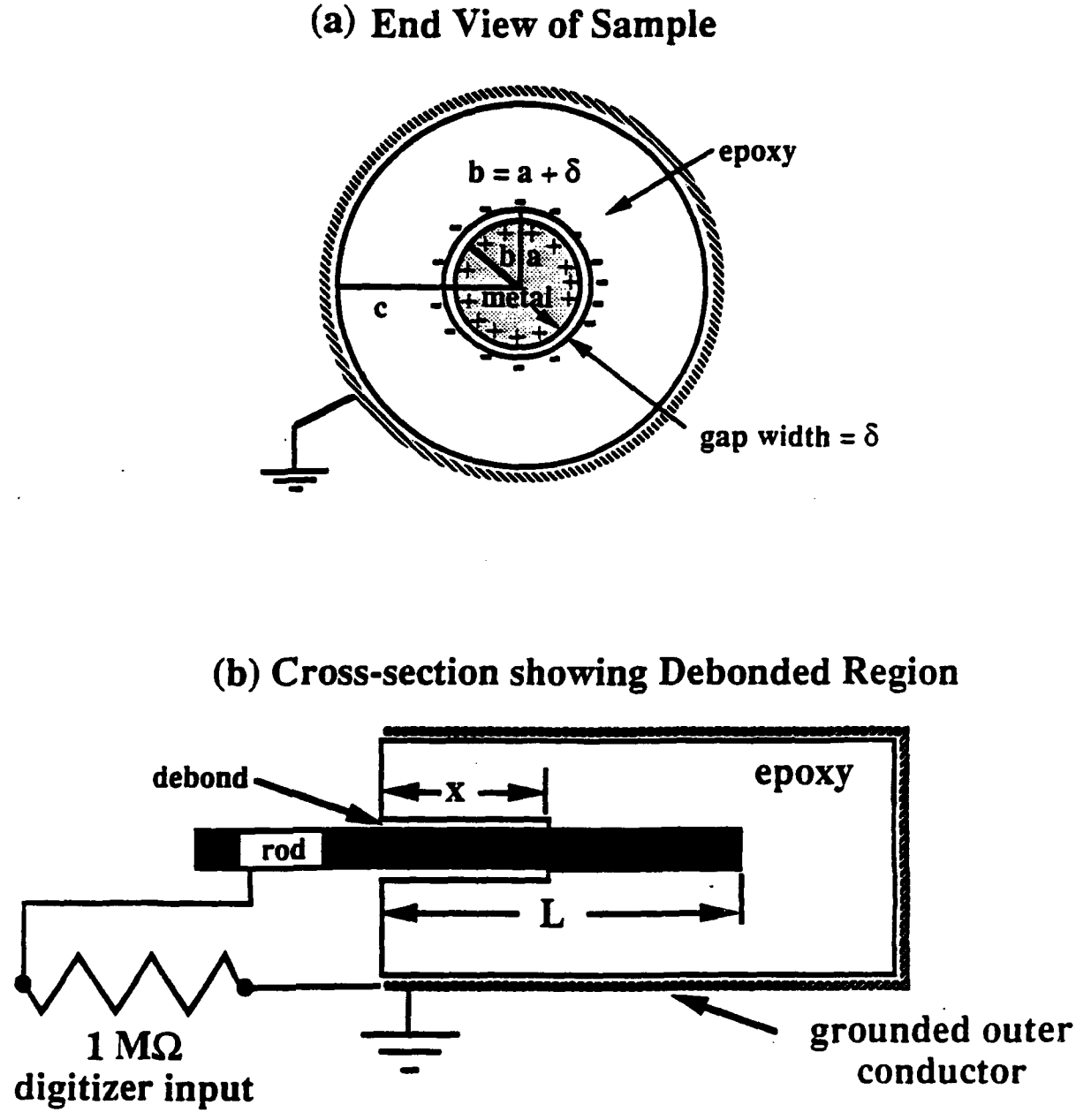
(a) End View of Sample
epoxy
b = a + δ
b
a
metal
c
gap width = δ
(b) Cross-section showing Debonded Region
debond
x
epoxy
rod
L
1 MΩ
digitizer input
grounded outer
conductor

Fig. 6

X. # Fracto-emission during the interfacial failure of a metal–oxide-semiconductor system: Au–SiO_2–Si

D. L. Doering,[a] J. T. Dickinson, S. C. Langford, and P. Xiong-Skiba[a]
Department of Physics, Washington State University, Pullman, Washington 99164-2814

(Received 1 September 1989; accepted 9 October 1989)

Two fracto-emission components (electron and photon emission) produced by the adhesive failure of gold films peeled in vacuum from oxidized silicon were measured for different oxide thicknesses. The Au adhesive strength was found to decrease with increasing oxide thickness, whereas the fracto-emission intensities and durations increased significantly with oxide thickness. We interpret these results in terms of interfacial charge created during the formation of the metal–oxide-semiconductor (MOS) structure, leading to charge separation during fracture and to subsequent charge transport within the MOS structure.

I. INTRODUCTION

The metal–oxide-semiconductor (MOS) thin film system is of great importance in modern electronics and other areas of high technology. In a number of circumstances, the mechanical properties of the interfaces are of key importance. Interfacial failure can occur as a consequence of several factors including mechanical (both residual and external), thermal, and electrical stresses. In this study, we focus on the effect of oxide thickness on the adhesive strength of the gold–oxide interface and on the fracto-emission properties during adhesive failure.

During the fracture of a material, a fresh surface is created which is often in a highly energetic state. The resulting surface energy can be dissipated in a variety of ways including acoustic and thermal phonon generation, electronic deexcitation and fracto-emission. Fracto-emission (FE) refers to the emission of electrons, ions, photons and/or neutral particles as a consequence of the cohesive fracture of homogeneous materials and the adhesive, interfacial failure of heterogeneous materials.[1–3] FE intensities and fluctuations depend strongly on the competition between the energy dissipation mechanisms which are in turn related to the properties of the materials involved and the nature of the fracture. In general, insulators have relatively long excited state lifetimes and produce the most intense FE, whereas clean metals produce no FE. Weak electron emission has been observed during the fracture of silicon, a semiconductor, although the dominant excitation is the production of free charge carriers.[4,5]

We present observations of electron emission (EE) and photon emission (phE) resulting from adhesive failure between a thin Au film and an oxidized Si surface. We attribute the emissions during and immediately after failure to electrical discharges resulting from charge separation across the MOS structure. In several systems, charge separation at fracture has been shown to result in particularly intense FE.[6–10] This charge separation can lead to microdischarges which yield phE, EE, and other emissions. Further, the intense electron and ion bombardment of the charged surfaces during electrical breakdown results in high densities of energetic surface defects. Recombination and decay of these defects can result in FE long after the fracture event. We find that the oxide thickness plays a critical role in the intensity and duration of these emissions, the thicker oxides being associated with especially intense, long-lasting emissions. This suggests that the oxide serves to electrically isolate the fracture surface from the semiconducting Si substrate, preventing rapid, nonradiative dissipation of separated charge and destruction of surface excitations by tunneling through the oxide.

II. EXPERIMENTAL

The samples were cut from commercial boron-doped (111) Si wafers obtained from S.E.H. America, Inc. The resistivity of the bulk material was 10–20 Ω cm. After an HF acid etch, the samples were divided into two categories. One set of samples was heated to 1000 °C in atmosphere to create an oxide of variable thickness increasing with the duration of treatment. The oxide thicknesses were estimated by the color of the samples in white light. Typical thicknesses used ranged from 500 to 1200 Å. The other sets of samples did not undergo thermal oxidation; one set was handled in air and therefore should have an oxide of ~20 Å in thickness, which we refer to as a "native oxide." The third set of samples were handled in an Ar atmosphere glove box (and transferred directly to the evaporator) and should contain less of an oxygen coverage prior to deposition. We optimistically refer to these specimens as having "no oxide." All the samples were coated on the polished side with a vapor deposited gold layer ~50 nm thick. The deposition was done in an ion pumped vacuum system at a pressure of 10^{-7} Torr.

The basic experiment consisted of pulling (peeling) the Au film from the native and thermal oxide covered Si surfaces while simultaneously monitoring both the EE and phE. The specimens were tested in a turbomolecular pumped high vacuum system at pressures below 10^{-6} Torr. Figure 1 shows a schematic diagram of the sample and experimental setup. The unpolished, uncoated side of the samples were epoxied to an aluminum holder and the polished, Au-coated surface was bonded to an epoxy drop attached to a pulling pin. The area of the Au film covered by the drop, i.e., the area involved in the peel event, was ~0.3 cm^2. The pin was loaded in direct tension using a polymer monofilament line to avoid torsional stresses. This arrangement also insured that the

 0734-2101/90/032401-06$01.00 © 1990 American Vacuum Society

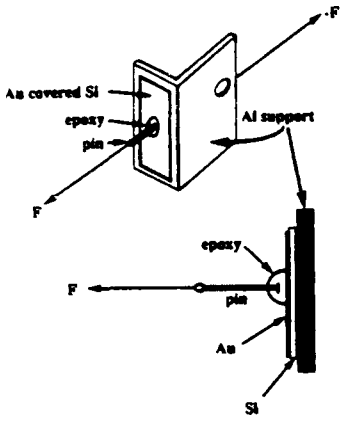

FIG. 1. Schematic diagram of the sample peeling configuration. The Si substrate is glued to the aluminum holder with epoxy. A portion of the Au film is attached to the loading apparatus by a metal pin imbedded in an epoxy drop. The load is applied to the metal pin through monofilament fish line.

peeled Au film was removed quickly from the detection region so that all emission after the failure was from the surface of the oxidized Si only. A load cell attached to the sample mount measured the applied force during loading. From this record, the critical force at failure (F_m) was obtained. A Channeltron electron multiplier (CEM) and a photomultiplier tube were placed on either side of the sample for simultaneous EE and phE detection. In general, the EE signals were significantly higher than the phE signals due to the higher collection efficiency of the CEM. (The bias on the front of the CEM attracts electrons regardless of the direction of their initial velocity.) The electron and photon signals were accumulated by parallel multichannel scalers which were part of a LeCroy 3500 Data Acquisition system. The data were recorded at 2 ms/channel over a total of 4096 channels for both electron and photon counters. This gave a total duration of data acquisition of 8 s. For display purposes, the data were frequently merged into longer time interval blocks (e.g., 24 ms/block).

III. RESULTS

The EE, phE, and F_m were found to vary over a wide range in intensity within a given type of sample. This is undoubtedly due to the sensitivity of this type of test to small irregularities in sample geometry. Although the adhesive forces may be quite uniform, the value of F_m depends critically on the flaws and stress concentrations at the edges of the epoxy pad. Nevertheless, general trends in the results were found to be highly significant. About 50 samples of each type were tested.

A. Au from Si with native oxide

Figure 2 shows the EE, phE, and load force for a sample of Au on Si with only the native oxide. The time and force at fracture are indicated by the load curve in Fig. 2(c). The

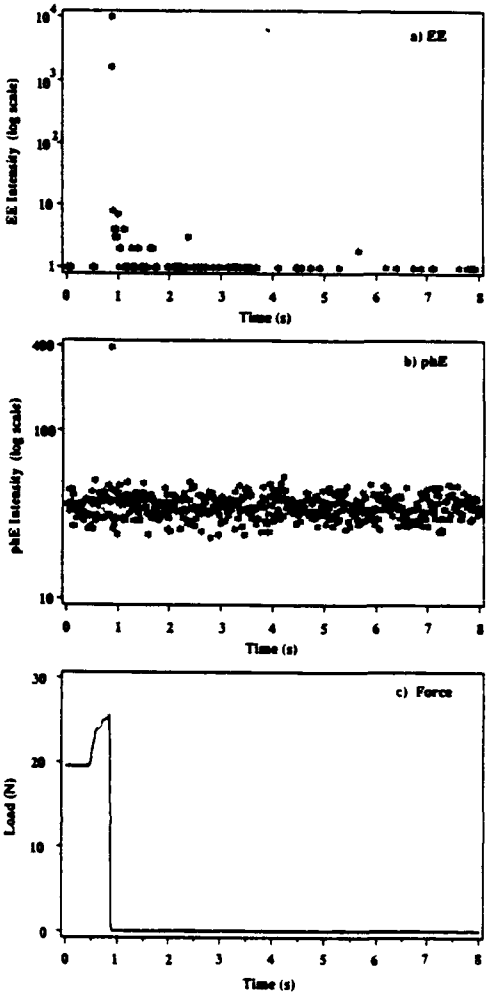

FIG. 2. (a) Electron emission, (b) photon emission, and (c) measured load accompanying the peeling of an Au film from an Si substrate with a native oxide. The sharp drop in the load curve shows the time of fracture.

force required to peel the Au film was about 26 N in this case. This was typical of samples with only native oxides, although some samples were found to exceed the strength of the monofilament line. To the eye, the separation of the Au from the substrate appeared very clean. Both the EE and phE signals show an emission peak immediately upon fracture, i.e., within one channel of the onset of fracture. The peak electron intensity at $\sim 10^4$ counts/channel is ~ 25 times higher than the phE peak partially due to the relative collection efficiencies of the two detectors. The width of the main peak was only ~ 2–4 ms wide, consistent with very intense emission during the failure event, followed by very rapid decay. A weak tail in the EE remains above the background level for a few seconds after fracture. The corresponding tail in the phE, if it exists, is obscured by the relatively high background level of the photomultiplier tube. As

we discuss below, there was considerable variation in F_m and the FE intensities which was basically due to the fracture mechanics of our particular loading situation.

No emission was observed during the loading of this sample. However, several strong samples showed phE during loading due to interfacial failure between the pulling pin and the epoxy, internal to the epoxy. This metal–epoxy failure is the subject of an independent paper.[12]

B. Au from thermally oxidized Si

EE, phE, and force measurements for a sample with an oxide thickness of ~1000 Å is shown in Fig. 3. The load at failure was typically an order of magnitude smaller for the thermal oxides than the native oxides. This reflects qualitatively differences in the strength of adhesion of the Au film with these two substrates. EE and phE begin immediately at fracture with a rise time of only one channel, again consistent with very intense emission during failure. Both the EE and phE decay exponentially over the next five or six channels (~120 ms). After the initial burst, an intense, slowly decaying after-emission persists for several seconds. This emission often continues well beyond the duration of data collection as in Fig. 3. For the thickest oxides, emission continues for over a minute. The phE of Fig. 3 also remains well above background for at least a few seconds; the subsequent integrated emission intensity remains above prefracture levels for even longer. We believe that the EE and phE signals behave essentially the same, and that EE and phE involve similar emission mechanisms. However, the EE measurements provide much more information than phE about the after-emission tail because of a higher signal-to-noise ratio. Cooling of the PMT would greatly reduce this background noise and enhance the use of the phE signal to investigate these excitations that remain on the oxide surface after fracture.

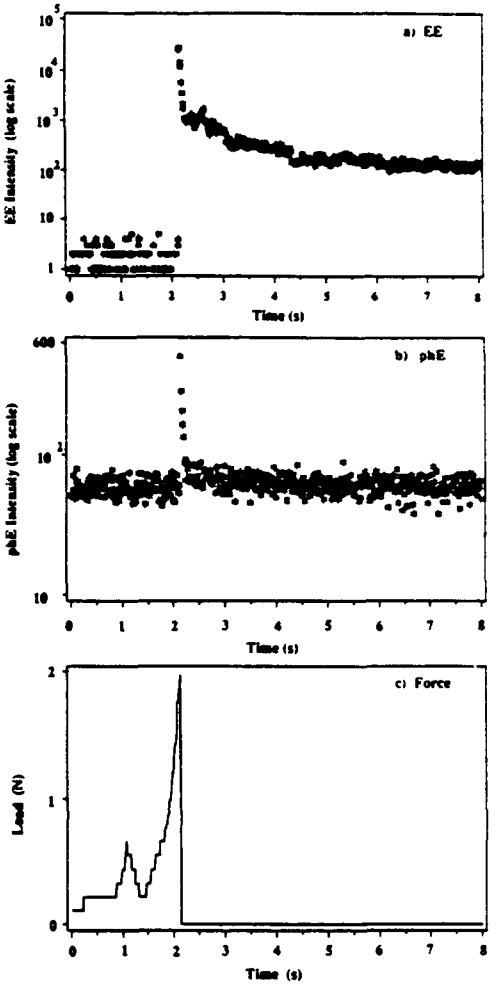

FIG. 3. (a) Electron emission, (b) photon emission, and (c) measured load accompanying the peeling of an Au film from an oxidized Si surface. The oxide thickness is ~1000 Å. The sharp drop in the load curve shows the time of fracture.

C. Au from "clean" Si

A few samples were prepared with a minimum exposure to oxygen by carrying out the Si chemical etching under an Ar atmosphere. The etched sample was transferred directly to the deposition chamber for gold coating. Although we did not have the capability of quantifying contamination of the etched surface prior to the metal deposition, in all likelihood the oxygen uptake was minimal.

Upon adhesive failure of the gold film, very few electrons were observed above background as shown in Fig. 4(a) (observed over a longer time scale than the previous data). Somewhat unexpected, the signal is noisy for some time after fracture. Simultaneous measurements of the photon emission showed no detectable signal above background. These results confirm the general trend of decreasing emission with decreasing oxide thickness, presented graphically in Fig. 4(b) (averages shown).

IV. DISCUSSION

At least two mechanisms appear to be responsible for the observed EE and phE that are characterized by time relative to failure. First, prompt emission occurs *during* the failure event. Since the duration of the peel event is much shorter than the sampling interval, this accounts for the typical one-channel peak in emission at failure. This emission decays rapidly. Prompt emissions from the thermal oxide have a clear exponential tail lasting ~120 ms, while those from the native oxide decay more rapidly. Second, the after-emission (most evident for thick oxides) persists for long times after the Au film is removed from the detection region. This emission is thus from the oxide alone, not the Au. (Note also that

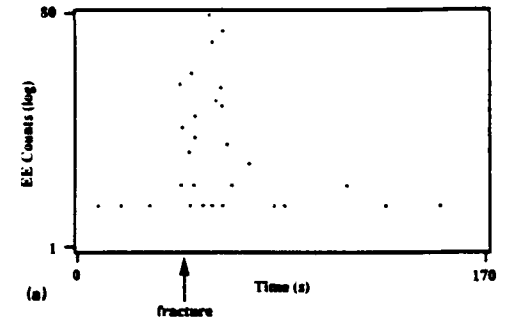

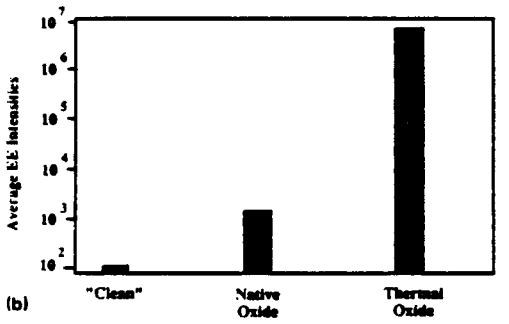

FIG. 4. (a) Electron emission accompanying the peeling of an Au film from a "clean" Au–Si interface. The Si substrate was HF etched in an Ar atmosphere and transferred directly into the metal deposition chamber. (b) Comparison of average EE totaled over 8 s accumulation time for the three types of substrates.

the cohesive failure of metals does not yield FE.) The oxide thickness plays a critical role in the emission behavior in both cases.

We attribute the intense emission *during* failure to electrical discharges across the gap between the two fracture surfaces as a consequence of charge separation. In a variety of fracture systems, charge separation on newly created surfaces can lead to electrical breakdown or microdischarges.[8,9] Local charge separation can result from the separation of an intrinsic dipole, common at material interfaces, where the associated charge separation and resulting FE can be especially strong. Such dipoles are expected in MOS structures because of the difference between the electron affinity of Si and the work function of Au.[13] Thus a potential difference exists between the two materials and the intervening oxide is polarized. A simplified charge density vs position diagram of the MOS structure is shown in Fig. 5. The various charges can be attributed to the effects of sample bias, polarization, $Si–SiO_2$ interface states, and Si band bending. The net effect of these conditions is expected to be a negative charge on the Au film relative to the Si substrate. We assume that the locus of fracture is between the Au film and the oxide layer, therefore yielding a negative charge on the metal and a positive charge on the oxide surface.

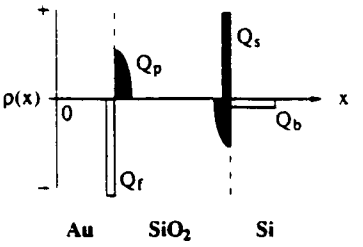

FIG. 5. Schematic diagram of the charge density vs position in the $Au–SiO_2–Si$ system. Q_f is the free charge on the Au film, Q_p is the bound polarization charge in the oxide, Q_s is the net charge of the $SiO_2–Si$ interface states, and Q_b is the free charge in the Si due to band bending. Some trapped charge within the oxide is also expected.

The presence of negative and positive charges on the Au and oxide surfaces, respectively, was confirmed by measurements on each piece after the fracture event. The sign of the charge on the oxide surface was determined by electrically isolating the sample from the loading apparatus, connecting it to an electrometer, and recording the electrometer output with a digital transient recorder. When the Au film was peeled off, the current from the Si sample after fracture indicated a residual positive charge on the sample (i.e., on the oxide). The sign of the charge on the Au-coated epoxy drop was measured by pulling it through a ring which was attached to ground through an electrometer. As the drop passed through the ring, the charge on the drop induced an opposite charge on the ring causing a transient current in the electrometer—first in one direction as the drop approached the ring and then in the other direction as the drop moved away. The sign of these currents indicated that the Au surface was indeed charged negatively, in agreement with our model.

The separation of the charge across the $Au–SiO_2$ interface can result in electrical breakdown when failure occurs at this interface. The Au and the oxide act as oppositely charged capacitive plates being separated by fracture. Flow of charge to surface asperities then results in high local electric fields which eventually result in breakdown and consequently intense EE and phE. The degree of charge separation is limited by tunneling of charge carriers through the oxide, which is severely hindered by the presence of a thick oxide layer. Thus the degree and duration of charge separation on the native oxide are much less than on the thermal oxide accounting for the much more intense and long lasting emissions from the thermal oxide. The rapid, initial decay of EE and phE following failure is presumably due to the decay of electronic surface excitations created during failure, largely due to the bombardment of the charged oxide surface by particles created in the breakdown process. As previously mentioned, because of differences in the loading and initial flaws between samples (i.e., fracture mechanics), the load at failure for the native oxide specimens was quite variable.

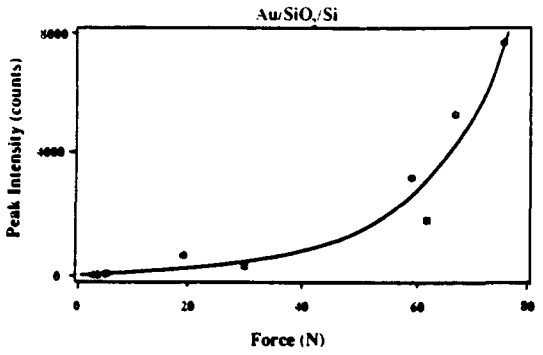

FIG. 6. The electron emission peak intensity (2 ms/channel data) vs applied force at failure for the Au–SiO_2–Si native oxide specimens. Stronger samples result in faster separation of the surfaces due to higher crack speeds which in turn leads to higher charge densities by inhibiting reneutralization.

Thus, because low strength specimens will tend to have slower peel velocities as compared to high strength films, we might expect that reneutralization would occur more readily for low strength samples and therefore exhibit smaller emission curves. In Fig. 6, we plot the peak EE intensity vs force-at-failure (F_m) for several native oxide samples. As can be seen, there is an increasing emission with F_m as predicted. We have previously quantified the increase in EE signals from interfacial failure with crack speed for slower cracks,[14,15] namely fracture of filled elastomers, and seen nearly exponential growth in intensity vs speed.

If the emission during interfacial failure were due directly to bond breaking or localized heating, the FE intensity should increase with the adhesive strength. However, the observed emission increases with oxide thickness, whereas as the oxide thickness increases, the adhesive strength decreases. This suggests that processes such as charge separation and increased excited state lifetimes (due to reduced conductivity) are critical to the increased emission. Thus, for thin or native oxide surfaces the excitations dissipate rapidly and result in intense emission.

Charge separation across the MOS structure may also help explain the relative strengths of the Au–oxide interface in the thermal and native oxides. Au does not form strong chemical bonds to SiO_2, but bonds via van der Waal forces. The dipole formation should contribute to the adhesion, also. The potential difference between the Au and Si is expected to be roughly independent of oxide thickness in thermal equilibrium. The electrostatic force required to separate the charged surfaces in the limit of small separations is proportional to the surface charge densities and the local electric fields, both of which increase linearly with the capacitance of the structure. The increased separation of the Au–oxide and Si–oxide interfaces in the thermal oxide samples relative to the native oxide samples results in a net reduction in capacitance of about a factor of 25. Thus the adhesion of the native oxide would be expected to be a couple orders of magnitude greater than the thermal oxide. This effect may be masked by the effect of mechanical flaws in the sample; nevertheless, from our crude F_m measurements, the observed increase in strength in the native oxides is at least an order of magnitude.

The EE and phE after-emission occurs well after the Au film is out of the interaction region. This rules out small arcs or microdischarges between surfaces as a source of this emission. However, excited states, surface defects, and excess charge will remain on the oxide. On a thin, native oxide, the nearby conductive Si substrate will allow surface excitations to dissipate rapidly. In the extreme, the "clean" Au–Si interface yielded very small amounts of emission. In contrast, on thicker films, excited states will have much longer lifetimes due to the decreased interaction with the substrate. Weinberg has observed the slow decay of excess charge applied to an oxide surface in a Si–O structure to take hours for 1000 Å thermally grown oxide films.[16] Therefore, on time scales of seconds, the oxide surface is effectively isolated from the conductive Si substrate. The energy required for the after-emission of phE and EE from the thick oxides is provided by the relaxation or recombination of these defects on the oxide surface. Recombination of electrons and holes trapped at surface defects can result in decidedly nonexponential kinetics similar to those observed from the thermal oxides. In addition, the thicker oxides will support a greater number of defects. The combination of increased defect densities and longer excitation lifetimes could produce the dramatic increases in emission noted for the thick oxide layers. In a parallel study, we have shown that 1 keV electron bombardment of identical SiO_2 films creates an excited oxide layer that emits sustained, spontaneous EE at room temperature.[17] We expect that the same type of excitations are occurring during separation of the Au films from the substrate.

V. CONCLUSIONS

We have examined the Au–SiO_2–Si system during interfacial failure using fracto-emission. The thickness of the oxide layer plays an important role in the total emission from the system. The adhesive strength of the Au film is significantly reduced with increasing oxide thickness, but the EE and phE intensities increase dramatically in both intensity and duration. During the Au–SiO_2 failure event, an emission peak which decreases in a rapid exponential manner is observed immediately upon fracture while the Au film remains near the sample. This emission is likely the result of charge separation between the two surfaces which produces microdischarges in the gap. Afterward, the oxide surface continues to emit as relaxation of surface excitations and defect states in the oxide occur and excite weakly bound electrons at the surface. This is also strongly dependent on the oxide thickness. For thin or native oxides, the surface interacts with the Si bulk to readily dissipate either surface charges or electronic excitations. However, this interaction is extremely weak on the poorly conducting thick oxides where both emission during fracture and the after-emission are greatly increased in spite of the weakening of the adhesive strength. For films with very little oxide present, the electron emission from adhesive failure is extremely small due to the loss of charge separation by reneutralization via conduction.

ACKNOWLEDGMENTS

The authors wish to thank S.E.H. America, Inc., Vancouver, WA, for providing the Si wafers and Professor Kerry Hipps, Washington State University, for use of his sample preparation facilities. This work was supported by the Ceramics and Electronic Materials Division of the National Science Foundation under Grant No. DMR 8601281, the Office of Naval Research under Contract No. N00014-87-K-0514, the Washington Technology Center, and the Petroleum Research Fund under Grant No. PRF 19196-G5.

[a] Permanent address: Department of Physics, Wesleyan University, Middletown, Connecticut 06457-6036.

[1] J. T. Dickinson and L. C. Jensen, in ASM Proceedings for 13th International Symposium for Testing and Failure Analysis, Los Angeles, CA, November, 1987 (unpublished).
[2] L. A. K'Singam, J. T. Dickinson, and L. C. Jensen, J. Am. Ceram. Soc. **68**, 510 (1984).
[3] B. V. Deryagin, N. A. Krotova, and V. P. Smilga, *Adhesion of Solids* (English translation) (Consultants Bureau, New York, 1978).
[4] J. T. Dickinson, M. K. Park, E. E. Donaldson, and L. C. Jensen, J. Vac. Sci. Technol. **20**, 436 (1982).
[5] J. T. Dickinson, in *Adhesive Chemistry—Developments and Trends*, edited by L. H. Lee (Plenum, New York, 1984).
[6] J. T. Dickinson, *Adhesive Bonding*, edited by L. H. Lee (Plenum, New York) (in press).
[7] J. T. Dickinson, L. C. Jensen, and S. Bhattacharya, J. Vac. Sci. Technol. A **3**, 1398 (1985).
[8] J. T. Dickinson, D. L. Doering, and S. C. Langford, in *Atomic and Molecular Processing of Electronic and Ceramic Materials: Preparation, Characterization, and Properties*, edited by I. H. Aksay *et al.* (Materials Research Society, Pittsburgh, 1988), pp. 39–46.
[9] S. C. Langford, D. L. Doering, and J. T. Dickinson, Phys. Rev. Lett. **59**, 2795 (1987).
[10] J. T. Dickinson, L. C. Jensen, and A. Jahan-Latibari, J. Vac. Sci. Technol. A **2**, 1112 (1984).
[11] F. Lukes, Surf. Sci. **30**, 91 (1972).
[12] Ma Zhen Yi, J. T. Dickinson, and D. L. Doering (in preparation).
[13] A. Goetzberger and S. M. Sze, in *Applied Solid State Electronics*, edited by Raymond Wolfe and C. J. Kriessman (Academic, New York, 1969), Vol. 1, pp. 153–238.
[14] J. T. Dickinson and L. C. Jensen, J. Polym. Sci. Polym. Phys. Ed. **20**, 1925 (1982).
[15] J. T. Dickinson, L. C. Jensen, and H. L. Schreuder-Stacer, J. Rubber Chem. Technol. (in press).
[16] Z. A. Weinberg, Solid State Electron. **20**, 11 (1977).
[17] P. Xiong-Skiba, D. L. Carroll, and D. L. Doering, J. Vac. Sci. Technol. A **8**, 1549 (1990).

XI. Scanning tunneling microscope observations of MgO fracture surfaces

S. C. Langford, Ma Zhenyi, L. C. Jensen, and J. T. Dickinson
Physics Department, Washington State University, Pullman, Washington 99164-2814

(Received 3 October 1989; accepted 18 December 1989)

Scanning tunnel microscope (STM) observations of surfaces of single crystal MgO fractured in three-point bend and coated with thin gold films are reported. Macroscopically, the fracture geometry employed yields a smooth, approximately (027) surface along the tensile side of the sample, and a heavily stepped (001) surface along the compressive side. STM observations of the tensile side show smooth regions approximately (027) in orientation with relatively little relief. These smooth regions are separated by rough regions which often could only be partially imaged with the present instrument. The compressive side showed much more varied structures, with many (001) features as well as features approximately (720) in orientation. Fractal dimension measurements were made on topographs of tensile and compressive side features. Observations of triangular features on the compressive side of one MgO sample show evidence of interaction between the growing crack and dislocation structures. The significance of these microscopic measurements to energy dissipation processes during crack growth in MgO are discussed.

I. INTRODUCTION

The development of the scanning tunneling microscope (STM) has improved the resolution of topographic measurements on conducting and semiconducting materials to atomic levels. Although wide band gap insulators are not suitable for direct STM observations, these materials can be studied with somewhat reduced resolution after applying thin (20–60 Å) films of a conducting material.[1,2] Other techniques, including the use of the atomic force microscope (AFM), are currently under development and promise to yield atomic resolution of fracture surfaces of insulators as well.

Observations of fracture surface topography (fractography) are important tools in the study of fracture.[3,4] Many important elements of the fracture process are reflected in surface features. In the case of brittle fracture, fractography is especially valuable because of the severe constraints imposed on many other techniques by the characteristically high crack velocities involved. STM and AFM techniques have the potential to improve the resolution of fractographic techniques to atomic levels. These techniques may thus address a key obstacle to our understanding of dynamic crack growth: our lack of information on processes at atomic and near-atomic scales. The digital output of these tools is also well suited for numerical analysis, facilitating the computation of quantitative measures of surface structure. Among these, fractal measures are of current interest because of their apparent correlation with material toughness.[5,6]

In this work we describe STM observations of gold-coated, single crystal MgO surfaces created by fracture in three-point bend. MgO is a high resistivity, model ceramic whose fracture properties are of special interest because its semibrittle character facilitates the study of the effects of plastic deformation on fracture behavior.[7–12] We report observations of nm-scale features characteristic of these fracture surfaces and fractal dimension measurements made from typical STM topographs. Evidence for the interaction of the advancing crack with dislocation-related features is also presented.

II. EXPERIMENT

Clear, single-crystal MgO of nominal 99.99% purity was obtained from W. & C. Spicer Ltd. and cut with a diamond saw into samples approximately $1.6 \times 6 \times 12$ mm^3. The cut surfaces were nominally parallel to the crystallographic {100} cleavage planes of MgO. The samples were mechanically polished and loaded to fracture in three-point bend across a support span of 6.4 mm. The samples were promptly transferred to a high vacuum system for gold coating. After cooling the sample to liquid nitrogen temperature, it was coated by evaporation of gold from an alumina boat at a pressure of 1×10^{-5} Pa. The film thickness was monitored with a quartz crystal microbalance adjacent to the sample mount. The sample was then warmed to room temperature over the course of some hours and transferred to a second vacuum system equipped with a McAllister STM 100 scanning tunneling microscope equipped with chemically etched tungsten tips. STM measurements were carried out at pressures of 10^{-8}–10^{-7} Pa. The topographic data were acquired at 256 points per scan, with 64–256 scans per topograph. Scanning was performed in a "back and forth" fashion, yielding one set of scans for each scan direction. The two sets of scans, designated "even" and "odd," were analyzed separately. The STM data displayed here were smoothed once using a weighted eight point average. In some cases, a median filter was also employed.

The use of very thin gold films deposited at low temperatures to facilitate STM observations of insulating materials was reported by Jaklevic *et al.*[1,2] They obtained lateral resolutions of ~10 Å and vertical resolutions of < 0.5 Å with gold films 20–60 Å thick. At this level, no structure attributable to the gold film (atomic steps, grain boundaries, granularity) was observed, despite the reproducible observation of atomic steps on single-crystal Au(111) surfaces under simi-

 0734-2101/90/043470-08$01.00 © 1990 American Vacuum Society

lar conditions. Rather, the behavior of the gold films was similar to that of liquid films wetting the insulator surface. On MgO we found that adequate film continuity was obtained with films as thin as 20 Å.

Determination of the relative orientation of the tensile and compressive surfaces was made by fixing the sample to a goniometer and measuring the angle of rotation required to bring a HeNe laser beam from normal incidence on the compressive side to normal incidence on the tensile side. This process yielded an average angle of 16.6° ± 0.3° over a set of five samples. Comparison of STM scans taken on both sides of the sample often allowed us to infer the orientation of arbitrary planes in each scan.

Fractal dimension estimates were made by Fourier transform and box dimension techniques. A "Fourier" fractal dimension D_f was computed from the averaged power spectra of the individual surface scans making up a surface topograph. In the case of fractional Brownian surfaces, the value of the power spectrum $F(\omega)$ scales as $(1/\omega)^{\beta}$, where $D_f = 3.5 - \beta/2$.[13,14] As suggested by Bonnell,[15] an average $F(\omega)$ was obtained over multiple STM traces. To minimize the effect of the discontinuities at the beginning and end of each scan, the average slope of each topograph was removed by subtracting a plane defined by a least squares fit to the topograph. A "Welch window" was also applied to the data prior to the Fourier transform to minimize the remaining end effects.[16] For surfaces which do not meet the condition of fractional Brownian character, some uncertainty exists in the application of this method. However, an analysis of a geometric figure[17] of known fractal dimension $D = 2.5$ yielded $D_f = 2.60 \pm 0.07$, the uncertainty being the uncertainty in the fit of the slope, β, to the data. Thus, the method appears to give fairly reasonable results even in the extreme case of geometrically fractal objects.

For comparison purposes, fractal box dimension measurements[17] were also made on several topographs. The fractal box dimension D_b was computed by determining the number of cubes required to cover the surface defined by the STM topograph as a function of cube size. Care is required in the interpretation of box dimension measurements due to the self-affine, as opposed to self-similar, character of these surfaces. This self-affinity results from the failure of vertical relief to scale linearly with horizontal surface feature dimensions. Globally, self-affine features do not show fractal character, i.e., in the limit of large cubes such surfaces appear two dimensional. However, in the limit of small cubes, self-affine surfaces show fractal character in that the number of cubes required to cover the surface scales with $(1/b)^{D_b}$, where b is the length of a cube edge. In this work, the largest cubes employed had sides equal to the maximum vertical relief of the surface, and the smallest cubes had sides equal to twice the distance between successive scans. Box dimensions computed with this range of cube sizes appeared to be fairly insensitive to noise while avoiding the tendency toward two dimensionality. Reliable measurements apparently require a large number of scans per topograph. Fourier methods were thus used on topographs composed of fewer scans. Given adequate counting statistics, our D_b measurements generally agreed with our D_f measurements on the same surface to within ± 0.1. Improvements in the data processing may eventually improve this agreement.

III. RESULTS

In our three-point bend geometry, fracture usually initiates at a pre-existing flaw on the edge of the tensile side of the sample. Fracture then proceeds along a (001) plane to produce a smooth "mirror" zone ~ 100 μm in diameter. At the edge of the mirror zone, extensive crack branching results in a rough, hackled surface. In this geometry, many of the crack branches eventually coalesce to form a broad, smooth surface along the tensile side of the sample propagating in the [100] direction but inclined about 16° to the (001) cleavage plane. This behavior is evident in Figs. 1(a) and 1(b), which show optical micrographs of a typical fracture surface illuminated from above with light parallel to the normals of the compressive and tensile surfaces. A diagram indicating the orientation of the various surface features is shown in Fig. 1(c). The bright features in Fig. 1(a) are parallel to the (001) plane, while the bright features in Fig. 1(b) are parallel to the (027) by virtue of the direction of illumination. The abrupt jogs in the surface steps between the tensile and compressive sides indicate that crack growth was arrested in this region. The macroscopic surface steps on the compressive side show that crack growth here proceeds at right angles to crack growth on the tensile side, i.e., in the [010] direction. Further, the brightness of the compressive side features indicates that fracture here is largely confined to the (001) plane. We have designated the plane inclined along the tensile side of the sample the (027) plane, which is a relatively low-index plane having the approximate orientation of the observed surfaces.

A. Tensile side

A STM image of a smooth region on the tensile side appears in Fig. 2(a). The orientation of this surface is ~ (027) over the region of the scan, with some short steps 10–20 Å high. Some patches of the scan are consistent with (001) planes, the largest being about 150 × 400 Å^2 in this scan. Considerable coalescence and breakup of these step like features is apparent along the path of the crack. In the smoothest portions of this and similar scans, the (001) steps necessary to accommodate the surface inclination are not visible. Average power spectra of the STM surface scans of Fig. 2(a) are shown in Fig. 2(b) for the two scanning directions. These power spectra are reasonably linear over frequencies corresponding to wavelengths from 10 to 500 Å along the surface. The corresponding fractal dimension for this region is $D_f \sim 2.36 \pm 0.07$. The number of scans in this image was not adequate for reliable box dimension estimates. Smooth regions, such as that shown in Fig. 2(a), are typically separated by rough regions which we could only partially image, presumably due to anomalies in the gold film.

Two images of a rougher region appear in Figs. 3(a) and 3(b). Figure 3(b) is a smaller scan of an adjacent region near the one in Fig. 3(a). The approximate direction of crack growth is from top-left to bottom-right. These images show evidence of extensive crack branching. The surface is largely

Optical Photographs of MgO Fracture Surfaces

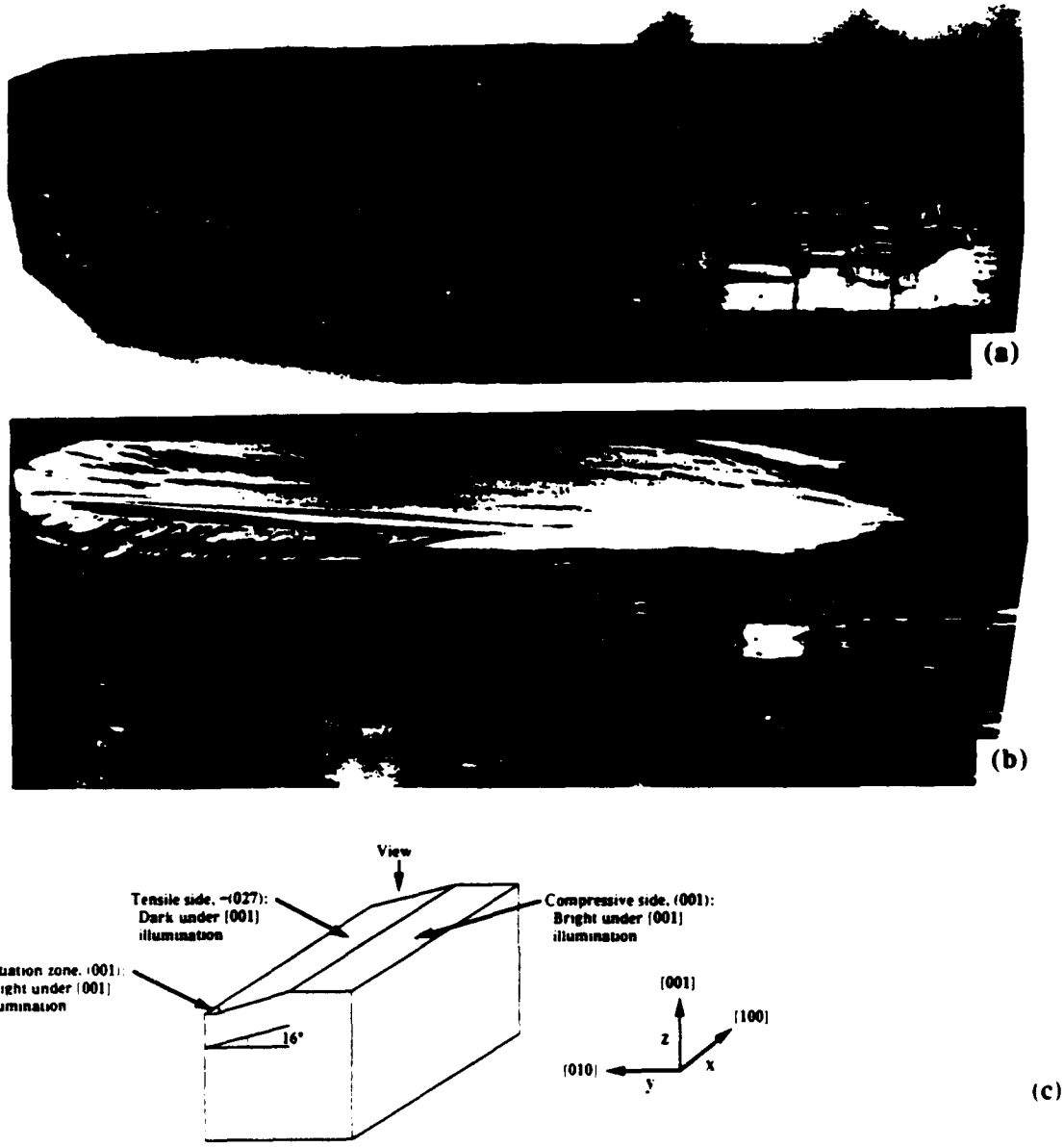

FIG. Optical photographs of a MgO fracture surface produced in three-point bend (a) illuminated along the [001] direction, normal to the compressive side, and (b) illuminated along the [027] direction, normal to the tensile side. The geometry of the features is indicated in (c). In (a), the initiation zone is at the upper right hand corner of the sample.

composed of small, parallel plateaus at different "elevations" on the fracture surface. The plateaus are separated by gently sloping regions with more distinct steps aligned parallel to the direction of crack growth. At least two plateau orientations appear to propagate stably in Fig. 3. Two plateaus with different orientations are evident in the top, central portion of Fig. 3(b). These two surfaces are inclined to one another by an an angle of about 31°. This is very nearly equal to the 32° angle between two {027} family surfaces parallel to the x-axis, suggesting that crack propagation on either of these {027} planes is preferred over the intermediate (001) plane.

Both Fourier and box dimensions of a somewhat larger area containing those shown in Fig. 3 were computed from

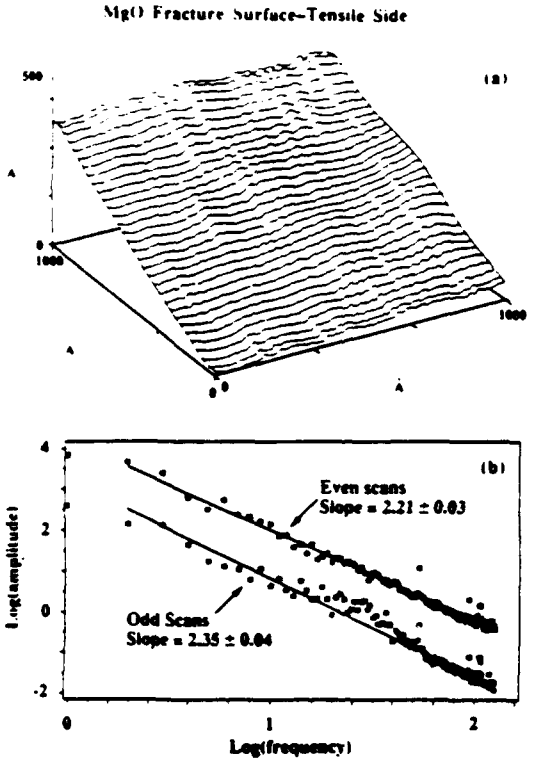

FIG. 2. (a) A typical STM topograph of a smooth surface on the tensile side. The orientation of this surface is approximately (027). (b) Power spectra of the scans making up the topograph of (a). The lines which extend through the points were used in the slope calculation.

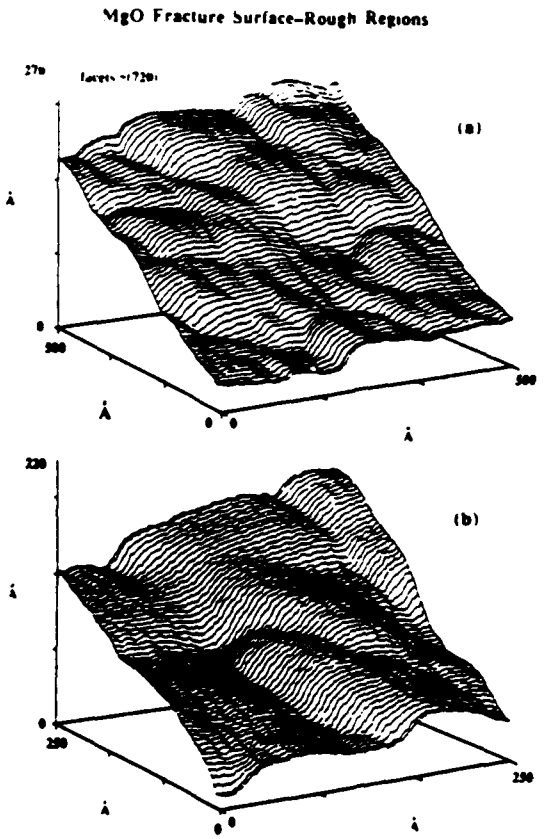

FIG. 3. STM topographs of a rough region on the tensile side of a sample. The topograph of (b) was taken in a region near the surface shown in (a).

the topograph shown in Fig. 4(a). For purposes of the analysis, the average slope of this 256-scan topograph has been removed. The box dimension box counts and power spectra are displayed on log-log plots in Figs. 4(b) and 4(c), respectively. The slope of the linear portion of the box count curve $\{\log [N(b)]$ versus $\log(1/b)\}$ indicates a fractal dimension D_b of about 2.44. The oscillations in the box count at large cube sizes (low $1/b$) are an artifact of the analysis. The power spectra show a long linear section with a slope of -2.33, corresponding to a fractal dimension, $D_f = 2.34$. The linearity of the curves in Figs. 4(b) and 4(c) is strong evidence for consistent fractal character over more than a decade of length scales.

A parameter which appears to be relevant to the resulting topography of the fracture surface is the crack velocity. Average crack velocity measurements made with timing strips along the tensile side of the crystal yielded values in the 3–5 km/s range, and almost always in excess of 4 km/s. This is a substantial fraction of the Rayleigh wave velocity on (001) surfaces in the [100] direction (5.5 km/s). The Rayleigh wave velocity represents an upper limit on the crack velocity in that a growing crack behaves much like a propagating surface wave.

B. Compressive side

A typical scan taken from the compressive side of the sample appears in Fig. 5(a). Here the crack propagated approximately from corner to corner, from right to left. The scanned region is (001) in overall orientation, but obviously shows a great deal of structure on smaller scales. The largest (001) patch in this scan is about 300×300 Å^2, but several smaller features have ~(027) as well as other intermediate orientations. The average feature size on the compressive side is typically much larger than that on the smooth portions of the tensile side, suggesting more uniform, less "chaotic" crack growth. At several places in the figure, V-shaped valleys appear to grow and disappear. To aid the reader, several of these V-shaped features have been identified in Fig. 5(a) by lines along their minima. The planes making up the walls of fully developed features share similar non-(001) orientations, suggesting that crack growth on these planes is stable over limited distances.

The averaged power spectra of the scans of Fig. 5(a) are shown in Fig. 5(b). The linear portion of these curves correspond to $D_f = 2.01 \pm 0.16$, which is consistent with a non-fractal character. However, the distinctly nonlinear form of the power spectra is inconsistent with fractional Brownian character, so that the interpretation of this result is open to question.

Topographs of other regions on compressive side surfaces did show definite fractal character, including the topograph shown in Fig. 6(a). This surface is composed of two (001) planes separated by a roughly 500 Å step. The box dimen-

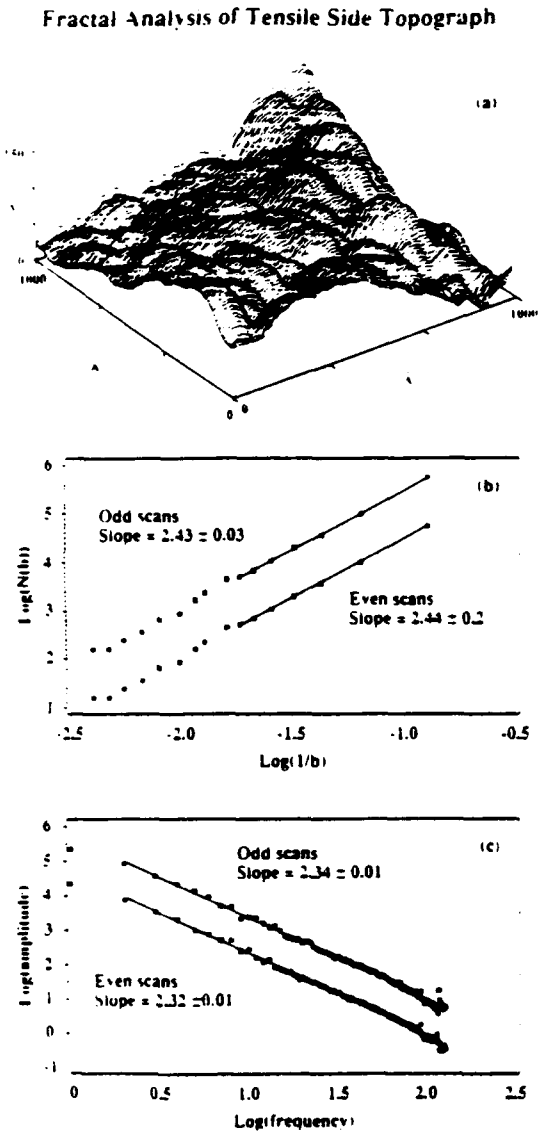

FIG. 4. Fractal analysis of a tensile side topograph. (a) Topograph with background slope subtracted for analysis. (b) Log-log plot of $N(b)$, the number of cubes of edge length b required to cover the topograph, versus $1/b$. (c) Power spectra of the scans making up the topograph.

sion analysis of Fig. 6(b) indicates a fractal box dimension $D_b = 2.42$. The linear portions of the power spectra shown in Fig. 6(c), however, are consistent with a higher fractal dimension $D_f = 2.58$. Although the power spectra of Fig. 6(c) are considerably more linear than that of Fig. 5(b), it is not clear that a single fractal dimension characterizes the scan over much of the range of scale. The fractal box dimension measurement is less ambiguous in this regard, and thus

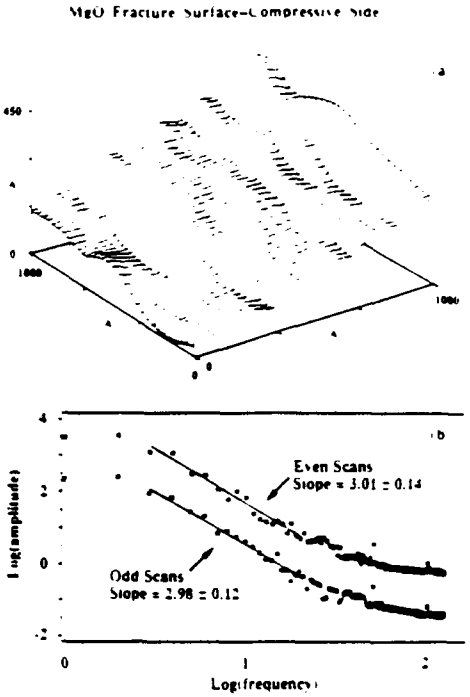

FIG. 5. (a) STM topograph of a typical region on the compressive side. The region shown is mostly (001) in orientation. (b) Power spectra of the topograph of (a). The lines extend through the points used in the slope calculation.

is probably the more reliable fractal measure in this case. In general, the power spectra of compressive side surfaces were generally considerably less linear than those from the tensile side surfaces, leading to uncertainties in the fractal dimensions inferred from the slope of any linear portion.

Direct crack velocity measurements were not attempted on the compressive side due to the shortness of the path traveled by the crack. However, certain fractographic features on the compressive side appear to be due to interaction of the advancing crack with reflected longitudinal acoustic waves. From the spacing between these features, crack velocities on the order of 2–3 km/s are estimated. Thus, crack velocities on the compressive side are significantly lower than on the tensile side.

C. Triangular features on compressive side

One series of scans revealed several peculiar triangular structures on the compressive side of a sample. Two scans of one of these features appear in Fig. 7, taken with a slight shift in the origin. The crack propagated roughly from the top of the figure down. The triangular features display a sharp step up to 300 Å high and oriented roughly parallel to the (110) or ($1\bar{1}0$) plane. The bottom of the hole can be quite rough, but becomes gently sloping as one moves away from the (110) step. Frequently one observes broad features formed as the main crack passes beyond the triangular hole, as if the

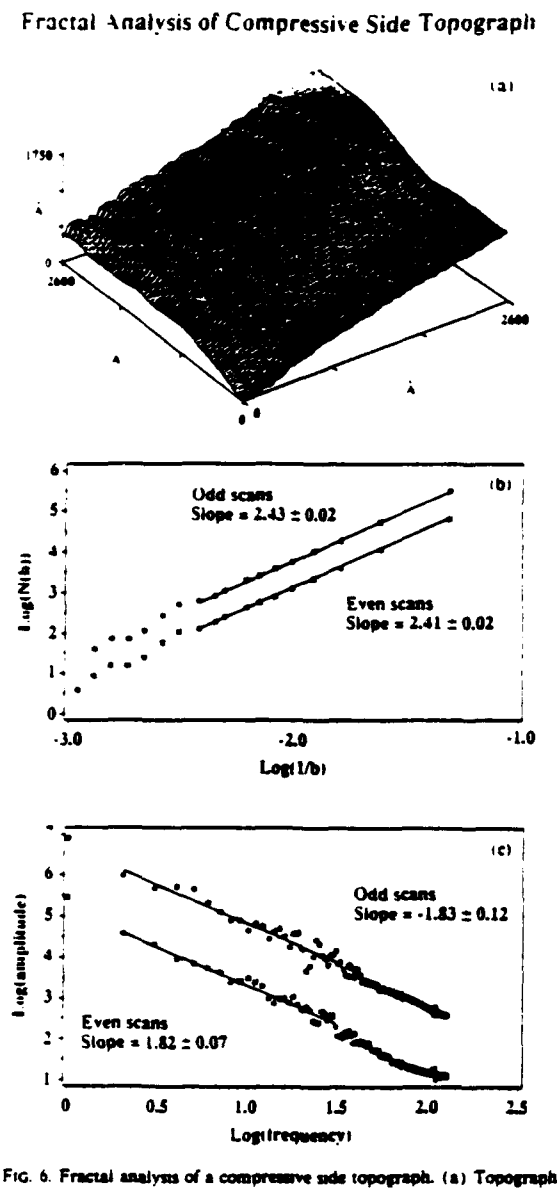

FIG. 6. Fractal analysis of a compressive side topograph. (a) Topograph without background slope subtracted. (b) Log-log plot of $N(b)$, the number of cubes of edge length b required to cover the topograph, versus $(1/b)$. (c) Power spectra of the scans.

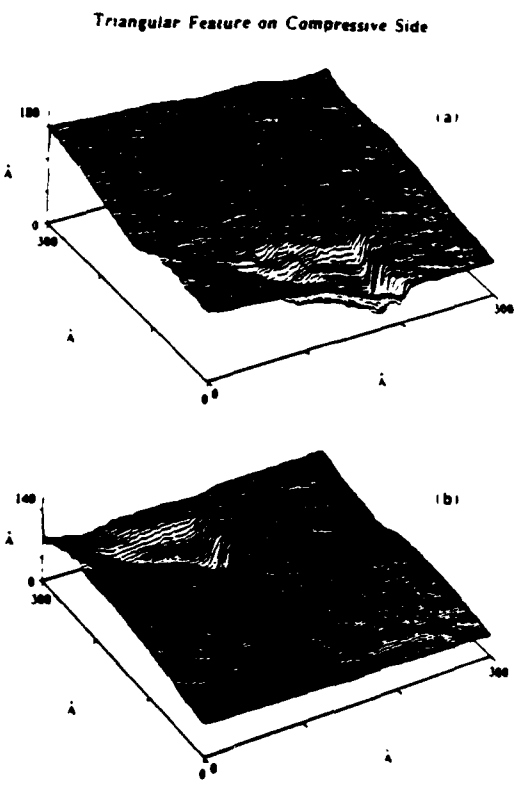

FIG. 7. Two scans of a triangular feature on the compressive side of one sample with slight shifts in the origin.

crack was deflected by an extended structure in the bulk. As discussed below, plastic deformation on the compressive side of the crystal prior to failure is believed to play an important role in creating these structures.

IV. DISCUSSION

The presence of $-(027)$ fracture surfaces requires that the crack leave the normal (001) cleavage plane of MgO. On the tensile side of the sample, the crack initially propagates in the [100] direction on the (001) plane, and eventually rotates about the axis defined by the [100] direction. A similar departure from the normal cleavage planes was reported by Miles and Clarke in thermally shocked MgO.[7] Stokes, Johnston, and Li have published photographs of MgO fracture surfaces formed in three-point bend which are very similar to our own,[8] but made no mention of this effect. Interestingly, the dimensions of the samples used in their work were about double ours in each dimension. Rice has reported a crack branching angle of $16° \pm 5°$ for MgO in flexure,[4] in close agreement with our observations. However, Rice may have referred to a different branch geometry. We often observe both macroscopic (027) and $(0\bar{2}7)$ surfaces on the tensile side of the same sample, but rarely on the compressive side. In contrast, on the scale of tens of nm, surfaces with {027} orientations are frequently observed on both tensile and compressive sides. This observation may be related to the fact that crack propagation on each side proceeds in a crystallographically equivalent direction ([100] versus $[0\bar{1}0]$), so that crack growth in each region experiences equivalent effects of crystal anisotropy.

Surfaces intermediate in orientation between (001) and (027) are also observed in this fracture geometry on both tensile and compressive sides (cf. Figs. 3 and 5). Since relatively large areas of {027} surfaces are observed, this sug-

gests that the production of {027} surfaces is to some degree a stable process in rapid crack growth. The intermediate orientations may well be produced as an accelerating crack moves from the minimum energy (001) configuration to a dynamically more stable {027} configuration. The presence of the "preexisting" tensile side crack during fracture through the compressive side macroscopically constrains the crack on the compressive side to a roughly (001) orientation. Competition between the dynamically more stable {027} family surfaces and the global constraint to (001) may explain the roughness of the surface on the nm scale and the larger feature sizes observed on the compressive side relative to the tensile side. Differences in crack velocity and dynamic stress intensity (an effective "crack driving force") may also affect surface feature size and roughness.

The cause of the apparent stability of {027} family cracks in this geometry is not clear. Samples loaded in three-point bend experience significant shear stresses and these can alter the course of a crack. However, the expected distribution of shear and tensile stresses in these samples is inconsistent with the rather uniform tendency to form {027} surfaces. A more likely explanation lies in the forces of constraint experienced by material near the crack tip. The presence of the crack results in a dramatic stress concentration at the crack tip. The tremendous tensile stresses normal to the crack are accompanied by somewhat smaller tensile stresses in the plane of the crack. The constraint provided by relatively unstrained material at some distance from the crack tip which hinders the contraction of the material in the plane of the crack, thus enforcing a state of plane strain near the crack tip. Given the elastic constants of single crystal MgO, one can show that a surface inclined 16.9° to the (001) plane allows the simultaneous relaxation of both normal and in-plane components of stress. This is consistent with the observed inclination of 16.6° ± 0.3°. In any scenario, the initial formation of these features requires a high degree of crack branching or nucleation, followed by coalescence of the resulting microcracks.

The propagation of a crack on a (027) plane requires significantly more energy than on a (001) plane. Tasker and Duffy[18] have estimated that the energy required to form an atomic step on a (001) surface is about 3.72×10^{-10} Jm^{-1}. An additional energy term due to a repulsive force between steps is significant at step spacings less than a few lattice constants. Assuming uniformly distributed atomic steps, the energy required to form a (027) surface is about 25% more than that required for a (001) surface. Although some reduction in energy is possible by formation of larger steps, Atomic Force Microscope observations in our laboratory of *uncoated* MgO surfaces indicate that on smoother portions of the tensile side, the steps are indeed atomic.[19] In addition, the vertical resolution in Figs. 2 and 3 is sufficient to reveal steps as large as 2–4 atomic layers, and these are not seen. In rapid crack growth, the available energy exceeds that required for (001) surface formation, so that the production of higher index surfaces is energetically allowed. The major factor dictating the extent of deviation from the (001) orientation may well be crack speed.

The plateau-like features of Fig. 3 suggest that the microscopically rough regions of tensile side fracture correlate with extensive microcracking. Optical micrographs of the tensile side of the fracture surface under normal (027) illumination often show evidence of finger-like structures. These structures are not visible in Fig. 1 due to the poor illumination of this region. Nor are the fingers typically observed in STM micrographs, suggesting that adjacent fingers are very nearly coplanar. If the fingers or analogous structures correspond to the smooth regions identified by the STM, the rough areas are likely regions between adjacent fingers. These fingers apparently grow and branch at high velocity through the tensile side of the sample while remaining very nearly coplanar. Fracture through the material between the fingers occurs somewhat later, perhaps after substantial local plastic deformation. The combination of the small edge mismatch or overlap between adjacent fingers and a high degree of plastic deformation could result in a very rough fracture surface on length scales probed by the STM. The small size of the features in Fig. 3, typically less than 100 nm, would make them invisible to optical microscopy and standard SEM techniques. STM scans of areas significantly larger than the presently attainable 3 × 3 μm^2 should reveal any finger-like structure in the smooth areas, if present.

Fractal analysis of topographs of tensile side features yielded fractal dimensions consistently in the 2.3–2.5 range. The surface roughness required to form these fractal surfaces indicate that substantial crack deflection or branching occurs over the range of length scales probed by the STM. This substantially increases the energy required for crack advance beyond that required to produce the already energetic {027} surfaces. The fractal nature of these features might result from a dynamic instability in rapid crack growth. Analysis of fluctuations in the intensity of triboluminescence emitted during the fracture of MgO in this geometry suggests that crack growth is actually chaotic.[20] Associated with chaotic fluctuations in the progress of the crack front may be growth and coalescence of microcracks in the process zone which would lead to fractal structures, analogous to certain diffusion and aggregation processes which exhibit chaotic fluctuations and fractal geometry.[21]

The fractal dimension measurements of the compressive side scans were less consistent. The power spectra were typically less linear than those of tensile side scans and thus were less amenable to a fractal description. However, the box dimension measurements of some scans were well behaved, with values comparable to those of tensile side surfaces. Some portions of the compressive side have little, if any, fractal character, being comparable in this regard to large area, low-energy cleavage surfaces. Other portions of the compressive side are fractal, similar to the tensile side surfaces. Local variations in crack velocity or other fracture parameters may lead to variations in fractal character on the compressive side.

The transition from fractal to nonfractal character could involve a transition from chaotic to nonchaotic behavior in crack dynamics, i.e., a gradual shift in the length scales asso-

ciated with chaotic or fractal fluctuations. Slow, stable crack growth along (001) cleavage planes may involve "branches" confined to subatomic length scales, leaving no extended features on the fracture surface. Rapid, off axis crack growth involves branching and coalescence in a larger volume (process zone) which could determine the maximum length scale for which fractal features are observed. It is reasonable that the size of the process zone is controlled by the local crack velocity or stress intensity. The lower crack velocities on the compressive side relative to the tensile side are consistent with an association between crack velocity and fractal character.

The triangular features observed in Fig. 7 are strong evidence for dislocation/crack interactions. The energy required for the formation of {110} family surfaces is on the order of 2.92 Jm^{-2},[18] more than double that required for the formation of {001} surfaces. Thus, crack branching to form two {001} surfaces is energetically preferred over propagation on a {110} surface. Significantly, observations of {110} fracture surfaces have been largely confined to plastically deformed material in which stress concentrations at the intersection of slip bands have resulted in fracture proceeding on a plane parallel to the {110} family slip plane.[8,9] When a (110) crack reaches a critical (Griffith) length, the crack typically branches to a nearby (001) plane.

The geometry of these features is consistent with the formation of cracks by the Keh mechanism.[11] The required geometry of intersecting cracks and slips bands is shown in Fig. 8. The Keh crack is formed as dislocations on (101) and (011) slip planes pile up against immobile dislocations formed at the plane intersection. These cracks have been observed in indented and impacted MgO,[10,11] and contrast with Cotrell and Stroh cracks in that they involve different slip geometries. Slip on {101} and {011} planes during the bending deformation of single crystal MgO have been observed by Bruneau and Pratt.[12] Typically, slip on the compressive side was observed to be largely confined to the $(110)/(1\bar{1}0)$ system. However, slip on the $(101)/(10\bar{1})$ system was observed near the region of loading nose contact. In three-point bend, fracture passes through the region of loading nose contact, so that interactions between these two sets of slip planes may be expected. Given the geometry of Fig. 10, the propagating crack encounters the (101) and (011) slip planes soon after intersecting the Keh crack. Corresponding features in Fig. 7 show that the main crack was in fact deflected upon encountering these slip planes. The presence of these features on the fracture surface require the near intersection of two slip planes and the main fracture plane. By plastically deforming the samples prior to fracture, a high density of slip plane intersections can be produced, thereby enhancing the number of such structures. To monitor the extent of plastic deformation introduced, we can measure the prefailure triboluminescence intensity, which has been linked to the motion of dislocations in MgO.[25] Using such techniques in combination with STM and AFM measurements, we plan to study such features in detail.

Mechanism for Production of Triangular Features

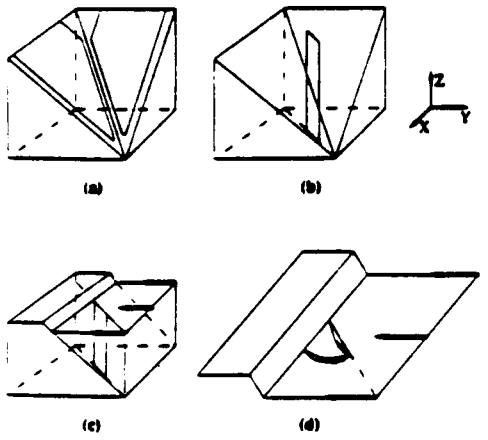

FIG. 8. The formation of a Keh crack and resulting triangular feature. (a) Dislocations on the (101) and (011) slip systems. (b) Production of a Keh crack (the vertical rectangle) in the $(1\bar{1}0)$ plane. (c) Intersection of cleavage crack with the Keh crack. Arrows indicate direction of cleavage crack growth. (d) Production of triangular feature as the cleavage crack runs around the Keh crack and against the slip band in the (011) plane.

V. CONCLUSIONS

STM observations of gold coated MgO fracture surfaces formed in three-point bend indicate that under conditions of rapid crack growth, a crack can propagate stably on non-crystallographic planes with steps no larger than 5–10 Å over distances of hundreds of nm. The tensile surface of these samples is composed of smooth regions with approximately {027} orientation separated by much rougher regions. These observations are consistent with the simultaneous growth of parallel finger-like cracks on nearby planes with approximately {027} orientation, followed by a complex series of microcracking events through the material between adjacent fingers. Small regions with this orientation are found on the compressive side, but the compressive side appears to be for the most part constrained to (001) surfaces. The average feature size on the compressive side of the sample was typically much larger. Triangular features on the compressive side of one sample are evidence for interesting interactions between slip bands to produce Keh cracks, and the interaction of both with the main fracture event. The production of high energy surfaces with extensive microcracking can dissipate a great deal of energy relative to that required to form the low-energy (001) cleavage surface of MgO. Crack deflection by slip bands would also augment energy dissipation during crack growth.

Presently, the process of crack branching is poorly understood.[22–24] Recent observations by Ravi-Chandar and Knauss[24] support a model which involves the nucleation, coalescence, and interaction of microcracks in a "process zone" in front of the crack tip. Our observations suggest that such a model may be applicable to rapid crack growth even in semi-brittle crystalline materials.

With the resolution available with STM and AFM techniques, small features which presumably reflect early stages in the process of nucleation and coalescence may be observed. The ability of fractal analysis to characterize certain

complex experimental and theoretical results may provide a powerful means of comparing theory and experiment. STM and AFM observations promise to contribute to our understanding of dynamic fracture on atomic and near-atomic length scales, especially as they relate to energy dissipation and crack nucleation and coalescence. This understanding should ultimately improve our ability to predict the consequences of fracture in brittle materials.

ACKNOWLEDGMENTS

This work was supported by the Office of Naval Research, Contract No. N00014-87-K-0514, the Ceramics and Electronic Materials Division of the National Science Foundation under Grants Nos. DMR 8601281 and DMR 8912179, and the Washington Technology Center. The authors wish to thank John Hirth and Richard Hoagland, Washington State University, Dawn Bonnell, University of Pennsylvania, and Jack Mecholsky, Pennsylvania State University, for helpful discussions.

[1] R. C. Jaklevic, L. Elie, Weidian Shen, and J. T. Chen, J. Vac. Sci. Technol. A 6, 448 (1988).
[2] R. C. Jaklevic, L. Elie, Weidian Shen, and J. T. Chen, Appl. Phys. Lett. 52, 1656 (1988).
[3] Roy W. Rice, in *Fractography of Glasses and Ceramics*, edited by J. R. Varner and V. D. Frechette (American Ceramic Society, Westerville, OH, 1988), pp. 3–56.
[4] Roy W. Rice, in *Fractography of Ceramic and Metal Failures*, edited by J. J. Mecholsky, Jr. and S. R. Powell, Jr. (ASTM STP 827) (ASTM, Philadelphia, 1982), pp. 5–103.
[5] J. J. Mecholsky, D. E. Passoja, and K. S. Feinberg-Ringel, J. Am. Ceram Soc. 72, 60 (1989).
[6] B. B. Mandelbrot, D. E. Passoja, and A. J. Paullay, Nature 308, 721 (1984).
[7] G. D. Miles and F. J. P. Clarke, Philos. Mag. Ser. 8 6, 1449 (1961).
[8] R. J. Stokes, T. L. Johnston, and C. H. Li, Philos. Mag. Ser. 8 4, 920 (1959).
[9] A. S. Argon and E. Orowan, Philos. Mag. Ser. 8 9, 1023 (1964).
[10] A. S. Keh, J. C. M. Li, and Y. T. Chou, Acta Metall. 7, 694 (1959).
[11] W. F. Adler and T. W. James, in *Fracture Mechanics for Ceramics, Rocks, and Concrete*, edited by S. W. Freiman and E. R. Fuller, Jr., (American Society for Testing and Materials, Philadelphia, 1981), pp. 271–290.
[12] A. A. Bruneau and P. L. Pratt, Philos. Mag. Ser. 8 7, 1871 (1962).
[13] B. B. Mandelbrot and R. F. Voss, in *Noise in Physical Systems and 1/f Noise*, edited by M. Savelli, G. Lecoy, and J-P. Nougier (Elsevier, Amsterdam, 1983), pp. 31–39.
[14] D. L. Turcotte, Annu. Rev. Fluid Mech. 20, 5 (1988).
[15] D. A. Bonnell, Department of Materials Science, University of Pennsylvania (private communication).
[16] W. H. Press, B. P. Flannery, S. A. Teukolsky, and W. T. Vetterling, *Numerical Recipes* (Cambridge University, Cambridge, 1986), pp. 423–429.
[17] B. B. Mandelbrot, Phys. Scr. 32, 257 (1985).
[18] P. W. Tasker and D. M. Duffy, Surf. Sci. 137, 91 (1984).
[19] S. Anderson, J. T. Dickinson, and L. C. Jensen (in preparation).
[20] S. C. Langford, Ma Zhenyi, and J. T. Dickinson, J. Mater. Res. 4, 1272 (1989).
[21] Paul Meakin, in *Phase Transitions and Critical Phenomena*, edited by C. Domb, and J. L. Lebowitz, (Academic, London, 1988), Vol. 12, pp. 335–489.
[22] J. P. Dempsey and P. Burgers, Int. J. Fract. 27, 203 (1985).
[23] K. Ravi-Chandar and W. G. Knauss, Int. J. Fract. 25, 247 (1984).
[24] K. Ravi-Chandar and W. G. Knauss, Int. J. Fract. 26, 65 (1984).
[25] S. C. Langford, J. T. Dickinson, and L. C. Jensen, J. Appl. Phys. 62, 1437 (1987).

XII. Scanning Tunneling Microscope Observations of Polymer Fracture Surfaces

D. M. Kulawansa, S. C. Langford, J. T. Dickinson
Department of Physics
Washington State University
Pullman, WA 99164-2814

and

R. P. Dion
The Dow Chemical Company
Designed Thermoplastics Research
Midland, MI 48667

Abstract

Scanning tunneling microscope observations of gold-coated polymer fracture surfaces are reported. We compare nm-scale surface features of poly(methyl methacrylate) (PMMA) fractured under three different loading conditions: in tension at room temperature, in tension at liquid nitrogen temperature, and in the double cantilever beam geometry at room temperature (slow crack growth). Fracture surfaces of polystyrene and polycarbonate loaded in tension at room temperature are also described. Each of these surfaces show distinctive nm-scale features which we interpret in terms of the fibrils, steps, and voids. The resolution of these images is sufficient to greatly complement other fractographic studies.

INTRODUCTION

Observations of fracture surface topography (fractography) have contributed greatly to our understanding of fracture,[1] since many important fracture process are reflected in surface features. In the case of brittle fracture, fractography is especially valuable because direct observations of the very rapid crack growth in brittle materials is quite difficult. The development of scanning tunneling microscopy (STM) offers the possibility of resolving the topography of smooth conducting and semiconducting surfaces to atomic levels. Atomic force microscopy (AFM) has provided similar information on smooth insulating surfaces, e.g., NaCl[2] and BN.[3] Atomic resolution has not been achieved with either technique on rougher surfaces, which are commonly encountered in brittle fracture. Nevertheless, the sub-nanometer resolution of AFM and STM on fracture surfaces is in many instances a substantial improvement over alternate microscopies with minimal sample preparation.

Although insulators lack the necessary conductivity for direct STM observations, these materials can be imaged with somewhat reduced resolution after applying thin (10-60 Å) films of a conducting material[4-6] We estimate the horizontal resolution of our method applied to polymer surfaces to be on the order of 0.5 nm. Since relatively rough surfaces cannot now be imaged with atomic resolution, the lack of atomic resolution with coated surfaces is not a serious limitation relative to the principle alternative, AFM. However, in any probe-based microscopy, images of rough surfaces can be distorted due to the non-negligible size of the probe tip relative to the size of the imaged features. Reiss et al.[7] and Denley have addressed this problem for the case of the STM.[8] In most cases, artifacts due to surface-tip interactions are readily identified. Although the fracture surfaces discussed below may be considered rough on the nm-scale, we emphasize that they are all microscopically quite smooth. Regions with vertical relief greater than a few hundred nm cannot be reliably imaged with our instrument.

In this work we describe STM observations of gold-coated polymer surfaces formed under a variety of conditions. These include fracture surfaces of poly(methyl methacrylate) (PMMA) loaded in tension at room temperature, in tension at liquid nitrogen temperature, and in the double

cantilever beam geometry at room temperature. Fracture surfaces were also formed by slow, controlled crack growth using the double torsion geometry. Finally, observations on polystyrene (PS) and polycarbonate (PC) samples fractured in tension at room temperature are presented to demonstrate the effect of polymer composition. To ensure that the observed features were representative, a great number of scans were taken: about 190 scans of all PMMA fracture surfaces combined, and about 100 each of PS anc PC. Although the total *area* sampled by each of these scans is small, they are representative of much larger portions of the fracture surface.

EXPERIMENT

PMMA samples were prepared from commercial material (Plexiglass MG–Rohm and Haas) by machining 0.32 cm sheet into 6.3 x 1.3 cm^2 rectangles. These samples were notched with a saw in the middle of the gauge length. The PS was Styron 680 (The Dow Chemical Company), with molecular weights M_w = 194,700 and M_n = 74,000, and glass transition temperature T_g = 108 °C. The PC was Calibre 300-10 (The Dow Chemical Company), with M_w = 42,400 and M_n = 21,900, and T_g = 159 °C. Both PS and PC samples were machined into unnotched dogbones from compression molded bars, 6.3 x 1.3 x 0.32 cm^3. PMMA double torsion samples were prepared from 0.16 cm sheet machined to 7.6 x 2.5 x 0.16 cm^3 and edge notched with a hot scalpel blade.

After fracture, 6 x 6 mm^2 sections, 1.5 mm thick, were cut from the fracture surface and promptly transferred to a high vacuum system for gold coating. After cooling to liquid nitrogen temperature, the samples were coated by gold evaporated from an alumina boat at a background pressure of 1 x 10^{-5} Pa. The metal film thickness was monitored by a quartz crystal microbalance adjacent to the sample. The films employed in this work were 35-50 Å thick. The sample was then warmed to room temperature over the course of several hours. This coating procedure yielded reliable conductivity. Tests on cleaved single crystal mica and flat silica glass plates showed minimal evidence of surface roughness due to the gold overlayer.

STM measurements were carried out in air with a double tube instrument[9] equipped with etched tungsten tips. The topographic data were acquired at 256 points per scan, with 128 or 256 scans per topograph. Scanning was performed in a "back and forth" fashion, yielding one set of scans along each scan direction. Some of the STM data displayed here were smoothed once using a moving eight point average.

The use of very thin gold films deposited at low temperatures to facilitate STM observations of insulating materials was reported by Jaklevic et al.[4,5] They obtained lateral resolutions of ~10 Å and vertical resolutions of < 0.5 Å with gold films 20-60 Å thick. At this level, no structure attributable to the gold film (atomic steps, grain boundaries, granularity) was observed, despite the reproducible observation of atomic steps on single-crystal Au(111) surfaces under similar conditions; the gold appeared to "wet" the insulator surface like a liquid film wets a high surface energy substrate. Needless to say, the unavoidable roughness of the gold and the interaction between surface roughness and the finite size of the STM tip combine to prevent atomic resolution.

Our STM observations were made on macroscopically smooth portions of each fracture surface, although structure was observed in the scanned regions by scanning electron microscopy (SEM). SEM micrographs of the scanned regions of all three materials were consistent with failure along the craze boundary, rather than through the craze itself. Since PMMA frequently fails through the craze (by fibril fracture), we note that the material used in this study did fail by fibril fracture in unnotched samples. However, notched samples failed along the craze boundary. As craze boundary failure yields smoother surfaces than fibril fracture, notched PMMA samples were employed in this work.

RESULTS AND DISCUSSION

PMMA: Room Temperature Tensile Fracture

Figure 1 shows a typical scan of a PMMA fracture surface produced at room temperature and located near the fracture origin. This region of the surface shows structure over a broad range of length scales. In the upper left hand side of the scan are some relatively flat areas separated by steps. These flat areas are inclined to the overall plane of the fracture surface. Given that we are looking at the craze boundary, this indicates that the thickness of the craze is not uniform in this region. STM images of fracture surfaces of more brittle materials (single crystal MgO) often show similar features,[6] suggesting that craze growth can locally respond to the rapid changes in principle stress that yield small scale crack branching in the fracture of more brittle materials.

In the lower right portion of Fig. 1 are several ridges, 10-20 nm apart. One is identified by the arrow in Region A. We attribute these ridges to instabilities in the craze front that yield void "fingers" which advance ahead of the nominal craze front. The formation of craze fibrils involves the growth of voids into the deformed material at the craze tip. Analogous processes are observed when a viscous fluid (e.g., fresh rubber cement) is squeezed between two glass slides, which are then wedged apart. These voids grow and form fingers with characteristic dimensions which depend on the rate of separation and the viscoelastic properties of the fluid. The wavelength of the fastest growing instability determines the characteristic separation between fibrils along a polymer craze front.

The ridges are due to the highly oriented nature of the polymer between the void fingers during fibril formation. As oriented polymeric material is stiffer than unoriented material, stress concentrations develop at the boundary between oriented and unoriented material which favors fracture along this boundary. Thus the ridges outline regions of oriented material along the fracture surface, and the spacing between ridges reflects the wavelength of the instability along the craze front. These ridges show bumps along their length which probably reflect oriented material at the

ends of "craze fibrils" which have formed along the ridges. If the crack were able to follow the boundary between oriented and unoriented material accurately, the presence of ridges would indicate that the drawing process is not isotropic, i.e. that volume of the partially oriented material at the end of a growing fibril is not spherical, but is strongly elliptical. However, the momentum of a growing crack hinders its ability to following oscillating topography along the direction of crack growth, and thus ridges would be expected even if material were drawn into the fibrils isotropically. Ridges also appear on some of the flatter portions in the background (Region B of Fig. 1), but their relief is much reduced. This may reflect a lower degree of molecular orientation in these regions, which have experienced rapid changes in the maximum principle stress. The ability of the crack to follow the complex topography of the craze boundary in this region may also limit the vertical relief of the observed ridges.

A similar PMMA fracture surface is shown in Fig. 2. A band composed of short (15 nm), parallel ridges crosses the figure from upper left to center right. One end of the band is indicated by the arrow. This band appears to mark the intersection of a craze branch with the fracture surface. Craze branches can be formed at modest crack velocities, while the fracture surface is still macroscopically smooth.[10] (Surface roughening occurs only at crack velocities sufficient for the initiation of cracks in the craze branches.[10]) Thus we identify the ridges in this band as intact (unfractured) craze fibrils, each about 15 nm long. The distance between the unbroken fibrils of Fig. 2 are in the 9-16 nm range, the average separation being 11 nm, somewhat less than the distance between ridges in Fig. 1 (10-20 nm). A smaller fibril spacing is consistent with the relatively high stress intensities required for craze branching.

As fibril diameter measurements have been made in PMMA, direct measurements of the fibril diameter are desirable. Although direct measurements are difficult in Fig. 2, an average fibril diameter can be estimated from the average fibril separation, D_o, assuming that fibrils formed during rapid crack growth have a geometry similar to those formed in slower, *in situ* TEM observations. The ratio of the fibril length to the length of the same material before deformation

(the drawing ratio, λ) has been observed to be about 2 in PMMA.[11] If drawing does not change the density of the fibril material, the mean fibril diameter and spacing are related by[11]

$$D = D_0\lambda^{-1/2}, \qquad (1)$$

With $\lambda \sim 2$, the average fibril diameter should be about 8 nm. Fibril diameter measurements made at temperatures well above those in this work have been made by Paredes and Fischer using small angle X-ray scattering (SAXS) measurements. Samples strained *in situ* at 85 °C yielded fibril diameters in the 20-30 nm range.[12] The mean fibril diameter was observed to scale with the inverse of the drawing stress. Since the drawing stress at room temperature should be considerably higher than at 85 °C, we expect significantly smaller fibrils in our work, in agreement with Fig. 2.

Deep cavities, such as that shown in Fig. 3(a), are also occasionally observed. The band-like features in the background are steps were most likely formed as the main crack encircled the cavity, where the cavity was formed in the region ahead of the advancing crack. We attribute the cavity to secondary fracture in the region ahead of the crack tip. A similar process is responsible for much larger hyperbolic features typical of failure *through* the craze,[13] rather than along the craze boundary. Figure 3(b) shows schematically the geometry responsible for this feature. Small ridges are found on the steps in the background; however, they are obscured in this plot by their small vertical relief relative to the depth of the trough. Note that the depth of this cavity may be somewhat greater than indicated in the scan due to the non-negligible size of the STM tip.

Steps are frequently observed on these PMMA fracture surfaces. These steps often disappear and reappear in an irregular fashion, as seen in Fig. 4. The steps of Fig. 4 are about 2 nm high. Long, fairly parallel steps are occasionally observed, including some of the band-like steps of Fig. 3. The minimum separation of relatively long, parallel steps is typically 75-125 nm. Robertson and Mindroiu have suggested that the minimum distance between steps is typically 7-12 times the size of the smallest observed "longitudinal structures" in SEM observations of a cross-

linked polystyrene fracture surface.[14] Their longitudinal structures probably correspond to the ridges observed in our STM scans. We expect that nearby steps along the boundary of the growing craze are not stable unless they have a critical size; this critical size should scale roughly with the spacing between the "void fingers" in the craze itself. This expectation is supported by comparisons among the three materials observed in this study. We point out that SEM observations of such features are rather difficult, due to the very low relief of these features.

Occasionally, V-shaped troughs are observed in PMMA. A small area scan of one of these features appears in Fig. 5(a). The two sides of the trough meet at approximately 80°. Note that the surface on the left is rather rough, with sharp, small features (resembling small fibrils), while the surface on the right is much smoother. Similar V-shaped features have been observed during *in situ* observations of crack growth in thin PMMA films when a crack-bridging ligament is torn.[15] These ligaments can be produced when the main crack makes a close encounter with an advance crack. In Fig. 5(b), we show schematically the sequence of events leading to the formation and tearing of a ligament. The smooth surface (labeled) of the trough would be formed during the relatively smooth crack growth along the craze boundary, while the rough surface (labeled) would be formed during the rupture of the ligament itself. Again, we suspect that this image is somewhat distorted, i.e. it is likely that the trough in Fig. 4 is somewhat deeper than shown.

PMMA: Low Temperature Tensile Fracture

In general, PMMA surfaces produced by fracture at liquid nitrogen temperature were considerably smoother than those produced at room temperature. The deep cavities and V-shaped features of Figs. 3(a) and 5(a) were completely missing from the low temperature fracture surfaces. A typical low temperature fracture surface is seen in Fig. 6. This surface is characterized by a large number of shallow, asymmetrical troughs. One side of each trough slopes gently, while the other is quite steep. Although they are not regularly spaced, a weak ~100 nm periodicity is observed. Again, these features are consistent with crack growth along the craze-bulk boundary.

If crazed material lies below the viewed surface, the holes could be associated with fibril contraction or voids beneath the skin.

Occasionally very regular step structures were observed as in Fig. 7(a). These steps are roughly 100 nm apart and 15 nm high. The ridges which characterize these surfaces are about 10 nm apart and are quite parallel. Regularly space bumps are observed along each ridge at intervals of about 20 nm. The bumps in each ridge are aligned with those of adjacent ridges. The simplest interpretation of this structure is that each bump represents the end of a craze fibril beneath a polymer skin. Given this interpretation, the fibril spacing along the direction of crack growth is twice the spacing between the void fingers at the craze front. This suggests that care must be taken in reporting measurements of fibril spacing to specify (if possible) the relationship between the measured dimension and the direction of craze growth. The average spacing between ridges formed at liquid nitrogen temperature (10 nm) is somewhat smaller that that observed at room temperature (Figs. 1 and 3).

Fibril growth by the meniscus instability mechanism favors the formation of fibrils in rows from the breakup of the material between void fingers at the craze tip, i.e., along the ridges observed in our STM scans. These fibril rows have been previously observed in TEM studies of crazing in thin films.[16] However, the alignment of fibrils in one row with those in adjacent rows is usually is poor. This makes measurements of fibril diameters and spacing difficult.[16] Figure 7(a) suggests that at low temperatures, fibrils along adjacent rows can be formed in lock-step, side by side each other. This unusual regularity may be a consequence of the tight constraints on the process of craze growth provided by the nearby steps, as well as the low temperature.

A 25 x 25 nm^2 scan of a pair of adjacent bumps is shown in Fig. 7(b). [Note that this image has been rotated about 50° counterclockwise relative to Fig. 7(a).] These bumps show a distinctive "airfoil" structure, gently sloping to a peak as one proceeds from the lower right to the upper left, then falling precipitously at the upper right. We propose that this airfoil structure is a consequence of the momentum of the crack as it passes over the oriented material adjacent to the craze. The crack is slow to be deflected as is approaches the oriented material, accounting for the

gradual portion of the slope. It then overshoots the oriented portion and must bend sharply toward the stress concentration at the craze boundary. We also note that the size of the bumps in Fig. 7(a) is a strong function of distance from nearby steps. The bumps of Fig. 7(b) are located near a step and are thus somewhat shorter than bumps midway between steps. The tallest bumps are located midway between steps where higher drawing stresses are higher than those adjacent to a step; these higher drawing stresses increase the volume of oriented material near the end of fibrils grown midway between steps.

PMMA: Slow Crack Growth

As crack velocity and failure mechanisms are often intimately linked, observations were made on fracture surfaces formed during slow crack growth in the double torsion geometry at room temperature. The crack velocity in the region of our STM observations was about 1 cm/s. Macroscopically, these fracture surfaces are much smoother than surfaces produced in tensile failure, where typical crack velocities are in excess of 100 m/s. A typical scan is shown in Fig. 8(a). An arrow indicates the general direction of crack growth. This surface has a scalloped appearance; a few of the larger, semicircular "scallops" are shown in greater detail in Fig. 8(b). We suggest that these features reflect periodically arrested crack growth along the craze boundary, i.e. that crack growth was incremental rather than continuous. Failure along craze boundaries during slow crack growth in PMMA has been previously observed.[17doyle2]

Crack advance and arrest in this sample would be the result of interactions between the moving crack and acoustic waves in the sample. Assuming a typical tongue (40 nm long) was formed during a single crack "jump," the average frequency of crack jumps along the crack front is about 200 kHz. Standing longitudinal waves along the direction perpendicular to the plane of the crack have frequencies in this range. The frequency of the lowest harmonic with an antinode in the middle of the sample is ~100 kHz, assuming the full 2.5 cm width of the sample.

Fig. 8(b) shows some of the (roughly) semicircular "scallops" in greater detail. To guide the eye, we have outlined the edges of these features with white lines. The inset in Fig. 8(b) shows a schematic diagram of the formation of these features. Note that these semicircular surfaces are not parallel to the overall fracture plane. These surfaces regions were formed as the crack jumped along the craze boundary. The cross-section of the craze is wedge shaped, with its sharp end pointed along the direction of craze/crack growth. As the crack jumps along the craze boundary from the wide end of the craze wedge toward the thin end, the resulting surface is inclined to the overall fracture plane. The jump distance is typically a small fraction of the distance to the craze tip. Between crack jumps, during the "crack arrest" portion of the cycle, the wide end of the craze at the crack tip stretches and widens, yielding rough steps or ledges between the semicircular surfaces. These rough regions are evident between the semicircular regions of Fig. 8(b). Note that the crack jumps during each cycle of craze growth appear to nucleate at a large number of places along the crack front, with one nucleation site for each semicircular feature. Since failure along the craze boundary is typically associated with rapid crack growth (perhaps due to adiabatic heating),[18] this suggests that the local crack velocity during the crack jumps is quite high.

Polystyrene

PS fracture surfaces also show a variety of morphologies, evident in Fig. 9. The surface elevation in Fig. 9 changes by roughly 40 nm in Region A, near the intersection of two major "fracture planes." More precisely, fracture in this region may have occurred along the boundary of two intersecting or overlapping crazes. The change in Region A is accommodated by a series of small, localized steps, typically 5 nm in height. SEM photographs of this general region of the surface show patches of craze on a smooth, flat base, indicating that crack growth was principally along the boundary between the craze and the bulk material. Thus these steps should reflect local variations in craze thickness. Given that craze growth typically advances ahead of crack growth by

some tens of μm,[19] the presence of small, localized steps suggests that craze growth near the intersection of these major fracture planes occurred in small "jumps," incrementally rather than continuously. These jumps may well be the result of interactions between the two growing crazes and acoustic waves.

Region B of Fig. 9 is characterized by a large number of small ridges, similar to those seen on PMMA, but often larger and more distinct. Several ridges from another region of the fracture surface are shown in Fig. 10. On PS surfaces, these ridges are typically 10-15 nm apart. Again, we attribute these ridges to the growth of finger-like voids at the craze front. Donald and Kramer have made *in situ* TEM measurements of distance between voids during *slow* craze growth in PS, obtaining values in the 20-30 nm range.[16] Their measurements are consistent with the "most probable spacing," Λ_c, given by the fastest growing wavelength of instabilities along the craze front. Their estimate assumes plastic behavior of the form $\varepsilon = \varepsilon_0(\sigma/\sigma_0)^n$, where $\dot{\varepsilon}$ and σ are the equivalent strain rate and the equivalent stress in tension and $\dot{\varepsilon}_0$ and σ_0 are material parameters. An effective craze tip strain rate is given by $\dot{\varepsilon}_{eff} = 2(n+2)v_0/(3^{1/2}\,h)$, where v_0 is the velocity of craze growth and h is the craze thickness at the craze tip. The resulting "fastest growing" wavelength (from Fields and Ashbey[20]) is

$$\Lambda_c = 2\pi\, 3^{1/2} \left(\frac{3^{1/2}\,\Gamma\, h}{2\sigma_0}\right)^{1/2} \left(\frac{\dot{\varepsilon}_0}{\dot{\varepsilon}_{eff}}\right)^{1/2n}, \qquad (2)$$

where Γ is the surface energy. The principle uncertainty is in h (the thickness of the craze at the craze tip). Measurements of h by Donald and Kramer fall in the 5-20 nm range, and following them we use this range to provide bounds on Λ_c. Typical values for the materials parameters are n = 17, Γ = 0.4 J/m^2, and $\dot{\varepsilon}_0 = 1.7 \times 10^{-5}$ s^{-1}. The crack velocity in brittle fracture of PS at room temperature is on the order of 100 m/s, 10^{10} times faster than the craze velocity in the work of Donald and Kramer. In constant velocity crack growth, the crack and craze advance with the same velocity, resulting in a propagating "craze zone" of constant length.[18] Therefore, at a craze

velocity of 100 m/s, using the same estimate for the craze thickness (5-20) nm, we find that , 8 nm $< \Lambda_c <$ 17 nm, nicely bracketing the observed ridge spacing in this work. This agreement supports our interpretation of these features as reflecting void fingering during craze growth.

A very small-scale scan of the region between two ridges appears in Fig. 11. The circular cross section of the ridge on the left is quite evident, indicating that this ridge is roughly cylindrical in form. This aspect of the ridge geometry is rather difficult to explain. The great vertical relief of these features relative to PMMA is probably associated with the high drawing ratio of PS ($\lambda_{PS} \sim 4$ while $\lambda_{PMMA} \sim 2$).[11] Thus craze formation in PS requires a relatively high degree of molecular orientation, and the "boundary layer" of partially oriented material at the craze boundary should be relatively thick. As noted above, the high degree of molecular orientation perpendicular to the plane of the craze make fracture in the plane parallel to the craze costly in terms of energy. However, this orientation is accompanied by localized, directional decreases in tensile strength between the ridges. This results from the necessary disentanglement of chains which would otherwise join adjacent ridges. Thus the lowest energy fracture surface may resemble a set of parallel cylindrical surfaces, despite the relatively high surface area of this structure. Three-dimensional stresses (plane strain) at the crack tip may also play an important role in surface formation, providing components of tensile stress along "directions of weakness." These ridges would likely survive relaxation processes following fracture, as extended molecular chains tend to "coil up" upon stress relief and would be unlikely to reform entanglements between ridges. These ridges are commonly observed, but appear to be "washed out" in the presence of rapid changes of surface topography.

Figure 11 also clearly shows constrictions along the length of the ridges. The "bumps" between constrictions are similar to those seen on ridges in PMMA. These bumps indicate the presence of fibrils below the surface, and the constrictions identify regions in which chains joining fibrils have disentangled. The reduction in tensile strength along the direction parallel to the fibril would explain the constrictions.

In PS, craze fibrils are often interconnected by a three dimensional web of branch fibrils.[21] Evidence for these interconnections appears in Fig. 12. In this region of the surface, the crack appears to have intersected the craze itself, leaving deep holes between the individual fibrils below. The craze fibrils themselves are oriented normal to the fracture surface, but the net of connecting branch fibrils are parallel to the fracture surface and form the roughly rectangular edges of the observed holes. These holes are probably much deeper than shown in Fig. 12, due to the non-negligible size of the STM tip. Nevertheless the structure is clearly resolved.

Polycarbonate

Among the materials studied here, PC is unique in its tendency to undergo macroscopic shear deformation prior to fracture. Each of the PC fracture surfaces describe below had formed through cold-drawn material in the necked region of dogbone tensile specimens. SEM scans of the general region imaged by the STM showed a great deal of crack branching on scales down to at least 100 nm. Although patches of craze were noticed elsewhere on the surface, none were observed in the region of STM observation. This distribution of craze patches seen in the SEM was consistent with a craze which lies completely on one fracture surface or the other.[10] Although the high density of molecular entanglements in PC favors shear deformation over crazing in thin PC films,[11] crazing generally accompanies fracture in bulk samples such as those studies in this work.

Region A of Fig. 13 shows set of closely spaced ridges on a PC surface. The average spacing of these ridges is about 3.8 nm. These fibrils are much smaller than those observed in PMMA and PS, but can be explained on the basis of material properties. Paredes and Fischer have performed SAXS measurements of fibril diameters at temperatures above 100 °C, obtaining average diameters in the 20-50 nm range.[12,22] The average fibril diameter was observed to scale with the macroscopic drawing stress according to the relation $\sigma_d \cdot D \sim 0.45$ J/m^2. The drawing stress during deformation (here about 100 MPa) provides a lower bound on the drawing stress

during crack growth, and thus can be used to provide an upper bound on the average fibril diameter. We then use equation 1 (with a draw ratio $\lambda \sim 2$ for PC) to provide an upper bound on the average void finger spacing (ridge spacing). A drawing stress of 100 MPa corresponds to an average fibril diameter of 4.5 nm, implying an upper bound on the ridge spacing of about 6.4 nm. This is well below the ridge spacings in PMMA and PS, and is above the ridge spacing observed in STM scans of PC fracture surfaces. We note that the small spacing between ridges might not be expected on the basis of PC's high surface energy (~0.24 J/cm^2 for PC vs ~0.04 J/cm^2 for PS),[11] as small fibrils yield large surface areas. The effect of high surface energy is probably compensated by a correspondingly high drawing stress.

PC fracture surfaces often show regions covered with bumps. In Region B of Fig. 13 these bumps are about 8 nm in diameter. Figure 14 shows a surface with distinctly different overall topography, but the bumps in the central region of the scan are similar in size and shape to those in Fig. 13. The relation between these bumps and the material or fracture properties in not clear. These bumps may be related to instabilities in the process of crack growth along the craze boundary.[23]

Step-like features are also observed on PC fracture surfaces. In the lower left portion of Fig. 14, we see a set of angular ridges about 20 nm wide. Their angular form is inconsistent with the more rounded ridges discussed above, so we identify them as fracture steps. In a different scan, shown in Fig. 15, similar features are indicated by the arrow in Fig. 15. The typical distance between steps on PC is considerably less than those on PMMA and PS. This may again be related to the unusually small void finger spacing, which would allow for the stable propagation of smaller steps. Step formation may also be related to structures created by shear deformation during loading and fracture. The orientation of the steps in Fig. 14 suggests that failure occurred along regions of concentrated shear deformation. These would be analogous to the macroscopic flap-like steps observed by SEM following the fracture of cold drawn PC.[24]

CONCLUSION

STM observations of glassy polymer surfaces show a great deal of structure on the nm-scale. Narrow ridges observed on these surfaces reflect the interaction of the moving crack with the inhomogeneous, partially oriented material along the craze boundary. Thus we expect the ridge spacing to equal the spacing between fibril rows formed during craze growth. In the case of PS, this interpretation is supported by agreement with *in situ* TEM measurements on growing crazes when account is made for the high craze velocities encountered in brittle fracture. Even at these high craze velocities, the meniscus instability model quantitatively accounts for the range of observed ridge spacings in PS. STM observations suggest that the fibrils spacings parallel and perpendicular to the direction of crack growth can be quite different. Simple descriptions of fibril distribution commonly assume directional uniformity in fibril spacing; more detailed models will need to account for the possibility of anisotropic distributions.

Among the PMMA surfaces studies here, those formed at liquid nitrogen temperature are much smoother on the nm-scale than those formed at room temperature, yet show distinctive shallow troughs. Occasionally, quite regular, structured surfaces occur, which we attribute to the orderly production of fibrils in rectangular arrays. This order is likely the consequence of constraint provided by closely spaced steps, as well as the low temperature. PMMA fracture surfaces formed during low speed crack growth in a double cantilever beam geometry show features indicating intermittent crack growth and arrest which appear to be related to standing longitudinal acoustic waves generated by crack/craze growth.

Significant differences are also observed between the surfaces of the PMMA, PS, and PC formed in tension at room temperature. In particular, PS surfaces showed particularly well defined ridges, consistent with the high degree of drawing in fibril formation relative to PMMA and PC. This drawing allows for the orientation of a significantly greater volume of material in the craze boundary layer. The ridge spacing in PC is significantly smaller than those in PMMA and PS; although this is perhaps unexpected on the basis of the high surface energy of this material, it is

consistent with trends in fibril diameter observed in SAXS measurements at higher temperatures. Further, the characteristic step sizes on PMMA and PC surfaces scale roughly with the the observed ridge (fibril) spacing. This is broadly consistent with the scaling observed by Robertson and Mindroiu.[14]

The potential resolution of probe-based microscopies has not been reached for routine observations of insulating surfaces. Improved resolution may eventually allow the direct observation of molecular orientation and mobility at fibril surfaces. These observations would help elucidate the roles of molecular entanglement, reptation, and bond breaking in fibril growth and failure, particularly if observations can be made on unrelaxed fibrils. A more detailed understanding of the molecular processes associated with deformation and failure is important if we are to fully exploit our ability to design polymers on the molecular scale with specific mechanical properties.

ACKNOWLEDGMENTS

This work was supported by The Dow Chemical Company, the Office of Naval Research under Contract No. N00014-87-K-0514, the Ceramics and Electronics Materials Division of the National Science Foundation under Grant DMR 8912179, and the Washington Technology Center.

REFERENCES

1. A. C. Roulin-Moloney, in Fractography and Failure Mechanisms of Polymers and Composites, edited by A. C. Roulin-Moloney, (Elsevier Applied Science, London, 1989), pp. 43-86.
2. D. Rugar and P. Hansma, Phys. Today 43, 23 (1990).
3. T. R. Albrecht and C. F. Quate, J. Appl. Phys. 62, 2599 (1987).
4. R. C. Jaklevic, L. Elie, Weidian Shen, and J. T. Chen, J. Vac. Sci. Technol. A 6, 448 (1988).
5. R. C. Jaklevic, L. Elie, Weidian Shen, and J. T. Chen, Appl. Phys. Lett. 52, 1656 (1988).
6. S. C. Langford, Ma Zhenyi, L. C. Jensen, and J. T. Dickinson, J. Vac. Sci. Technol. A 8, 3470 (1990).
7. G. Reiss, J. Vancea, H. Wittmann, J. Zweck, and H. Hoffmann, J. Appl. Phys., 67, 1156 (1990).
8. D. R. Denley, J. Vac. Sci. Technol. A 8, 603 (1990).
9. J. W. Lyding, S. Skala, J. S. Hubacek, R. Brockenbrough, and G. Gammie, Rev. Sci. Instrum. 59, 1897 (1988).
10. M. J. Doyle, J. Mater. Sci. 18, 687 (1983).
11. E. J. Kramer, Adv. Polym. Sci. 52/53, 1-56 (1983).
12. E. Paredes and E. W. Fischer, Makromol. Chem. 180, 2707-2722 (1970).
13. F. Lednicky and Z. Pelzbauer, J. Polymer Sci. C 38, 375 (1972)
14. R. E. Robertson and V. E. Mindroiu, Polym. Eng. Sci. 27, 55 (1987).
15. D. G. Gilbert, P. W. R. Beaumont, and W. C. Nixon, J. Mater. Sci. Lett. 3, 961 (1984).
16. A. M. Donald, and E. J. Kramer, Philos. Mag. A 43, 857 (1981).
17. M. J. Doyle, A. Maranci, E. Orowan, and S. T. Stork, Proc. Royal Soc. London A 329, 137-151 (1972).

18. Walter Döll, in in Fractography and Failure Mechanisms of Polymers and Composites, edited by A. C. Roulin-Moloney, (Elsevier Applied Science, London, 1989), pp. 387-436.

19. W. Döll, Adv. Polym. Sci. 52/53, 104-168 (1983).

20. R. J. Fields and M. F. Ashby, Philos. Mag. 33, 33 (1976).

21. P. Beahan, M. Bevis, and D. Hull, Philos. Mag. Series 8, 24, 1267 (1971).

22. E. Paredes and E. W. Fischer, J. Polym. Sci. Polym. Phys. Ed. 20, 929-930 (1982).

23. R. J. Bird, J. Mann, G. Pogany, and G. Rooney, Polymer 7, 307 (1966).

24. R. J. Morgan and J. E. O'Neal, Polymer 20, 375 (1979).

FIGURE CAPTIONS

FIG. 1. STM image of a PMMA fracture surface formed in tension, showing fibril-like structures in Regions A and B, which are indicated by arrows.

FIG. 2. Another STM image of a PMMA fracture surface showing fibril-like structures lying in depressions. One such structure is indicated by the arrow.

FIG. 3. (a) STM image of a cavity in a PMMA fracture surface formed in tension. Such cavities are probably formed in the crazed region ahead of the crack tip, as shown in (b).

FIG. 4. STM image of steps on a PMMA fracture surface formed in tension. The step widths are typically 25-45 nm.

FIG. 5. (a) STM image of a V-shaped trough on PMMA fracture surface formed in tension. Similar troughs are formed during the failure of crack bridging ligaments. The sequence of ligament formation and failure is shown schematically in (b).

FIG. 6. A typical image of PMMA fracture surface formed in tension at 76 K in vacuum. The surface shows holes spaced at irregular intervals.

FIG. 7. (a) STM image of a PMMA fracture surface formed in tension at 76 K in vacuum. Each step shows parallel rows of regularly spaced bumps. A small area scan of a pair of these bumps is shown in (b).

FIG. 8. (a) STM image of a PMMA fracture surface formed in double torsion at a crack velocity of about 1 cm/s. (b) A small area scan of a region in (a); the edges of the scallop features are shown in white. The general direction of crack growth is indicated by arrows.

FIG. 9. STM image of a PS fracture surface formed in tension. Tongue-shaped arrested cracks appear in Region A and fibril-like structures in Region B.

FIG. 10. STM image of fibril-like structures on a different PS fracture surface formed in tension. The diameters of these fibrils are 10-15 nm.

FIG. 11. A close up of the valley between two fibrils on a PS fracture surface.

FIG. 12. STM image of small cavities on a PS fracture surface formed in tension. The apparent diameter of these cavities is 4-10 nm at their mouths.

FIG. 13. STM image of a PC fracture surface formed in tension, showing fibrils in the lower left (Region A) and larger bumps in the upper right (Region B).

FIG. 14. STM image of a PC fracture surface formed in tension, showing ridges about 15 nm across. The bumps across the central portion of the figure are similar in size to those of Fig. 12.

FIG. 15. STM image of a PC fracture surface formed in tension. The arrow indicates one of several ridges which appear to be fracture steps.

REFERENCES

1. A. C. Roulin-Moloney, in Fractography and Failure Mechanisms of Polymers and Composites, edited by A. C. Roulin-Moloney, (Elsevier Applied Science, London, 1989), pp. 43-86.
2. D. Rugar and P. Hansma, Phys. Today 43, 23 (1990).
3. T. R. Albrecht and C. F. Quate, J. Appl. Phys. 62, 2599 (1987).
4. R. C. Jaklevic, L. Elie, Weidian Shen, and J. T. Chen, J. Vac. Sci. Technol. A 6, 448 (1988).
5. R. C. Jaklevic, L. Elie, Weidian Shen, and J. T. Chen, Appl. Phys. Lett. 52, 1656 (1988).
6. S. C. Langford, Ma Zhenyi, L. C. Jensen, and J. T. Dickinson, J. Vac. Sci. Technol. A 8, 3470 (1990).
7. G. Reiss, J. Vancea, H. Wittmann, J. Zweck, and H. Hoffmann, J. Appl. Phys., 67, 1156 (1990).
8. D. R. Denley, J. Vac. Sci. Technol. A 8, 603 (1990).
9. J. W. Lyding, S. Skala, J. S. Hubacek, R. Brockenbrough, and G. Gammie, Rev. Sci. Instrum. 59, 1897 (1988).
10. M. J. Doyle, J. Mater. Sci. 18, 687 (1983).
11. E. J. Kramer, Adv. Polym. Sci. 52/53, 1-56 (1983).
12. E. Paredes and E. W. Fischer, Makromol. Chem. 180, 2707-2722 (1970).
13. F. Lednicky and Z. Pelzbauer, J. Polymer Sci. C 38, 375 (1972)
14. R. E. Robertson and V. E. Mindroiu, Polym. Eng. Sci. 27, 55 (1987).
15. D. G. Gilbert, P. W. R. Beaumont, and W. C. Nixon, J. Mater. Sci. Lett. 3, 961 (1984).
16. A. M. Donald, and E. J. Kramer, Philos. Mag. A 43, 857 (1981).
17. M. J. Doyle, A. Maranci, E. Orowan, and S. T. Stork, Proc. Royal Soc. London A 329 137-151 (1972).
18. Walter Döll, in in Fractography and Failure Mechanisms of Polymers and Composites, edited by A. C. Roulin-Moloney, (Elsevier Applied Science, London, 1989), pp. 387-436.
19. W. Döll, "Optical interference measurements and fracture mechanics analysis of crack tip craze zones," Adv. Polym. Sci. 52/53, 104-168 (1983).
20. R. J. Fields and M. F. Ashby, Philos. Mag. 33, 33 (1976).
21. P. Beahan, M. Bevis, and D. Hull, Philos. Mag. Series 8, 24, 1267 (1971).
22. E. Paredes and E. W. Fischer, J. Polym. Sci. Polym. Phys. Ed. 20, 929-930 (1982).
23. R. J. Bird, J. Mann, G. Pogany, and G. Rooney, Polymer 7, 307 (1966).
24. R. J. Morgan and J. E. O'Neal, Polymer 20, 375 (1979).

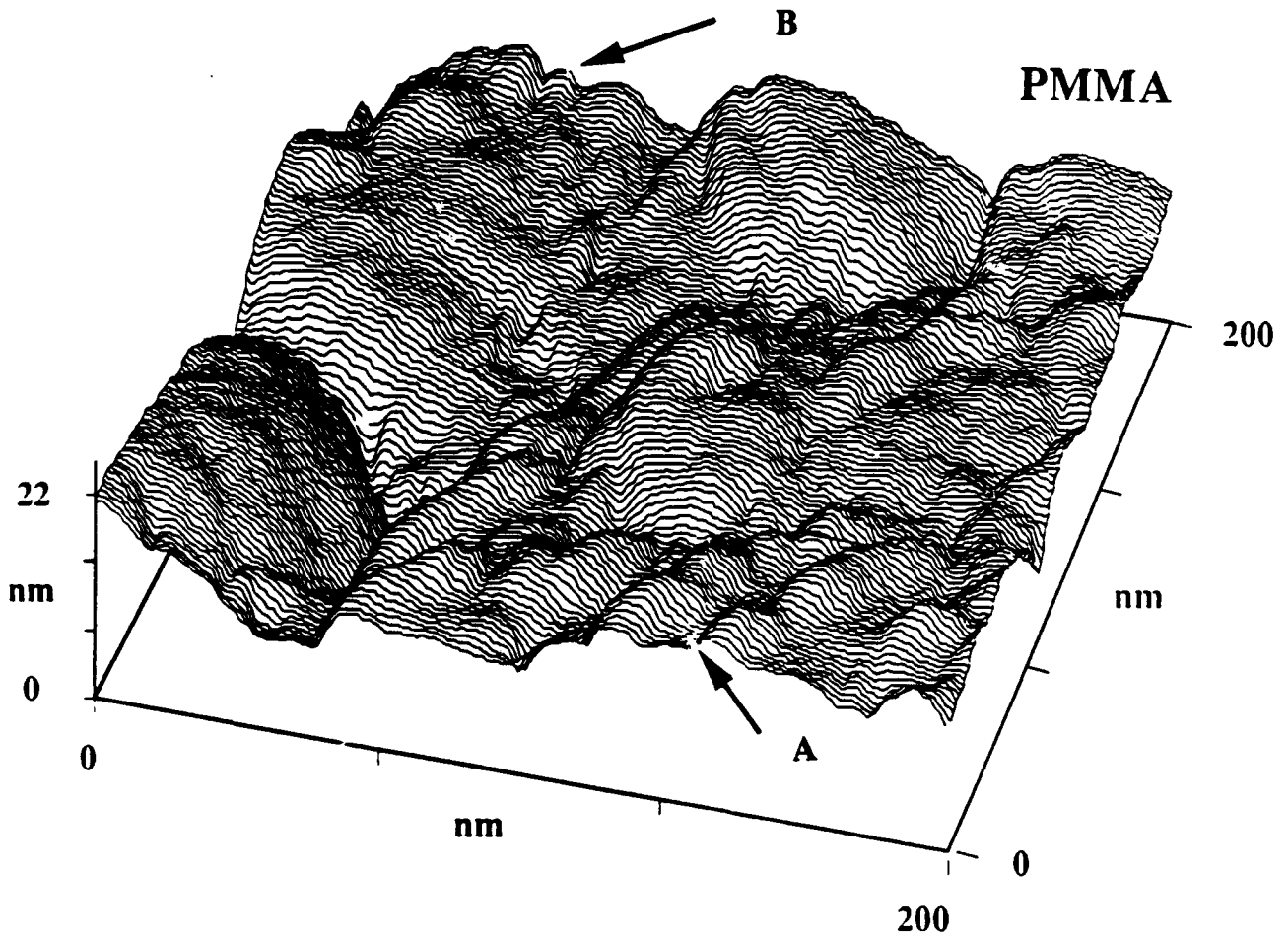

FIG. 1

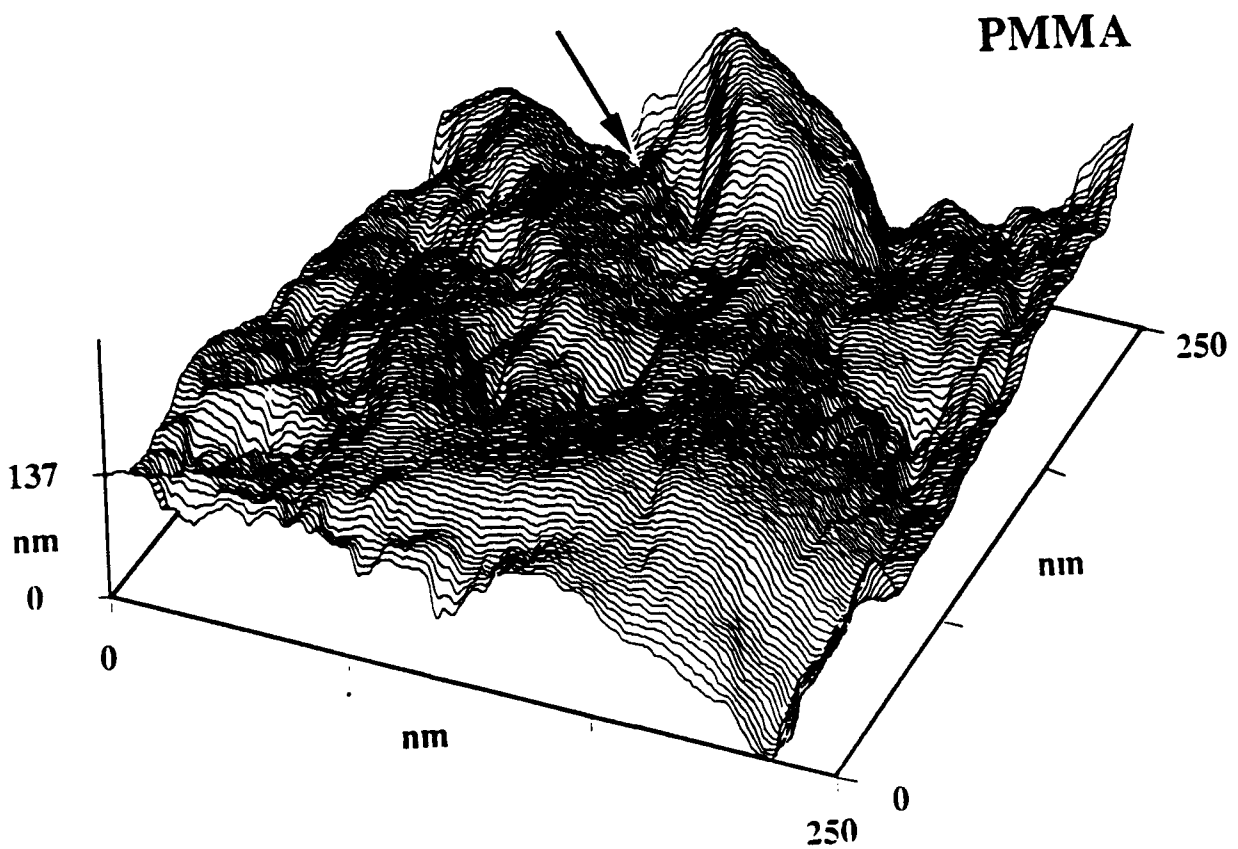

FIG. 2

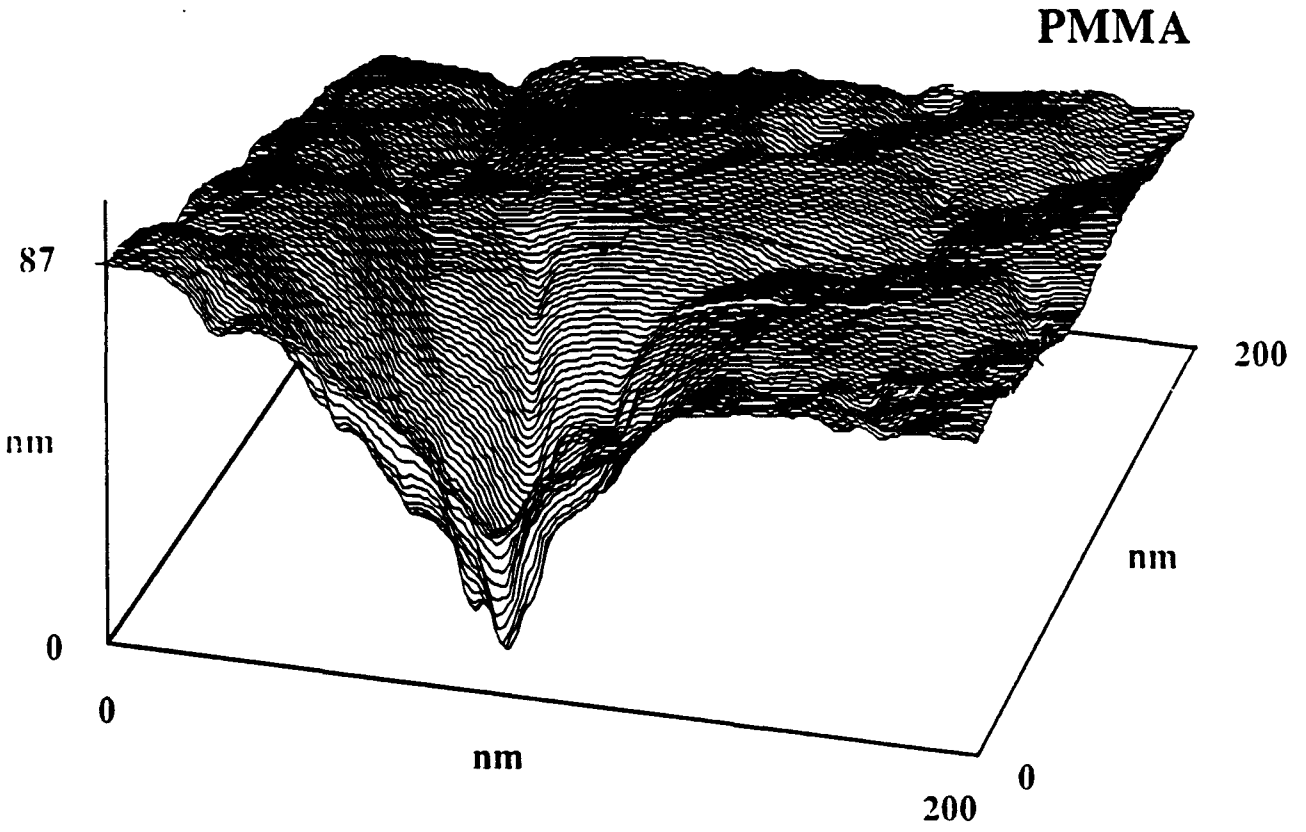

(a)

FIG. 3(a)

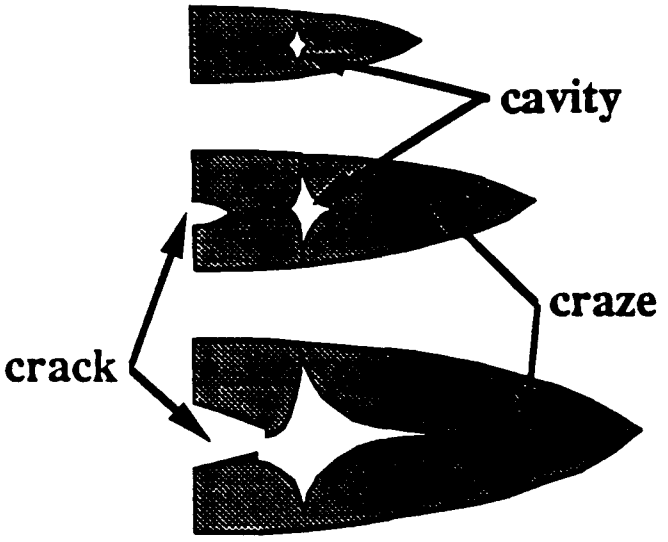

FIG. 3(b)

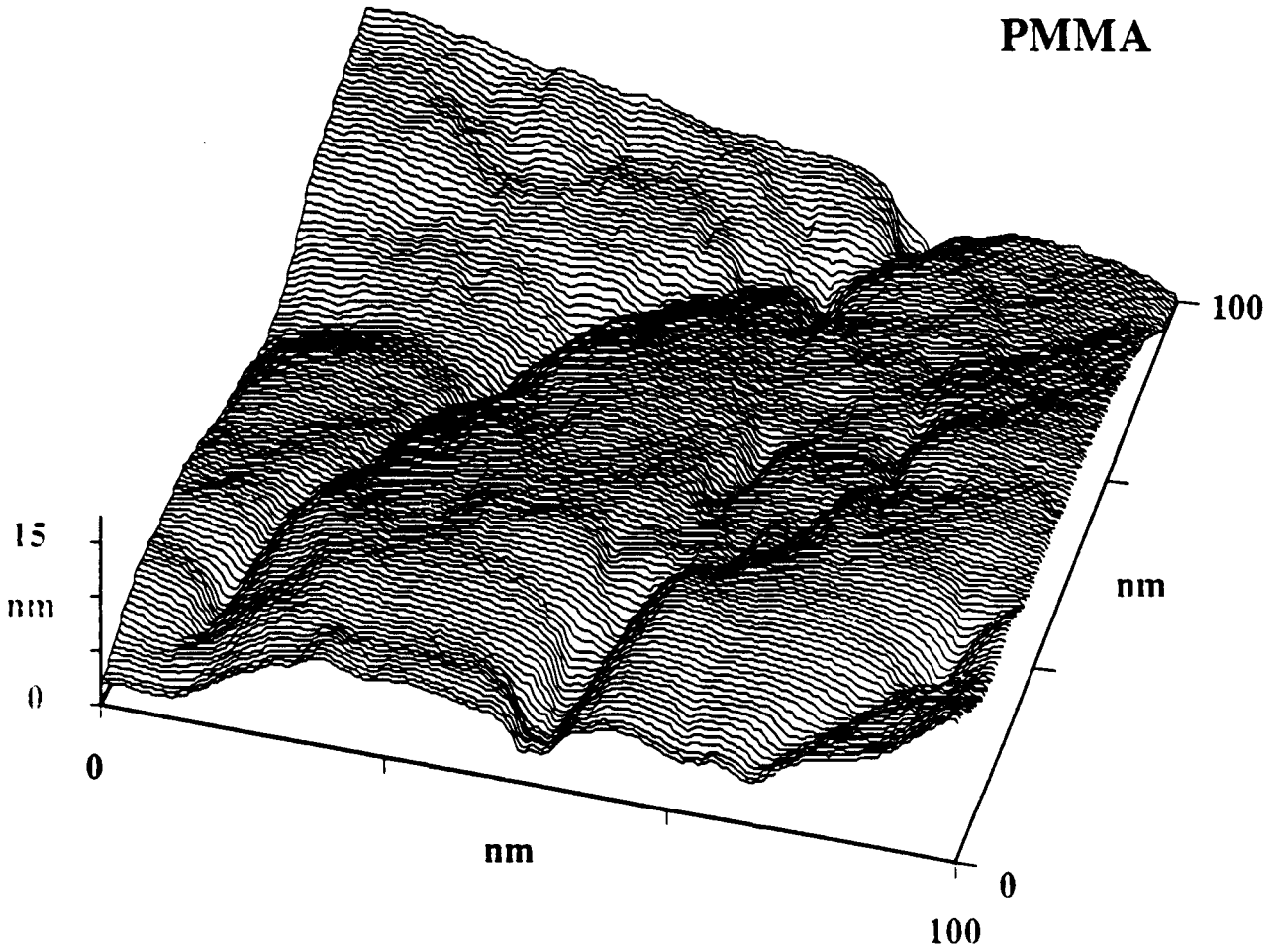

FIG. 4

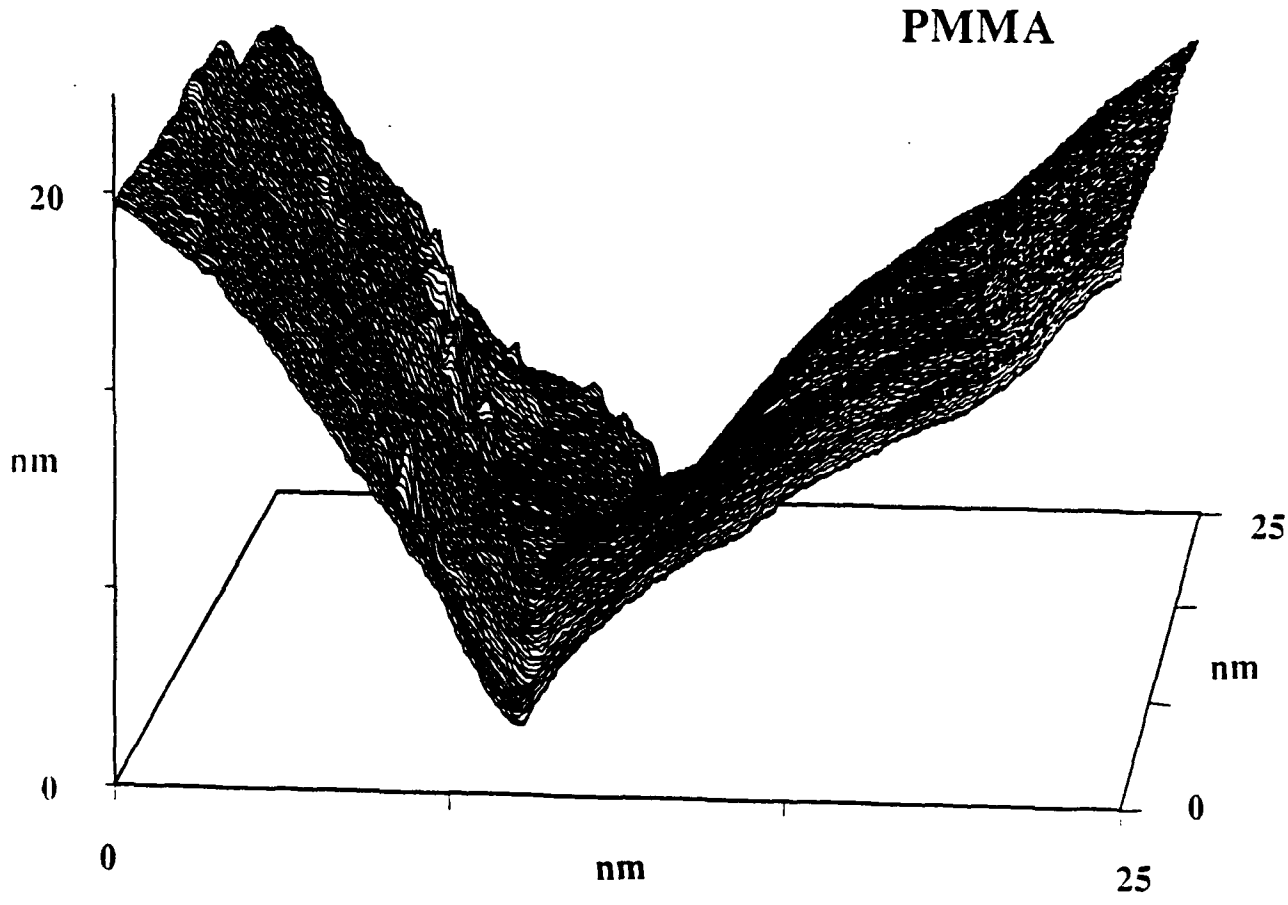

(a)

FIG. 5(a)

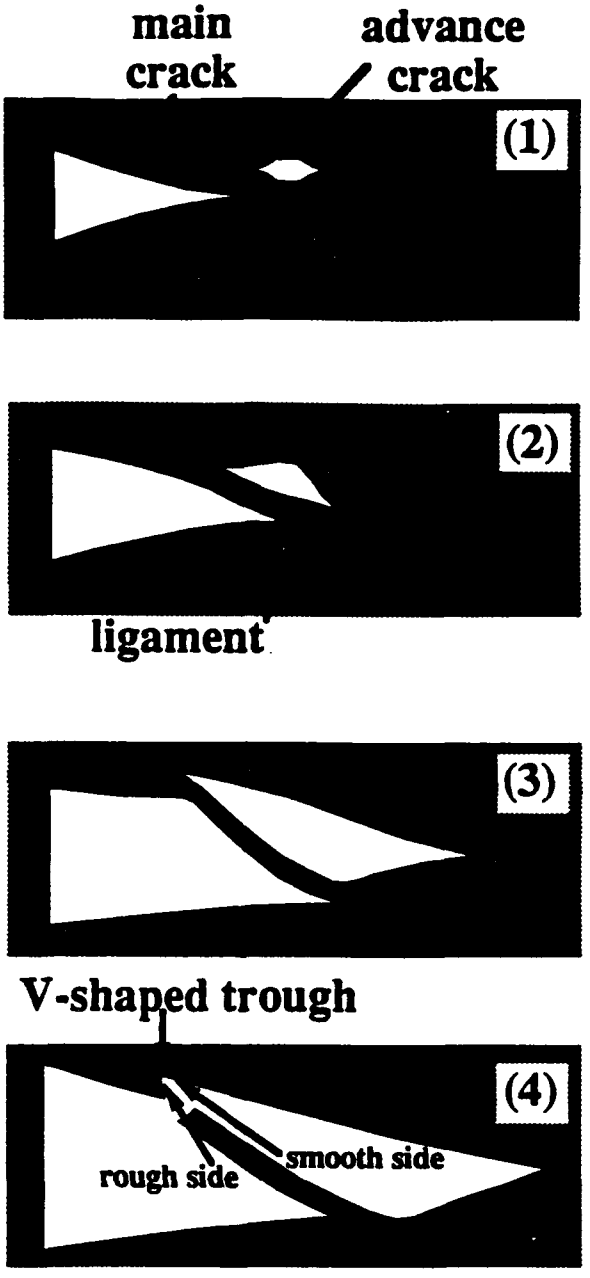
main crack
advance crack
(1)
(2)
ligament
(3)
V-shaped trough
(4)
rough side
smooth side

(b)

FIG. 5(b)

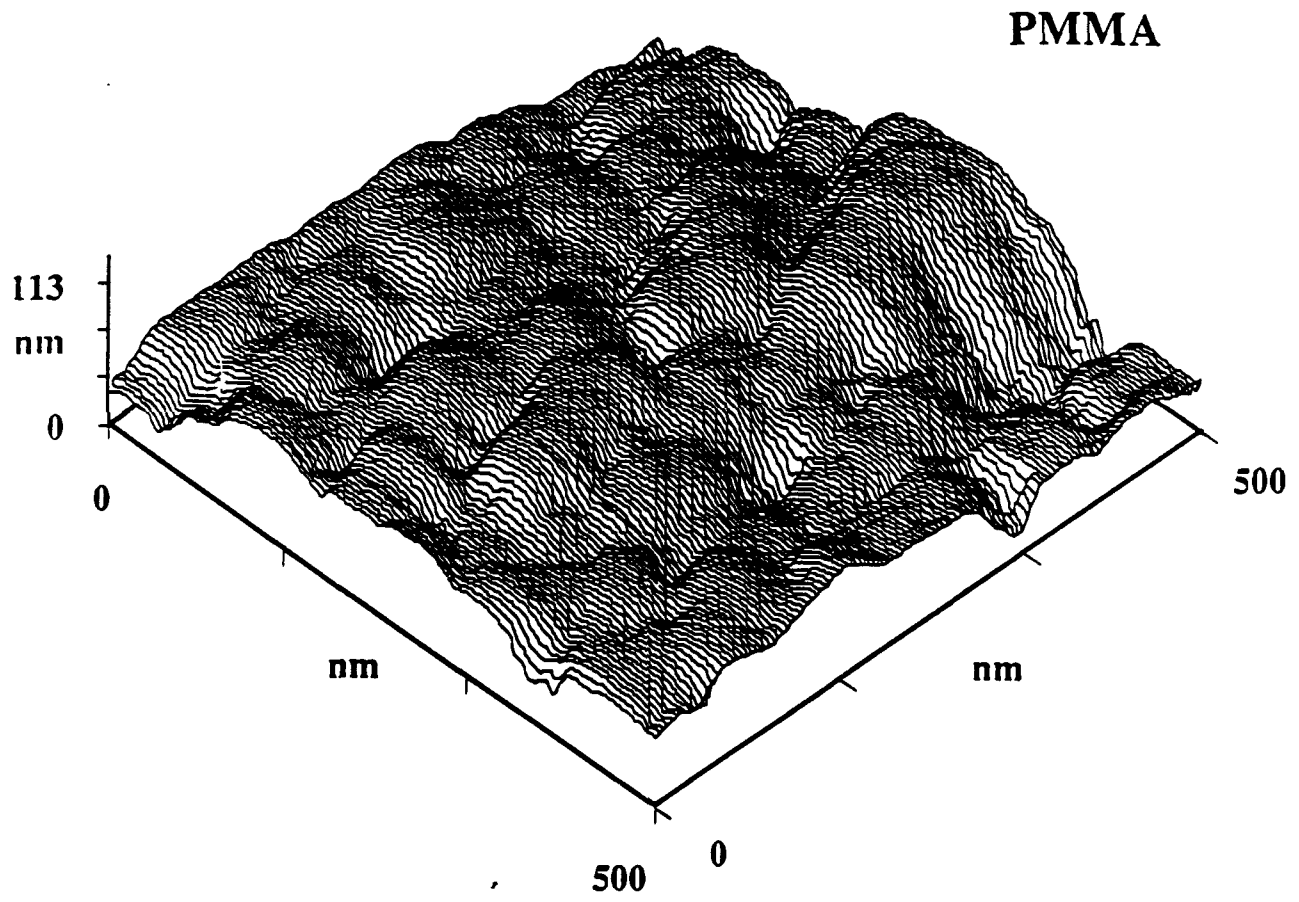

FIG. 6

PMMA

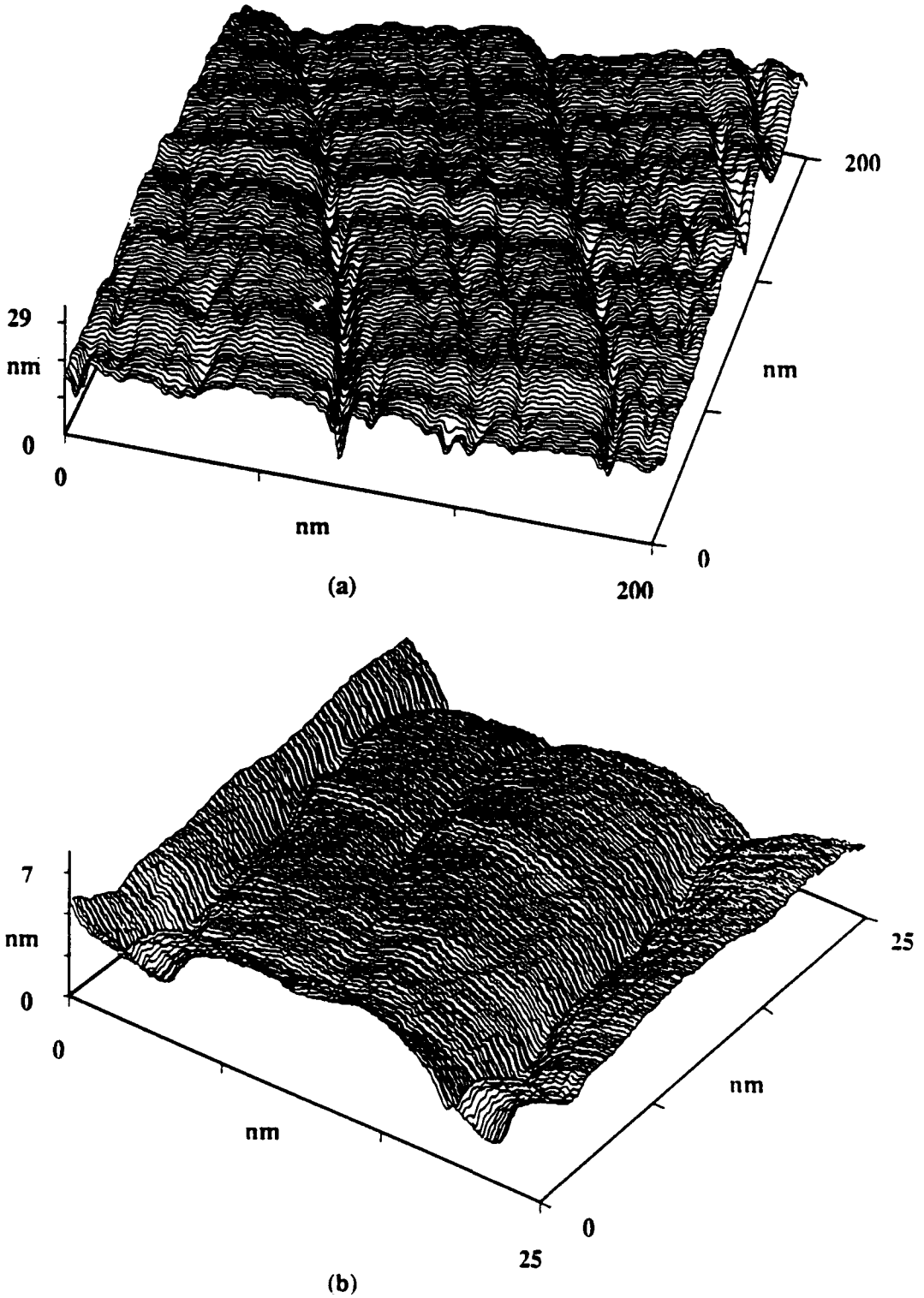

FIG. 7

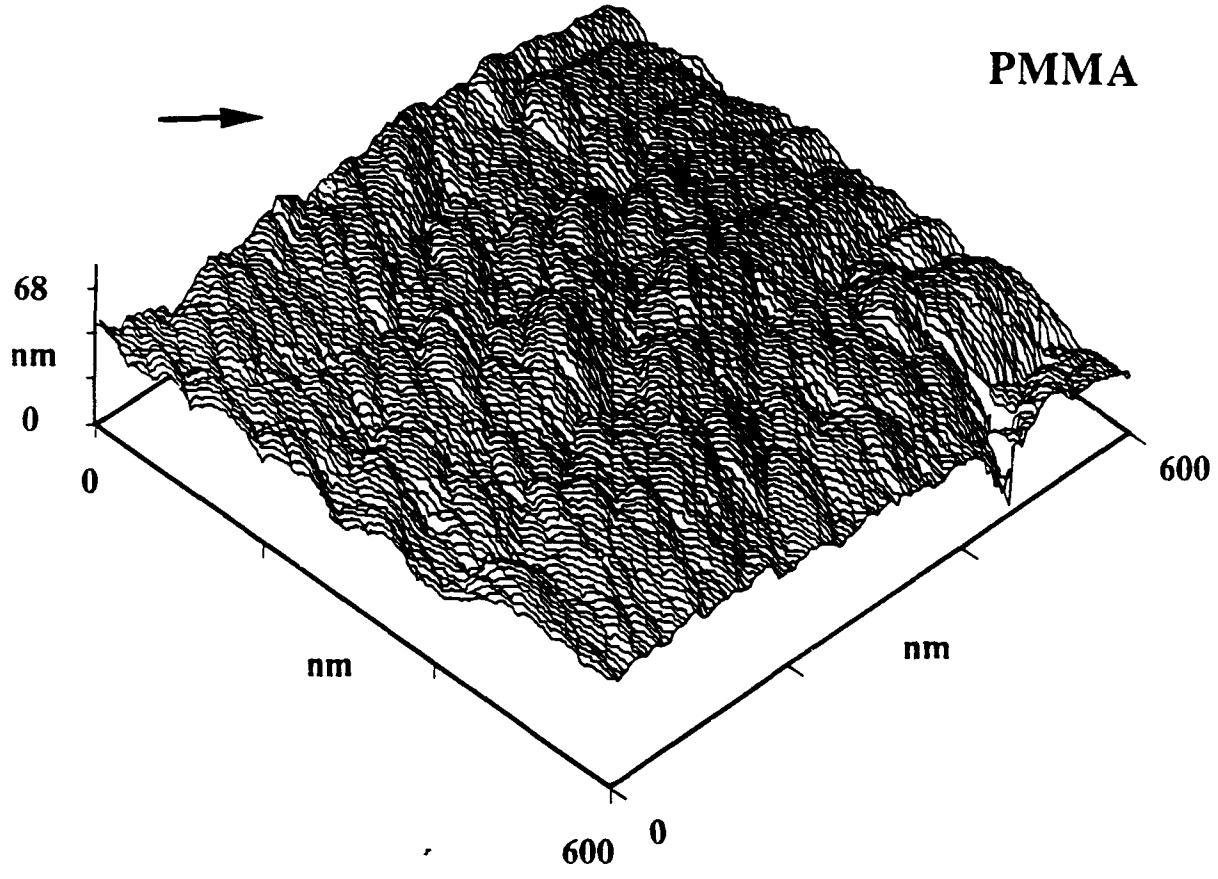

(a)

FIG. 8(a)

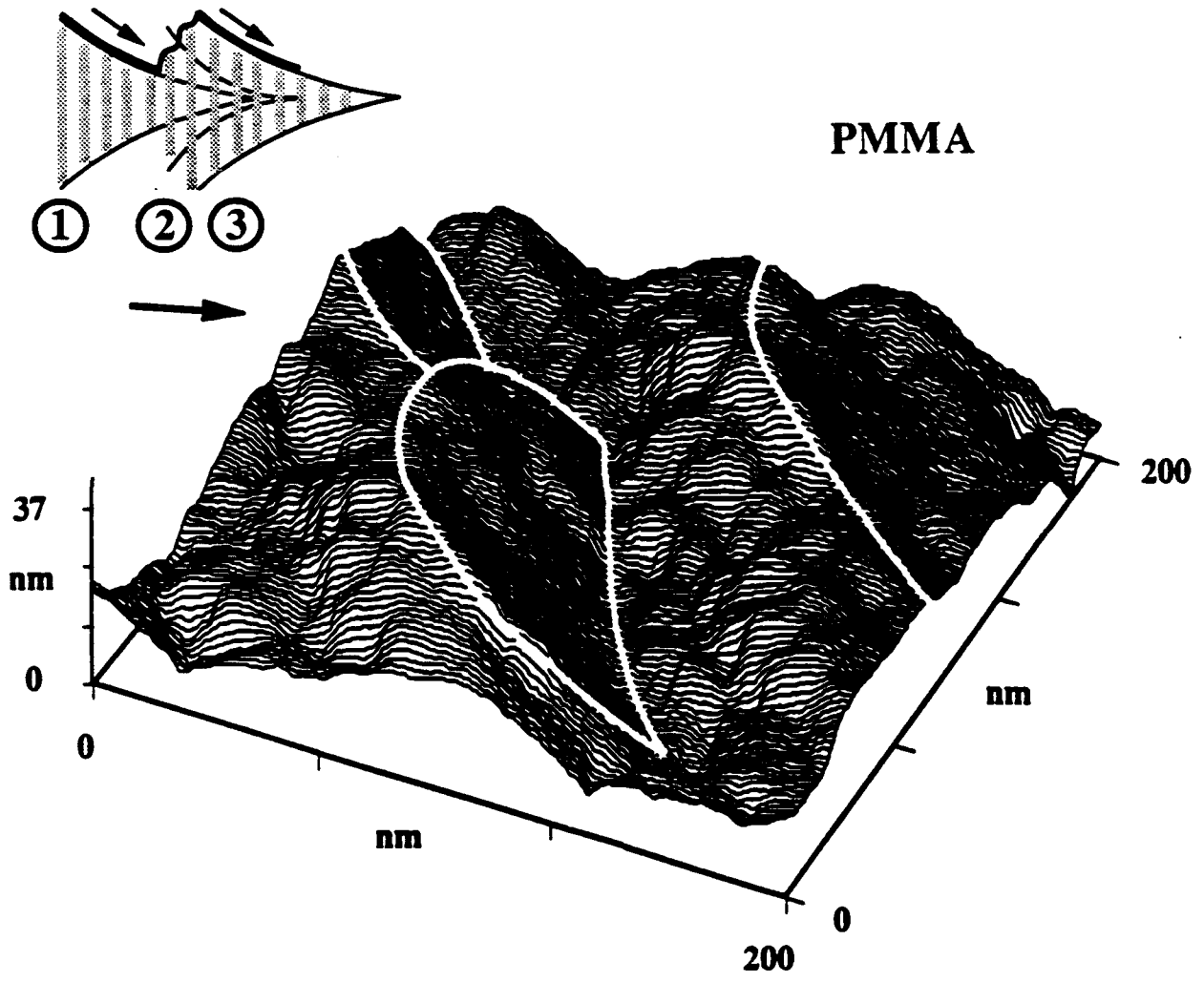

FIG. 8(b)

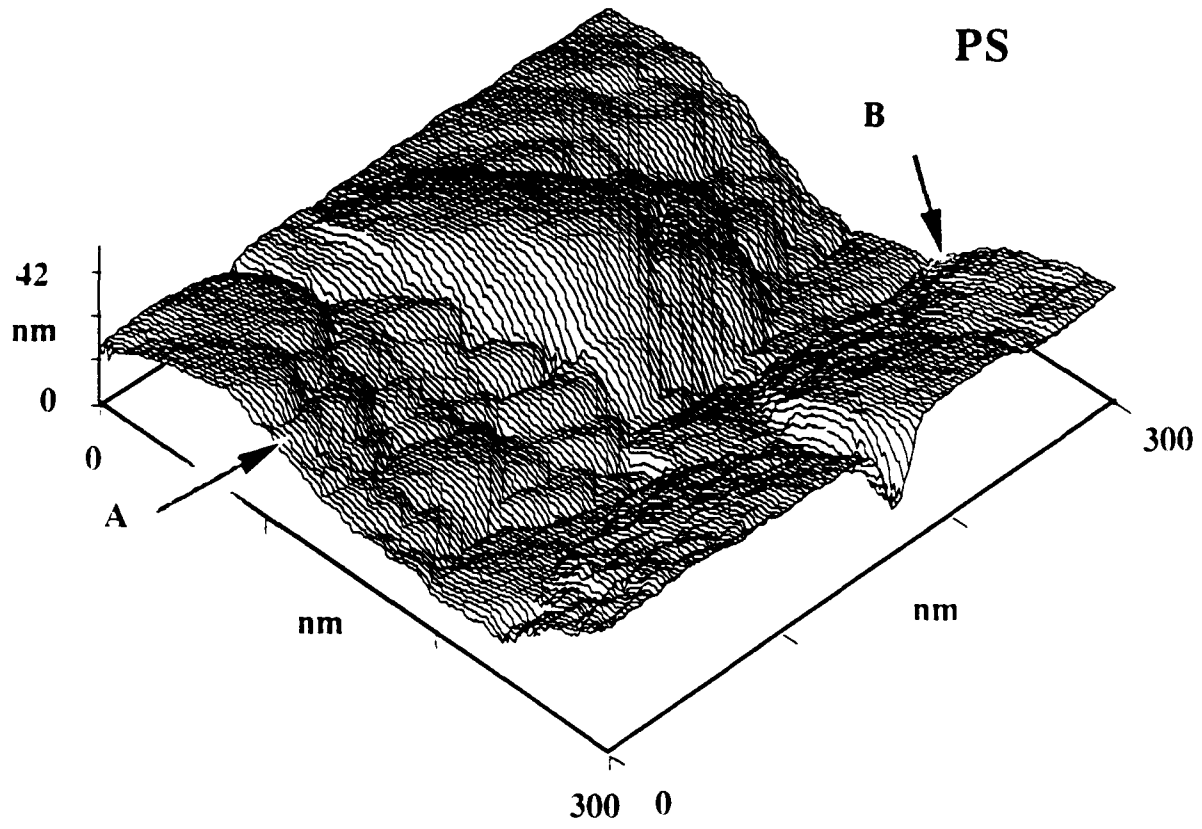

FIG. 9

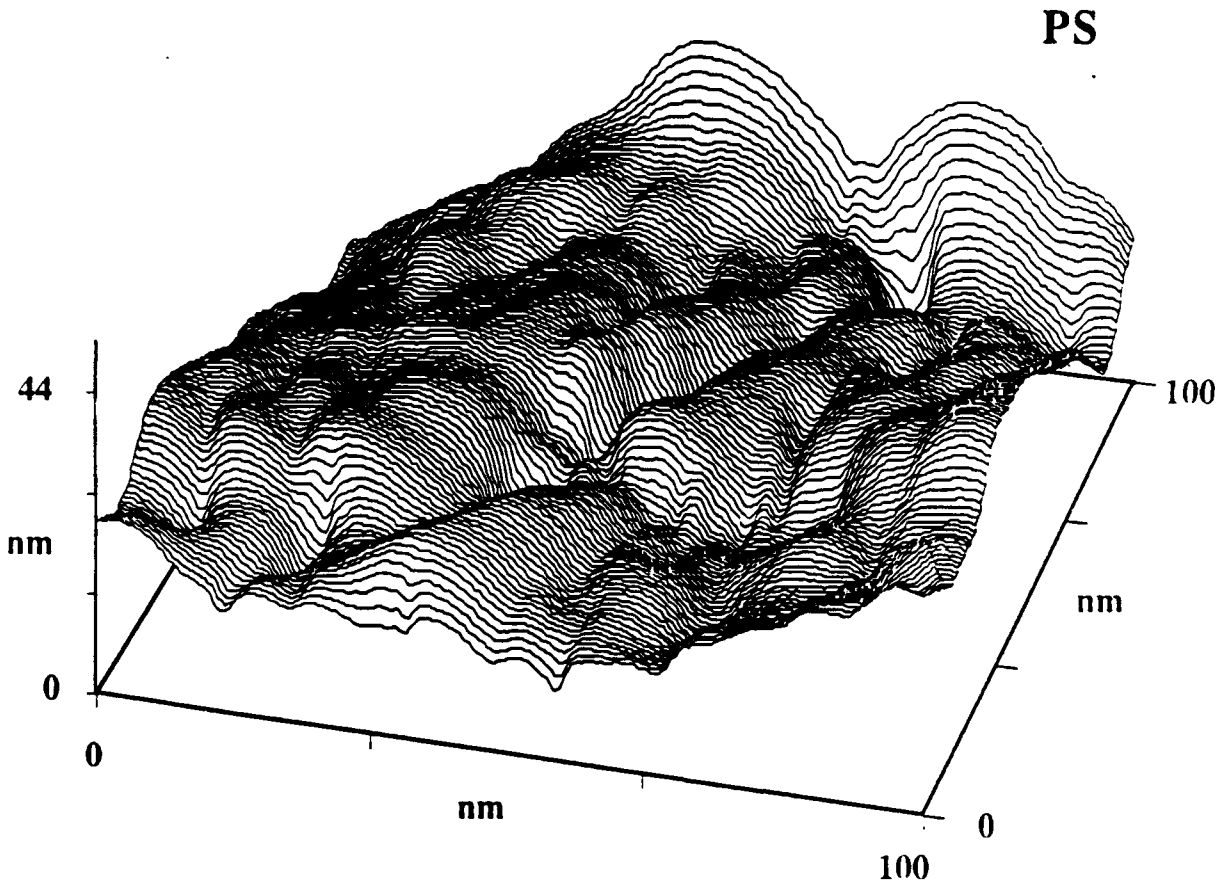

FIG. 10

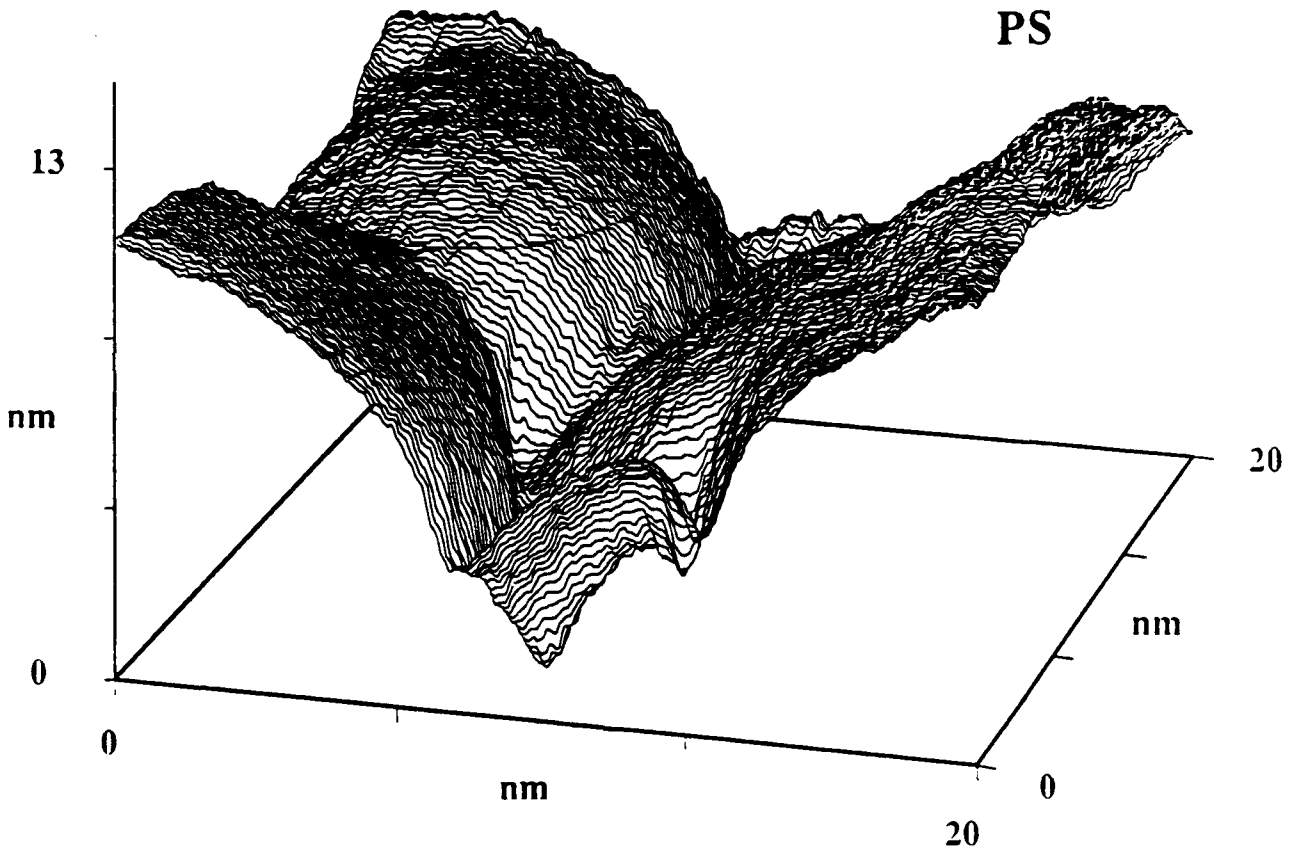

FIG. 11

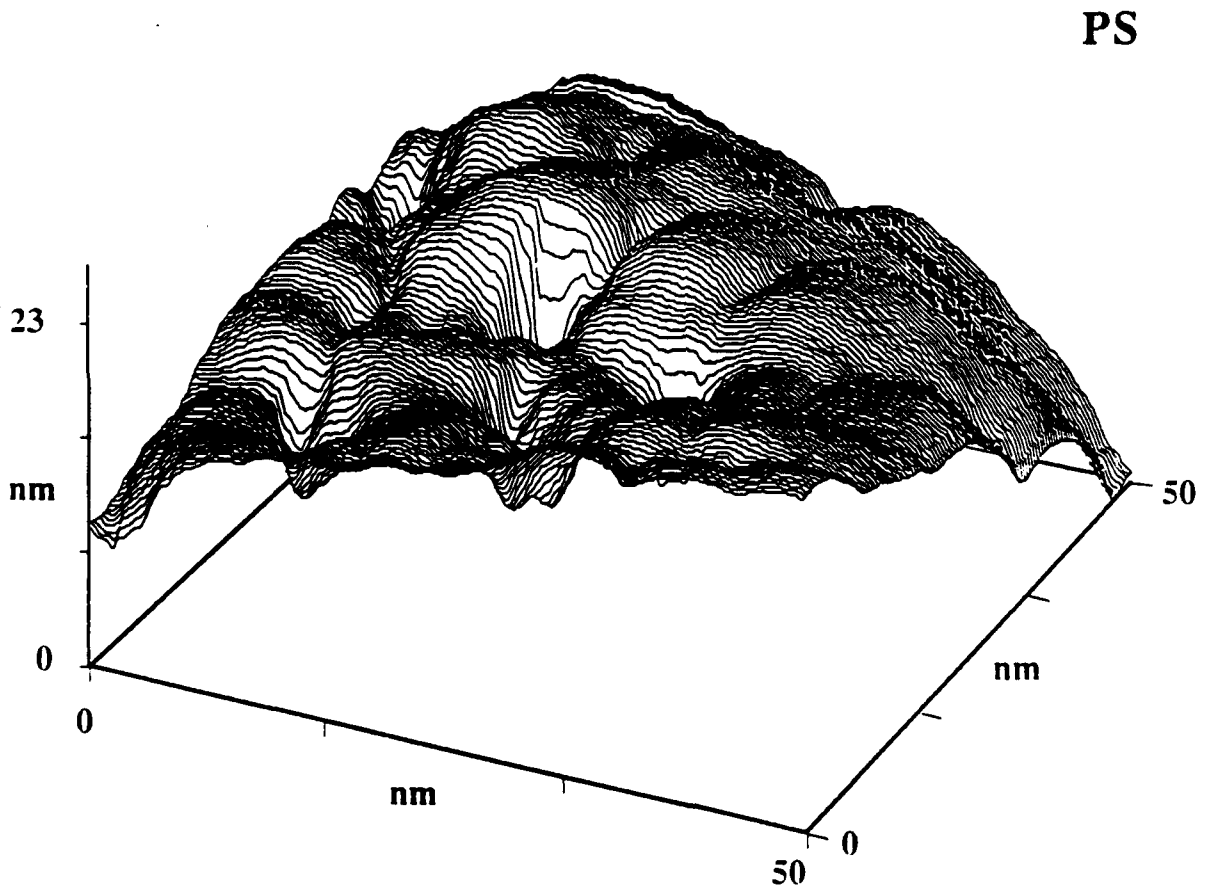

FIG. 12

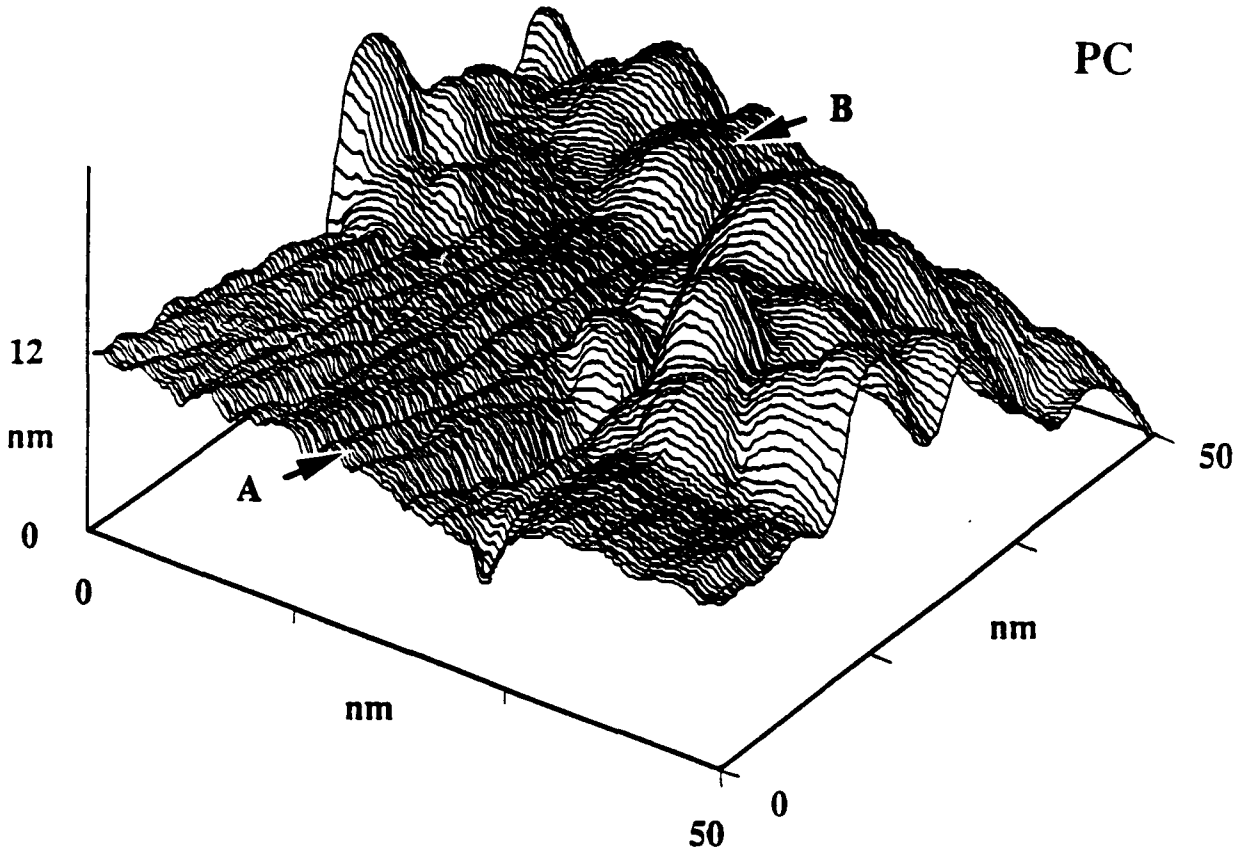

FIG. 13

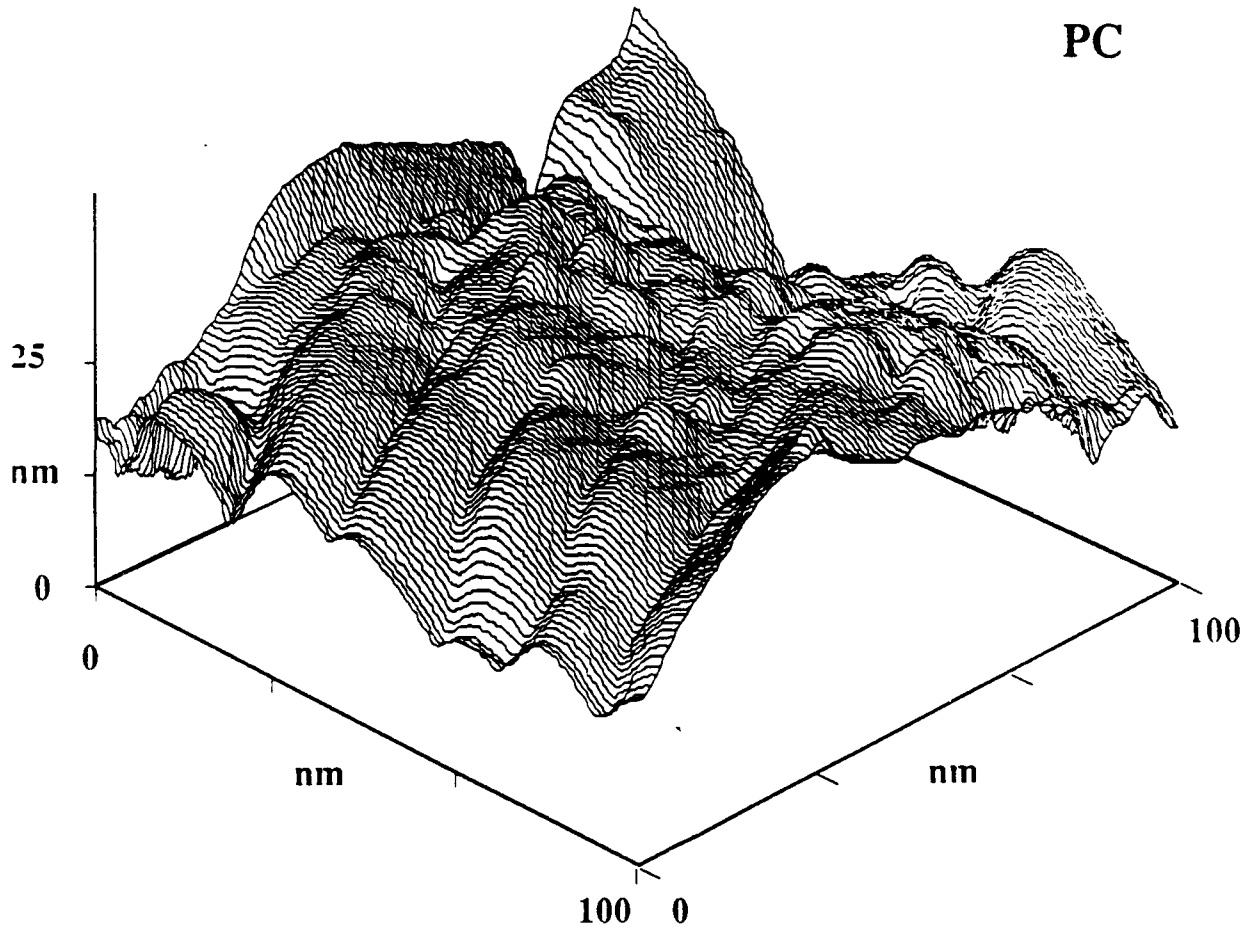

FIG. 14

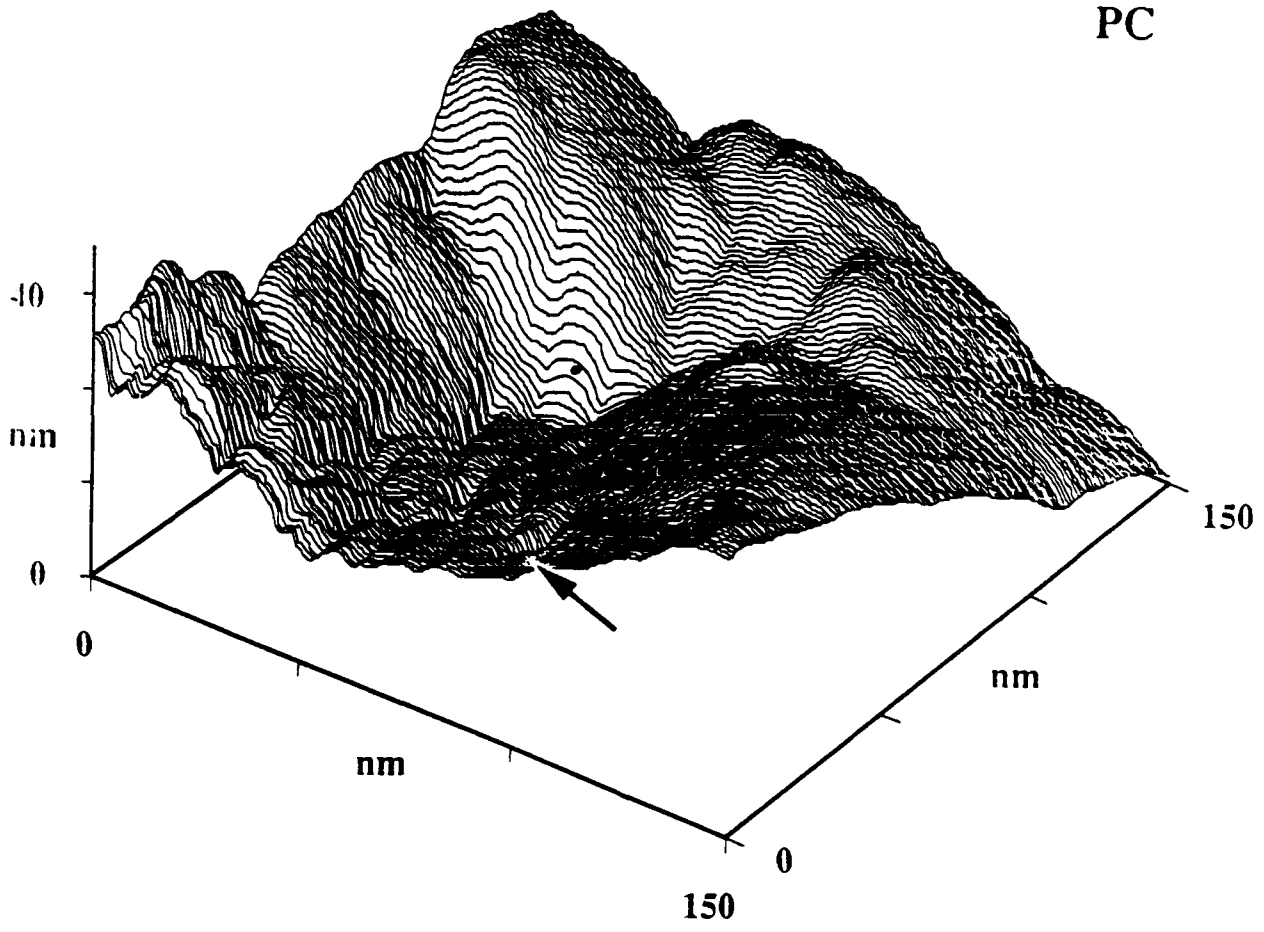

FIG. 15

XIII. Consequences of simultaneous exposure of inorganic solids to excimer laser light and an electron beam

J. T. Dickinson, S. C. Langford, L. C. Jensen, and P. A. Eschbach
Department of Physics, Washington State University, Pullman, Washington 99164-2814

L. R. Pederson and D. R. Baer
Pacific Northwest Laboratory, Richland, Washington 99352

(Received 3 January 1990; accepted for publication 24 April 1990)

In previous work we examined the changes in surface topography of sodium trisilicate glass ($Na_2O \cdot 3SiO_2$) with exposure to pulsed 248-nm excimer laser light at fluences of 2.6–5 J/cm^2 (per laser pulse), as well as the character of the products emitted from the glass surface (e.g., $\pm$ ions, electrons, ground state and excited neutral atoms and molecules). At fluences above a threshold, ablative etching occurs only after a number of preliminary laser pulses. In this work, we show a dramatic synergism in the ablation process by simultaneous bombardment of the glass surface with 0.5–2 keV electrons *and* laser pulses. Extensive etching can be initiated immediately and sustained indefinitely at subthreshold fluences. Reflection electron energy loss spectroscopy performed on electron-bombarded surfaces shows band gap states growing with exposure. We propose that surface and near-surface defects produced by inelastic scattering of the electron beam provide single-photon absorption centers, facilitating etching at subthreshold fluences. The potential for single-photon driven etching/ablation of other wide band gap dielectric materials is also discussed. These studies also support the hypothesis that etching and damage of such surfaces can occur after prolonged exposure to laser irradiation alone due to an accumulation of absorption centers.

I. INTRODUCTION

In previous work,[1,2] we examined the surface modifications and emission products accompanying the irradiation of sodium trisilicate glass with relatively high fluence/pulse (2.7–5.0 J/cm^2) 20-ns 248-nm excimer laser pulses. Irradiation at these laser intensities produced rapid etching accompanied by a visible, near-surface plume composed of a high density of electrons, positive ions (Na^+, Si^+, H^+), neutral atoms (O, Na, Si), the molecule NaO, and elecronically excited Na atoms (Na*). Recently we have demonstrated conclusively the presence of negative ions in the plume and determined their identity [discussed below, in relation to Fig. 1(c)][3].

The highly energetic ionic and excited neutral species were evidence of strong laser-"free electron" interactions (an inverse bremsstrahlung effect) which accelerate the electrons in the plume directly and the positive ions by virtue of electrostatic attraction to the electrons. Of particular interest here is the fact that the onset of etching (and, in coincidence, the onset of intense particle emission) requires repeated bombardment of the surface for several pulses; at higher fluences fewer initial pulses were needed. Such an induction or incubation requirement has been observed in the ablation of a number of materials (see, for example, Ref. 4).

We attributed this incubation process to the production of absorption centers under intense 248-nm radiation, consistent with observations of the formation of E' centers and nonbridging oxygen-hole centers during excimer laser irradiation.[5] These defects can then contribute to stronger coupling of the laser pulse to the near-surface region, e.g., by photon/free electron heating, which rapidly increases the surface temperature and subsequent release of matter. Subthreshold irradiation of the sodium trisilicate glass surface at 248 nm shows[6] copious photoelectron and Na^- emission. The electron-emission intensity varies linearly with laser-pulse-energy density, whereas the ion-emission intensity increases much more rapidly with fluence described well by the combination of a two-photon photoelectronic process *and* a nonlinear thermal process.[6]

Because electron bombardment of such materials result in defect production, we predicted that simultaneous (and perhaps sequential) electron (e^-) beam and laser exposure might lead to enhanced effects, namely measurable increases in particle emission intensities and surface etch rate, perhaps even at subthreshold fluences. (The threshold fluence is arbitrarily defined as a fluence per pulse where $< 10^2$–10^3 laser pulses produces no etching.) We show here that this is indeed the case and examine the response of the glass to various combinations and time sequences of e^- bombardment and laser pulses. We also present preliminary results on the simultaneous laser and e^- beam bombardment of NaCl, LiF, and amorphous SiO_2. The results have important implications regarding the use of UV lasers for surface modification, ablative etching, laser ablation deposition, and damage of optical materials.

II. EXPERIMENT

Details of the experimental setup for particle detection are given in Ref. 1. All of the laser experiments were conducted in a diffusion pumped, liquid nitrogen trapped vacuum chamber at a pressure of 10^{-5} Pa. Sample irradiation

 0021-8979/90/161831-06$03.00 © 1990 American Institute of Physics

was performed with a Lamda Physik EMG203 excimer laser operating at 248 nm (KrF). A repetition rate of 1 Hz was used to avoid any accumulative pulse-to-pulse heating of the surface. The laser fluence per pulse was varied by inserting various filters into the beam. The resulting fluence was determined from beam-energy measurements made with a Gentec ED 500 joule meter and the laser spot size, which was nominally 0.2×1.2 mm^2 at the sample surface. The electron beam was produced by a Varian Auger gun which provided a spot size of 1.5 mm diam over an energy range of 500–3000 eV at currents in the range of 50–300 μA.

A Channeltron electron multiplier (CEM), Galileo Electro-optics Model 4821, was used for detection of charged particles. The exposed front cone of the CEM was positioned 10 cm from the sample surface. Both positive and negative voltages could be applied to the front cone, thereby selecting positive or negative charges. In most of this work we were interested in detecting fairly intense ion bursts which provided enough current at the biased CEM front cone to be detected directly, without employing CEM gain. This experimental geometry is shown schematically in Fig. 1(a). The charge striking the cone yielded a current pulse which was capacitively coupled to an amplifier and digitized. By using the CEM in its normal geometry (with gain), charged-particle emission could also be observed at intensities many orders of magnitude lower (down to single-particle counting levels).

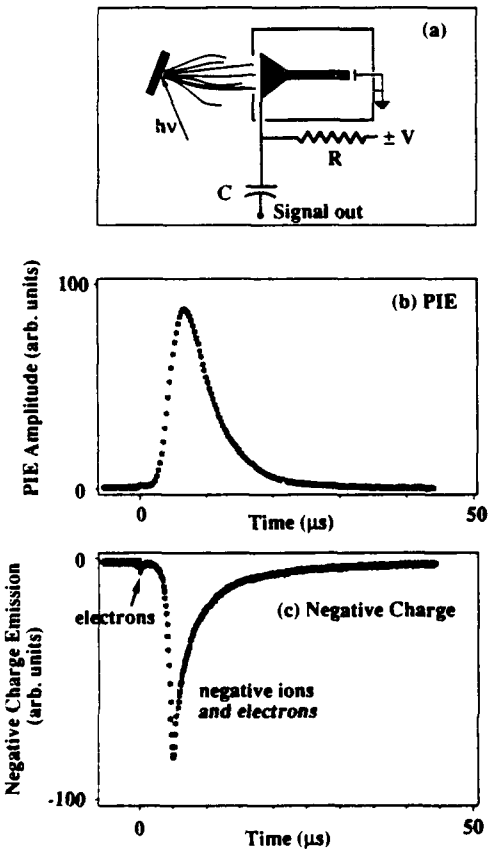

FIG 1 (a) A diagram of the sample and detector arrangement used to monitor the emission of charged particles during laser irradiation. Typical time-of-flight curves (single laser pulse) for (b) positive and (c) negative charge. In this particular experiment, the current striking the front cone was capacitively coupled directly to a fast amplifier; the CEM was not used to provide gain.

Individual charged-particle bursts could be detected as a function of arrival time relative to the laser pulse. Typical positive-ion and negative-particle emission signals are shown in Figs. 1(b) and 1(c). Note that the sign ($\pm$) of the signal is consistent with current flow due to positive charge for Fig. 1(b) and negative charge for Fig. 1(c). Measurements with unbiased detectors show a fast, negatively charged emission peak, and a slower, positively charged emission peak. The fast, negative peak corresponds to the small, fast peak in the negative-charge emission of Fig. 1(c) and is attributed to low-energy photoelectrons. The slower, positive emission peak corresponds to the large, broad peaks of both Figs. 1(b) and 1(c). Thus the slow negative emission of Fig. 1(c) is comoving with a dense cloud of positive ions to which it is electrostatically coupled. These slower negative particle emissions are exmamined in greater detail in a related paper,[3] in which we show that the majority of the negative charge consists of electrons. However, substantial numbers of negative ions (O^-, Si^-, NaO^-, and perhaps $NaSi^-$) are also detected and have been identifed by time-of-flight mass spectroscopy. Combined electrostatic and magnetic fields were required to separate the negative ions from the high densities of electrons and positive ions in the plume.

Reflection electron energy loss spectra (REELS) of the sodium trisilicate glass were obtained in a separate vacuum system. The REELS electron gun was concentric with a PHI Model 25-270AR double pass cylindrical mirror energy analyzer. Spectra were taken with a 300-eV, 10-nA primary beam with a spot diameter of approximately 5–10 μm. Clean glass surfaces were obtained in the REELS system by *in situ* fracture at a pressure of 7×10^{-7} Pa.

III. RESULTS AND DISCUSSION

In a previous study,[1] we showed that the only positive ion detected at subthreshold fluences is Na^+. More recent work[6] indicates that the positive-ion-emission (PIE) intensity increases in a nonlinear fashion with fluence/pulse and jumps dramatically at higher fluences, accompanied by significant etching and simultaneous appearance of a Na-rich plume. At fluences below the etching threshold (down to 60 mJ/cm^2), the PIE intensity is a strongly nonlinear function of fluence. The low-fluence PIE time-of-flight also shows little fluence dependence, contrary to a thermal mechanism. Therefore, the PIE mechanism below the threshold is photoelectronic, as opposed to photothermal, in nature. At higher fluences, thermal emission mechanisms dominate. We have satisfactorily modeled the fluence dependence of the PIE intensity over the full range of fluences studied by the combination of two mechanisms: (i) a two photon process, and (ii) a parallel thermal emission process driven by laser-induced heating of "free electrons" excited across the band gap. At sufficient free carrier densities, the surface material is heated rapidly to temperatures where thermal emission is

significant and etching result. The induction or incubation behavior, where repeated laser bombardment is required for the onset of etching,[1] indicates that the transition from photoelectronic to photothermal PIE is sensitive to the presence of surface defects from which electrons may be excited across the band gap.

In the absence of the e^- beam, no evidence of etching or plume formation is evident at a fluence/pulse of 1 J/cm^2. In Fig. 2(a), we show a sequence of 50 laser pulses (left hand side of the plot) which at the detector sensitivity employed here produced essentially no PIE. At the arrow, a 150-μA (current density of 6 mA/cm^2), 1500-eV electron beam was directed onto the bombarded region. Immediately, PIE is detected. We show the observed peak intensities for 50 additional laser pulses. A Na* plume was visually observed accompanying these PIE bursts. Thus, at a relatively low laser fluence, e^- bombardment can produce a dramatic increase in the extent of the laser interaction with the surface. The e^- beam thus appears to lower the threshold for strong coupling to the surface and therefore rapid etching by the excimer laser.

If during a sequence of simultaneous e^- and laser bombardment (with the above parameters), we simply turn off the e^- beam [see Fig. 2(b)], the PIE gradually decreases over a few pulses (1-Hz period), followed by occasional, sporadic bursts; continued laser bombardment for < 100 pulses brings the ion emission down permanently. This suggests that the e^--beam-induced damage is stable for at least a few seconds and that multiple pulses can etch the damaged region away, returning the material to its original state. We also conducted experiments in which a laser beam struck the surface during a ~ 100-ms time interval when the e^- beam was temporarily directed away from the sample. The absence of the e^- beam during the 20-ns laser pulse did not significantly affect the resulting PIE. This is consistent with the very small number of incident and secondary electrons produced by the electron gun in the laser-irradiated region of the sample over the duration of the pulse. We estimate $\sim 10^7$ e^- are produced in a volume containing roughly 10^{20} atoms of the solid, excluding the free charge carriers produced by the laser pulse.

Further evidence of long-lived defects is shown in Fig. 3. The left hand side of each trace shows the PIE prior to e^- beam exposure for 10 laser pulses at 1.8 J/cm^2. The laser beam was then blocked while the surface was exposed to a 1.5-keV, 6-mA/cm^2 e^- beam for 60 s. After the e^- beam was turned off, an additional waiting time (5, 60, or 240 s) was allowed for the decay of defects produced by the e^- beam before laser irradiation was reinitiated. The arrow indicates the first laser pulse after this delay. The intensity of the first and subsequent pulses show little evidence of any

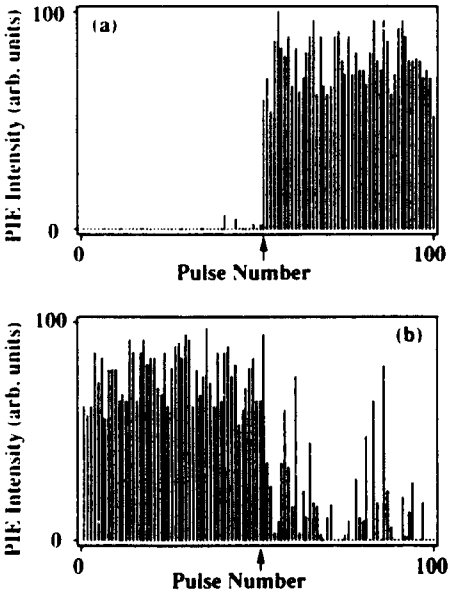

FIG. 2. Peak PIE due to successive laser pulses with and without simultaneous electron irradiation at 1.5 keV. In (a) the electron current density at the interaction region is initially zero and is raised to ~ 6 mA/cm^2 at the arrow. In (b), the electron current density is initially ~ 6 mA/cm^2 and is reduced to zero at the arrow.

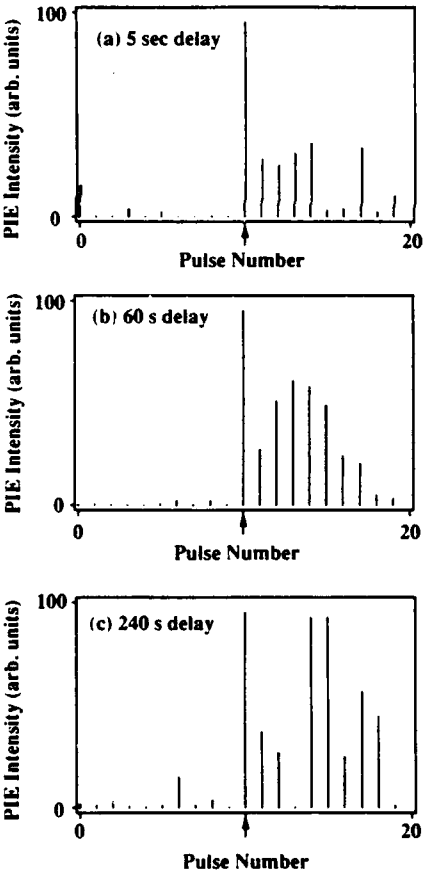

FIG. 3. Peak PIE due to successive laser pulses without simultaneous electron irradiation, but before and after a 60 s electron irradiation at 1.5 keV and 6 mA/cm^2. The sequence of laser pulses after electron irradiation was delayed by (a) 5 s, (b) 60 s, and (c) 240 s, respectively, from the end of electron irradiation.

"decay" due to the waiting time. Thus the e^- beam-induced modification of the material is very stable and furthermore is not thermal in nature since the sample would have cooled significantly in these long waiting intervals.

Systematic studies of electron dose and electron energy dependence of the enhanced emission have not yet been competed, but we can state a few qualitative observations for parameters in the neighborhood of the following values: e^- beam current density ~ 6 mA/cm^2, e^- beam kinetic energy ~ 1.5 keV, exposure times prior to laser pulse ~ 1 s, laser fluence/pulse ~ 1.5 J/cm^2. At values near these we find that increasing either the e^- beam current or the e^- beam kinetic energy increases the intensity of the enhanced emission. The effect of increasing the integrated exposure time prior to the laser pulse appears to saturate after a few seconds. As one approaches 2.5–3-J/cm^2 laser energy density, the e^- beam current necessary to induce an immediate enhancement of PIE intensity decreased. Above the threshold laser energy density, where etching and plume formation are self sustaining, applying a 1.5-keV, 6-mA/cm^2 electron beam enhanced the PIE intensities and visibly brightened the plume. At laser energy densities greater than ~ 6 J/cm^2, no enhancement was observed, suggesting that laser-induced damage dominated over any additional defects created by the electron beam.

Further evidence of defect formation due to electron bombardment was obtained by REELS performed on a fresh fracture surface of the sodium trisilicate glass. Three REELS traces taken after successive electron-beam exposures at 300-eV incident kinetic energy are shown in Fig. 4. The REELS data taken immediately after fracture show no states in the energy loss range from -2 to -6 eV. (Zero energy is defined by the elastic peak). Following five minutes of electron beam exposure, two peaks appear at -4 and -6 eV where no peaks appeared previously. After ten minutes of electron-beam exposure, the two peaks are very well defined. Similar changes in RHEELS spectra appeared during ion bombardment. The strong correlation between the loss peaks observed in the -2 to -6 eV region and the amount of e^- beam exposure is consistent with the production of surface defects by electron irradiation. Although selection rules differ between electron- and photon-induced transitions, some transitions appear to be available at the damaged glass surface at 5 eV, the energy of 248 nm photons. REELS experiments by Rowe[7] on amorphous silica films showed peaks at 3.5, 5.1, and 7.2 eV which were attributed to a metastable surface phase of approximately SiO composition, consistent with loss of oxygen.

Enhanced "fast" electron emission and slow negative charge emission (NCE) (electrons and negative ions electrostatically coupled to the positive ion cloud) also results from combined laser/e^- beam stimuli. In Fig. 5, we show the bursts of negative charge emission for a sequence of 1.3 J/cm^2 laser pulses at a frequency of 1 Hz. The fast electron [Fig. 5(a)] and slow negative charge [Fig. 5(b)] intensities were taken simultaneously. The first 20 laser pulses are prior to e^- beam exposure. At the first arrow, the laser beam was blocked and the surface was bombarded at 6 mA/cm^2 and 1.5 keV for 1 min. The electron beam was then turned off and surface was irradiated with 20 more laser pulses. Both the fast electrons and the slower negative charge show substantial increases in intensity after e^- beam exposure, followed by gradual decays. At the second arrow ($\sim$pulse 41), the e^- beam was turned on and left on as the laser pulses continued; here we observe strong, sustained enhancements of both these emissions. Thus both the fast electrons and the slow NCE show the same dependence on e^- beam exposure as the PIE.

Etching and/or surface damage on wider bandgap dielectrics at very high fluences have been previously observed at 248 nm by Kuper and Stuke[8] and by Dreyfus.[9] This dam-

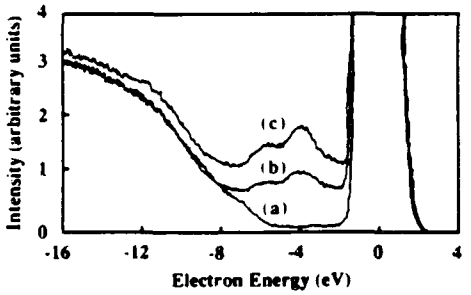

FIG 4 REELS spectra of a sodium trisilicate fracture surface taken (a) immediately after fracture, (b) after 5 min of exposure to the electron beam, and (c) after ten minutes of exposure to the electron beam.

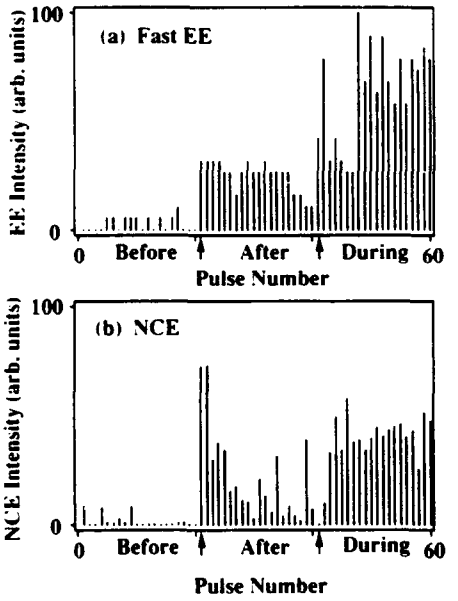

FIG 5 (a) Fast electron emission and (b) probable negative ion emission prior to, after, and during electron irradiation (1.5 keV, 6 mA/cm^2). Immediately prior to the first arrow, the laser beam was blocked and the surface exposed to the electron beam for 60 s; the electron beam was then turned off and laser irradiation continued. At the second arrow, the electron beam was turned on and left on for the remainder of the laser pulses.

age is presumably due to multiphoton absorption processes which populate the conduction band of these materials. Laser heating of the conduction electrons results in surface damage when adequate electron densities are achieved.[10] Surface damage due to intense laser irradiation is quite sensitive to the presence of defects, which facilitate damage at much lower fluences. Such defects can be produced in the course of laser irradiation itself. For example, E'-center (Si $^{-}$ Si) production in SiO_2 has been attributed to the nonradiative decay of neutral excitons produced by two-photon excitations.[11] Devine[12] has provided further evidence for a two-photon process in amorphous SiO_2 (Suprasil W) by exposure to laser light at both 4.6 and 6.4 eV. Increased absorption due to defects produced during the course of laser irradiation is consistent with our earlier observations of an incubation/induction exposure to the laser prior to etching.[1] Other defects with the potential to enhance particle emission intensities include the nonbridging oxygen-hole center,[13] (Si-O$^{\cdot}$) and the peroxy radical[14] (Si-O-O$^{\cdot}$); both provide occupied energy levels in the band gap.

Many of the same defects produced by multiphoton processes in wide band gap materials can be produced by e^- irradiation at relatively low e^- energies. Electron irradiation at higher energies than explored in our studies have been shown to create oxygen vacancy defects, including the E_1'-center, in fused silica.[15] Transient increases in UV absorption at 5 eV have been observed subsequent to pulsed electron irradiation.[16] Vigouroux *et al.* suggest that at least one of these defects can be stabilized by trapping an additional implanted electron.[17] A high density of electron traps is necessary to explain their observations of surface charging on fused silica under electron irradiation. Electron irradiation of silica at energies in the 2–8 keV range is also known to cause removal of oxygen from the surface,[18] resulting in stable, silicon-rich surface layers with high defect densities.[19] Silicon-rich films produced by evaporation of "silicon monoxide" onto silicon substrates have been found to ablate much more readily than stoichiometric SiO_2 films.[20] Silicon-rich surfaces layers produced by electron irradiation should therefore be expected to facilitate the ablation of fused silica and similar materials.

We therefore propose that in our experiments such defects, produced either by intense laser light or by electron bombardment, results in increased 5-eV photon absorption resulting in high densities of free electrons in the near-surface region.[6] At sufficiently high laser fluences and electron densities, the later part of the laser pulse heats these electrons via inverse bremsstrahlung, initiating substantial heating in the near-surface material and subsequent decomposition and ionization.

We have made preliminary observations of enhanced particle emission with e^- beam exposure from single-crystal NaCl and LiF as well as amorphous SiO_2. The intrinsic band gaps of these materials are 8.6, 13.6, and 8.9 eV, respectively. Figure 6 shows the response of PIE from these three materials to e^- beam exposure at laser fluences below those required for sustained PIE emission. This was determined by first raising the fluence to very high levels until PIE was observed, then lowering the fluence until the PIE dropped

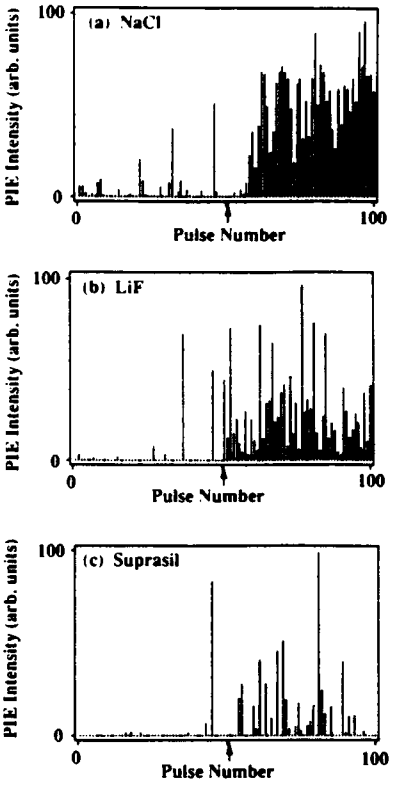

FIG. 6. Peak PIE from (a) NaCl (at 2.8 J/cm^2), (b) LiF (at 6.7 J/cm^2), and (c) fused silica (Suprasil II, at 7.8 J/cm^2) due to successive laser pulses first without, then with simultaneous electron irradiation at 1.5 keV. The arrow marks the first laser pulse after the electron beam was turned on.

dramatically. As shown in Fig. 6, a few PIE bursts were observed in all three materials during subsequent laser pulses in the absence of the electron beam. At the arrow a 6-mA/cm^2, 1.5-keV electron beam was turned on. Either on the first pulse or very soon afterwards, the PIE intensity increases dramatically showing that electron-induced damage can enhance material removal from these materials.

We assume that for the amorphous SiO_2, the defects produced by the electron beam are those previously discussed. For the NaCl and LiF, the dominant defect stable at room temperature is the F-center (an electron trapped at a halide vacancy). High F-center densities are readily produced in the near-surface region of alkali halides by electrons with keV energies.[21] The LiF F-center absorbs strongly at 248 nm (5 eV), whereas NaCl F-band centers at 2.7 eV. Two-photon absorption could ionize these F-centers, leading to laser heating of conduction electrons as discussed above for sodium trisilicate glass. Other processes which may contribute to enhanced conduction electron densities are single-photon ionization of an F$^-$ center (two electrons trapped at a halide vacancy) and resonant two-photon absorption across the band gap involving an α center (a halide vacancy with no trapped electrons); however, the densities of these latter two defects may well be two small to produce the large effects observed here.

IV. CONCLUSION

Considerable work remains in the detailed characterization and explanation of these combined beam effects. Scanning electron micrographs of glass surfaces etched by laser only and by the combined radiation sources showing distinctly different topographies will be published elsewhere. Further experiments are planned to characterize the defects responsible for low-fluence etching and particle emission from these materials and to determine the possible role of transient defects, which are frequently observed under electron bombardment of wide band gap materials. In materials like the binary glasses, the enhanced diffusion of some components under electron irradiation[22] may also significantly affect the laser/surface interaction.

The technological application of low-energy electrons to modify the etching and other surface effects of laser radiation may prove extremely useful for a number of materials, including wide band gap dielectrics and strongly absorbing materials such as polymers and perhaps semiconductors. By controlling the energy of the electron beam, the distribution of defects versus distance from the surface can be very easily controlled. The resulting localization of absorption may minimize certain undesired consequences of laser irradiation, such as bulk heating and consequent diffusion. In sodium trisilicate glass, it appears possible that the proper choice of laser-and electron-beam parameters may yield high etch rates without the thermal-stress-induced fracture observed at high laser fluences.[1] In the case of photoablative deposition, it may be possible with combined laser/e^- beam processing to achieve higher deposition rates without unwanted formation of particulates (ejecta). Chemical modification of material surfaces by laser radiation may also benefit from simultaneous e^- irradiation. For instance, Igarashi *et al.*[23] have recently shown that they can transform surface layers of $BaTiO_3$ from an insulator to a *n*-type semiconductor (oxygen deficient) with KrF excimer laser radiation. Combining laser irradiation with an electron beam may provide useful control of localization and/or extent of the transformation. Furthermore, well characterized defect chemistry created by controlled electron bombardment may prove useful in elucidating damage mechanisms in optical thin films and other optical materials.

ACKNOWLEDGMENTS

The authors wish to thank Brad Pate, Washington State University, for helpful discussions. The WSU portion of this work was supported by the Office of Naval Research under Contract No. N00014-87-K-0514, the National Science Foundation under Grants Nos. DMR 8601281 and DMR 8912179, and the Washington Technology Center. The PNL activities were supported by the U.S. Department of Energy (BES-DMS) and through internal Exploratory Research of the Molecular Science Research Center under Contract No. DE-AC06-76RLO-1830.

[1] P. A. Eschbach, J. T. Dickinson, S. C. Langford, and L. R. Pederson, J. Vac. Sci. Technol. A 7, 2943 (1989).
[2] P. A. Eschbach, J. T. Dickinson, and L. R. Pederson, in *Laser- and Particle-Beam Chemical Processes on Surfaces*, edited by A. W. Johnson, G. L. Loper, and T. W. Sigmon (Materials Research Society, Pittsburgh, 1989), p. 385.
[3] S. C. Langford, L. C. Jensen, J. T. Dickinson, and L. R. Pederson, J. Appl. Phys. (to be published).
[4] S. Lazare and V. Grainer, J. Appl. Phys. **63**, 2110 (1988).
[5] R. A. B. Devine, C. Fiori, and J. Robertson, in *Defects in Glasses*, edited by F. L. Galeener, D. L. Griscom, and M. J. Weber (Materials Research Society, Pittsburgh, 1986) p. 177.
[6] P. A. Eschbach, J. T. Dickinson, S. C. Langford, L. C. Jensen, L. R. Pederson, and D. R. Baer, "Precursors to the photo-ablation of sodium trisilicate glass due to UV Excimer irradiation," submitted to *In-Situ Patterning: Selective Area Deposition and Etching*, MRS Proceedings, Symposium B, 1989 Fall Meeting, Boston, MA, edited by A. F. Bernhardt, J. G. Black, and R. Rosenberg.
[7] J. E. Rowe, Appl. Phys. Lett. **25**, 576 (1974).
[8] S. Kuper and M. Stuke, MRS Symp. Proc. **129**, 375 (1989).
[9] R. W. Dreyfus, IBM T. J. Watson Research Center, private communication.
[10] N. Bloemberger, IEEE J. Quantum Electron. **QE-10**, 375 (1974).
[11] T. E. Tsai, D. L. Griscom, and E. J. Friebele, Phys. Rev. Lett. **61**, 444 (1988).
[12] R. A. B. Devine, Phys. Rev. Lett. **62**, 340 (1989).
[13] M. Stapelbroek, D. L. Griscom, E. J. Friebele, and G. H. Siegel, Jr., J. Non-Cryst. Solids **32**, 313 (1979).
[14] A. H. Edwards and W. Beall Fowler, Phys. Rev. B **26**, 6649 (1982).
[15] M. Antonini, P. Camagni, P. N. Gibson, and A. Manara, Radiat. Effects **65**, 41 (1982).
[16] T. Tanaka, T. Eshita, K. Tanimura, and N. Itoh, Cryst. Lattice Defects and Amorph. Mat. **11**, 221 (1985).
[17] J. P. Vigouroux, J. P. Duraud, A. Le Moel, C. Le Gressus, and D. L. Griscom, J. Appl. Phys. **57**, 5139 (1985).
[18] J. T. Dickinson, M. A. Loudiana, and A. Schmid, in *Adhesion, Sealants and Coatings for Space and Health Environments*, edited by L. H. Lee, (Plenum, New York, 1988), pp. 467–475.
[19] J. R. Pitts and A. W. Czanderna, Nucl. Instrum. Methods Phys. Res. B **13**, 245 (1986).
[20] R. A. B. Devine and C. Fiori, Radiat. Effects **99**, 675 (1986).
[21] R. A. Nunes, H. J. Kalinowski, S. Paciornik, A. M. De Souza, and L. C. Scavarda Do Carmo, Nucl. Instrum. Methods Phys. Res. B **32**, 222 (1988).
[22] P. Mazzoldi and A. Miotello, Radiat. Effects **99**, 39 (1986).
[23] K. Igarashi, H. Saito, T. Fumioka, S. Fujitsu, K. Koumoto, and H. Yanagida, J. Am. Ceram. Soc. **72**, 2367 (1989).

208

XIV. PRECURSORS TO THE PHOTO-ABLATION OF SODIUM TRISILICATE GLASS DUE TO UV EXCIMER IRRADIATION#

P. A. ESCHBACH,* J. T. DICKINSON,* S. C. LANGFORD,* L. C. JENSEN,*
L. R. PEDERSON,** AND D. R. BAER**
* Washington State University, Pullman, WA 99164-2814
**Pacific Northwest Laboratory, Richland, WA 99352
Appeared in Mat. Res. Soc. Symp. Proc. 158 (1990), pp. 463-469.

ABSTRACT

On polished sodium trisilicate glass surfaces, a fairly distinct threshold in laser fluence is observed to commence ablative etching. An incubation or induction effect is also seen where a series of laser pulses is required to induce etching. In this paper we examine features of the charged particle emission over a broader range of fluences (in particular, at lower fluences) to identify those factors which control the onset of etching. Laser--free electron heating is proposed as a dominant mechanism.

INTRODUCTION

In previous work,[1] we examined the changes that occur in sodium trisilicate glass and the resulting plume products when the glass was irradiated with relatively high fluence (2.7 - 5.0 J/cm^2) 248 nm excimer laser light. Irradiation at these high fluences produces high etch rates (typically 200 nm per laser pulse) accompanied by a visible near-surface plume composed of large quantities of electrons, positive ions (Na^+, Si^+, H^+); neutral atoms (O, Na, Si); molecular NaO; and electronically excited Na atoms. Energetic ionic and excited neutral species in the plume indicate the presence of strong laser-plume interactions. At fluences ~2.7 J/cm^2 (which we define as an approximate threshold), a induction or incubation period involving bombardment of the surface with a few laser pulses was required to induce etching and plume formation.

In this paper we examine the interaction of 248 nm excimer radiation with sodium trisilicate glass at fluences below that required for the onset of plume formation and rapid surface etching, i.e., below about 2.7 J/cm^2, to identify those factors which control the onset of etching. We show that significant electron and Na^+ emission is observed even at relatively low fluences. To within the sensitivity of our measurements, other charged and neutral species seen at fluences above the etching threshold were not observed at low fluences. Near-surface defect states appear to play an important role in the subthreshold emission processes. Increasing the near surface defect density by low energy (1 KeV) electron irradiation is shown to *lower* the threshold for plume formation and the onset of rapid etching. The manipulation of defect densities by particle irradiation and composition control may have important applications in ablative etching, laser ablation deposition, and the prevention of damage to optical materials.

EXPERIMENT

Details of the particle detection experiments are given in references 1-3. All of the laser experiments were conducted in a diffusion pumped, liquid nitrogen trapped vacuum chamber at a pressure of 10^{-5} Pa. Sample irradiation was performed with a Lamda Physik EMG203 excimer laser operating at 248 nm (KrF). The laser fluence was varied by inserting various filters in the beam. The beam energy was measured with a Gentec ED 500 joule meter. Charge particles were detected with an appropriately biased Channeltron electron multiplier (CEM), Galileo Electro-optics model 4039. When high particle currents were encountered, the CEM was operated in a "zero gain" mode, using the biased CEM front cone merely to collect the detected current. Ion identification was accomplished with a UTI 100C quadrupole mass spectrometer (QMS) with the ionizer removed. An electron beam for simultaneous bombardment of the glass surface was produced by a Varian Auger gun which provided a spot size of 1.5 mm diameter over an energy range of 500-3000 eV at currents in the range of 50-300 μA.

Reflection electron energy loss spectra (REELS) of the sodium trisilicate glass was obtained in a different vacuum system, maintained at pressures < 10^{-6} Pa. The REELS data were

taken with PHI Model 15-255G double pass energy analyzer mounted concentrically with an electron gun operated at 300 eV and 10 nA. The spot diameter was 5-10 μm. Clean glass surfaces were obtained in the REELS system by in-situ fracture.

RESULTS AND DISCUSSION

Electron Emission. The highly energetic ionic and excited neutral particles accompanying etching at high fluences was attributed to inverse bremsstrahlung acceleration of electrons in the near-surface region of the vacuum, which results in ion acceleration by electrostatic attraction.[1] This process requires substantial electron and ion densities in this region during the early portion of the laser pulse; subsequent interactions with the laser pulse elevate both the electron and surface temperatures. In the context of the inverse bremsstrahlung model, the photoelectron and ion emission intensities play a crucial role in determining the onset of plume formation and rapid etching. The electron emission intensity vs laser fluence is shown in Fig. 1.

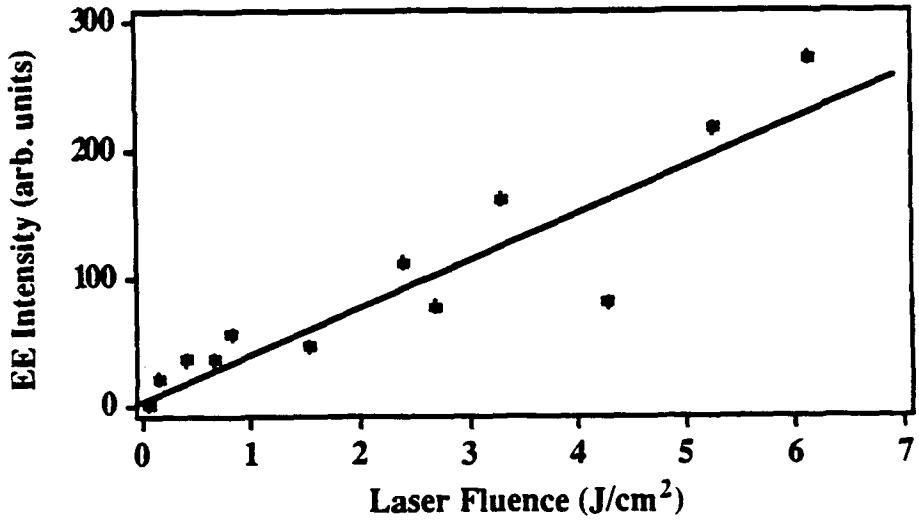

Fig. 1. The Electron Emission Intensity vs Laser Fluence. Note that it is linear, implying a single photon process.

Over a wide range of fluences, including those sufficient for plume formation, EE is a linear function of laser fluence. First order dependence of EE on laser fluence has also been observed during the laser irradiation of fused silica.[4] Given the transparency of sodium trisilicate glass at 5 eV,[5] this suggests that the emission is a single photon process involving mid-gap defect states. In our experiments, the EE intensity was quite stable from pulse to pulse, in contrast to other emissions (e.g., positive ion emission), suggesting that the observed EE at these fluences is not very sensitive to surface conditions. Further, the observed EE was a relatively strong function of laser repetition rate, falling markedly at rates above ~20 Hz. This dependence is likely due to depletion of filled traps which require times on the order of 50 ms to replenish. The simple first order process observed also suggests that overall charging of the surface was not very extensive; substantial charge transfer would be expected to introduce non-linear behavior.[6]

Positive Ion Emission (PIE). Positive ions are also emitted at fluences well below the threshold for plume formation and rapid etching. The low fluence positive ions were mass analyzed with a quadrupole mass spectrometer. Within our sensitivity, all PIE was mass 23, i.e., Na^+. Estimates of E fields along the ion flight paths allow time-of-flight analyses which indicate that the ion energies are substantially less than 1 eV. This is in stark contrast to high fluence PIE which typically displayed energy distributions with peaks in excess of 10 eV. As noted above, we attribute this difference to inverse bremsstrahlung acceleration of electrons coupled with "wake-like" acceleration of positive ions towards the electrons moving away from the surface.

Plots of PIE Intensity (averages over 50 laser pulses) vs laser energy are shown in Figures 2a(log) and 2b (linear) intensity scales. Attempts to use simple first order heating and an Arrhenius equation[7] for the PIE emission rate were unsuccessful in fitting the data over the full range of

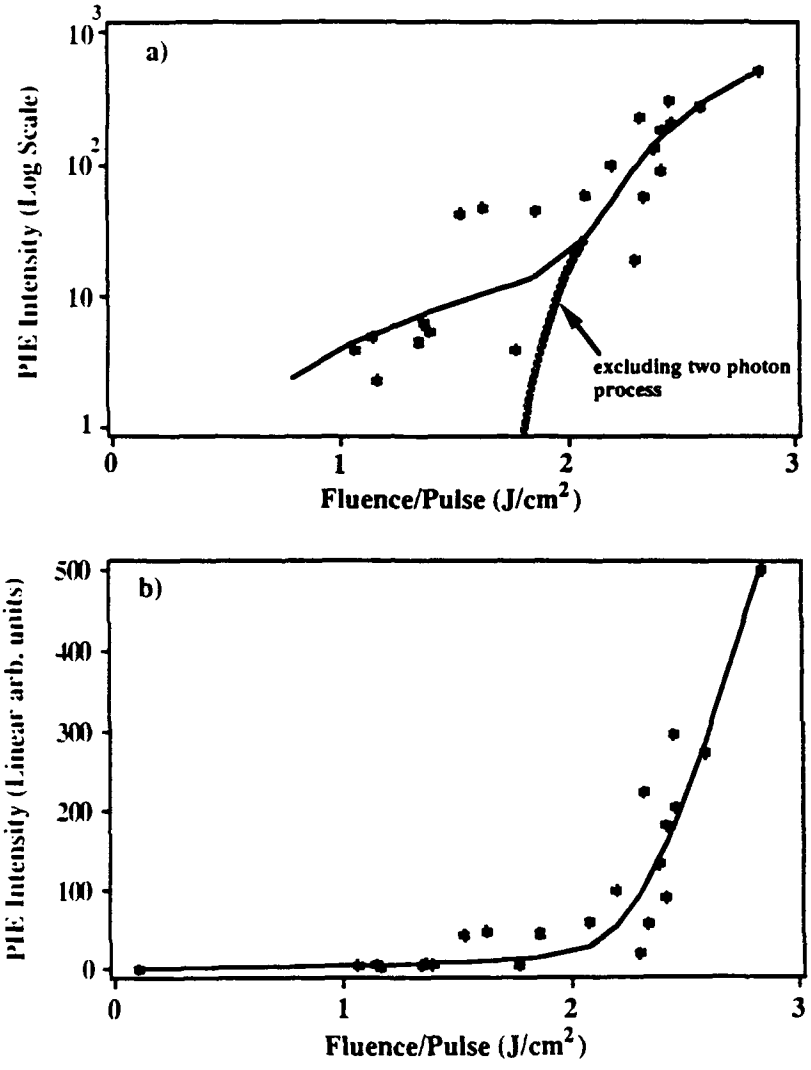

Fig.2 Positive Ion Emission Intensity vs laser fluence/pulse. a) log intensity scale, b) linear intensity scale. The solid lines represent a fit to equation 3. The hatched line indicates the consequences of discarding the first term $\sim f^2$.

fluences. At lower fluences,the data were consistent with a non-thermal, two photon process. i.e., $I_{PIE} \sim f^2$, where f is the fluence/pulse (Note that is we assume a "square wave" laser pulse, the photon flux F (photons/cm^2/s) and the fluence/pulse, f, are proportional). Two photon excitations in this material would yield electronic states above the band gap; the emission of Na^+ under these conditions most likely involves electronic defects. Ohuchi et al.[8] have proposed that electron stimulated desorption of Na^+ from sodium trisilicate glass involves a trapped hole precursor. Two photon production of related defects has been previously reported.[9,10]

At higher fluences, the rapidly increasing PIE intensity is consistent with a heating mechanism consisting of *simultaneous* single photon--free electron release (from defects) accompanied by laser heating of the free electrons by the laser pulse itself. This is similar to multiphoton free electron production + heating proposed by Shen et al[11] for the heating and damage of wide band gap, defect-free materials . An equation describing the temperature rise due to laser--free electron heating has been derived by Epifanov[12,13] and is given by:

$$\frac{\partial T(\mathbf{r},t)}{\partial t} = \frac{C}{\rho c} T^{1/2}(\mathbf{r},t)\, n_c\, F^{3/2}(\mathbf{r},t) \qquad 1)$$

where C is a constant involving parameters of the material, r is the mass density of the glass, c the heat capacity, n_c the free electron density, and F is the photon flux (photons/cm^2/s). For single photon--free electron generation, n_c would be proportional to $n_d F$ (or $n_d f$),where n_d is the density of defects capable of releasing electrons. Integrating this equation (assuming F constant and uniform over the interaction volume *during* the laser pulse), we obtain a temperature rise, ΔT, given by:

$$\Delta T = K_1 \cdot f^{5/2} + \frac{K_1^2}{1200} f^5 \qquad 2)$$

Substituting this non-linear heating mechanism into an Arrhenius term and combining with the two photon emission process discussed above, we obtain for I_{PIE} the equation:

$$I_{PIE} = a_1 f^2 + a_2 EXP(-b/(K_1 \cdot f^{5/2} + \frac{K_1^2}{1200} \cdot f^5)) \qquad 3)$$

where a_1, a_2, b, and K_1 are adjustable parameters.

The solid lines in both Fig. 2a and 2b are generated from a non-linear least squares fit to the raw data using this equation. The hatched line shows the effect of ignoring the first term ($\sim f^2$) of this equation. Although there is considerable scatter, the overall fit is quite reasonable. In addition, when we take PIE data with the full gain of the Channeltron electron multiplier at fluences as low as 0.1 J/cm^2, we continue to find a strongly non-linear intensity vs. fluence dependence, consistent with this equation. The significant influence of the second term coincides with the very beginning of the onset of plume formation and etching of the glass surface in what appears to be somewhat like an avalanche. In fact, no avalanche (usually attributed to electron multiplication) is required for this PIE behavior; the higher order heating is sufficient to explain the rapid rise in PIE with fluence. We therefore propose that the dominating factor for these strong laser surface interactions is the free carrier density,n_c. n_c, in turn is directly related to the density of defects serving as sources for single photon generated free electrons, consistent with the observed first order electron emission results (Fig. 1).

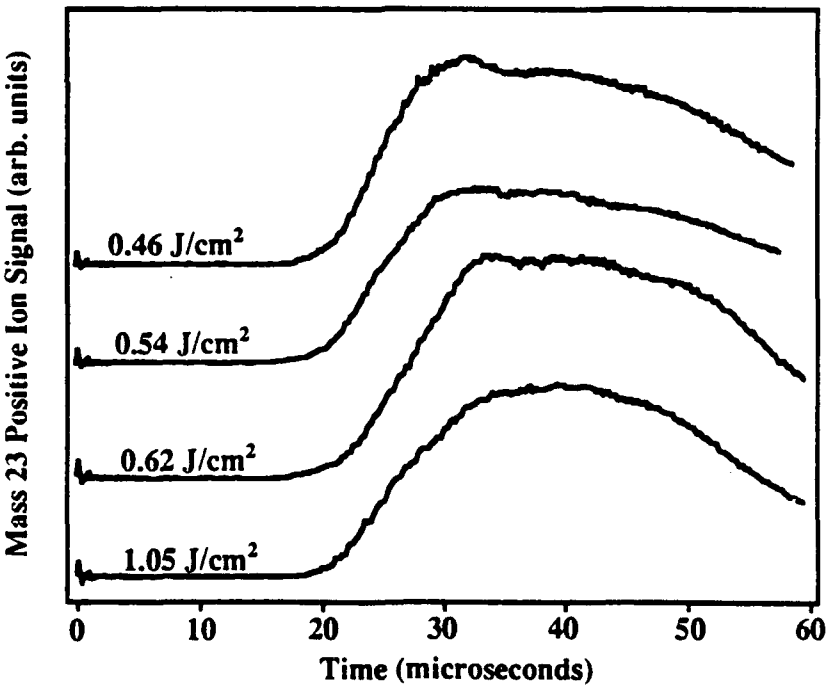

Fig. 3. Mass 23 (Na+) positive ion signals vs time for different fluences (0.46 - 1.05 J/cm^2). The laser pulse struck the surface at t = 0.

212

Further evidence for these two mechanisms involves the time-of-flights of the PIE at low fluence. Until one approaches the threshold fluence, the time interval between the laser pulse and the arrival of the ions at the detector were insensitive to laser fluence. Fig. 3 shows the mass 23 PIE signal vs time (through the QMS) for for different fluences between 0.4 J/cm^2 to 1.05 J/cm^2, where most of the ion flight path was in near zero **E** field.

Little difference in flight times are seen; such behavior is inconsistent with a thermal emission mechanism, which would yield energy distributions dependent on surface temperature and would therefore depend on laser fluence. The Na^+ emission mechanism at low fluences thus appears to be photoelectronic in nature rather than thermal, and is further support for the non-thermal first term in eq. 3.

Once the surface has been irradiated at high fluences to induce etching and plume formation, a plume could be maintained at lower fluences (e.g., ~0.7 $F_{threshold}$). At fluences barely above the threshold for plume formation, the decrease in PIE noted above was still observed, but was eventually followed by a dramatic increase in PIE accompanied by plume formation and the onset of rapid etching. Immediately below the threshold, the onset of plume formation often required thousands of shots with little PIE. At higher fluences (> 2.7 J/cm^2),[1] we observed a similar but much shorter pre-treatment for plume formation. In each case, this induction period is apparently required to produce the accumulation of damage in the form of near-surface defects. We have recently determined that in the range of fluences near threshold and higher, there is also copious negative ion emission which appears to be principally an oxygen containing ion (O^- or OH^-) and has many characteristics of the PIE in terms of fluence dependence.

Effect of Electron Irradiation on PIE. To investigate if electron beam induced states are capable of promoting strong interactions of 248 nm with the glass, we examined the effect of simultaneous and sequential electron and laser irradiation. In Fig. 4 we show the effect of simultaneous electron and laser irradiation on PIE at a laser fluence well below the etching

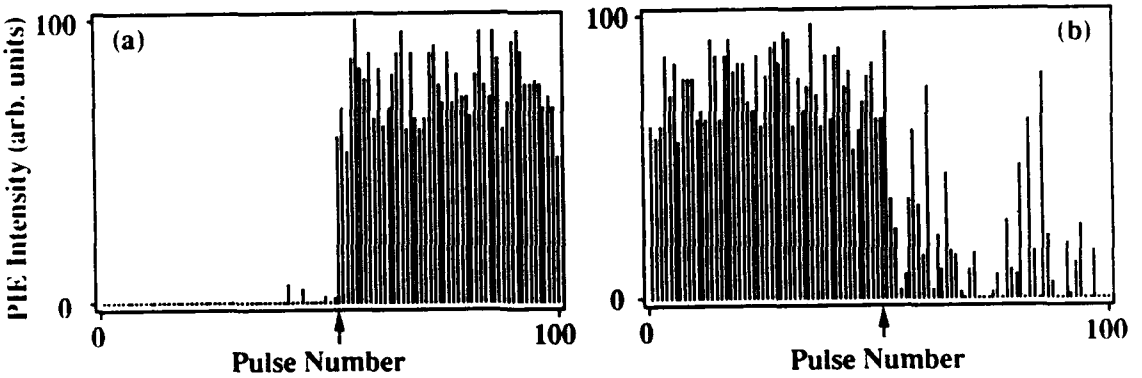

Fig. 4. Peak PIE due to successive laser pulses with and without simultaneous electron irradiation at 1.5 keV. In (a) the electron current density at the interaction region is initially zero and is raise to ~3 A/cm^2 at the arrow. In (b), the electron current density is initially ~3 A/cm^2 and is reduced to zero at the arrow.

threshold. In Fig. 4(a), the electron beam is initially off and is turned on midway through the sequence of pulses. The effect of the electron beam is an immediate increase in PIE emission. A visible plume, signaling the onset of rapid etching, accompanied the rise in PIE. In Fig. 4(b), the electron beam is initially on and is turned off midway through the sequence. The intense PIE during electron irradiation decays over several laser pulses. This decay indicates that the electron irradiation not only shortens the induction time for the onset of etching, but also lowers the etching threshold. Electron irradiation apparently results in the efficient production of states which enhance PIE and plume formation, presumably by increasing the absorption at 248 nm and increasing n_c. As discussed elsewhere,[3] electron irradiation combined with laser irradiation may prove useful for a variety of surface modification and deposition processes.

Reflection Electron Energy Loss Spectroscopy (REELS). REELS measurements were made to identify possible surface states which might participate in the emission processes. The consequences of electron bombardment of the surface could also be analyzed. Three REELS spectra are shown ih Fig. 5 for 0, 5, and 10 minutes of exposure time. The REELS data taken at 0 min. after in situ fracture show no states in the -2 to -6 eV energy range. (The energy zero is defined by the elastic peak.) Following five minutes of electron beam exposure, peaks appear in the range of -2 to -6 eV. These peaks were very well defined after ten minutes of electron beam exposure. These results suggest that absorption sites for 5 eV photons are produced by damaging the surface. The build-up (as beam exposure time increases) of electron energy loss peaks in the range from -2 to -6 eV suggests that defects are created by electron or ion beams. These shallow electronic levels which may be responsible for light absorption and electron emission at low laser fluences are associated with surface and/or defect states. REELS studies on amorphous SiO_2 films show loss peaks at 3.5, 5.1, and 7.2 eV which are attributed to a metastable surface phase of nearly monoxide stoichiometry.[14] These energy losses are close to surface levels seen on pure Si (where the electron affinity of silicon is 4.2 eV and the band gap is 1.1 eV), suggesting that the levels responsible are indeed within 5 eV of the vacuum level and capable of participating in photostimulated electron emission.

The creation of E' centers by excimer laser irradiation at 5 eV has been observed by Stahis and Kastner[15] in high purity amorphous silicon dioxide (Suprasil and Suprasil W) with electron paramagnetic resonance (EPR) techniques. Absorption of light in photoinduced E' centers would be consistent with the observed delay in the onset of laser etching seen on polished surfaces.

These filled states are possible sources for the free electrons created in the near surface region which couple with the laser light as discussed above. Collisions of the electrons within the first few tenths of microns of the glass surface would eventually elevate the temperature to the softening or melting point of the glass at high fluences, resulting in the hydrodynamic type sputtering observed.[1]

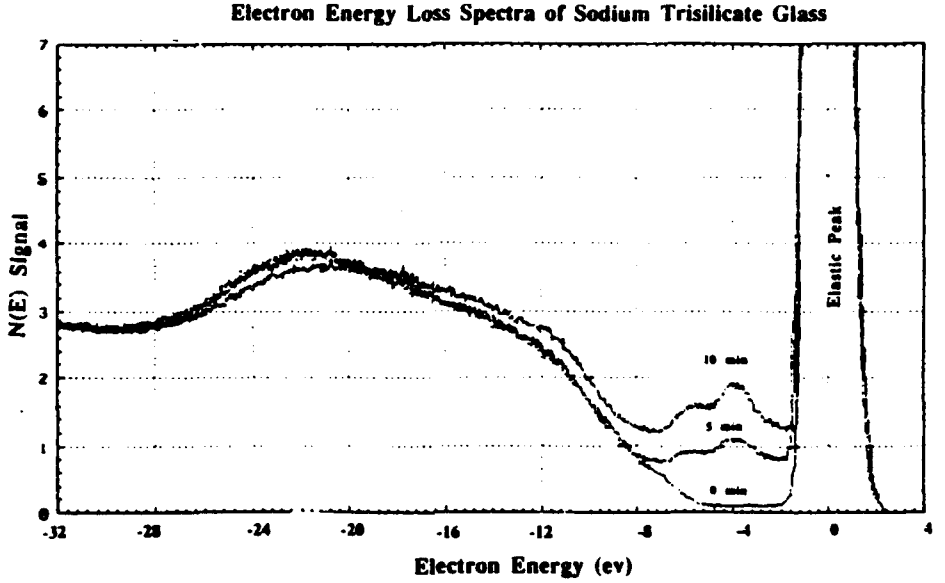

Fig. 5. Electron Energy Loss Spectra of sodium trisilicate glass.

Surface Roughness. At higher fluences, increased absorption of energy in the near surface region could also be due to an enhancement caused by surface roughness. While polished glass requires twenty or more pulses to induce etching at 2.7 J/cm^2, unpolished glass etches immediately upon irradiation with the laser. Wood[16] has noted that electric field concentrations at scratches increase as the index of refraction squared; thus, the corresponding energy density at a crack is enhanced by the fourth power of the refraction index. The real part of the refraction index for sodium trisilicate is very near three halfs which yields an energy density enhancement of five at a crack. In previous work,[1] we noted that after ten pulses at high fluence, polished sodium trisilicate glass displays fracture craters. These craters on the polished glass could enhance the energy

density causing more damage to the surface until the surface was rough. Thus, surface roughening may also play a significant role in the onset and extent of etching of silica based glasses.

CONCLUSION

We have presented measurements of the pre-threshold charged particle emission from 248 nm laser bombardment of sodium trisilicate glass and indicate that electron emission and simultaneous laser--free electron heating are the dominating mechanisms for subsequent release of large quantities of material including charged species, neutrals, and eventually ejecta. We showed that creating defects with another radiations source, namely an electron beam,[3] can greatly reduce the laser intensity required to begin etching the glass surfaces. Extension of these concepts to other inorganic targets is now in progress.

ACKNOWLEDGMENTS

The authors wish to thank Brad Pate, Washington State University, for helpful discussions. The WSU portion of this work was supported by the Office of Naval Research under Contract N00014-87-K-0514, the National Science Foundation under Grant DMR 8601281, and the Washington Technology Center. The PNL activities were supported by the U. S. Department of Energy (BES-DMS) and through internal Exploratory Research of the Molecular Science Research Center under Contract DE-AC06-76RL0-1830.

REFERENCES

1. P. A. Eschbach, J. T. Dickinson, S. C. Langford, and L. R. Pederson, J. Vac. Sci. Technol. A7(5), 2943 (1989).
2. P. A. Eschbach, J. T. Dickinson, and L. R. Pederson, MRS Symp. Proc. 129, 385-392 (1989).
3. J. T. Dickinson, S. C. Langford, L. C. Jensen, P. A. Eschbach, L. R. Pederson, and D. R. Baer, submitted to J. Appl. Phys.
4. G. Tetite, P. Agnostini, G. Boiziau, J. P. Vigouroux, C. Le Gressus, and J. P. Duraud, Optics Comm. 53, 189 (1985).
5. A. Miotello and F. Toigo, Nucl. Instru. Methods Phys. Res. B32, 258 (1988).
6. T. L. Gilton and J. P. Cowin, "Laser Induced Electron Emission: Space Charge and Electron Acceleration," conference presentation, ACS National Meeting 1988, L.A.
7. R. W. Dreyfus, "Are Laser-Ablated Monolayers Accurately Characterized by Their Ion Emission?," in Microbeam Analysis 1989, P. E. Russell, Ed., San Francisco Press, Inc., San Francisco , pp. 261-263 (1989)
8. F. Ohuchi and P. H. Holloway, J. Vac. Sci. Technol. 20, 863 (1982).
9. T. E. Tsai, D. L. Griscom, and E. J. Friebele, Phys. Rev. Lett. 61, 444 (1988).
10. R. A. B. Devine, Phys. Rev. Lett. 62, 340 (1989).
11. X. A. Shen, S. C. Jones, and P. Braunlich, Phys. Rev. Lett. 62, 2711 (1989).
12. A. S. Epifanov, Sov. Phys. JETP 40, 897 (1975).
13. S. C. Jones, P. Braunlich, R. T. Casper, X. A. Shen, and P. Kelly, Optical Engineering (1989).
14. J. E. Rowe, Appl. Phys. Lett. 25, 576 (1974).
15. J. H. Stahis, M.A. Kestner, Phys. Rev. B, 29(12), 7079 (1984).
16. R. M. Wood, in *Laser Damage in Optical Materials*, Adam Hilger, ed. pp. 5-7, (1986)

XV. Negative charge emission due to excimer laser bombardment of sodium trisilicate glass

S. C. Langford, L. C. Jensen, and J. T. Dickinson
Physics Department, Washington State University, Pullman, Washington 99164-2814

L. R. Pederson
Pacific Northwest Laboratories, Richland, Washington 99352

(Received 4 April 1990; accepted for publication 18 June 1990)

We describe measurements of negative charge emission accompanying irradiation of sodium trisilicate glass ($Na_2O \cdot 3SiO_2$) with 248-nm excimer laser light at fluences on the order of 2 J/cm^2 per pulse, i.e., at the threshold for ablative etching of the glass surface. The negative charge emission consists of a very prompt photoelectron burst coincident with the laser pulse, followed by a much slower plume of electrons and negative ions traveling with a high density cloud of positive ions, previously identified as primarily Na^+. Using combinations of **E** and **B** fields in conjunction with time-of-flight methods, the negative ions were successfully separated from the plume and tentatively identified as O^-, Si^-, NaO^-, and perhaps $NaSi^-$. These negative species are probably formed by gas phase collisions in the near-surface region which result in electron attachment.

I. INTRODUCTION

The character of the particle emission during laser ablation is an important probe of the interaction of intense radiation with solids. These interactions have proven important in the development of controlled ablation for material removal from surfaces and in the understanding of radiation induced damage to optical components. The chemical, internal energy, and charge states, as well as translational kinetic energies of the emitted products also have direct consequences in the understanding of deposition chemistry and thin film growth by laser ablation vapor deposition, e.g., of ceramic superconductor thin films.[1,2] The properties of the particles in the plume often depend strongly upon laser fluence, surface composition, and surface preparation.

We have previously identified and characterized the neutral and positive ion emission accompanying the irradiation of sodium trisilicate glass by 248 nm (KrF) excimer laser radiation.[3-6] Previous work on this material at fluences above the threshold for rapid etching, ~ 2.7 J/cm^2, has resulted in the identification of several ablation products from sodium trisilicate glass, including electrons, H^+, Na^+, and Si^+ ions, neutral O, Si, and NaO, and long lived, excited neutral Na (Na Rydbergs). At these fluences, an intense yellow plume due to Na D line emission is readily visible. The production of Na $3P_{1/2,3/2}$ and other excited states, including high-lying Na Rydberg states, most likely requires comoving electrons and Na^+ ions. The high energies of the positive ion and excited neutral components of the plume are attributed to strong laser-plume interactions. Electron heating via inverse bremsstrahlung is accompanied by electrostatic acceleration of the positive ions in the wake of the electrons. Early attempts in our laboratory to use static electric fields to convincingly identify the type of negative charge (e.g., electrons versus negative ions) contained in the plume failed miserably due to interference from the presence of excess positive charge. Here we report successful characterization of the negatively charged emission accompanying laser ablation of this material and make tentative identifications utilizing time-of-flight (TOF) techniques with combined **E** and **B** fields to separate and refine the observed emissions. We note that identification of negative molecular ions by optical spectroscopy is generally hindered by the lack of appropriate excited states; thus TOF techniques are useful in making these identifications.

II. EXPERIMENT

Glass sample preparation was standard and is described elsewhere.[3,4] The $Na_2O \cdot 3SiO_2$ samples were mounted in front of a quartz window in a vacuum system maintained at a pressure of $\sim 10^{-4}$ Pa. 20-ns pulses of 248-nm radiation provided by a Lambda-Physik Model EMG-203 excimer laser (KrF) were focused onto the sample to form a 1×0.2 mm^2 spot. Fluences from 0.1 to 6 J/cm^2 were obtained with neutral density filters. Charged particles were detected with a Channeltron electron multiplier (CEM), Galileo Electro-optics Model 4039, positioned either in line of sight of the sample or at the end of a 25.4-cm time-of-flight (TOF) drift tube to be described in more detail below. CEM output was amplified and signal averaged, typically over 50–200 laser pulses.

III. RESULTS

Typical positive and negative charge signals detected by a bare CEM positioned 10 cm from the sample surface during bombardment at a laser fluence of 1.8 J/cm^2 are shown in Fig. 1. The initial ringing signal in Fig. 1(a) is electromagnetic pickup induced by the laser discharge. The positive signal, which begins to rise ~ 7 μs after the laser pulse, is due to positive ion emission (PIE) and is delayed by the transit time from the sample to the detector. The negative signal shows an intense, fast peak arriving within 100 ns of the laser pulse. Subsequently, the emission drops in intensity, then

 0021-8979/90/204253-05$03.00 © 1990 American Institute of Physics

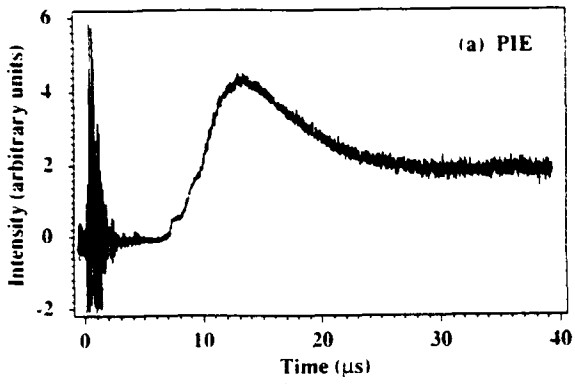

FIG. 1. Total (a) positive ion emission and (b) negative charge emission signals detected by an CEM positioned about 10 cm from the sample. The CEM front cone was biased -300 V for the detection of positive ions and $+100$ V for the detection of negative charge. The laser pulse occurred at time $t = 1$ μs, coinciding with the radio frequency noise signal in (a).

rises again to a second peak in a few microseconds. Note that there is always current to the detector during the time interval between the two maxima. The major focus of this letter is the characterization of these negative components of the emission which we collectively refer to as negative charge emission (NCE).

Charge measurements made with unbiased collectors (without gain) indicate the *net* charge of the emission versus arrival time. An initial fast negative signal is observed which corresponds to the initial fast electron peak of Fig. 1(b); these are photoelectrons emitted by single photon excitations at the glass surface.[4] The signal then becomes large and positive (and remains so thereafter) in a peak corresponding to the slower features of both Figs. 1(a) and 1(b). Thus, the "slow" NCE is moving within a cloud of positive ions, where the positive charge density is much greater than the negative charge density. Thus, the negative charge moves in a potential well created by the positive ion cloud and tends to be screened from external electric and magnetic fields. Therefore, a clean separation of the various charged components by dc fields is very difficult. Some separation is suggested in Fig. 1 by the fact that the slow NCE peak [Fig. 1(b)] is shifted to earlier times relative to the PIE peak [Fig. 1(a)].

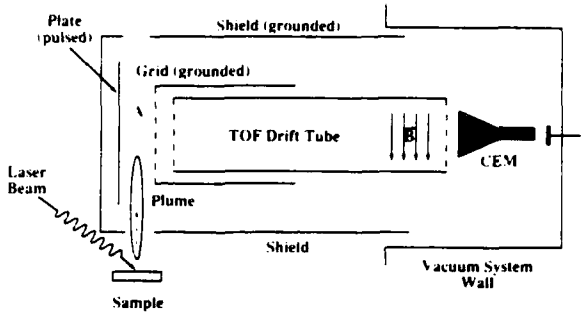

FIG. 2. Diagram of apparatus to direct a pulse of charge from the laser plume through the TOF tube.

More extreme procedures were required to identify the slow negatively charged species.

A diagram of the experimental geometry is shown in Fig. 2. Charge separation was achieved by means of electric fields in the region labeled A, between the plate and the grid. This field could be either static or pulsed as desired. With small, static fields, charged particle trajectories were such as to produce relatively broad TOF curves since the entire sequence of charge emission and plume motion are sampled. **B** fields were used to distinguish between electrons and more massive negative ions in the TOF tube. Field strengths of ~20-G yield electron orbits with diameters of less than 10 cm, even at electron energies of 1 keV; this curvature is small enough to effectively prevent electron detection. In contrast, a 16-amu negative ion orbits in such a field with a diameter of 6–20 m. Consequently, the effect of the **B** field on the negative ion trajectory is minimal.

Figure 3 shows two sets of TOF data taken with the plate grounded and $+900$ V on the TOF tube, with and without an applied **B** field. The voltage of the CEM front cone was maintained at $+400$ V to reject any electrons

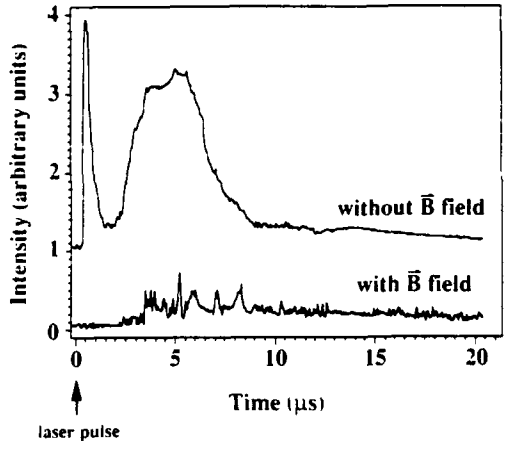

FIG. 3. Negative charge detected through a TOF tube with the plate grounded, with and without a **B** field in the detector end of the TOF tube. The laser pulse occurred at time $t = 0$.

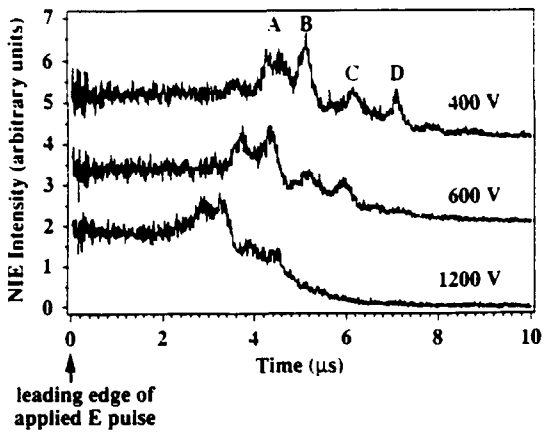

FIG. 4. Negative ion signal intensity vs time of flight at TOF tube voltages of +1200, +600, and +400 V. The E field pulse was applied at time $t = 0$. The laser pulse occurred at $t = -22\ \mu s$ on this time scale, i.e., 22 μs before the E field was applied. For subsequent reference, the four prominent peaks are labeled A, B, C, and D.

created in the interior of the tube by collisions with the tube wall. In the absence of the **B** field an intense, prompt emission is observed after the laser pulse, followed by a broad peak with a long tail. The **B** field cuts off the prompt electron peak and most of the broad peak that follows; nevertheless, the remaining signal is real and reproducible. This result confirms that the fast peak consists of electrons, as does the major portion of the slow NCE. Static field data taken with the **B** field and at various drift tube potentials produces TOF shifts which are consistent with ionic masses.

This result is confirmed by TOF measurements after pulsing the plate to $\pm$ 100 V. The resulting transient **E** field sweeps particles of the appropriate charge from the extraction region, labeled A in Fig. 2, into the TOF tube. This pulse was applied after a variable delay following the laser pulse to coincide with the arrival of the plume in region A. Negative voltage pulses, intended to push negative particles into the drift tube, still allow a small number of positive ions to enter the tube. Nevertheless, sufficient separation is achieved to inject a pulse of negative charge into the drift tube with a fairly well-defined origin in space and time. Typical negative ion TOF signals (20-μs pulse to $-$ 100 V; **B** field present) at three tube voltages are shown in Fig. 4, where $t = 0$ coincides with the leading edge of the applied pulse. A background signal is observed prior to the pulse due to ions and/or electrons which drift through the grid into the entrance of the TOF tube. The pulse duration and amplitude were sufficient to prevent ions which had not yet reached the extraction region directly in front of the TOF tube from entering the tube, greatly reducing the background following the TOF peaks. Significantly, the measured shift of these peaks with V_{tube}, where V_{tube} is the potential applied to the drift tube, are consistent with both the mass and charge of negative ions.

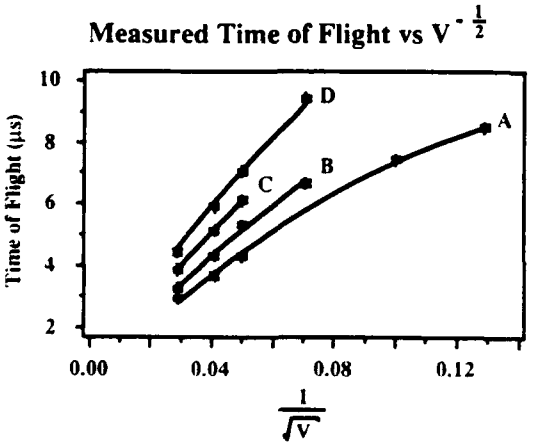

FIG. 5. Plots of TOF peak positions vs $V_{tube}^{-1/2}$, where V_{tube} is the potential applied to the TOF tube, for the mass peaks labeled A, B, C, and D in Fig. 4.

A plot of the peak positions versus $V_{tube}^{-1/2}$ appears in Fig. 5. Under ideal conditions (i.e., the ions enter the tube at $t = 0$ with a kinetic energy equal to $q \cdot V_{tube}$), these plots would be straight lines, which obviously is not the case. To determine the masses corresponding to these peaks, we were required to model the extraction process along with other portions of the ion trajectories to the detector. For simplicity, we assumed that the peaks correspond to ions positioned initially midway between the pulsed plate and grounded entrance grid (region A in Fig. 2) at the time of the pulse, thereby accounting for the energy imparted to the ions by the plate potential in region A. This initial kinetic energy is the cause of the curvature in the otherwise linear TOF vs $V^{-1/2}$ plots. This allowed a one-parameter fit (ion mass) to each of the curves in Fig. 5. The masses determined on the basis of this model for the peaks A, B, C, and D, respectively, are 20, 28, 40, and 54 amu.

These mass assignments must be regarded as approximate due to uncertainties in the analysis. For example, we found that some positive ions entered the TOF tube with the negative ions. This tends to increase the observed TOF due to shielding effects, particularly at lower flight tube voltages and lower masses. Although the analysis of the first peak yielded mass 20, a linear least-square analysis of only the high voltage portion of the data indicates a significantly lighter mass, ~16 amu. We therefore assign this peak to O^-, which is a known stable negative ion and an expected species from a silica system. Peaks B and C are consistent with masses 28 and 39 (Si^- and NaO^-, respectively). Si^- and NaO^- are also stable negative ions, frequently observed in negative secondary ion mass spectroscopy (SIMS). The identity of the fourth peak, D, at about mass 54, is open to question; but we note that a species with the composition $NaSi^-$ would have a similar mass. As seen in Fig. 4, the heights of the last two peaks are generally small and their positions correspondingly uncertain. In summary, our current assignments for these negative ion species are O^-, Si^-, NaO^-, and perhaps $NaSi^-$. As a check of our technique, a similar analysis of the positive ion TOF data yielded masses 23 (Na^+) and 43 (attributed to mass 44, SiO^+); both of these masses were previously detected and identified using quadrupole mass spectroscopy.[7] The presence of propor-

tionally small numbers of negative ions apparently had little influence on the PIE mass determinations.

IV. DISCUSSION

We have discussed elsewhere proposed mechanisms regarding the coupling of laser radiation with surfaces of wide band-gap materials to produce the observed photoelectrons, positive ions, and neutral species; this interaction is based on a photoinduced defect model.[4,5] In addition, we have discussed the role of laser/plume interactions which can increase the kinetic energy of photoelectrons by as much as 10^2 eV via an inverse bremsstrahlung mechanism.[3] These energetic electrons in turn electrostatically accelerate the positive ions to the 10–60 eV energies observed previously. In the near-surface region, the interaction of electrons and neutral species could also result in the formation of negative ions through collisions resulting in electron attachment given sufficiently high collision probabilities between departing neutral species and low energy free electrons. Gas phase electron attachment cross sections typically peak in the 0–1 eV region. Direct emission of negative ions of highly electronegative molecules from surfaces has been observed via surface ionization processes, e.g., UF_n on Pt or C surfaces;[7] these processes require the electron affinity of the atom or molecule to be greater than the work function of the surface. Negative ion emission can also accompany highly exothermic reactions, e.g., SF_n adsorption on alkali metal surfaces.[8] Although we cannot rule out direct emission from the glass surface, collisional attachment of electrons to neutral particles seems a more likely mechanism. We note that three of the emitted neutral species previously reported[1] (O, Si, and NaO) coincide with the negative ion mass assignments above.

The negative ions, with energies of a few eV, are among the slower charged particles in the plume and exhibit a very long, low energy tail, consistent with the slow decay in Fig. 1(b). These energies are still higher than the 0.1–0.6 eV energies seen for the neutral species, suggesting that the negative ions are accelerated subsequent to their formation. We propose that the necessary acceleration of the negative ions results from a second wake effect, namely the acceleration of negative particles by electrostatic attraction to the positive charge cloud; i.e., the fast electrons (heated by laser/plume interactions) pull the positive ions which pull the negative ions.

We expect that the presence or absence of particular negative ion species in the plume may occasionally be used to infer the presence or absence of a given neutral species. For instance, the copious Na^- emission even at subthreshold fluences requires significant oxygen emission in some form to maintain a reasonable surface stoichiometry, and it appears that this emission is atomic rather than molecular (O_2^-). O^- is readily observed in negative SIMS of oxide covered Si surfaces,[9] and would be expected among the ablation products if significant quantities of O_2 were emitted. The absence of both neutral O_2 and O^- is consistent. As previously discussed,[4,5] defect formation associated with the depletion of the surface and near-surface region of oxygen may significantly increase absorption at 248 nm in the early stages of irradiation, resulting in the gradual onset of rapid etching at fluences near the threshold. An oxygen deficiency at the surface would make the emission of molecular oxygen especially unlikely.

V. CONCLUSIONS

Despite the uncertainty in the above mass assignments, the data provide strong evidence for the presence of both electrons and several negative ion species in the laser plume. Furthermore the negative ions observed are consistent with electron attachment to neutral species in the near-surface region where collisions are likely to be frequent. By varying the timing of the voltage pulse provided to the plate, we found that the distinctness and intensity of the negative ion peaks grew with the pulse delay until at least 25 μs after the laser pulse. This may be due to an actual increase in the negative ion intensities at later times (attachment to lower energy neutrals is more probable); but decreased interference from positive ion peaks may also be involved. Positive ion peaks were more intense at shorter delay times (down to at least 10 μs). Pulsing the plate as the most intense portion of the plume passed the entrance of the drift tube, particularly at high laser fluences, often yielded unresolved peaks due to the inability of the electric field employed to cleanly separate the positive and negative charges. A combination of reduced laser fluence and increased pulse voltage might overcome this problem.

Although the negative ion emissions accompanying laser ablation can be weak, they reflect important processes involving ablation products in the surface and near-surface regions. Specifically, they reflect the emission of initially neutral species which depend on the defect states of the irradiated surface. As the condition of the surface is often dynamic, control of the laser/substrate interaction demands knowledge of these changes. An understanding of how surfaces change under irradiation, and how these changes in turn affect absorbance of incident laser light and plume formation, should facilitate the choice of optimal ablation targets and laser beam parameters for controlled material removal. In addition, knowledge of the complex electrostatic processes occurring within the plume following the laser pulse should facilitate the control of the densities and energies of charged particles in the plume. This control may significantly enhance the quality of thin films deposited by laser ablation.

ACKNOWLEDGMENTS

We wish to thank Peter Eschbach of Pacific Northwest Laboratories for helpful discussions. This work was supported by the Office of Naval Research under Contract No. N00014-87-K-0514, the National Science Foundation under Grant No. DMR 8912179, and the Washington Technology Center. The PNL activities were supported by the U.S. Department of Energy (BES-DMS).

D. Dijkkamp, T. Venkatesan, X. D. Wu, W. A. Shaheen, N. Jisrawi, Y. M. Min-Lu, W. L. McLean, and M. Croft, Appl. Phys. Lett. **51**, 619 (1987); S. Witanachchi, H. S. Kwok, X. W. Wang, and D. T. Shaw, Appl. Phys. Lett. **53**, 234 (1988).

P. A. Eschbach, J. T. Dickinson, S. C. Langford, and L. R. Pederson, J. Vac. Sci. Technol. A **7**, 2943 (1989).
P. A. Eschbach, J. T. Dickinson, S. C. Langford, L. C. Jensen, and L. R. Pederson, MRS Symp. Proc. **158**, 463 (1990).
J. T. Dickinson, S. C. Langford, L. C. Jensen, P. A. Eschbach, L. R. Pederson, and D. R. Baer, J. Appl. Phys. **68**, 1831 (1990).
P. A. Eschbach, J. T. Dickinson, and L. R. Pederson, MRS Symp. Proc. **129**, 385 (1989).
P. F. Dittner and S. Datz, J. Chem. Phys. **68**, 2451 (1978).
Yicheng Wang, M. A. Huels, D. R. Gallagher, L. D. Doverspike, and R. L. Champion, Phys. Rev. Lett. **61**, 1194 (1988).
K. Nakamura, H. Hirose, A. Shibata, and H. Tamura, Jpn. J. Appl. Phys. **16**, 1307 (1977).

XVI. Mass spectroscopy study of products from exposure of cyclotrimethylene-trinitramine single crystals to KrF excimer laser radiation

J. T. Dickinson, L. C. Jensen, D. L. Doering,[a] and R. Yee[b]
Department of Physics, Washington State University, Pullman, Washington 99164-2814

(Received 25 September 1989; accepted for publication 3 January 1990)

We report mass spectroscopic measurements of the charged particle, neutral, and excited neutral species emitted from the irradiation of single-crystal cyclotrimethylene-trinitramine (RDX) with 248-nm, 20-ns laser pulses. At laser fluences above 5 mJ/cm^2 we observe RDX decomposition products of relatively small mass in both neutral and ionic states. With increasing fluence we see clear etching of the crystal, an increase in kinetic energy of the products, and the appearance of an intense, excited neutral species which we identify as NO in an energetic, long-lived electronic excited state. Evidence is also presented for a sustained decomposition reaction ignited by the laser pulse.

I. INTRODUCTION

When absorbing materials are subjected to relatively intense, short-wavelength laser radiation, processes categorized as *photochemical* and *photothermal* can occur which result in the ejection of atomic and molecular fragments from the surface. When such removal of material is significant, resulting in measurable localized "etching" of the surface, it is referred to as photoablation.[1] Explosive molecular crystals tend to absorb radiation in the ultraviolet[2] with potential for initiating photodecomposition reactions in the near-surface region. Laser bombardment of explosive crytals has been previously reported. Yang and Menichelli[3] used a *Q*-switched ruby laser to detonate pentaerythritol tetranitrate (*PETN*), *cyclotrimethylene-trinitramine* (RDX), and tetryl utilizing the shock wave produced by strong light absorption in a metal film. Tang *et al.*[4] have examined decomposition of explosives by analysis of the $\pm$ ion products from 266-nm, 5-ns laser pulses on RDX, PETN, AgN_3, and $Pb(N_3)_2$ using laser ionization mass analysis (LIMA). These workers reported rapid (but not self-sustained) decomposition of RDX and PETN and for low fluences, the decomposition of the azides. At higher fluences, the azides detonated under laser bombardment. For RDX, Tang *et al.*[4] saw both positive- and negative-ion masses ranging from 16–176 amu. A number of ionic species observed in this study coincide in mass with several of the decomposition products observed by Zhao, Hintsa, and Lee[5] in gas-phase infrared multiphoton dissociation of RDX. Also, there has been evidence presented[6] of uv sensitization of liquid nitromethane due to creation of a nitromethane aci ion ($CH_2NO_2^-$).

In this work, we report on the consequences of bombarding single crystals of RDX with pulses of excimer laser light at 248 nm. We show that at laser fluences above 5 mJ/cm^2 we observe RDX decomposition products of relatively small mass in both neutral and $\pm$ ionic states, as well as photoelectrons. With increasing fluence we see clear etching of the crystal, an increase in kinetic energy of the products, and the appearance of an intense, long-lived excited neutral species. We identify this excited neutral as NO in a metastable electronic state. We present evidence of both thermal and nonthermal processes involved in creating the observed products along with their observed energy distributions. We also present evidence of a sustained decomposition reaction which continues for many microseconds following the laser pulse.

II. EXPERIMENT

Single crystals of high optical quality RDX were grown from an acetone solution in dimensions of approximately 1 cm in length and a few mm in thickness. Prior to mounting, the crystals were cleaved in air which generally exposes [001] surfaces.[7,8] RDX has an orthorhombic structure (space group *Pbca*) with $a = 1.308$ nm, $b = 1.157$ nm, $c = 1.071$ nm, and $z = 8$.[9] The samples were mounted on a translatable stage in a vacuum chamber maintained at a pressure of 10^{-5} Pa or less. The laser beam was directed through a quartz window at an angle of about 20° to the sample surface normal.

The radiation source was a Lambda Physik Model EMG 203 excimer laser, which produced 20-ns pulses of 248-nm radiation (KrF). The laser energy/pulse was measured with a Gentec ED 500 joule meter. The laser beam was focused by a lens of 1-m focal length to produce a 0.5×1 mm^2 rectangular spot on the sample surface with a maximum fluence of 5 J/cm^2. Neutral density filters were used to reduce the fluence by calibrated amounts. Optical microscopy of the ablated surfaces demonstrated that the beam was generaly uniform in the central portion, but showed some irregularities on the edges due to slight misalignment of the optical components.

Time-of-flight (TOF) measurements of ions and excited neutral particles were made with a Chenneltron electron multiplier (CEM), Galileo Electro-Optics Model 4821. Excited neutrals can be detected when their internal energy is sufficient to cause Auger de-excitation (e.g., metastable atoms and molecules) or autoionization (e.g., high-lying Rydberg states) upon collision with the CEM. Ions and excited neutrals were distinguished by comparing intensity measurements made with positive and negative biases on the

[a] Permanent address: Department of Physics, Wesleyan University, Middletown, CT 06457-6036
[b] Permanent address: Chemistry Division, Naval Weapons Center, China Lake, CA 93555-6001

 0021-8979/90/083641-11$03.00 © 1990 American Institute of Physics

CEM front cone. The CEM front cone was typically masked so that only a small portion was in line-of-sight with the sample to prevent detector saturation.

A Bessel box energy analyzer, described by Craig and Hock,[10] could be placed between the sample and the CEM to provide low-resolution energy analysis of the charged particles.

Mass determination of the ground-state neutral particles was obtained with a Finnegan Model 4001 quadrupole mass spectrometer (QMS) with a CEM detector. With the ionizer "on" and the axis of the QMS aligned to provide a line-of-sight path from the target through the QMS to the CEM, both excited neutrals and ionized ground state neutral particles were detected. Positive-ion-mass determination was obtained with a UTI Model 100C QMS with the ionizer removed. The potential on the focus plate in front of the mass filter was varied to maximize collection and focusing of the externally generated ions. Line-of-sight was avoided to prevent detection of excited neutrals. Calibration of the quadrupoles was checked by leaking in Kr providing singly ionized peaks at 80, 82, 83, 84, and 86 amu as well as well resolved doubly ionized peaks at 42 and 43 amu.

Measurements of light emission from excited species in the near-surface region were made initially with a Gencom Thorn EMI Model 9924QB photomultiplier tube (PMT) with a quartz window, positioned at the end of a silica fiber optics cable mounted on a vacuum system flange. The target end of the fiber optics cable was equipped with a slit aperture and collimating lenses to ensure that only light directed along the axis of the cable (perpendicular to the target surface normal) was detected. This allowed localizing the region of space probed by the detector, e.g., for the observation of temporal variations in light intensity as light emitting atoms/molecules passed in front of the slit. For spectral analysis of this spatially selected light, the output of the fiber optic cable was attached to a Thermo Jarrell Ash Monospec-18 spectrometer employing a 150-lines/mm grating. An EG&G Model 1421 gated, intensified, position-sensitive detector responsive to light in the region between 200–830 nm was used with an EG&G Model 1460 optical multichannel analyzer to acquire both time-averaged and time-resolved spectra.

III. RESULTS

A. Surface topography

When crystals of RDX are exposed to 248-nm excimer laser light at fluences >90 mJ/cm^2, we observe etching of the crystal in the shape of the laser beam. No "pre-exposure" of repeated laser pulses was required before etching commenced. No evidence of any residue or surface melting was observed. Etch rates were not measured but showed a very strong fluence dependence, increasing rapidly with increasing fluence. On crystals that displayed different facets there was no apparent dependence of the etch rate on surface crystal orientation. At fluences ≥ 150 mJ/cm^2 the crystal usually exhibited extensive internal fracture and frequently shattered into small pieces.

Thinner crystals ($\lesssim 1$ mm) showed ablation from the back side in addition to the front side. Whereas the etch pit on the front side was rectangular (shape of the laser profile), the back pit was circular in cross section. One sample formed a clean 50-μm hole at the center and bottom of the front surface rectangular pit [see Fig. 1(a)] which opened into a rough, conical etch pit on the back side [Fig. 1(b)]. The roughness on the back side was due to multiple fracture, whereas the hole was cleanly etched with no appearance of melting or fracture. A slightly thicker sample also showed ablation from both front and back with no hole formed in the front etch pit, suggesting that the hole is eaten from the *backside* towards the front. The hole shows circular symmetry about the center of the rectangular laser beam. This indicates that decomposition is nucleating at the most intense part of the laser spot in a rather nonlinear fashion. Close examination of the walls of the hole showed some crystallographic-like facets.

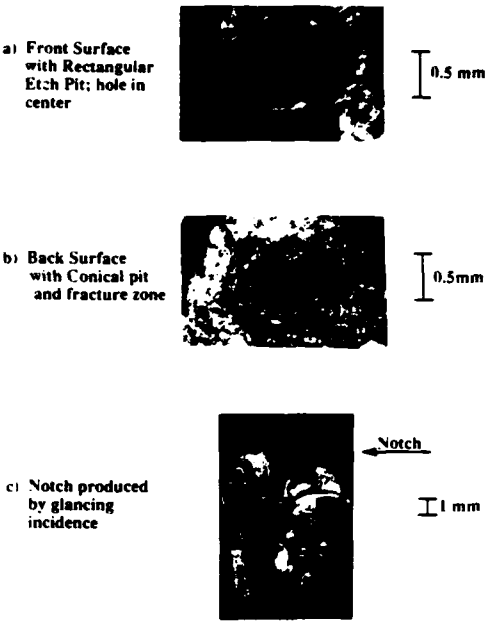

FIG. 1. Optical microscope images of the front and back surfaces of an RDX crystal after bombardment with a 248-nm excimer laser light. The front surface (a) shows the etch pit with a circular hole passing through the entire crystal. The back surface (b) shows the hole opening into a conical structure lined with extensively fractured material. (c) The consequences of glancing incidence on the side of the crystal: A clean notch is etched.

At fluences of 1 J/cm^2 we calculate a radiation pressure pulse of $< 10^4$ N/m^2 which is too small to cause the extensive fracture we observe. More likely, pressure arises from conversion of solid RDX to gaseous products, similar to the effects described by McBride,[11] and the change in volume results in fracture. When the back of the crystal is ablating, at higher fluences one could observe small fragments being ejected from the crystal.

Figure 1(c) shows the effect of a glancing incident laser on the edge of the crystal, namely producing a clean notch. Other parts of this crystal were also hit by the laser at earlier times.

TABLE I. QMS detected mass peaks due to neutral emission from laser bombardment of RDX.

Approximate threshold (mJ/cm^2)	Mass (amu)	Assigned parent(s)	Relative intensity at 125 mJ/cm^2
5	46	NO_2	6
5	30	NO, H_2CO	100
5	28	N_2, H_2CO, CO	86
5	27	HCN	97
5	26	CN, HCN	57
5–10			
5–10	44	N_2O	21
5–10	42	C_2H_4N and/or CH_2NN	8
5–10	29	H_2CO	22
5–10	18	H_2O	93
5–10	17	OH, H_2O	85
5–10	16	O, NO, H_2O	39
5–10	15	NH, NO^{2+}, C_2H_4N, and/or CH_2NN	27
5–10	14	N, CN, HCN, NO, N_2O	63
5–10	13	CH, H_2CO, C_2H_4N, and/or CH_2NN	20
5–10	12	C, CN, HCN, CO	52
20	2	H_2; higher mass parents	39
The following extremely small peaks were detected at 125 mJ/cm^2 only under conditions of reduced laser spot size; the intensities are given relative to mass 30 acquired at the same reduced spot size.			
	120	$CH_2NNO_2NO_2$	0.5
	81–83	$C_2N_2H_x + H_x$ ($x = 0,1,2$)	~1
	75	$CH_2NNO_2 + H$	5
	52,54,56	$CH_2CH_2N_2 - H_x$ ($x = 0,1,2$)	2.5

B. Ground-state neutrals

Copious neutral gas emission from the crystal was observed. At high laser fluences, a nearby Bayart-Alpert pressure gauge would show an order of magnitude increase in vacuum system pressure (10^{-5} to 10^{-4} Pa) with each laser pulse. With the Granville-Phillips QMS (ionizer on) we measured the mass of the emitted neutral species. At low fluences (~5 mJ/cm^2) the ion mass peaks generated from ionization of neutral species consisted of only five masses (46, 30, 28, 27, and 26). By analysis of expected cracking fractions and time distributions, these appear to be small mass dissociative products with no additional fragmentation and can be assigned to the parent species shown in Table I. As the fluence is increased to ~5–15 mJ/cm^2, additional peaks appear, again assigned by taking into account cracking fractions and time distributions, shown in Table I. At fluences ≥20 mJ/cm^2, mass 2 appears and grows with increasing fluence and is assigned to both H_2 and higher mass parents containing hydrogen.

In Fig. 2, we plot the detected signals (versus time) for the QMS set at the masses shown and a fluence of 125 mJ/cm^2. Intensity units for these plots are arbitrary, but relative intensities at this fluence are given in Table I in the right-hand column and shown plotted in Fig. 3. Due to interference with the ion blast, our quadrupole mass spectrometer could not resolve mass 1 so that we were not able to determine conclusively if atomic hydrogen was a product. The higher mass peaks (~52 amu) were found only after extensive searching and reduction (by masking) of the spot size of the laser beam hitting the sample. As we shall discuss below, both the fluence and the spot size greatly affected the physical and chemical processes triggered by the laser. Unless stated otherwise, the laser beam was unmasked and therefore full size (0.5×1 mm^2).

If one takes the product distribution for the unmasked bombardment and assumes standard cracking fractions for the "parent" products (at 70-eV electron bombardment energy), one calculates C:N:O:H ratios of approximately 1:2:2:2, which is in agreement with the stoichiometry of the RDX molecule. The intense peaks are fragments ≤mass 46 which suggests that the decomposition paths are nearly complete. All of the molecular species ≤mass 46 observed here are seen in both ir multiphoton dissociation[5] and thermal decomposition[12–14] of RDX. The atomic emission and the extremely small contributions above mass 46 differ dramatically from these other forms of decomposition. We searched carefully under a variety of laser beam conditions for mass 74 (the concerted decomposition product seen in Ref. 5) but never observed it—a small mass 75 was observed, as mentioned above and attributed to $CH_2N_2O_2 + H$. However, we note that the ratio of H_2CO/N_2O is seen to be near unity, consistent with one of the decomposition paths of the concerted decomposition intermediate $CH_2N_2O_2$ namely,

$$CH_2N_2O_2 \rightarrow H_2CO + N_2O. \quad (1)$$

We also note that the ratio of HCN/H_2CO is roughly 5, which is consistent with HCN being created by the second decomposition path,

$$CH_2N_2O_2 \rightarrow HCN + HONO \quad (2)$$

at very close to the same branching ratio reported by Zhao and co-workers.[5]

Although the reaction pathways are not completely defined by our data, our results suggest decomposition consistent with the computer fits to the major TOF peaks shown in Fig. 2. The individual curves show the fraction of each parent mass which is assumed to be created at or near the time of the laser pulse and which travels to the ionizer as the parent. The TOF model curves were generated from Maxwellian velocity distributions corresponding to two temperatures, namely 1100 and 3000 K. Obviously, if the laser fluence is changed, the observed shifts in the TOF curves would require changes in this temperature, namely increasing fluence would result in higher equivalent temperatures. The use of two temperatures is only for convenience; temperature versus time distributions would be more appropriate. Nevertheless, the fits in general are fairly good, requiring a relatively small number of parent molecules in comparison with multiphoton ir dissociation.[5] Note that some of the products required only one temperature, namely ~1100 K for CN(26), H_2CO(29), and masses 40–46 amu. The TOF curves seen for the very small peaks at masses 52, 54, 56 showed broad structures perhaps due to dissociation of heavier components.

Although HONO is a likely product in our study, it was not directly detected as mass 47, nor were significant amounts of mass 47 required to fit our mass 30, 17, and 16 TOF peaks (the cracking pattern of HONO produced by electron bombardment[5] contains little, if any, mass 47). Oyumi and Brill[14] have pointed out that in studies of RDX thermal decomposition, heterogeneous (in our case surface-gas-phase components) and gas phase reactions can lead to C-N bond cleavages, producing N_2O, H_2CO, whereas N-NO_2 bond cleavage is most likely in the condensed phase yielding HCN without producing equivalent amounts of HONO. They also showed that at heating rates of ~50 K/s and pressures of 1 and 70 atm there was a significant shift in products with increasing pressure due to reactions involving gas phase collisions versus direct thermolysis reactions. Thus, our lack of direct detection of HONO may be due to similar collisional effects.

C. Excited neutrals

At fluences >100 mJ/cm^2, a fast signal appears that has the following properties:

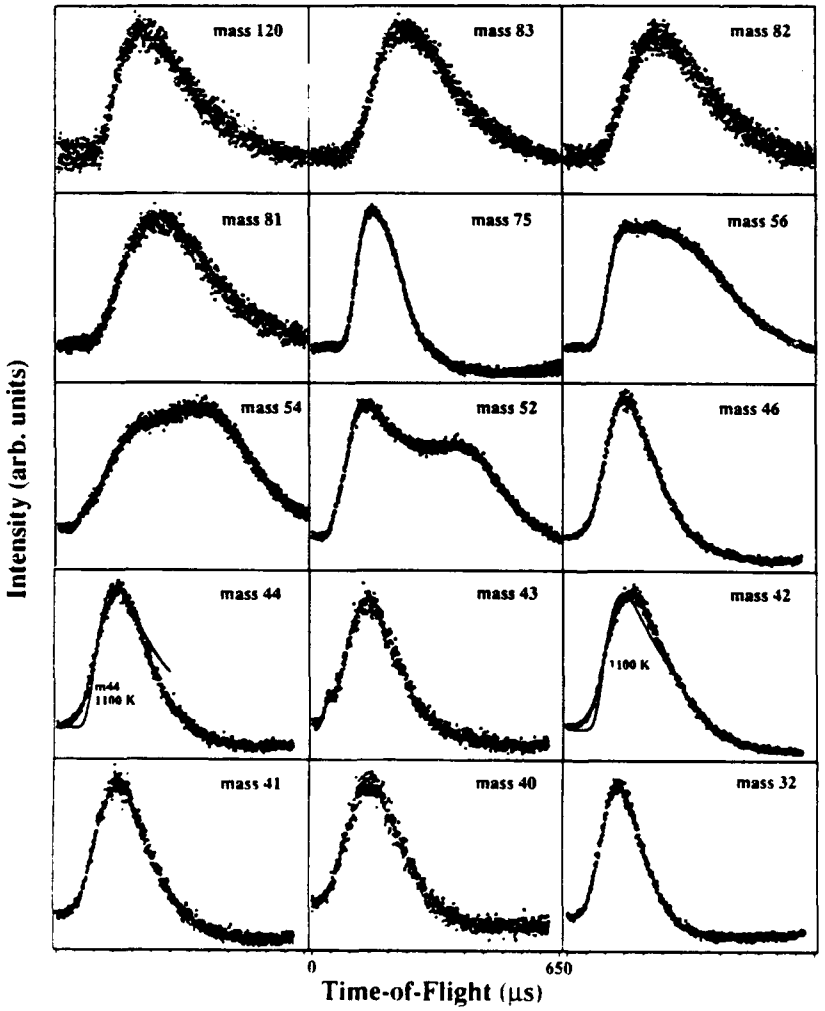

FIG. 2. The detected time-of-flight curves for the observed neutral species emitted from the front surface of the RDX crystal acquired with a quadrupole mass spectrometer. The laser fluence was 125 mJ/cm^2. The curve fits shown for the major peaks are superpositions of Maxwellians for the parent masses and effective temperatures shown.

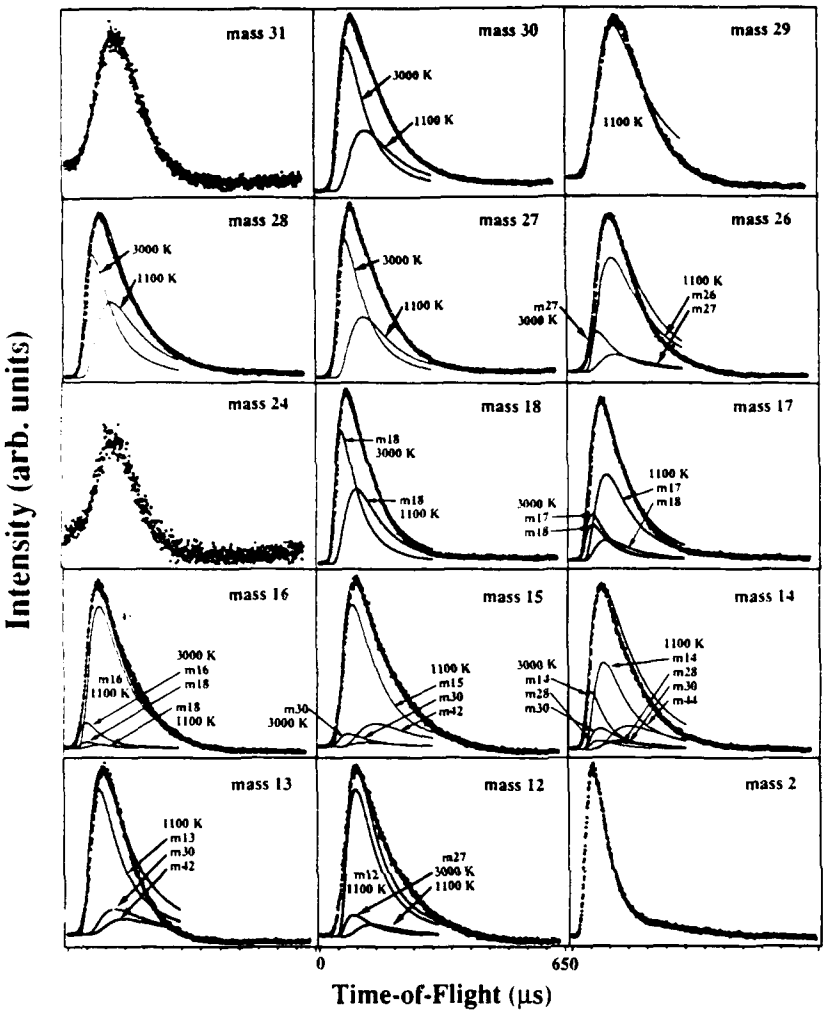

FIG. 2. (*continued*)

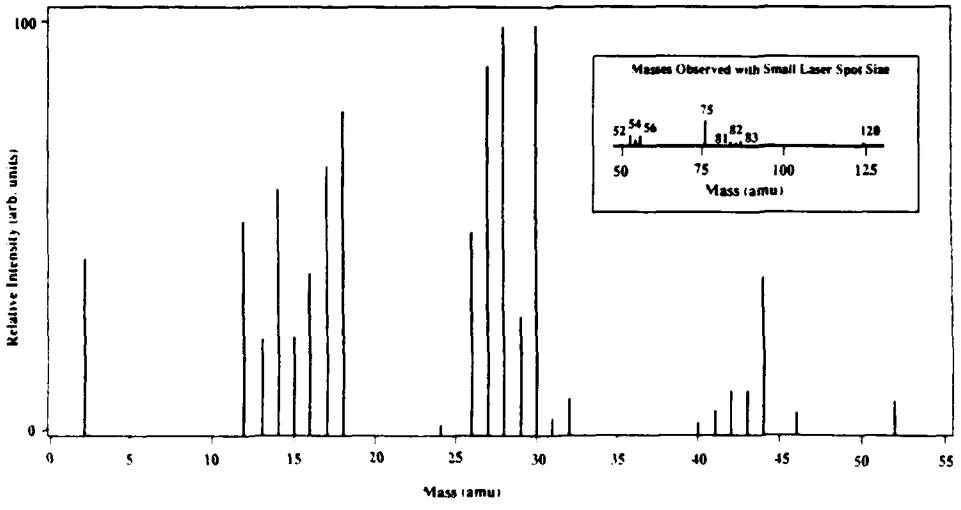

FIG. 3. The relative intensities of the quadrupole mass spectrometer signals for data shown in Fig. 2. The inset shows the intensities for the peaks observed with reduced laser spot size.

(1) The signal is very sensitive to alignment of the irradiated point on the sample and the QMS—strict line-of-sight is required from the surface to the CEM. If a silica window was placed in front of the entrance to the ionizer, no signal was observed (therefore, energetic photons due to collisions with surfaces could be ruled out).

(2) The signal is detected by the CEM with unshifted peak position independent of the following conditions: (i) ionizer on/ionizer off; (ii) mass filter on/mass filter off; (iii) mass setting, with mass filter on; and (iv) the presence of $\pm$ voltages on all ionizer electrodes (positioned at the entrance to the mass filter). We have reported on similar long lifetime, excited neutral signals originating from laser bombardment of polymers[15] and a sodium trisilicate glass.[16] We provided evidence that such signals were due to neutral atoms/molecules in an excited electronic state (e.g., a metastable or long-lived Rydberg level). We have argued that the production of such fast species occurs via reneutralization of *ionic* species leaving the material. Simple, nondissociative ion-electron recombination in the gas phase requires a third body to conserve energy and momentum; thus, collisions with other gaseous species is a strong requirement. As mentioned earlier, in all of these materials, including RDX, there are high densities of gas created with each laser pulse which can provide a third body.

A series of excited neutral time distributions is shown in Fig. 4 for a number of laser fluences. Note that the TOF peak position decreases only slightly with increasing fluence, whereas the intensity increases dramatically with fluence, changing by a factor of more than 350 for an increase of a factor of 10 in fluence (from 70 to 700 mJ/cm^2). The detection of such a particle is likely by collisional de-excitation at the front surface of the CEM ($\sim$5 eV). Obviously, the lifetime of these particles must be $\sim$50 μs or longer. Well known long-lived metastable and Rydberg states occur in H_2, N_2, NO, and CO, and CO_2.[17,18] We present evidence

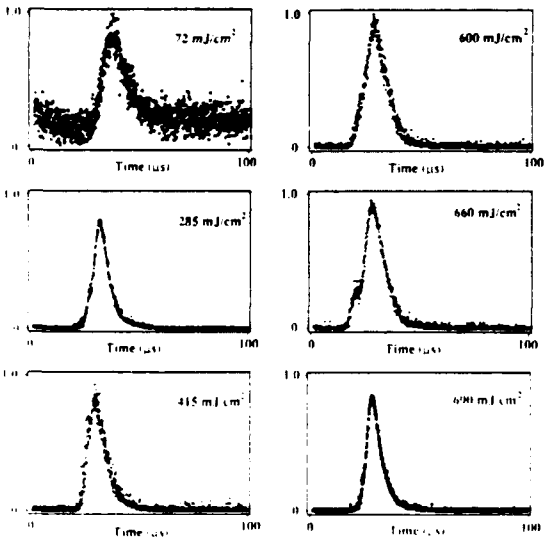

FIG. 4. The excited neutral time-of-flight distributions acquired at different laser fluences.

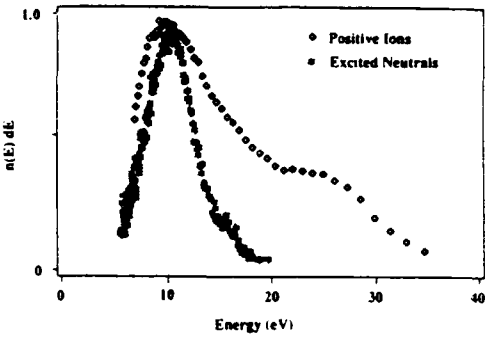

FIG. 5. Energy distribution curves for the excited neutral (with an assigned mass of 30 amu) and the mass 30 ion signal, assigned to NO^+. The strong similarity in these energy distributions supports the mass 30 assignment for the excited neutral.

below that the mass of this excited species is 30 amu and is therefore very likely NO*. Accepting this mass, the kinetic-energy distribution of this excited particle is shown in Fig. 5 for a laser fluence of 300 mJ/cm^2, showing a maximum at $\sim$10 eV and extends out to over 15 eV. Such kinetic energies are clearly nonthermal *and* are also too high to arise from a simple photodissociative process.

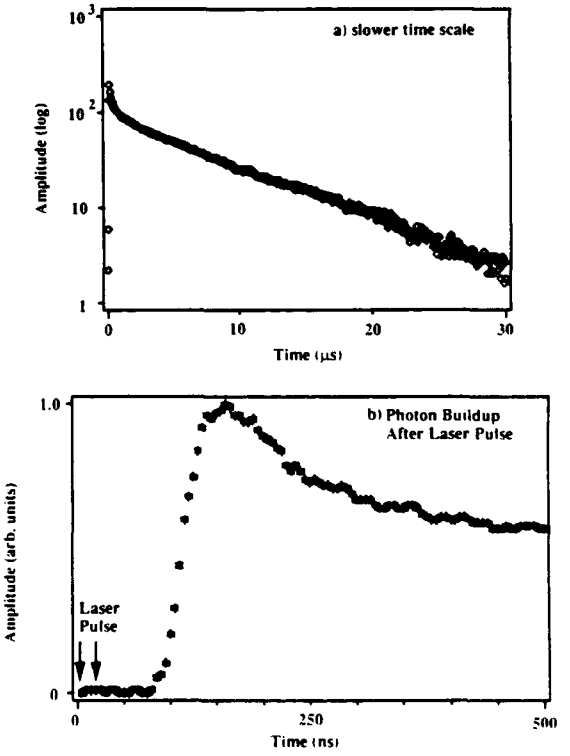

FIG. 6. (a) Photon emission from the surface region of the crystal showing the time dependence of the near UV-VIS emission relative to the laser pulse. (b) the time interval near the time of the laser pulse.

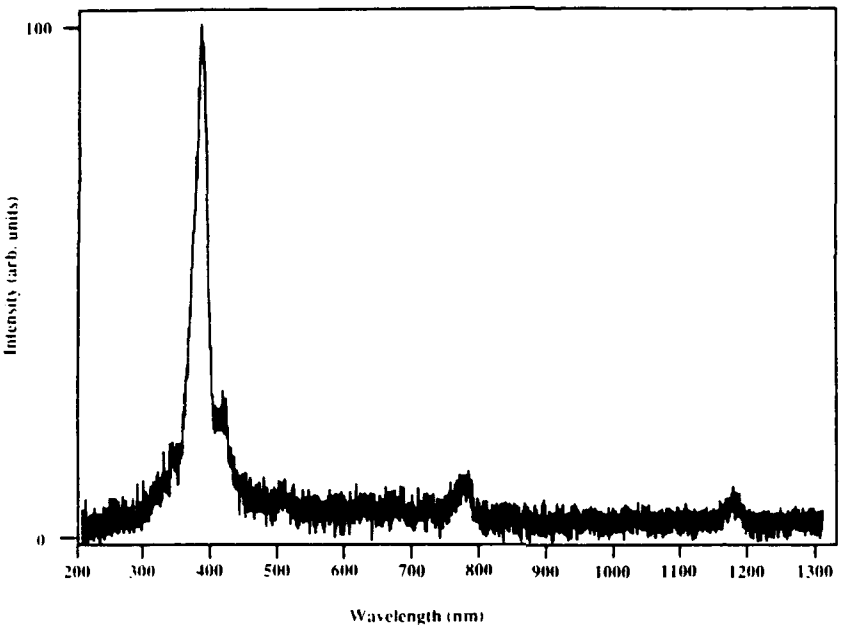

FIG. 7. The spectrum of the photon emission emitted from near the sample surface over the time interval 200 ns to 1.2 μs after the laser pulse.

D. Photon emission

We continued the search for other evidence of products in excited states by examining the near-surface region of the RDX crystal for visible light emission. Other than fluorescence in the crystal itself, the only light detected occurred directly at the surface of the crystal. Figure 6(a) shows the *total* near UV-visible emission (log intensity scale) versus time on a relatively slow time scale, for a laser fluence of 130 mJ/cm^2, measured with a fiber optics bundle pointed directly at the crystal surface coupled to a photomultiplier (PMT). Figure 6(b) shows on a linear intensity scale and faster time scale, the rise in photon intensity versus time, where $t = 0$ represents the beginning of the laser pulse. We note from these two curves that there is a clear *delay* in the build up of the light emission after the laser pulse and the light is sustained for several tens of microseconds. Using the time resolution capabilities of the optical multichannel analyzer, we analyzed the emission spectrum versus time after the laser pulse. Figure 7 shows the resulting low-resolution emission spectrum taken at a fluence of 600 mJ/cm^2, acquired over a 1-μs time interval, starting 200 ns after the onset of the 20-ns laser pulse. The spectrum remains unchanged over the time interval of a few μs after the laser pulse where it is eventually lost in noise. The spectrum is due entirely to the allowed $B\,^2\Sigma^+ \rightarrow X\,^2\Sigma^+$ transitions in the diatomic radical CN (the features at $\sim$775 and 1160 nm are higher-order diffraction peaks). There is no evidence of the RDX fluorescence and phosphorescence spectra seen by Marinkas.[19] The RDX fluorescence *should* be missing due to the 100-ns delay—Marinkas reports a lifetime < 2 ns. If we probe the light emission with either the PMT or the spectrometer just a few cm further out from the surface (i.e., *not* viewing the surface) no detectable light is observed. Since the lifetime of the CN $B\,^2\Sigma^+$ states are $\sim$60 ns,[20] any CN* created at the surface could only travel distances < 0.1 cm from the surface and therefore these states are being *created* at times considerably longer than the duration of the laser pulse. Two important conclusions are suggested.

First, the production of CN* is occurring after laser stimulation on a time scale of $\sim$100 ns in a expanding reaction zone due to pressure dependent chemistry. A likely mechanism for this creation on such a long time scale is chemiluminescence involving products from the decomposition. For example, CN $B\,^2\Sigma^+ \rightarrow X\,^2\Sigma^+$ chemiluminescence has been shown to arise from the following reactions (from Refs. 21, 22, and 23, respectively):

$$C + NO \rightarrow CN^* + O,$$

$$C^+ + N_2O \rightarrow CN^* + NO^+,$$

$$C_2(a^3\Pi) + NO \rightarrow CN^* + CO.$$

Similarly, Faust *et al.*[24] have suggested that delayed, pressure-dependent chemiluminescence they observed following photofragmentation of a variety of simple molecules was due to ion-molecule reactions following stimulation.

Second, to produce a 10–100 μs duration in the creation of CN*, the reactants must be produced for times of several tens of microseconds after the laser pulse. We therefore conclude that there is a sustained exothermic reaction at the RDX surface, originally ignited by the laser, continuing *after* the laser pulse. For the fluences used here, this reaction builds up in a few tens of ns, then dissipates on the time frame of 10–10$^{1.2}$ μs as opposed to running away due to some form of dissipation (e.g., thermal conductivity) which counters the growth of the energy releasing decomposition.

E. Sustained emission of neutral species

To prove that such sustained reactions are present, we constructed a "total neutral-emission" probe, drawn schematically in Fig. 8(a), consisting of an ionizer from a QMS

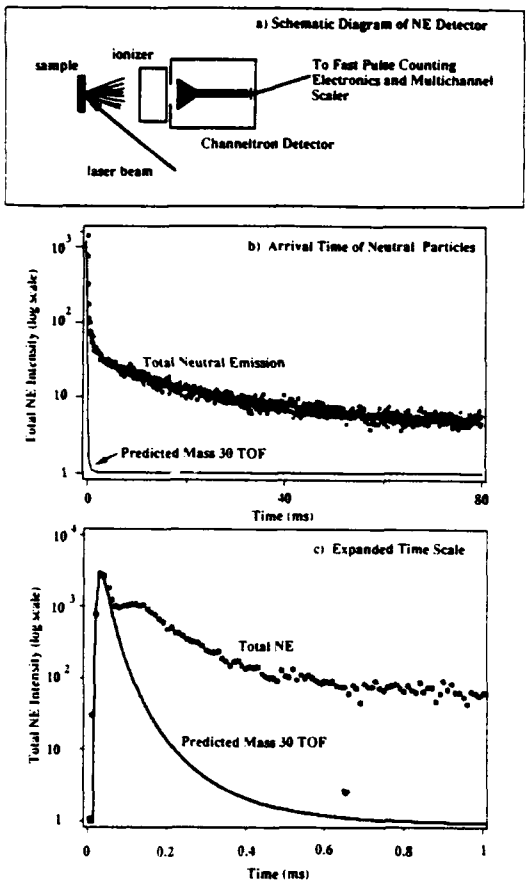

FIG. 8. (a) Schematic diagram of the neutral emission detector for probing in a very sensitive way the total gaseous emission following the laser pulse. (b) The resulting pulse-counted emission for a time period of 80 ms. The solid curve shows the mass 30 emission which would be detected at the position of the ionizer used in this study (4 cm). (c) The first 1 ms of the above data.

followed directly by an electron multiplier (CEM) placed out of direct line of sight. To increase our sensitivity to low fluxes of neutrals, we ran the CEM in a pulse-counting mode (thus, every ion detected by the CEM was converted to a countable pulse). Without any incident laser light, the background gases led to negligible counts during data acquisition. The resulting signal (ion counts/1 μs time interval) from incident neutrals accumulated for 20 successive laser pulses ($t = 0$) is shown in Fig. 8(b) and on an expanded time scale, Fig. 8(c). If we generate the appropriate time-of-flight distribution for the heaviest of the major neutral species, mass 30, by transforming the mass 30 curve fit for the data shown in Fig. 2 to appropriate shorter times due to a shorter flight path, we see the superimposed curves shown with solid lines, again plotted on a log scale to emphasize trends at long times. Under this high-sensitivity pulse counting mode of acquiring neutral emission, we see that the tail is, in fact, sustained well after the decay of the faster component and is consistent with the above interpretation of a sustained decomposition reaction. For the initial steep part of the decay, the time constant is nearly equal to the decay in the photon emission (attributed to excited CN*) observed after the laser pulse. Thus, these signals serve as evidence that at the completion of the laser pulse, there is a continuation of the decomposition which damps out in a few milliseconds. This long decay cannot be attributed to pump out of our vacuum system in response to a pressure pulse; the latter has a measured characteristic decay constant of ~ 400 ms which probably corresponds to the flat part of these curves.

One further attribute of the mass selected neutral emission not discussed above, which suggests that a reaction is being induced in the crystal, is that we discovered that at constant fluence (incident laser energy per unit area) masses above mass 46 were detectable only if we reduced the spot size of the bombarded region. Figure 9 shows the intensity of (a) the mass 75 peak and (b) the total pressure increase as a function of spot size, both of which are clearly nonlinear. As the spot size is increased, mass 75 first rapidly increases, then decreases to zero; the other masses above 50 amu behave similarly. The total pressure change (representing the total amount of gas released per laser shot) increases nearly exponentially with spot size (the detector used for this measurement saturated at ~ 0.3-mm^2 spot size—thus terminating the curve).

If the neutral emission were caused by a mechanism that

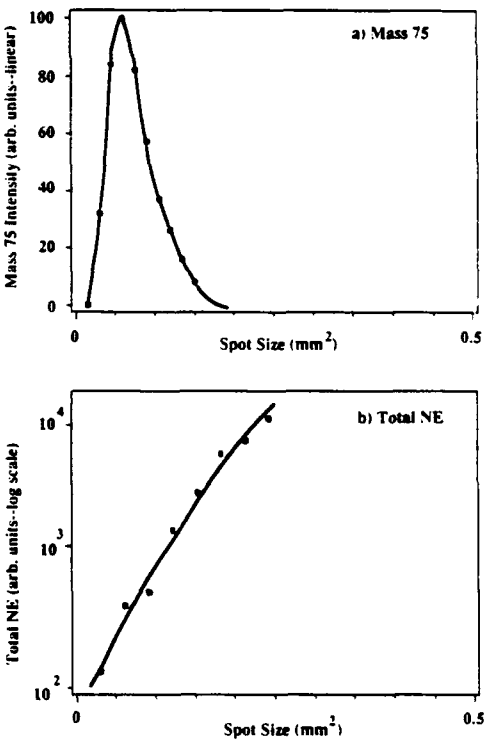

FIG. 9. (a) The emission intensity (arbitrary units—linear scale) for mass 75 vs spot size of the focused laser beam on the crystal surface. The laser fluence was kept constant at 120 mJ/cm^2. (b) The total pressure change (arbitrary units, log scale) from ablation of the RDX at the same laser fluence (120 mJ/cm^2) vs spot size.

only involved the number of photons striking each absorption center, there should be a simple linear dependence of the individual products and total gas emission on the spot size. On the contrary, this area (volume) effect suggests that the effectiveness or probability of igniting a sustained decomposition reaction increases and this reaction propagates into a larger portion of the crystal in a nonlinear fashion as more of the crystal is exposed to the laser. The disappearance of masses 52–120 amu at larger spot sizes is perhaps caused by higher numbers of collisions of these heavier products with other gas molecules due to a significant increase in gas density, which result in their demise.

F. Positive- and negative-ion emission

Preliminary studies of the charged-particle emission from RDX show the emission of positive ions over a wide range of fluences. In near-field free-drift conditions, the positive ions exhibit velocities of similar magnitude to the excited neutral emission, showing an increase in velocity with fluence. By slight displacement of the QMS from direct line of sight to the bombarded region we were able to separate the excited neutrals from the positive-ion emission (PIE) and achieve mass selection and therefore determine the ion masses. Figure 10 shows the signals corresponding to the only three positive ion species detectable above our noise, namely, 30, 18, and 42 amu, acquired at a fluence of 350 mJ/cm^2. Their relative intensities are approximately 100:8:3, respectively, and we assign to these masses NO, H_2O, and CH_2NN and/or C_2H_4N. Although these correspond to large peaks with the same identity in the LIMA measurements of Tang *et al.*, they see larger peaks which are completely missing from our PIE spectrum (e.g., 12 [C^+], 15 [CH_3^+], and 27 [HCN^+]—Tang's assignments shown in square brackets).

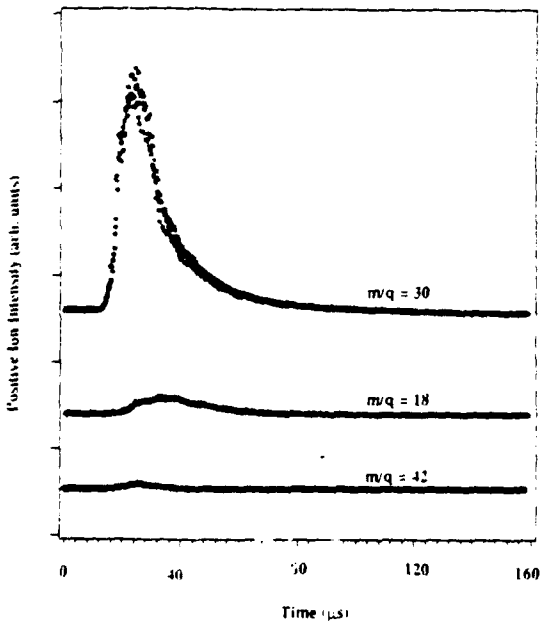

FIG. 10. Positive-ion signals corresponding to quadrupole mass filter settings of 30, 18, and 42 amu. Laser fluence = 350 mJ/cm^2.

In our case, most of the emitted ions are mass 30 (NO^+). Letting *all* of the ions drift under essentially field-free conditions (there is some field penetration of the front cone of the CEM detector tending to accelerate ions near the completion of their flight path), the resulting TOF can be transformed into an energy distribution which we attribute to the dominant mass 30 ions. The resulting distribution function is shown in Fig. 5 (symbol: ◇) for a laser fluence of 350 mJ/cm^2, approximately the fluence used to generate the excited neutral-energy distribution (symbol: *). The ion-energy distribution (◇) is consistent with initial kinetic energies calculated from the mass selected mass 30 ion data (e.g., Fig. 10) where the flight path purposefully included applied accelerating fields. From Fig. 5, we see that the PIE energy distribution peaks at ~10 eV, and is quite similar to the excited neutral-energy distribution if we allow for some broadening of the ion distribution due at least partially to stray E fields. The similarities in these energy distributions provides strong evidence that the excited neutral is a mass 30 ion which has been (a) accelerated away from the surface, and (b) neutralized in the near-surface region where collisions can occur with high frequency. This mass 30 PIE time-of-flight signal is considerably faster than the slower ground-state neutrals, e.g., as shown in Fig. 2, which we have attributed primarily to NO. The NO molecule is known to have one long-lived excited state, namely the $a^4\Pi$ state, with a lifetime >0.1 s and lying 4.8 eV above the ($X^2\Pi$) ground state.[25] A second state with possible long lifetime is the $b\,^4\Sigma^-$ which lies 6 eV above the ground state. In terms of detection by impact with the CEM front cone surface, the latter is more likely to release electrons by deexcitation. We therefore attribute the formation of this excited species to the collisional reneutralization of energetic NO^+ into a long-lived excited state of NO.

There appears to be little evidence of laser-plume interactions such as seen in excimer laser irradiation of polymers and glass reported earlier. The latter could cause acceleration of positive ions as explained in Ref. 15. In RDX a more likely source of PIE kinetic energy is an electrostatic effect. The rapid removal of photoelectrons from the crystal leaves behind a distribution of positive charge which can accelerate the positive ions away from the surface. The resulting ion energy distributions are thus a measure of the electrostatic potentials at the positions where the ions were created. A simple electrometer measurement with an electrode placed on the edge of one of the RDX crystals confirmed that the crystal was charging positively upon incidence of laser light. In addition, copious electron emission was detected using a Channeltron biased positively. The electron emission was confirmed by the submicrosecond time-of-flight of negative charge at a detector several cm away from the bombarded region.

For the sake of completeness, the emission of negative ions were also observed, as indicated by microsecond flight times. These negative ions exhibited TOF behavior consistent with ionic species over a range of masses somewhat low-

er than the positive ions, although we have not as yet determined their masses nor kinetic energies. Tang *et al.*[4] observed intense negative-ion emission from RDX (at 266 nm) corresponding to CN^-, $CH_2N_2^-$, and perhaps $CNCH_2NO^-$ in addition to other masses.

IV. DISCUSSION

Neither a simple photochemical nor photothermal mechanism can explain all of these observations. The following preliminary model is proposed for the ablation process observed in RDX.

(1) Under laser irradiation, photochemical and possibly photothermal decomposition of the RDX molecules is initiated in the surface and near-surface region of the crystal. As a function of fluence, the penetration of higher-intensity UV into the crystal and therefore the depth of the process zone increases. Electrons and ionic products are produced by photonic processes (nonthermal). Some heating of the surface due to laser absorption does occur, however, via vibronic transitions. The exothermicity of the decomposition results in 0–1-eV kinetic energies of fragments in regions of high density. Thus, chemical energy, converted to kinetic energy of the fragments leads to thermalization in the near-surface region. Consequently, many of the uncharged products have a Maxwellian velocity distribution, consistent with the establishment of equilibrium. We propose that the higher temperature (i.e., 3000 K) portions of the time-of-flight curves seen for example at 18, 27, and 30 amu correspond to the laser-induced decomposition.

(2) The initial excitation liberates sufficient energy to initiate a self-sustaining decomposition reaction which appears to reach a peak in ~ 100 ns and lasts for tens of microseconds after the laser pulse. The effective temperature of this chemistry is lower (~ 1100 K); masses 26 and 29 were dominated by this low temperature component in the time-of-flight curves.

(3) The removal of the NO_2 from the RDX molecule may occur in a direct fashion without an intermediate. Several other products are consistent with secondary decomposition paths from the concerted decomposition intermediate $CH_2N_2O_2$ discussed by Zhao and co-workers.[5]

(4) The 383-nm photon emission seen at the surface over several microseconds in duration is attributed to chemiluminescence from CN. This is consistent with the continuation of the decomposition reaction some time after the laser pulse, which serves as a source of reactants to create the CN*.

(5) At constant laser fluence (energy/area) the onset of the sustained decomposition reaction depends on the size of the laser beam due to a volume effect regarding the transport of energy between portions of the crystal. The highly localized holes observed in some of the crystals are attributed to the etching occurring during the sustained reaction. When extensive decomposition occurs inside the crystal (e.g., at high fluences), sufficient pressures build up to result in fracture. When such fracture occurs on the back side of the crystal gases blowing off the backside carry away ejecta (micron-sized pieces) produced by fracture. Increasing the size of the irradiated spot (at constant fluence) changes dramatically the extent of the decomposition reaction and can affect the products observed away from the surface. Larger spot size may result in a more intense sustained reaction through collective processes and and/or limited transport of heat away from the reaction zone.

(6) Recombination chemical reactions are occurring: Products such as H_2O, N_2, and NH are likely due to collisional reactions occurring in the process zone.

(7) Evidence for the occurrence of dynamic gas-phase processes are seen in the existence of the excited neutral species as well as the high-metastable and ion-energy distributions. The similarities between the excited neutral and the 30-amu positive ion leads us to propose that the excited neutral is NO in a long-lived electronic excited state created by reneutralization of energetic NO^+ ions. The combination of high kinetic energy and charge (or in the case of the excited neutral, several eV of internal electronic energy) takes a large amount of energy per particle away from the reaction zone.

(8) Negative ions may be a result of photoelectron collisions (at low energies) with molecular species in the process of dissociating (or remnants from earlier laser pulses).

V. CONCLUSIONS

Bombarding RDX with 248-nm laser pulses at fluences of 5–750 mJ/cm^2 results in a wide range of effects including photoelectron emission, production of $\pm$ ions, ground-state neutrals (2–120 amu), excited neutral CN, a long-lived excited neutral species identified as NO*, ablative etching of the crystal, and at higher fluences fracture of the crystal. We have presented evidence for the ignition of a sustained decomposition reaction which continues many tens of μs after bombardment. A number of additional studies are suggested such as the following:

(i) Developing a more detailed model for the production of the principle neutral species and explaining their velocity distributions.

(ii) Addressing a number of issues regarding the "hot" component in the neutral emission vs "cooler" component, i.e., proving that the former is directly laser induced and the latter is coming from the self-sustained reaction that follows. The corresponding reaction paths for these two types of emission are needed. Comparing measurements of front-side/backside emissions might be one way to proceed.

(iii) Carrying out a more detailed examination of the reactions creating the CN* and NO*.

(iv) Examining in more detail the etching of holes and phenomena responsible for fracture by laser bombardment.

(v) Probing the laser wavelength dependence of these phenomena.

(vi) Probing the spatial distributions of the gaseous products, similar to Parr's studies[26] of combustion of RDX using planar laser-induced fluorescence imaging.

ACKNOWLEDGMENTS

This work was supported by the Office of Naval Research Contract No. N00014-87-K-0514, Dr. R. S. Miller, Program Manager, and the Washington Technology Center.

We wish to thank Mark Dexter for his assistance in carrying out these experiments.

[1]R. Srinivasan, Science **234**, 559 (1986).
[2]W. A. Schroeder, P. E. Wilcox, K. N. Trueblood, and A. O. Dekker, Anal. Chem. **23**, 1740 (1951).
[3]L. C. Yang and V. J. Menichelli, Appl. Phys. Lett. **19**, 473 (1971).
[4]T. B. Tang, M. M. Chaudhri, C. S. Rees, and S. J. Mullock, J. Mater. Sci. **22**, 1037 (1987).
[5]X. Zhao, E. Hintsa, and Y. T. Lee, J. Chem. Phys. **88**, 801 (1988).
[6]R. Engelke, W. L. Earl, and C. McMichael Rohlfing, J. Phys. Chem. **90**, 545 (1986).
[7]J. T. Hagan and M. M. Chaudhri, J. Mater. Res. **12**, 1055 (1977).
[8]P. J. Halfpenny, K. J. Roberts, and J. N. Sherwood, J. Mater. Sci. **19**, 1629 (1984).
[9]C. S. Choi and H. P. Boutin, Acta Crystallogr. Sect. B Struct. Crystallogr. Cryst. Chem. **26**, 1235 (1970).
[10]J. H. Craig and J. L. Hock, J. Vac. Sci. Technol. **17**, 1362 (1980).
[11]J. M. McBride, B. E. Segmuller, M. D. Hollingsworth, D. E. Mills, and B. A. Weber, Science **234**, 830 (1986).
[12]M. Faber and R. D. Srivastava, Chem. Phys. Lett. **64**, 307 (1979).
[13]R. Behrens, Jr., in Proceedings of NATO Advanced Studies Institute on Chemistry and Physics of Energetic Materials, September, 1989, Alta-villa, Milicia, Sicily, edited by S. Bulusu (unpublished).
[14]Y. Oyumi and T. B. Brill, Combust. Flame **62**, 213 (1985).
[15]K. Tonyali, L. C. Jensen, and J. T. Dickinson, J. Vac. Sci. Technol. A **6**, 941 (1988).
[16]P. A. Eschbach, J. T. Dickinson, S. C. Langford, and L. R. Pederson, J. Vac. Sci. Technol. A (to be published).
[17]E. E. Muschlitz, Jr., in *Molecular Beams*, edited by J. Ross (Wiley Interscience, New York, 1966).
[18]R. S. Freund, in *Rydberg States of Atoms and Molecules*, edited by R. F. Stebbings and F. B. Dunning (Cambridge University Press, Cambridge, 1983), pp. 355–392.
[19]P. L. Marinkas, J. Lumin. **15**, 57 (1977).
[20]H. Okabe, *Photochemistry of Small Molecules* (Wiley Interscience, New York, 1978), p. 198.
[21]D. Brandt and Ch. Ottinger, Chem. Phys. Lett. **23**, 257 (1973).
[22]M. Tsuji, I. Nagano, T. Susuki, K. Mizukami, H. Obase, and Y. Nishimura, J. Phys. Chem. **90**, 3998 (1986).
[23]J. B. Lurie and M. A. El-Sayed, J. Phys. Chem. **84**, 3348 (1980).
[24]W. L. Faust, B. B. Craig, S. Chattopadhyay, and R. G. Weiss, J. Phys. Chem. **91**, 54 (1987).
[25]E. Miescher and K. P. Huber, in *Physical Chemistry: Series Two, Volume 3, International Review of Science*, edited by A. Buckingham (Butterworths, London, 1976), pp. 37–74.
[26]T. Parr, Naval Weapons Center (private communication).

Ser 432/84/211DYN
Revised January 1985

(DYN)

DISTRIBUTION LIST

Dr. R.S. Miller
Office of Naval Research
Code 432P
Arlington, VA 22217
(10 copies)

Dr. J. Pastine
Naval Sea Systems Command
Code 06R
Washington, DC 20362

Dr. Kenneth D. Hartman
Hercules Aerospace Division
Hercules Incorporated
Alleghany Ballistic Lab
P.O. Box 210
Washington, DC 21502

Mr. Otto K. Heiney
AFATL-DLJG
Elgin AFB, FL 32542

Dr. Merrill K. King
Atlantic Research Corp.
5390 Cherokee Avenue
Alexandria, VA 22312

Dr. R.L. Lou
Aerojet Strategic Propulsion Co.
Bldg. 05025 - Dept 5400 - MS 167
P.O. Box 15699C
Sacramenta, CA 95813

Dr. R. Olsen
Aerojet Strategic Propulsion Co.
Bldg. 05025 - Dept 5400 - MS 167
P.O. Box 15699C
Sacramento, CA 95813

Dr. Randy Peters
Aerojet Strategic Propulsion Co.
Bldg. 05025 - Dept 5400 - MS 167
P.O. Box 15699C
Sacramento, CA 95813

Dr. D. Mann
U.S. Army Research Office
Engineering Division
Box 12211
Research Triangle Park, NC 27709-2211

Dr. L.V. Schmidt
Office of Naval Technology
Code 07CT
Arlington, VA 22217

JHU Applied Physics Laboratory
ATTN: CPIA (Mr. T.W. Christian)
Johns Hopkins Rd.
Laurel, MD 20707

Dr. R. McGuire
Lawrence Livermore Laboratory
University of California
Code L-324
Livermore, CA 94550

P.A. Miller
736 Leavenworth Street, #6
San Francisco, CA 94109

Dr. W. Moniz
Naval Research Lab.
Code 6120
Washington, DC 20375

Dr. K.F. Mueller
Naval Surface Weapons Center
Code R11
White Oak
Silver Spring, MD 20910

Prof. M. Nicol
Dept. of Chemistry & Biochemistry
University of California
Los Angeles, CA 90024

Mr. L. Roslund
Naval Surface Weapons Center
Code R10C
White Oak, Silver Spring, MD 20910

Dr. David C. Sayles
Ballistic Missile Defense
Advanced Technology Center
P.O. Box 1500
Huntsville, AL 35807

Ser 432/84/340
Revised January 1985

(DYN)

DISTRIBUTION LIST

Dr. C.S. Coffey
Naval Surface Weapons Center
Code R13
White Oak
Silver Spring, MD 20910

D. Curran
SRI International
333 Ravenswood Avenue
Menlo Park, CA 94025

E.L. Throckmorton
Code SP-2731
Strategic Systems Program Office
Crystal Mall #3, RM 1048
Washington, DC 23076

Dr. R. Martinson
Lockheed Missiles and Space Co.
Research and Development
3251 Hanover Street
Palo Alto, CA 94304

C. Gotzmer
Naval Surface Weapons Center
Code R-11
White Oak
Silver Spring, MD 20910

G.A. Lo
3251 Hanover Street
B204 Lockheed Palo Alto Research Lab
Palto Alto, CA 94304

R.A. Schapery
Civil Engineering Department
Texas A&M University
College Station, TX 77843

J.M. Culver
Strategic Systems Projects Office
SSPO/SP-2731
Crystal Mall #3, RM 1048
Washington, DC 20376

Prof. G.D. Duvall
Washington State University
Department of Physics
Pullman, WA 99163

Dr. E. Martin
Naval Weapons Center
Code 3858
China Lake, CA 93555

Dr. M. Farber
135 W. Maple Avenue
Monnovia, CA 91016

W.L. Elban
Naval Surface Weapons Center
White Oak, Bldg. 343
Silver Spring, MD 20910

G.E. Manser
Morton Thiokol
Wasatch Division
P.O. Box 524
Brigham City, UT 84302

R.G. Rosemeier
Brimrose Corporation
7720 Belair Road
Baltimore, MD 20742

Ser 432/84/211DYN
Revised January 1985

(DYN)

DISTRIBUTION LIST

Dr. Anthony J. Matuszko
Air Force Office of Scientific Research
Directorate of Chemical & Atmospheric Sciences
Bolling Air Force Base
Washington, DC 20332

Dr. Michael Chaykovsky
Naval Surface Weapons Center
Code R11
White Oak
Silver Spring, MD 20910

J.J. Rocchio
USA Ballistic Research Lab.
Aberdeen Proving Ground, MD 21005-5066

G.A. Zimmerman
Aerojet Tactical Systems
P.O. Box 13400
Sacramento, CA 95813

B. Swanson
INC-4 MS C-346
Los Alamos National Laboratory
Los Alamos, New Mexico 87545

Dr. James T. Bryant
Naval Weapons Center
Code 3205B
China Lake, CA 93555

Dr. L. Rothstein
Assistant Director
Naval Explosives Dev. Engineering Dept.
Naval Weapons Station
Yorktown, VA 23691

Dr. M.J. Kamlet
Naval Surface Weapons Center
Code R11
White Oak, Silver Spring, MD 20910

Dr. Henry Webster, III
Manager, Chemical Sciences Branch
ATTN: Code 5063
Crane, IN 47522

Dr. A.L. Slafkosky
Scientific Advisor
Commandant of the Marine Corps
Code RD-1
Washington, DC 20380

Dr. H.G. Adolph
Naval Surface Weapons Center
Code R11
White Oak
Silver Spring, MD 20910

U.S. Army Research Office
Chemical & Biological Sciences Division
P.O. Box 12211
Research Triangle Park, NC 27709

G. Butcher
Hercules, Inc.
MS X2H
P.O. Box 98
Magna, Utah 84044

W. Waesche
Atlantic Research Corp.
7511 Wellington Road
Gainesville, VA 22065

Dr. John S. Wilkes, Jr.
FJSRL/NC
USAF Academy, CO 80840

Dr. H. Rosenwasser
AIR-320R
Naval Air Systems Command
Washington, DC 20361

Dr. Joyce J. Kaufman
The Johns Hopkins University
Department of Chemistry
Baltimore, MD 21218

Dr. A. Nielsen
Naval Weapons Center
Code 385
China Lake, CA 93555

Ser 432/84/340
Revised January 1985

(DYN)

DISTRIBUTION LIST

K.D. Pae
High Pressure Materials Research Lab.
Rutgers University
P.O. Box 909
Piscataway, NJ 08854

Dr. John K. Dienes
T-3, B216
Los Alamos National Lab.
P.O. Box 1663
Los Alamos, NM 87544

A.N. Gent
Institute Polymer Science
University of Akron
Akron, OH 44325

Dr. D.A. Shockey
SRI International
333 Ravenswood Ave.
Menlo Park, CA 94025

Dr. R.B. Kruse
Morton Thiokol, Inc.
Huntsville Division
Huntsville, AL 35807-7501

G. Butcher
Hercules, Inc.
P.O. Box 98
Magna, UT 84044

W. Waesche
Atlantic Research Corp.
7511 Wellington Road
Gainesville, VA 22065

Dr. R. Bernecker
Naval Surface Weapons Center
Code R13
White Oak
Silver Spring, MD 20910

Prof. Edward Price
Georgia Institute of Tech.
School of Aerospace Engineering
Atlanta, GA 30332

J.A. Birkett
Naval Ordnance Station
Code 5253K
Indian Head, MD 20640

Prof. R.W. Armstrong
University of Maryland
Dept. of Mechanical Engineering
College Park, MD 20742

Herb Richter
Code 385
Naval Weapons Center
China Lake, CA 93555

J.T. Rosenberg
SRI International
333 Ravenswood Ave.
Menlo Park, CA 94025

G.A. Zimmerman
Aeroject Tactical Systems
P.O. Box 13400
Sacramento, CA 95813

Prof. Kenneth Kuo
Pennsylvania State University
Dept. of Mechanical Engineering
University Park, PA 16802

T.L. Boggs
Naval Weapons Center
Code 3891
China Lake, CA 93555

Ser 432/84/211DYN
Revised January 1985

(DYN)

DISTRIBUTION LIST

R.E. Shenton
Atlantic Research Corp.
7511 Wellington Road
Gainesville, VA 22065

Brian Wheatley
Atlantic Research Corp.
7511 Wellington Road
Gainesville, VA 22065

Mike Barnes
Atlantic Research Corp.
7511 Wellington Road
Gainesville, VA 22065

Mr. G. Edwards
Naval Sea Systems Command
Code 62R32
Washington, DC 20362

Dr. Lionel Dickinson
Naval Explosive Ordinance
Disposal Tech. Center
Code D
Indian Head, MD 20340

C. Dickinson
Naval Surface Weapons Center
White Oak, Code R-13
Silver Spring, MD 20910

Prof. J.T. Dickinson
Washington State University
Dept. of Physics 4
Pullman, WA 99164-2814

Prof. John Deutch
MIT
Department of Chemistry
Cambridge, MA 02139

M.H. Miles
Dept. of Physics
Washington State University
Pullman, WA 99164-2814

Dr. E.H. deButts
Hercules Aerospace Co.
P.O. Box 27408
Salt Lake City, UT 84127

Dr. T.F. Davidson
Vice President, Technical
Morton Thiokol, Inc.
Aerospace Group
110 North Wacker Drive
Chicago, Illinois 60606

David A. Flanigan
Director, Advanced Technology
Morton Thiokol, Inc.
Aerospace Group
110 North Wacker Drive
Chicago, Illinois 60606

Mr. J. Consaga
Naval Surface Weapons Center
Code R-16
Indian Head, MD 20640

Dr. L.H. Caveny
Air Force Office of Scientific
Research
Directorate of Aerospace Sciences
Bolling Air Force Base
Washington, DC 20332

Naval Sea Systems Command
ATTN: Mr. Charles M. Christensen
NAVSEA-62R2
Crystal Plaza, Bldg. 6, Rm 806
Washington, DC 20362

W.G. Roger
Code 5253
Naval Ordance Station
Indian Head, MD 20640

Mr. R. Beauregard
Naval Sea Systems Command
SEA 64E
Washington, DC 20362

Dr. Donald L. Ball
Air Force Office of Scientific
Research
Directorate of Chemical &
Atmospheric Sciences
Bolling Air Force Base
Washington, DC 20332

Ser 432/84/340
Revised January 1985

Administrative Contracting
Officer (see contract for
address)
(1 copy)

Director
Naval Research Laboratory
Attn: Code 2627
Washington, DC 20375
(6 copies)

Defense Technical Information Center
Bldg. 5, Cameron Station
Alexandria, VA 22314
(12 copies)

Dr. Robert Polvani
National Bureau of Standards
Metallurgy Division
Washington, D.C. 20234

Dr. Y. Gupta
Washington State University
Department of Physics
Pullman, WA 99163

Ser 432/84/211DYN
Revised January 1985

(DYN)

DISTRIBUTION LIST

Mr. R. Geisler
ATTN: DY/MS-24
AFRPL
Edwards AFB, CA 93523

Naval Air Systems Command
ATTN: Mr. Bertram P. Sobers
NAVAIR-320G
Jefferson Plaza 1, RM 472
Washington, DC 20361

R.B. Steele
Aerojet Strategic Propulsion Co.
P.O. Box 15699C
Sacramento, CA 95813

Mr. M. Stosz
Naval Surface Weapons Center
Code R10B
White Oak
Silver Spring, MD 20910

Mr. E.S. Sutton
Thiokol Corporation
Elkton Division
P.O. Box 241
Elkton, MD 21921

Dr. Grant Thompson
Morton Thiokol, Inc.
Wasatch Division
MS 240 P.O. Box 524
Brigham City, UT 84302

Dr. R.S. Valentini
United Technologies Chemical Systems
P.O. Box 50015
San Jose, CA 95150-0015

Dr. R.F. Walker
Chief, Energetic Materials Division
DRSMC-LCE (D), B-3022
USA ARDC
Dover, NJ 07801

Dr. Janet Wall
Code 012
Director, Research Administration
Naval Postgraduate School
Monterey, CA 93943

Director
US Army Ballistic Research Lab.
ATTN: DRXBR-IBD
Aberdeen Proving Ground, MD 21005

Commander
US Army Missile Command
ATTN: DRSMI-RKL
Walter W. Wharton
Redstone Arsenal, AL 35898

Dr. Ingo W. May
Army Ballistic Research Lab.
ARRADCOM
Code DRXBR - 1BD
Aberdeen Proving Ground, MD 21005

Dr. E. Zimet
Office of Naval Technology
Code 071
Arlington, VA 22217

Dr. Ronald L. Derr
Naval Weapons Center
Code 389
China Lake, CA 93555

T. Boggs
Naval Weapons Center
Code 389
China Lake, CA 93555

Lee C. Estabrook, P.E.
Morton Thiokol, Inc.
P.O. Box 30058
Shreveport, Louisiana 71130

Dr. J.R. West
Morton Thiokol, Inc.
P.O. Box 30058
Shreveport, Louisiana 71130

Dr. D.D. Dillehay
Morton Thiokol, Inc.
Longhorn Division
Marshall, TX 75670

G.T. Bowman
Atlantic Research Corp.
7511 Wellington Road
Gainesville, VA 22065